

Laboratoire TIMC-IMAG, UMR5525 UJF – CNRS – INPG
Université Joseph Fourier – Grenoble I

**Modélisation et conception d'outils robotisés et de techniques de fraisage
pour l'arthroplastie total du genou**

**Modeling and Design of Robotized Tools and Milling Techniques
for Total Knee Arthroplasty**

THESE

Présentée par:

Christopher PLASKOS

pour obtenir le titre de

Docteur de l'Université Joseph Fourier

Spécialité : MODELISATION DES SYSTEMES VIVANTS

Date de soutenance : 1 décembre 2005

Composition du Jury :

Professeur Etienne Dombre, LIRMM, Université de Montpellier, rapporteur

Professeur Michel de Mathelin, LSIIT, Université de Strasbourg 1, rapporteur

Docteur Eric Stindel, LATIM, Université de Bretagne Occidentale, Brest, examinateur

Professeur Antony J Hodgson, University of British Columbia, Vancouver, Canada, co-directeur de thèse

Professeur Philippe Cinquin, TIMC-IMAG, Université Joseph Fourier, Grenoble, directeur de thèse

Abstract

Computer-assisted surgery (CAS) has brought enormous added value to medical interventions by providing precise measurement tools that permit surgeons to quantify and control their gestures. In total knee arthroplasty (TKA), CAS has significantly reduced implant alignment and positioning variability, which has been correlated to early failures requiring revision surgery.

There remains however a clinical demand for enhanced precision and capabilities that perhaps only robotics or ‘intelligent instruments’ coupled with navigation systems can offer.

In this work a novel robotic tool for bone-milling in CAS TKA is developed. Our miniature bone-mounted robot, named *Praxiteles*, attaches to the side of the knee and precisely positions a milling guide so that the surgeon can make the cuts manually.

Because manual milling is known to be an inherently unstable process, however, a predictive model was formulated and experiments were conducted in order to better understand and improve the bone-milling process. The physics of bone-cutting was first analysed in the simplest case possible: high-speed orthogonal (2D) and oblique (3D) single-edge cutting. This knowledge was then integrated into a flexible model for predicting milling forces as a function of the surgical parameters. We make recommendations for optimal milling techniques and tools based on an analysis of force and stability. Experimental results on cadavers with our new robot and milling technique are very encouraging, and we hope to start clinical trials in the future.

Keywords: computer and robot assisted surgery, total knee arthroplasty, modelling bone milling and cutting forces.

Résumé

La chirurgie assistée par ordinateur a amené une valeur ajoutée significative aux interventions médicales, en fournissant des outils de mesures permettant au chirurgien de quantifier et contrôler leurs gestes. En orthopédie et notamment pour la pose de prothèse totale de genou (PTG), la chirurgie assistée par ordinateur a réduit de manière significative les variations d’alignement et de position, paramètres directement corrélés aux échecs précoces nécessitant une chirurgie de reprise.

Les cliniciens restent néanmoins demandeurs d’une précision accrue et de possibilités additionnelles, qui semblent ne pouvoir être offertes que par de la robotique ou des ‘outils intelligents’ couplés à de la navigation.

Dans ce travail, un nouvel outil robotique dédié au fraisage de l’os pour les chirurgies des PTG a été développé. Notre robot miniature, appelé PRAXITELES, est fixé directement sur l’os sur l’un des côtés du genou, il positionne avec précision un guide de fraisage qui permet au chirurgien de faire manuellement les coupes.

Le fraisage manuel est un acte difficile avec peu de stabilité, c’est pourquoi, un modèle prédictif a été formulé, et des tests ont été menés pour mieux le comprendre et pour l’améliorer. La physique de la coupe osseuse a d’abord été étudiée dans le cas le plus simple : coupe à grande vitesse orthogonale (2D) et oblique (3D). Les résultats ont ensuite été intégrés dans un modèle flexible pour la prédiction des forces de fraisage comme fonction des paramètres chirurgicaux. A partir de l’analyse des forces et de la stabilité, nous faisons des recommandations sur les techniques de fraisages les plus optimales et sur le choix des outils. Des résultats expérimentaux sur cadavre avec notre nouveau robot et avec ces techniques de fraisage sont très encourageants et nous espérons démarrer des essais cliniques dans un futur proche.

Mots clés : Chirurgie assistée par ordinateur, robotique, prothèse total de genou, modèle de fraisage de l’os

List of Publications related to this thesis

1. Plaskos C, Cinquin P, Lavallée S, Hodgson AJ. Praxiteles: A Miniature Bone-Mounted Robot for Minimal Access Total Knee Arthroplasty. *International Journal of Medical Robotics and Computer Assisted Surgery*, 01:04, 2005 (In Press).
2. Plaskos C, Cinquin P, Lavallée S, Hodgson AJ. A Robotic Milling-Guide Positioner for Improved Resection Accuracy in Minimal Access Total Knee Arthroplasty. Submitted to the *1ères Journées De Navigation: Hanche – Genou*. Lyon, France. December 9-10, 2005. 7 pages.
3. Plaskos C, Cinquin P, Lavallée S, Hodgson AJ. Minimal access total knee arthroplasty using a miniature robot and a new side milling technique. 5th Annual Conference of the International Society for *Computer Assisted Orthopaedic Surgery*, Helsinki, Finland, June 19-22, 2005. pp 368-371.
4. Plaskos C, Lavallée S, Cinquin P, Hodgson AJ. How Will New CAOS Technologies Help Clinicians: Minimal Access Total Knee Arthroplasty Using the Mini-Praxiteles Robot. *MISmeetsCAOS Symposium Series*, Indianapolis Indiana, USA, May 19-21, 2005 pp. 376-385.
5. Plaskos C, Cinquin P, Hodgson AJ, Lavallée S. Safety and Accuracy Considerations in Developing a Small Sterilizable Robot for Orthopaedic Surgery. *IEEE International Conference on Robotics and Automation (ICRA)*, Barcelona, Spain, April 18-22, 2005 pp. 942-947.
6. Plaskos C, Masri BM, Cinquin P, Hodgson AJ, Lavallée S. Computer-assisted minimally invasive total knee arthroplasty using a miniature robot. *IMechE Knee Arthroplasty Conference – Engineering Functionality*, 7-9 April 2005, London, UK. pp. 183-186.
7. Plaskos C, Hodgson AJ, Lavallée S, Cinquin P, Optimal kinematic design and positioning of a small surgical robot for the knee. *Surgetica*, Chambery, France, January, 2005 pp. 173-181.
8. Plaskos C, Stindel E, Cinquin P, Hodgson AJ, Faguer B, Lavallée S. Praxiteles: a universal bone-mounted robot for image free knee surgery - report on first cadaver trials. Langlotz F, Davies BL, Stulberg SD, eds. *Computer Assisted Orthopaedic Surgery – 4th Annual Meeting of CAOS-International Proceedings*. 2004:67-8.
9. Plaskos C, Hodgson AJ, Cinquin P. Experimental validation of a force prediction algorithm for robot assisted bone-milling. Buzug TM, Lueth TC, eds. *Perspective in Image-Guided Surgery: Proceedings of the Scientific Workshop on Medical Robotics, Navigation and Visualization*. Remagen Germany, March 11-12, 2004. World Scientific. pp. 286-94.
10. Plaskos C, Hodgson AJ, Cinquin P. Modelling and optimization of bone-cutting forces in orthopaedic surgery. *Medical Image Computing & Computer Assisted Intervention (MICCAI) 2003*. pp. 254-261
11. Plaskos C, Hodgson AJ, Cinquin P. An orthogonal bone-cutting database for modelling high-speed machining operations. *Proc. of the 3rd International Conference of Computer Assisted Orthopaedic Surgery (CAOS) 2003*. pp. 280-1.

Table of Contents

Table of Figures.....	7
List of Tables 11	
Chapter 1: Introduction.....	13
1.0 <i>Objectives / Scope of the thesis.....</i>	13
1.1 <i>TKA - Motivation and Background.....</i>	14
1.1.1 TKA bone resections	14
1.1.2 Surgical exposure and technique.....	15
1.1.3 Accuracy of conventional cutting techniques	17
1.1.3.1 Sawing.....	17
1.1.3.2 Milling.....	18
1.1.4 Bone temperature considerations in TKA.....	18
1.1.5 Computer and robot assisted TKA	19
1.2 <i>Bone Cutting Mechanics.....</i>	20
1.3 <i>Description of Bone.....</i>	20
1.3.1 Bone composition and structure	20
1.3.2 Bone structure in the knee.....	22
1.3.3 Bone structure used in our cutting and milling experiments.....	23
1.4 <i>Chapter Overview</i>	24
Chapter 2: High-Speed Orthogonal and Oblique Bone-Cutting.....	25
2.0 <i>Chapter Summary.....</i>	25
2.1 <i>Introduction.....</i>	25
2.1.1 Previous Work.....	26
2.2 <i>Materials and Methods.....</i>	27
2.2.1 Workpiece Material – Bovine Bone	27
2.2.2 Orthogonal and Oblique Cutting Experiments.....	30
2.2.3 Data collection:.....	32
2.2.4 Data analysis:	33
2.3 <i>Results.....</i>	35
2.3.1 Orthogonal Cutting Force Curves	35
2.3.2 Oblique Cutting Force Curves.....	38
2.3.3 Effect of Cutting Velocity	39
2.3.4 Specific Cutting Energy	40
2.3.5 Observations on Chip Formation and Sub-Surface Damage	41
2.4 <i>Discussion.....</i>	47
2.4.1 Effect of Cutting Velocity – Comparison with Previous Low-Speed Data	47
2.4.2 Specific Cutting Energy	49
2.4.3 Application to the modelling of high-speed milling.....	50
2.4.3.1 Parasitic or edge forces	50
2.4.3.2 Chip formation.....	50
2.4.4 Fit of models.....	50
2.5 <i>Conclusions.....</i>	51
Chapter 3: Modelling High-Speed Bone Milling Forces.....	52
3.0 <i>Chapter Summary.....</i>	52
3.1 <i>Introduction.....</i>	52
3.2 <i>Milling Model Formulation</i>	53

3.2.1	Variation of Specific Cutting Energy with Specimen Orientation...	54
3.2.2	Chip Geometry in Milling.....	55
3.2.3	Milling Force Prediction Algorithm.	55
3.3	<i>Materials and Methods</i>	56
3.3.1	Experimental Procedure.....	56
3.3.2	Data Analysis	58
3.4	<i>Results</i>	61
3.4.1	Influence of feed-rate and cutting tool geometry on slot milling forces at low-speed	61
3.4.2	Influence of cutting speed on slot milling force components	62
3.4.3	Influence of radial cutting depth on milling force components	66
3.4.4	Influence of up- and down-milling on milling force components....	67
3.4.5	Influence of the number of cutting teeth.....	70
3.4.6	Influence of cutting direction with respect to fibre orientation.....	72
3.5	<i>Discussion</i>	73
3.5.1	Feed rate and radial immersion	73
3.5.2	Number of cutting teeth	74
3.5.3	Cutting rotational and surface speed.....	75
3.5.4	Temperature considerations	76
3.5.5	Optimizing Surface Accuracy	76
3.5.6	Model accuracy and relevance	77
3.6	<i>Conclusions and Tool Design Recommendations</i>	77
Chapter 4:	Development of a Miniature Bone-Mounted Robot for Total Knee Arthroplasty	79
4.0	<i>Chapter Summary</i>	79
4.1	<i>Introduction</i>	79
4.1.1	Objectives.....	82
4.2	<i>Robot Design Specifications</i>	82
4.2.1	Accuracy Requirements	82
4.2.2	Load Bearing Requirements.....	82
4.2.3	Sterilization Conditions	83
4.2.4	Safety Considerations	83
4.3	<i>Initial Robot Concept and Prototype Development for Conventional TKA</i> 84	
4.3.1	Description of robot architecture and components.....	85
4.3.2	Initial prototype construction	86
4.3.3	Computer Assisted Surgical Protocol (CASP).....	86
4.3.4	Manual adjustment and navigation system accuracy.....	88
4.3.5	Motor positioning accuracy and load capabilities	88
4.3.6	Robot calibration and positioning accuracy	90
4.4	<i>Analysis of Optimal Robot Positioning, Geometry, and Workspace</i>	91
4.4.1	Model formulation.....	91
4.4.1.1	Analysis dimensions and implant co-ordinate system	91
4.4.1.2	Description of variables	93
4.4.1.3	Kinematic model.....	94
4.4.1.4	Optimization cost function and constraints for calculating optimal robot placement.....	94
4.4.1.5	Calculating optimal robot geometry	95
4.4.1.6	Optimization tools.....	95
4.4.2	Results.....	97
4.4.2.1	Optimal robot positioning	97

4.4.2.2	Sensitivity of maximum distance value as a function of robot placement.....	99
4.4.2.3	Optimal robot geometry	100
4.4.3	Discussion	103
4.5	<i>Conclusions and Recommendations</i>	104
Chapter 5:	Robot Redesign for Minimal Access TKA.....	105
5.0	<i>Chapter Summary</i>	105
5.1	<i>Introduction</i>	105
5.1.1	Objectives.....	106
5.2	<i>Second Robot Concept and Prototype Development for MIS TKA.....</i>	106
5.3	<i>Redesigning the Fixation and Mechanical Adjustment Systems.....</i>	109
5.3.1	Experiments on fixation rigidity.....	109
5.3.1.1	Materials and methods - specimen preparation	110
5.3.1.2	Measurement coordinate system and data collection.....	112
5.3.1.3	Results	112
5.3.1.4	Discussion	116
5.4	<i>Improving the Accuracy and Safety of Positioning with the Motorized Guide and Reducing its Overall Size and Weight</i>	116
5.5	<i>Milling and Guide Systems</i>	118
5.5.1	Femoral milling guide.....	119
5.5.2	Adjustable tibial milling guide	119
5.5.3	Integrated milling tool with irrigation supply.	120
5.6	<i>Robot Calibration Procedure</i>	122
5.7	<i>Results on Robot Positioning and Milling Accuracy, Repeatability, and Stiffness.....</i>	124
5.8	<i>Proposed Surgical Technique with New Prototype Robot</i>	126
5.8.1.1	Preliminary cadaver tests	128
5.9	<i>Conclusions.....</i>	133
Chapter 6:	Conclusions and Future Work.....	134
6.0	<i>Thesis Summary</i>	134
6.1	<i>Future Work</i>	135
6.1.1	Robot design finalization and validation	135
6.1.2	Necessary precautions for ensuring milling safety.....	136
6.2	<i>Perspectives</i>	136
6.2.1	Intra-operative prediction of milling forces	136
6.2.2	Future applications – bone conserving implants	137
References	139	
Appendix A1: Orthogonal Cutting Forces with Exponential Model: $F = Kt^n + K_e$	146	

Table of Figures

Figure. 1.1 Anatomical co-ordinate system of the femur. The implant cut profile () is projected onto the sagittal plane, illustrating the five planar cuts of a typical TKA femoral implant.	14
Figure 1.2 Bone cuts made in TKA (Johnson & Johnson Orthopaedics).....	15
Figure 1.3 (a) Proximal tibial cut and (b) distal femoral cut made with slotted (left) and open (right) cutting guide (Johnson & Johnson Orthopaedics).	15
Figure 1.4 Surgical approaches and muscle exposure in conventional (broken lines) and less invasive (dotted lines) TKA (image from [Insall 2001]).	16
Figure 1.5 Conventional milling instrumentation for TKA [from Zimmer NexGen Surgical Technique].....	18
Figure 1.6 Taxonomy of computer-assisted TKA systems [from Stindel 2002].	19
Figure 1.7 The 7 hierarchical levels of organization of bone, from [Weiner 1998].	21
Figure 1.8 (a) The formation of fibrolamellar bone. The arrowheads show the original position of the original surface. (b) Block diagram of fibrolamellar bone – 2D networks of blood channels, sheathed by lamellar bone, alternate with parallel-fibered bone. [both from Currey 1984].....	22
Figure 1.9 Bone structure in the knee. [from Yamada 1983]	23
Figure 2.1.Schematic diagram illustrating how specimens for different cutting directions were removed from bone diaphysis for the different cutting modes.	27
Figure 2.2. Example of potted specimen milled to constant width (cutting direction transverse to osteons).	28
Figure 2.3. Microscopic images showing the structure of the bovine cortical bone specimens in the transverse plane. Both fibro-laminar (or plexiform, top micrograph) and osteonal (or Haversian, middle micrograph) structured bone is present. Bottom micrograph: Enlarged image illustrating osteon size (~200 μ m in diameter). Scale bar represents 100 μ m.	29
Figure 2.4. (a) Orthogonal (2D) and (b) oblique (3D) cutting parameters:	30
Figure 2.5. High-speed pendulum apparatus.	31
Figure 2.6. Profile images of the $\alpha=0^\circ$ (left) and $\alpha=20^\circ$ (right) rake angle cutting tools.	32
Figure 2.7. Data acquisition system: Piezoelectric force signal charge amplifiers (left), analogue filter (bottom right), digital oscilloscope (top right)	33
Figure 2.8. Example of the non-linear cutting force curve fit in the logarithmic and arithmetic domains.	34
Figure 2.9a: Tangential ($\ominus F_t$) and radial ($\blacktriangleleft F_r$) force components plotted against depth of cut for three different rake angles and cutting modes for large scale chip thickness (0- 200 μ m).	36
Figure 2.9b. Tangential ($\ominus F_t$) and radial ($\blacktriangleleft F_r$) force components plotted against depth of cut for three different rake angles and cutting modes for small scale chip thickness (0- 50 μ m).	37
Figure 2.10. Tangential ($\ominus F_t$), radial ($\blacktriangleleft F_r$) and lateral ($\dashv F_l$) force components plotted against depth of cut for obliquity angles $i = 25^\circ$ (upper row) and $i = 45^\circ$ (lower row) for three different rake angles in the across cutting mode.....	38
Figure 2.11. Effect of cutting velocity on tangential (F_t) and radial (F_r) force components at three depths of cut (t) in one bone sample. Parallel cutting mode, tool rake angle $\alpha=40^\circ$	39
Figure 2.12. Specific cutting energy vs. depth of cut plotted on log-log coordinates.....	40
Figure 2.13. Macro- and microscopic images of a dry bone chip at various magnifications. .	42

Figure 2.14. Various macroscopic images of bone chips for the parallel cutting mode.	43
Figure 2.15. Macroscopic images of cut bone chips illustrating change in chip formation mechanism with cutting depth, for 2.5–203 μm depths of cut.....	43
Figure 2.16. Macroscopic images of cut bone chips illustrating progressive change in chip formation mechanism with cutting depth, for 2–203 μm depths of cut – rake angle $\alpha=0^\circ$, across cutting mode.	44
Figure 2.17. Digital photographs of oblique bone cutting chips for small ($t=2\mu\text{m}$, left) and medium ($12 < t < 25\mu\text{m}$, right) depths of cut – across cutting mode.	45
Figure 2.18. Macroscopic photograph illustrating fracture path on a large bone chip fragment – depth of cut $t = 200\mu\text{m}$, tool rake angle $\alpha=20^\circ$, across cutting mode.	45
Figure 2.19. Subsurface damage was evident at very large depths of cut and low rake angles – depth of cut $t = 203\mu\text{m}$, rake angle $\alpha=0^\circ$, transverse cutting mode.	46
Figure 2.20. Macroscopic photographs of the tool rake (a) and clearance (b) faces taken after the cutting tests (tool rake angle $\alpha=20^\circ$).....	46
Figure 2.21: Comparison between high-speed (solid line, $v = 3.5\text{m/s}$) and low-speed (dashed line, $v = 7.7\text{mm/s}$) data.	48
Figure 2.22: Effects of cutting velocity on orthogonal forces – depth of cut $t = 76\mu\text{m}$, rake angle $\alpha=20^\circ$, across cutting mode.	49
Figure 3.1. A milling tool with J_N cutting flutes and S_M axial segments	53
Figure 3.2. Coordinate system for full immersion down-milling.	54
Figure 3.10. Measured and predicted mean milling force magnitude in x , y and z for slot milling with a cutter having two helical teeth (Tool ‘A’). Cutting conditions: cutting speed is $v=33.3\text{mm/s}$ (100 RPM, upper plot) and $v=1662.4\text{mm/s}$ (5000RPM, lower plot); axial depth of cut is 5.05mm; feed direction is parallel to the bone axis. Experimental trials: #12-16(A012_A016_100RPM.m) and #2,4,5,6,8 (A001_A010_5000RPM.m)	63
Figure 3.11. Measured and predicted instantaneous milling forces in x and y for full-immersion down-milling with a two fluted helical tool (Tool ‘A’). Cutting conditions: feed rates $f = 20, 70, 130, 250, 500 \text{ mm/min}$; rotational velocity $\omega = 100 \text{ RPM}$; feed direction is parallel to bone axis; axial depth of cut $a = 5.05\text{mm}$. Experimental trials: #12-16. (A012_A016_100RPM.m).....	64
Figure 3.12. Measured and predicted instantaneous milling forces in x and y for full-immersion down-milling with a two fluted helical tool (Tool ‘A’). Cutting conditions: feed rates $f = 20, 70, 130, 250, 500 \text{ mm/min}$; rotational velocity $\omega = 5000 \text{ RPM}$; feed direction is parallel to bone axis; axial depth of cut $a = 5.05\text{mm}$. Experimental trials: #2,4,5,6,8. (A001_A010_5000RPM.m).....	65
Figure 3.13. Measured and predicted mean cutting force magnitudes in x and y for slot milling with tool ‘A’ at 100 RPM and 5000 RPM, for equivalent <i>feed rates</i> (left column), and equivalent <i>feeds per tooth</i> (right column). The axial depth of cut was $a = 9.6\text{mm}$. Experiment #103-109 (5000RPM), 115-119 and 122-126 (100RPM).....	66
Figure 3.14. Experimental and simulated milling forces in x and y for half-immersion down-milling with a two fluted helical tool (Tool ‘A’). Cutting conditions: feed rates $f = 4, 52, 100, 200 \text{ mm/min}$; rotational velocity $\omega = 1000 \text{ RPM}$; axial depth of cut $a = 9.6\text{mm}$	68
Experiment #159-162	68
Figure 3.15. Experimental and simulated milling forces in x and y for half-immersion down-milling with a four fluted helical tool (Tool ‘C’). Cutting conditions: feed rates $f = 4, 52, 100, 200 \text{ mm/min}$; rotational velocity $\omega = 1000 \text{ RPM}$; axial depth of cut $a = 8.8\text{mm}$ for Tool ‘C’. Experiment #151-154	68
Figure 3.16. Experimental and simulated milling forces in x and y for half-immersion up-milling with a two fluted helical tool (Tool ‘A’). Cutting conditions: feed rates $f = 0.4, 5.2, 10.0, 20.0 \text{ mm/min}$; rotational velocity $\omega = 100 \text{ RPM}$; axial depth of cut $a = 8\text{mm}$.	69

Experiment #164-167	69
Figure 3.17. Measured and predicted milling forces in x and y for full-immersion down-milling with a two fluted helical tool (Tool 'B'). Cutting conditions: feed rates $f = 10, 20, 70, 130$ mm/min; rotational velocity $\omega = 5000$ RPM; axial depth of cut $a = 8$ mm. $f = 10$ and 20 mm/min data low pass filtered with cut-off equal to 10 times the tooth passing frequency Experimental trials: #97,98,101,102 (plot_simA096toA99.m)	71
Figure 3.18. Measured and predicted milling forces in x and y for full-immersion down-milling with a four fluted helical tool (Tool 'C'). Cutting conditions: feed rates $f = 10, 20, 70, 130$ mm/min; rotational velocity $\omega = 5000$ RPM; axial depth of cut $a = 8$ mm. ..	71
Experimental trials: #91-95 (plot_simA091toA95.m)	71
Figure 4.1 State of the art in large and mini TKA robots	81
Figure 4.3 Cadaver experiments with our first prototype robot: a) intra-operative planning of the femoral component position and size; b) navigation of the fixation arch on the bone; c) making the anterior chamfer cut with the saw-guide in position; d) verifying guide position before making the distal cut; e) percutaneous fixation of the arch and attachment of the milling guide e) milling the distal cutting plane in uni-compartmental knee arthroplasty (UKA).	87
Figure 4.4. A 0.01mm resolution dial gauge was used to measure the mechanical backlash, stiffness, and positioning reproducibility of the robot prototype.	89
Figure 4.5. All implants are aligned so that the distal cuts are collinear with the y axis, with the midpoints coincident with the origin.....	92
Figure 4.6. Robot positioning sequence for sawing, side milling, lateral milling.	93
Figure 4.7. Description of variables: positioning for the (a) distal cut and (b) anterior chamfer cut. Note that b_i is zero for all cuts except the distal.	94
Figure 4.8. Optimization routine to determine the single combination of L_1 and L_2 that results in the lowest d_{max} value for all implant shapes and sizes.	96
Figure 4.9. Optimal robot positioning and pose for all implant sizes, grouped by each shape : $L_1 = 60$ mm, $L_2 = 30$ mm, and $ b_{distal} = 10$ mm.	98
Figure 4.10. Contour plot of d_{max} values as a function of robot position X_θ for a typical implant. Contour lines are calculated within the bounds $(-50, -25) < X_\theta < (0, 25)$ and are drawn at 1mm intervals ($L_1 = 60$ mm, $L_2 = 30$ mm, and $ b_{distal} = 10$ mm). The robot is shown in five configurations corresponding to the five cuts for the optimal position. The largest gap distance of $d_{max} = 6.9$ mm is for the anterior cut	99
Figure 4.11 Cost function output (d_{max} values) as a function of robot geometry for implant shapes #1 and #8:.....	101
Figure 5.1 Actual incision and exposure obtained in less invasive TKA procedures.....	106
Figure 5.2 Various designs considered during the evolution of the robot.....	108
Figure 5.3 CAD model illustrating the various manual (—•—) and motorized (••••) DoF of the second version of the Praxiteles robot for minimal access TKA.....	109
Figure 5.4. Conceptual drawings (top) and cadaver photos (bottom) of the <i>Augmented 2 Pin</i> fixation: a short 'intramedullary' device used to augment the two pin fixation and guide the insertion to prevent intersection with femoral cutting planes.....	110
Figure 5.5 DEXA scan images of porcine knee specimens: non-decalcified (a); and decalcified for 1 (b); 2 (c); and 3 (d) days.	111
Figure 5.6. Experimental setup for load vs displacement measurements (left) and coordinate system (right) used to report the results.	112
Figure 5.7a Displacement [mm] vs. applied load [N] curve for the augmented 2 pin and the bicortical 2 pin fixation tests in the 1, 2 and 3 day decalcified bone specimen.	114
Figure 5.7b Rotation [°] vs. applied load [N] curves for the augmented 2 pin and the bicortical 2 pin fixation tests in the 1, 2 and 3 day decalcified bone specimen.	115

Figure 5.8 Harmonic Drives - Principle of operation (from the Harmonic Drives® catalogue)	117
Figure 5.9 Torsional stiffness characteristics of a Harmonic Drive Gear, HFUC size 8. (a) Angular deflection <i>vs.</i> applied torque; (b) Deflection <i>vs.</i> applied load at a distance of 40 mm from gear axis	117
Figure 5.10 Details of the robot 2 DoF gear unit	118
Figure 5.11 <i>Praxiteles</i> second prototype for milling and sawing in MIS TKA..... (left) the 2 DoF milling tool guide allows rotation and translation of the milling tool within the cutting plane. A single brake release button frees both axes of rotation when pressed. (right) a sliding joint in the plane of the saw-guide allows the guide tip to be abutted directly against the bone surface before making each cut. Robot shown with detachable motors	119
Figure 5.12 Tibial milling guide: 4 DoF (white dash-dot lines) are used to position the 2 DoF (not labelled) planar milling guide	120
Figure 5.13 Integrated milling tool with irrigation supply	121
Figure 5.14 (a) Attachment + cutter stiffness, K [N/mm] and (b) cutter tip deflection [mm] under 50N applied load <i>vs.</i> the extended length of attachment tube for our prototype..	122
Figure 5.15 Kinematic calibration procedure consisting of passive (P1-3) and active (A1-2) steps. The guide is automatically positioned to the distal cut (A3) after calibration. These images are displayed in the graphical user interface to guide the surgeon through the calibration procedure. The double headed arrow signifies that the brake can be released during the acquisition.....	123
Figure 5.16 Surgical Workflow.....	127
Figure 5.17 Tibial (a) and femoral (b) surface acquisitions.	129
Figure 5.18 Tibial sawing and milling guide. Tibial milling in the MIS surgeries was completed in stages, first with the medial and then the lateral condyle.	130
Figure 5.19 Insertion of the robot fixation pins.(a) the point probe can be used to guide and check pin insertion to avoid interference with the femoral cutting planes; (b) the pin insertion area on the medial femoral side is bounded by the following structures: posteriorly – by the anterior border of the medial collateral ligament when the knee is in extension, anterosuperiorly – by the posteroinferior border of the vastus medialis muscle when the knee is in flexion,.....	131
anterodistally – by the anterior, anterior chamfer, and distal cutting planes.	131
Figure 5.20 The leg can be positioned in various degrees of flexion depending on the cut to make room during milling.....	131
Figure 5.21 Latest <i>Praxiteles</i> milling system with refined manual adjustment mechanism and high-speed milling tool: (a) Femur before cutting in open surgery, (b) femur after all five planar cuts (c) trial components installed.	132
Figure 6.1 Application of milling model to intra-operative force prediction in TKA.	137
Figure 6.2 Application of the miniature robot to non-planar cuts and new implant designs. 138	
Figure A.12: Tangential (F _t) and radial (F _r) force components plotted against depth of cut for three different rake angles and cutting modes for large scale chip thickness (0-200μm):	146

List of Tables

Table 2.1. Experimental parameters tested in previous orthogonal cutting studies	27
Table 2.2. Range of experimental cutting parameters tested.....	32
Table 3.1. Range of experimental conditions tested	57
Table 3.2. Tool geometries used, as specified by the manufacturer.....	58
Table 3.3. Percentage increase in the measured mean force magnitudes with decreased cutting speed from 1662.5mm/s (5000RPM) to 33.3 mm/s (100RPM) at equivalent feeds per tooth c	62
Table 3.4. Measured and predicted mean forces for half-immersion down milling with 2 and 4 fluted tools for equivalent feed rates (1000RPM, $v=332.5\text{mm/s}$)	69
Table 3.5. Measured and predicted mean forces for full-immersion down milling with 2 and 4 fluted tools for equivalent feed rates (5000RPM, $v=332.5\text{mm/s}$)	70
Table 4.1 Risk table of guide positioning.....	84
Table 4.2 Mechanical Backlash, Stiffness, and Positioning Reproducibility Measurements for the Initial Prototype for Open TKA	89
Table 4.3. d_{max} values [mm] for all implant shapes and sizes : $X_0 = X_{0_optimal}$, $L_1 =$ 60mm , $L_2 = 30\text{mm}$, and $ b_{distal} = 10\text{mm}$	97
Table 4.4 Mean ($\pm SD$) $X_{0_optimal}$ position values [mm] for all implant shapes : $L_1 =$ 60mm , $L_2 = 30\text{mm}$, and $ b_{distal} = 10\text{mm}$	97
Table 4.5. Mean ($\pm SD$) $\partial d_{max}/\partial X_0 X_{0_optimal}$ values over all sizes for each implant shape : $L_1 = 60\text{mm}$, $L_2 = 30\text{mm}$, and $ b_{distal} = 10\text{mm}$	100
Table 4.6 Optimal individual robot geometries [*] L_1 and L_2 [mm] with minimized d_{max} values [mm], and partial derivatives [mm/mm] at the optimal lengths for each implant shape.	102
Table 4.7 d_{max} values [mm] for two ‘optimal’ robot geometries.....	102
Table 5.1 BMD values as a function of duration in decalcification solution	111
Table 5.2 Linear regression coefficients ($y = m x + b$) and square of the correlation coefficients (R^2) for the fixation compliance tests.....	113
Table 5.3 Mechanical Backlash, Stiffness, and Positioning Reproducibility Measurements for the Second Prototype for MIS TKA	125
Table 5.4 Final Guide Positioning Error	125
Table 5.5 Specifications of High-Speed Milling Motor	129
Table 5.6 Final cutting errors [$^\circ$] relative to guide position and implant planning	133

Chapter 1: Introduction

1.0 Objectives / Scope of the thesis

Good clinical outcomes in total knee arthroplasty (TKA) are normally associated with a postoperative leg alignment of 3° or less [Jeffery 1991][Ritter 1994]. Some clinicians suggest an even narrower window for optimal results and improved long-term survivorship. Although computer assistance (CA) has markedly improved alignment outcomes in TKA in comparison to the conventional technique, some alignment outliers still remain (for example, Jenny [2001] reports only ~84% (25/30) and 70% (21/30) of patients having errors <3° for navigated and conventional instrumentation, respectively).

Studies suggest that the manual bone-sawing process could be contributing a significant portion of error to overall leg alignment and implant positioning and fit [Plaskos 2002][Bathis 2005]. Milling could be a more accurate solution for TKA, though present systems have not yet gained widespread clinical acceptance due to the integration challenges in the operating room (bulky, costly, invasive instrumentation, increased operating time and safety concerns).

The ultimate goal of this work is therefore to improve implant positioning and fit in CA-TKA, by improving the bone milling and guiding process. In order to realise this, our objective was to design and develop a novel bone-mounted robot for carrying out planar resections in both conventional (open) and minimally invasive (MIS) CA-TKA, using a manually guided side-milling tool. It was a requirement that the system be compact in order to facilitate the integration into the operating room and to keep costs to a minimum. In addition, a side-milling technique was desired since it permits access to all cuts with a minimal exposure.

Because bone-milling is known to be somewhat ‘unpredictable’ in nature, however, with cutter forces increasing suddenly and unexpectedly, we needed to better understand the physics and to optimize the mechanics of the milling process before deploying it in the clinical setting. It was therefore necessary to measure the forces occurring in bone-milling for several different cutting conditions and tools, and to model those forces in order to explain why they behave as they do, and to explore means for minimizing this erratic behaviour.

Finally (or firstly) in order to build an accurate predictive model of the milling process that could be applied to any set of milling conditions, we needed to understand what happens at the interface between the bone and each cutting edge of the milling tool. It was therefore a first objective of this thesis to investigate experimentally the fundamental mechanics of bone-cutting in the simplest cases possible: orthogonal (or two dimensional) and oblique (three dimensional) single-edge cutting. Since modern surgical milling tools operate at a relatively high rotational speeds, it was a requirement that these experiments be carried out at high speeds never before tested so that we could quantify the interrelationships of cutting force and geometry for clinically relevant conditions.

1.1 TKA - Motivation and Background

Miniature robotized surgical instrumentation can potentially increase the precision and capabilities of the surgeon, improve outcomes and recovery times for the patient and reduce the large number of mechanical instruments required in the operating room, without imposing impractical variations from the conventional surgical technique.

Even though conventional total knee arthroplasty (TKA) is in general a very successful operation, TKA is an attractive application for computer and robotic assistance for a number of reasons. Firstly, knee mal-alignments of as little as 3° in the frontal plane (figure 1.1) have been correlated to early failures, so a high degree of implant placement accuracy is key for good clinical results [Ritter 1994]. Secondly, conventional TKA instrumentation systems that rely on mechanical jigs to aid bone resurfacing have been known to produce variable and suboptimal results with respect to implant alignment and fit of the femoral component [Laskin 1991]. Saw-guides, for example, that reference the anterior, posterior, and chamfer cuts from the distal cut may produce an outer femoral surface which is incongruent with the inner surface of the implant [Laskin 1991][Lennox 1988][Plaskos 2002]. Furthermore, manual instrumentation systems usually require that a number of guides be available in the operating room to cover the entire range of implant sizes (typically one template for each of the five to eight sizes), which can take up valuable space around the operating table and increase sterilization costs.

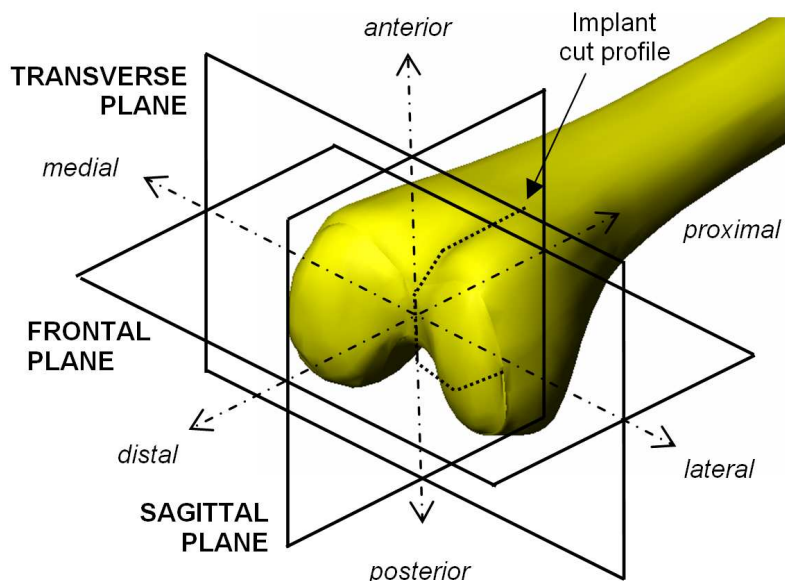


Figure. 1.1 Anatomical co-ordinate system of the femur. The implant cut profile (---) is projected onto the sagittal plane, illustrating the five planar cuts of a typical TKA femoral implant.

1.1.1 TKA bone resections

No less than six planar bone resections are required to perform a standard TKA (figure 1.2). Planar resections on the femur include the distal, anterior, posterior, and the anterior and posterior chamfer resections. These planes are arranged such that their lines of intersection are parallel to one another. Only one planar resection is required on the tibia: the proximal tibial resection (figure 1.3). Although supplementary cuts are typically required for particular implant designs to allow for intercondylar

prominences (especially in posterior stabilized implants), and for fixation stems or pegs, these resections are not addressed in this work. Neither are the patellar resections (not shown), which typically include one planar cut along with secondary holes for the implant pegs.

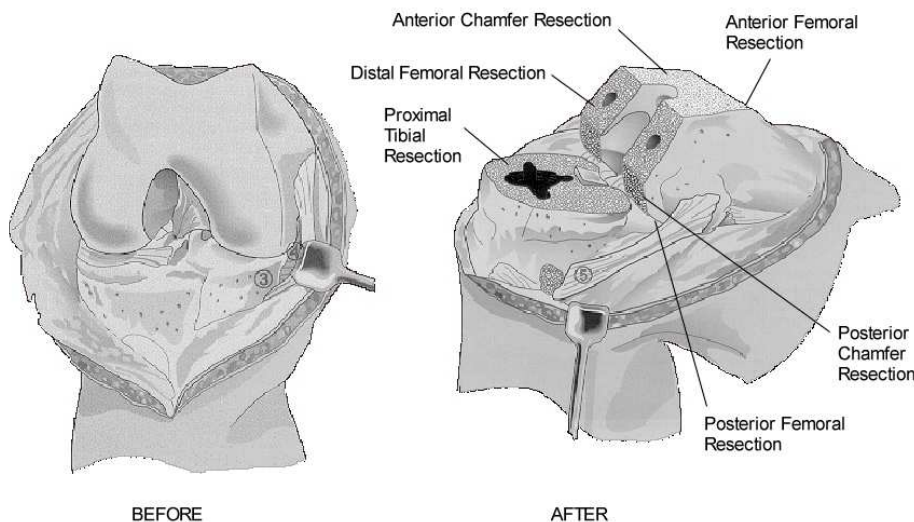


Figure 1.2 Bone cuts made in TKA (Johnson & Johnson Orthopaedics).

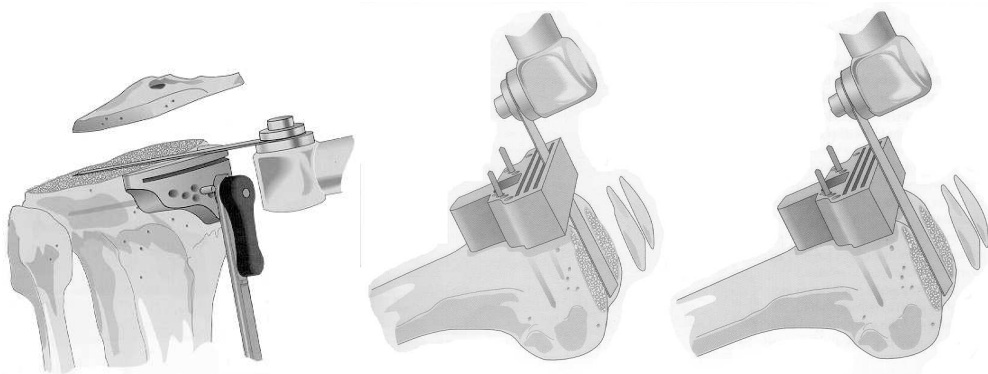


Figure 1.3 (a) Proximal tibial cut and (b) distal femoral cut made with slotted (left) and open (right) cutting guide (Johnson & Johnson Orthopaedics).

1.1.2 Surgical exposure and technique

In conventional TKA, the surgeon strives to achieve accurate component placement by adequately exposing the knee joint, properly orienting cutting guide blocks across the exposed aspects of the bones from the anterior side of the knee, and sawing off the worn joint surface by using the block surface or slot to guide the oscillating saw-blade (figure 1.3). The standard approach uses a 25-30 cm anteromedial skin incision extending proximally from just distal to the level of the tibial tubercle, followed by a medial 20-30 cm parapatellar arthrotomy which extends superiorly through the quadriceps tendon (figure 1.4) [Insall 2001].

Although the extent of the conventional or ‘open’ incision allows for lateral eversion and dislocation of the patella, thus exposing most of the structures in the knee joint, dividing the distal third of the

quadriceps muscle in this manner can have several repercussions for the patient. These include increased pain, blood loss, and time to ambulation, prolonged post-operative hospital stay and rehabilitation, and decreased range of motion and knee strength [Tria 2003].

Surgeons are beginning to use “minimal access” or “minimally invasive” surgical (MIS) techniques for TKA. Some techniques preserve the quadriceps mechanism entirely, while others use a ~2cm vastus medialis snip to facilitate patellar subluxation [Tria 2003][Bonutti 2004]. Femoral cuts are made from the anterior or medial side through a 6-14cm “mobile” incision that is moved to expose different aspects of the joint by flexing and rotating the knee. Approaching the bone cuts obliquely or medially circumvents the need to evert the patella, thus reducing morbidity and trauma to the extensor mechanism, and improving post-operative knee function, recovery rate and pain.

The primary surgical challenge in minimal access TKA is attaining precise implant cuts and alignment with the reduced bone exposure. Currently, the bone cuts are carried out by pinning a downsized cutting-block onto the side of the knee. Because sawing accuracy diminishes quickly with extension of the sawblade beyond the cutting-block, however, achieving accurate and reproducible cuts is very challenging [Plaskos 2002].

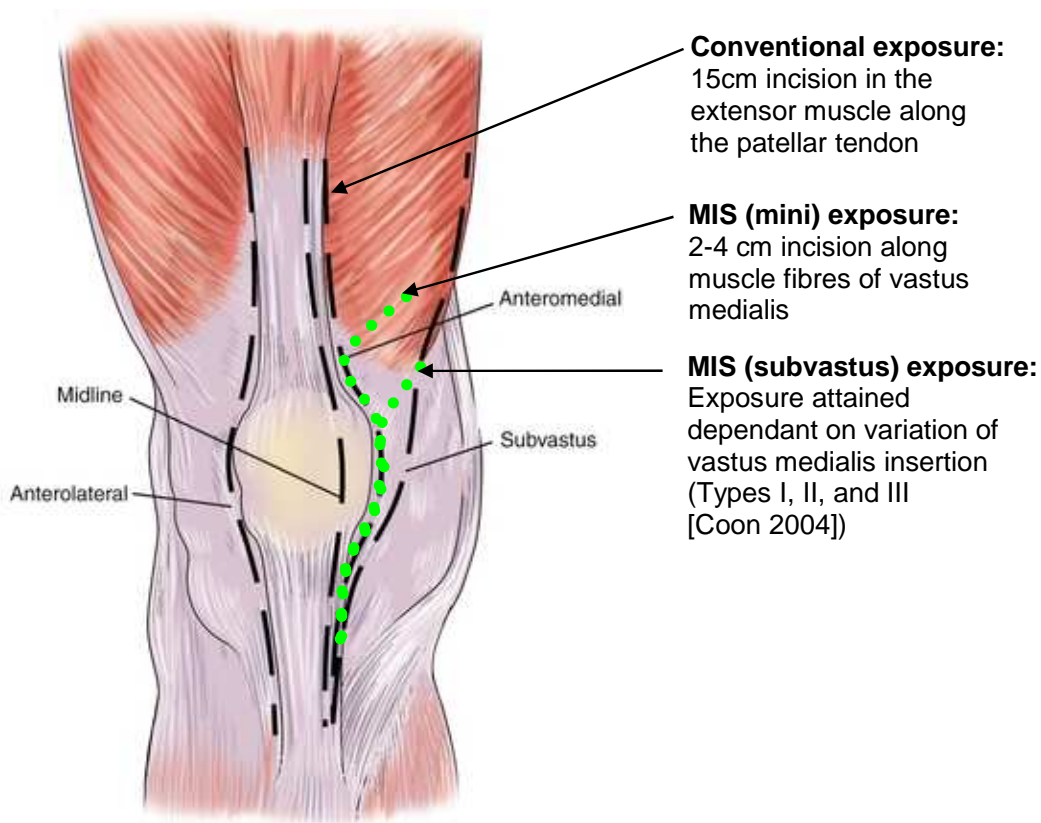


Figure 1.4 Surgical approaches and muscle exposure in conventional (broken lines) and less invasive (dotted lines) TKA (image from [Insall 2001]).

1.1.3 Accuracy of conventional cutting techniques

1.1.3.1 Sawing

Sawing errors are a result of (1) saw-blade bending, (2) misalignment between the blade and the guide planes, and (3) guide movement. Several studies have quantified the accuracy of conventional sawing techniques either on synthetic bones [Otani 1993][Matsen 1993], cadaver bones [Plaskos 2002][MacDonald 2004], or patients [Bathis 2005].

Otani measured maximum sagittal plane cutting errors caused by saw-blade toggle in a slotted A/P femoral cutting guide using balsa wood blocks. With a 1.5mm slot thickness, cutting errors reached ~0.9 mm (0.9°) and ~0.5 mm (0.3°) for standard (1.2mm) and thick (1.4mm) saw-blades respectively. The authors noted that these toggle angles could be caused by displacements of as little as ~2mm at the hand of the surgeon, and since it is very difficult to avoid displacements of this magnitude during cutting with an oscillating saw, the measured maximum errors are likely to be common in clinical practice. Otani also measured the relative motion between the A/P femoral cutting guide and the distal femur during bone cutting in cadavers with several different types of fixation methods. Pin fixation that relied only on the cancellous bone beneath the cutting guide could not provide tight fixation, allowing over 1 mm of motion. This motion was reduced when combined fixation methods were used (for example, augmenting fixation with an intramedullary rod).

In the study performed by Plaskos et al. [2002], eight orthopaedic surgeons of varying TKA experience made eighty-five resections on 19 cadaveric femurs and tibias and the planes of the resulting cut surfaces were compared to the guide planes. Varus/valgus alignment variability ranged from 0.4°-0.8° SD for expert and trainee surgeons, respectively. Sagittal variability was ~1.3° SD for both surgeon groups. Slotted cutting guides reduced the variability and eliminated the bias in the sagittal plane for experienced surgeons but did not significantly improve frontal plane alignment variability. Guide movement contributed 10%-40% of the total cutting error, depending on cut and guide type.

MacDonald [2004] found improved cutting flatness in cadaveric tibias by constraining the saw at the blade pivot point using a constraining jig that pinned to the tibia and strapped around the ankle.

Bathis [2005] measured cutting errors relative to the guide plane in live surgery with a computer navigation system. For the distal femoral cut, there was a mean varus/valgus deviation of 0.6° ($SD \pm 0.5^\circ$) and a mean flexion/extension deviation of 1.4° ($SD \pm 1.3^\circ$). For the proximal tibia, varus/valgus alignment showed a mean deviation of 0.5° ($SD \pm 0.5^\circ$). The mean sagittal variability was 1.0° ($SD \pm 0.9^\circ$).

Most of the described studies illustrate the difficulty in producing accurate cuts repeatedly with conventional sawing instrumentation, and many authors note that TKA resections often have to be recut due to cutting errors [Lennox 1988][Minns 1992][Mont 1997][Bathis 2005]. Although using a navigation system allows the surgeon to measure cuts accurately in surgery, and possibly correct each cut manually, this is clearly not the optimal solution for a number of reasons:

- (1) it can be time consuming
- (2) difficult to correct small errors with a saw blade
- (3) cannot correct cuts in which too much bone has been removed
- (4) attempts to correct errors could result in a non-flat cut.

Furthermore, a cutting error of 1° or 2° is not visually obvious in the patient and could easily go unnoticed if not checked quantitatively. Therefore, it is important for a cutting technique to be repeatable, permitting the surgeon to consistently achieve accurate resections on the first attempt.

1.1.3.2 Milling

Milling has been proposed as a more accurate alternative to sawing [Dueringer 1996a][Plaskos 2001]. We are however aware of only one commercially available system for carrying out conventional or manual milling in TKA (Zimmer *NexGen™ MICRO-MILL Instrumentation System*, figure 1.5). This system uses an end-milling technique and large milling frame that mounts on the medial, lateral and anterior side of the femur. It is not possible to access the posterior cut with end-milling, so a saw-blade is used. Plaskos [2001] evaluated a high-speed side-milling technique using a flat guide-plate and a slender cutting tool (3.2mm in diameter). Experiments on porcine bones with novice and expert users showed improved results over sawing, though deflection of the slender cutting tool was a problem at the back of the cut when the tool was fully extended.

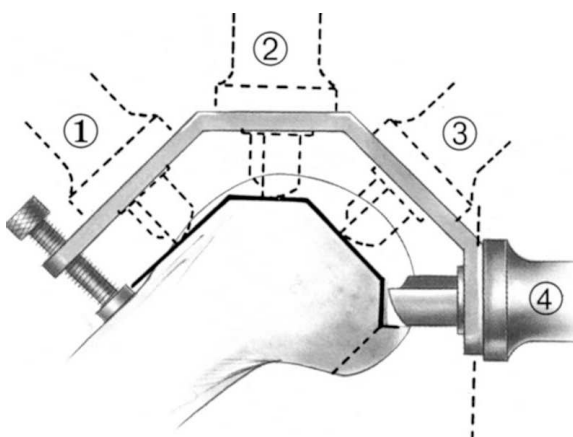


Figure 1.5 Conventional milling instrumentation for TKA [from Zimmer *NexGen Surgical Technique*].

1.1.4 Bone temperature considerations in TKA

The temperature at which thermal necrosis starts to occur in bone has been established in the literature to be 44-47°C if the bone remains at this temperature for more than one minute [Eriksson 1984]. Toksvig-Larsen [1989] measured the temperature in the tibia and in the saw blade during 30 knee arthroplasty operations. In the saw blade the median maximum temperature was 68°C (45-100°C). The corresponding bone temperatures at two levels approximately 2 and 3 mm below the cutting surface were 47°C and 42°C, respectively. Irrigation of the saw area with physiologic saline solution had only a minimal effect, possibly because the coolant did not penetrate into the interior of the bone where the actual cutting took place. They concluded that sawing in TKA may cause substantial temperate damage. In another laboratory test where they evaluated the thermal effects of 8 different saw-blades in bovine diaphyseal bone, only three out of 219 tests were below the 44-47°C critical necrosis limits [Toksvig-Larsen 1992]. Only with the use of a custom built saw-blade that had means for channelling the irrigation through the blade directly to the cutting sight were they able to show reduced cutting temperatures below this limit.

In a comparative study between milling and sawing, Dueringer [1996b] showed that bone-milling with the Zimmer *NexGen* system on bovine tibias resulted in lower temperatures below the thermal necrosis limit even without irrigation. The average temperature elevations for milling and sawing were 1.5°C and 8.3°C, respectively.

Mitsuishi [2005] measured the temperature during side-milling of the anterior femoral plane in robotic TKA on a cadaver. The experiment was performed and studied the effect of coolant using physiologic

saline refrigerated at 4°C. The cutting conditions were: cutting surface speed: 94.2m/min; feed per tooth: 0.02mm; width of cut: 2mm, axial depth of cut: 5mm. Maximum temperatures measured with thermography (thermal camera) at the cortical rim were 45°C and 35°C without and with coolant, respectively. Based on the results of this study, they concluded that irrigation should be applied to the tool tip during milling in surgery.

1.1.5 Computer and robot assisted TKA

Computer assisted TKA guiding systems have been classified as either passive, semi-active or active (figure 1.6). Navigation systems are considered as passive measurement tools that display information to the surgeon regarding the position of instruments relative to the patient anatomy and surgical plan. These systems can either be CT-less or CT based, and are widely used in TKA. Several recent studies have reported good results in overall limb alignment using either type of system (eg. [Haaker 2005]). Some studies do however reveal that alignment outliers are still present (for example, Perlick [2004] reports 4 out of 50 patients with deviations >3° in the frontal plane), suggesting that there could be room for improvement. A considerable portion of this error could be arising from the problems inherent to the manual sawing technique, as described in §1.0.3.1. Although navigation systems have proven to be very effective tools, current drawbacks include that do not help to improve the fit of the femoral component or reduce the number of cutting blocks needed in the operating room.

Commercially available active and semi-active robotic milling systems such as ROBODOC, and ACROBOT physically guide the milling tool in space with respect to a CT-based plan. Although they have shown to produce more accurate cuts [Bauer 2004][Jakopec 2001] [Mitsuishi 2005], these systems are currently quite large and not easily integrated into the operating room due to their size and requirements for bone immobilization. Smaller, bone-mounted robots have been presented as a solution to overcome this integration problem, which are connected directly to computer navigation stations [Ritschl 2004][Berardoni 2003]. Current systems only position conventional saw-guides for the surgeon, however, so they do not provide a real solution to the sawing accuracy problem. An in depth review of both large and bone-mounted systems for robot assisted TKA is given in chapter 4.

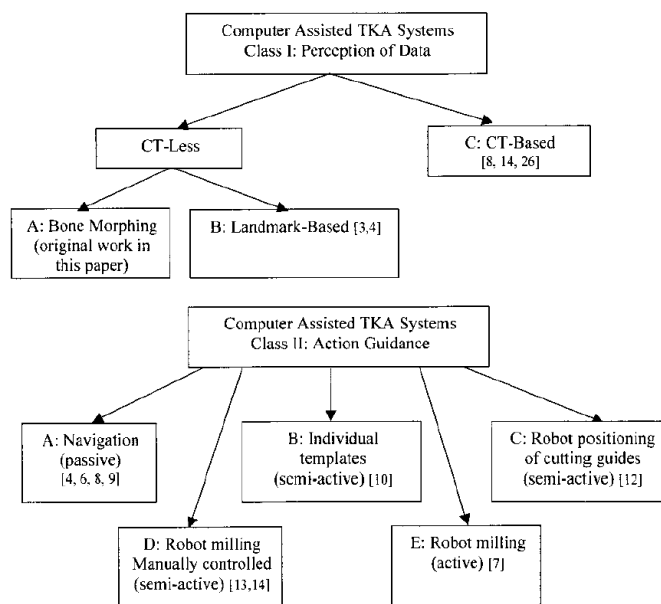


Figure 1.6 Taxonomy of computer-assisted TKA systems [from Stindel 2002].

1.2 Bone Cutting Mechanics

In comparison to the wealth of research published in industrial metal machining (e.g. Altintas 2000), relatively few studies exist on the mechanics of bone cutting. Jacobs [1974] and Krause [1987] have shown that metal cutting models such as Merchant analysis, which assumes that the material fails in an idealized ‘shear plane’ in front of the tool, have very limited applicability to the cutting of bovine cortical bone. Wiggins [1978] demonstrated experimentally that bovine bone exhibits very similar behaviour to human bone in orthogonal cutting.

More recently, Mitsuishi [2005] presented a study on the orthogonal cutting of dried porcine cortical and porous bone. Videos made in a scanning electron microscope (SEM) of single edge cutting at very low velocity (0.2mm/s) revealed that continuous cutting chips were formed when cutting at a depth of 6 μ m and ‘block destruction’ or catastrophic fracturing occurred when cutting at 10 μ m depth. The chip generation mechanism was characterized as a transition from ductile to brittle. Specific cutting pressures were reported to be on the order of 100-500 N/mm², depending on the rake angle, cutting direction, and undeformed chip thickness.

A major limitation of the previous works in bone cutting is that they have not investigated the mechanics of high-speed cutting, which is suspected to be different from low-speed cutting. In addition, no mathematical models are currently available for predicting forces in bone milling operations. This is of high interest, not only for optimizing the design of robotized milling tools, guides, instrumentation and techniques, as well as cutting accuracy and time, but also for improving safety and analysing stability in manual milling operations. Although milling tool and burrs have been commonly used in orthopaedic surgery for over 50 years, safety remains a primary concern as milling tools are known to be prone to ‘slipping’ unpredictably from the surgeons hands [Giraud 1991].

1.3 Description of Bone

Finally, this chapter would not be complete without providing some basic information on the structure and properties of bone material.

1.3.1 Bone composition and structure

Bone has been described as having a hierachal structure of seven layers (figure 1.7) [Wiener 1998]. Whole bone is categorized at the highest level and the three major components: collagen; carbon apatite; and water; which comprise the mineralized collagen fibril, are at the lowest level. Although the structure of bone differs dramatically as a function of the anatomical location (for example, the cancellous bone in the knee joint versus the cortical bone in the femoral diaphysis), it is well known that bone material itself in either structure is made up of a common building block: the mineralized collagen fibril.

The mineralized collagen fibril (figure 1.7, Level 2) is made up of carbon apatite crystals [$\text{Ca}_5(\text{PO}_4)_3(\text{OH})$] that are organized in layers that traverse across the fibril, giving each fibril an orthotropic property. Each crystal has average dimensions of ~3×25×50 nm and they form in and around a three-dimensional matrix of *Type I* collagen.

Mineralized collagen fibrils are typically found in aligned arrays or bundles (levels 3 and 4), so the mechanical properties of a fibril bundle depends on the relative three-dimensional alignment of the fibrils within each array. There are several diverse patterns of fibril array organization, though the most common arrangements are parallel-fibered arrays, which are characteristically found in bovine bone, and the plywood-like structure of lamellar bone, which is prominent in most mammals including humans.

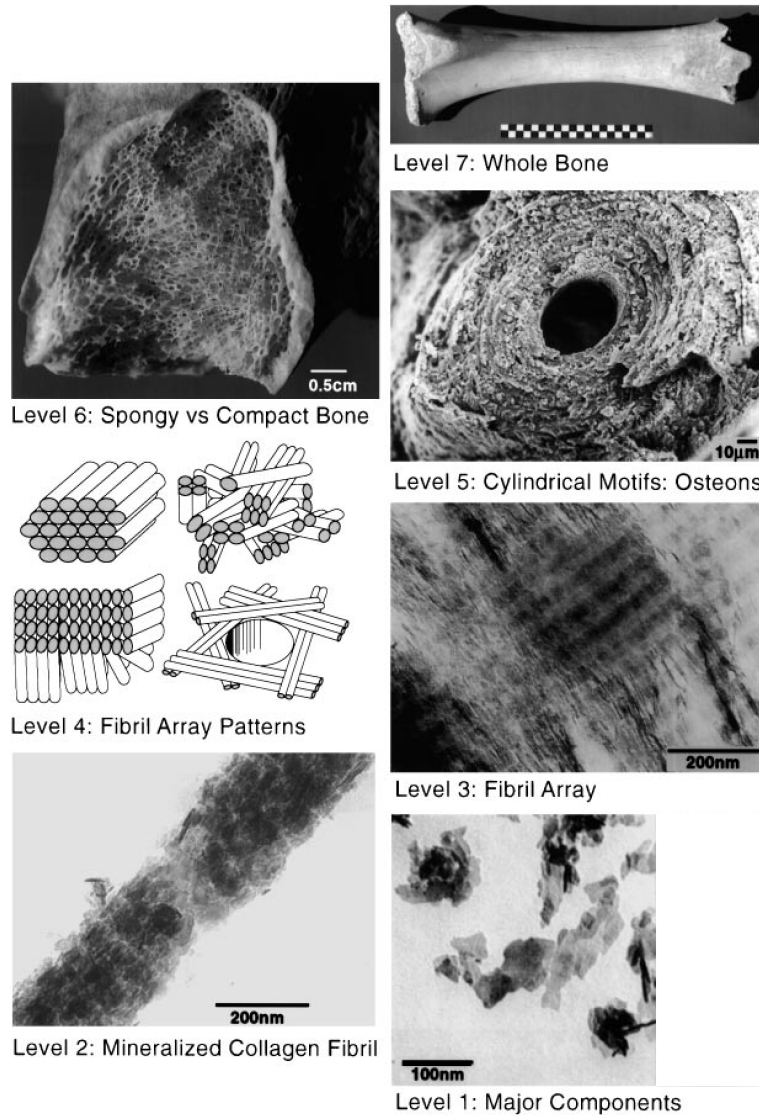


Figure 1.7 The 7 hierarchical levels of organization of bone, from [Weiner 1998].

- Level 1: Isolated crystals from human bone.
- Level 2: TEM micrograph of a mineralized collagen fibril from turkey tendon.
- Level 3: TEM micrograph of a thin section of mineralized turkey tendon.
- Level 4: Four fibril array patterns of organization found in the bone family of materials.
- Level 5: SEM micrograph of a single osteon from human bone.
- Level 6: Light micrograph of a fractured section through a fossilized (about 5500 years old) human femur.
- Level 7: Whole bovine bone (scale: 10 cm).

Primary parallel-fibered bone (figure 1.7, Level 4, top left) is essentially Level 3 bone extended to the micron or millimeter scale. During early development, parallel-fibered bone is first laid down along the bone axis (figure 1.8a) [Currey 1984]. Voids are left between successive layers of newly forming bone, which are subsequently filled with lamellar bone. The combination of the two is referred to as fibrolamellar or plexiform bone (figure 1.8b). The elastic modulus of parallel-fibered bone is ~26 GPa along the long bone axis and ~11 GPa in the orthogonal directions [Reilly 1975].

Lamellar bone with its so called ‘rotated plywood’ structure (figure 1.7, Level 4, bottom left) is the most common bone type in humans. These lamellae are often folded into osteon cylinders (Haversian systems) or ‘sausage-shaped’ lamellar cylinders in parallel-fibered bone.

The *secondary* osteonal structure of compact bone is a result of an internal remodeling process (figure 1.7, Level 5). Osteoclasts remove dead bone leaving behind large tunnels, which are then refilled with new bone by osteoblasts. A thin layer of cement is first deposited on the inside of the tunnel surface, followed by subsequent layers of lamellar bone. When the tunnel is almost full the process stops and narrow channel ~10-20 μm in diameter remains for blood to flow and deliver nutrients to the bone. Many small capillary-like features called canaliculi are also built into the structure, radiating out from the central blood vessel and housing osteocyte cells. The osteon also contains many elongated pores. The typical diameter of an osteon is on the order of ~200 μm .

Cancellous or trabecular bone occupies the epiphyseal and metaphyseal portions of the bones, (i.e. in the bone ends at the joints, figure 1.7, Level 6), and is surrounded by an approximately 1mm thick cortical shell. The simplest type of cancellous morphology has been described as network of randomly oriented cylindrical struts, each ~100 μm in diameter and 1mm in length. Plate like structures are commonly found when loading is primarily in one direction, giving bone its advantageous anisotropic properties. Adult cancellous bone is typically made up of primary lamellar bone or fragments of secondary osteonal bone [Currey 1984].

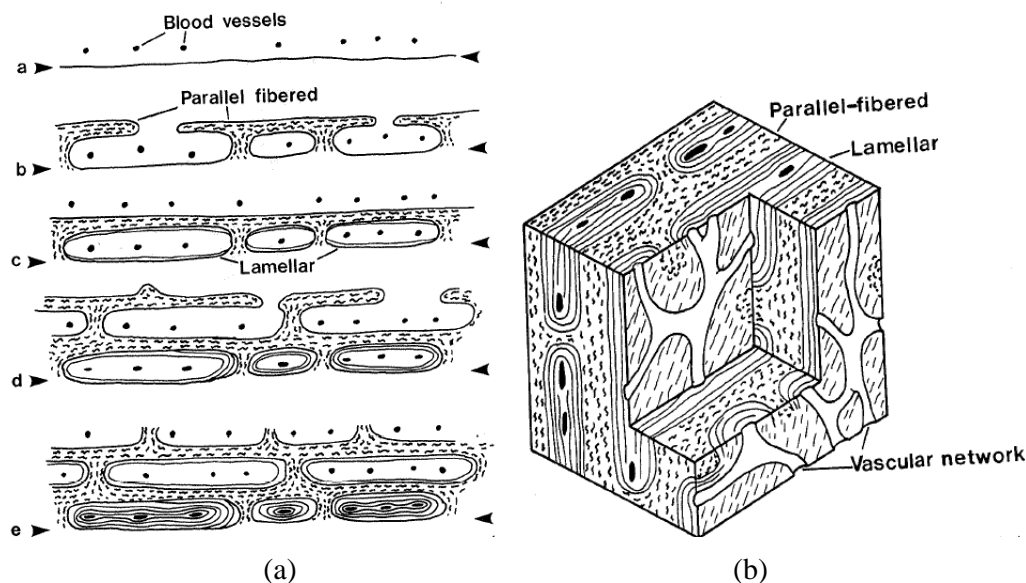


Figure 1.8 (a) The formation of fibrolamellar bone. The arrowheads show the original position of the original surface. (b) Block diagram of fibrolamellar bone – 2D networks of blood channels, sheathed by lamellar bone, alternate with parallel-fibered bone. [both from Currey 1984]

1.3.2 Bone structure in the knee

The bony anatomy in the knee joint is comprised of articular and calcified cartilage, and subchondral and trabecular bone. Yamada [1983] measured the thickness and density of the subchondral bone in the human knee joint with aging and osteoarthritis (figure 1.9). Subchondral bone thickness was defined as the radiographic high intensity area beneath the cartilage. Mean thickness and radiographic density varied from ~2-4mm and 1-1.5gr/cm³, respectively, depending on age, gender, and body mass

index. Mean cartilage thickness has been measured to be 2-3mm in the femur and tibia, with a range of 0.7-5mm [Koszyca 1996].

Trabecular bone modelling in the knee is considered to be governed by Wolff's law, with the maximum bone strength aligned in the direction of loading (this can be clearly seen in figure 1.9). Goldstein [1983] measured the elastic modulus and ultimate strength of human tibial trabecular bone as a function of the metaphyseal location. Trabecular bone properties varied as much as two orders of magnitude from one location to another, with stronger bone arising from the medial and lateral metaphyseal cortices toward the major medial and lateral contact regions.

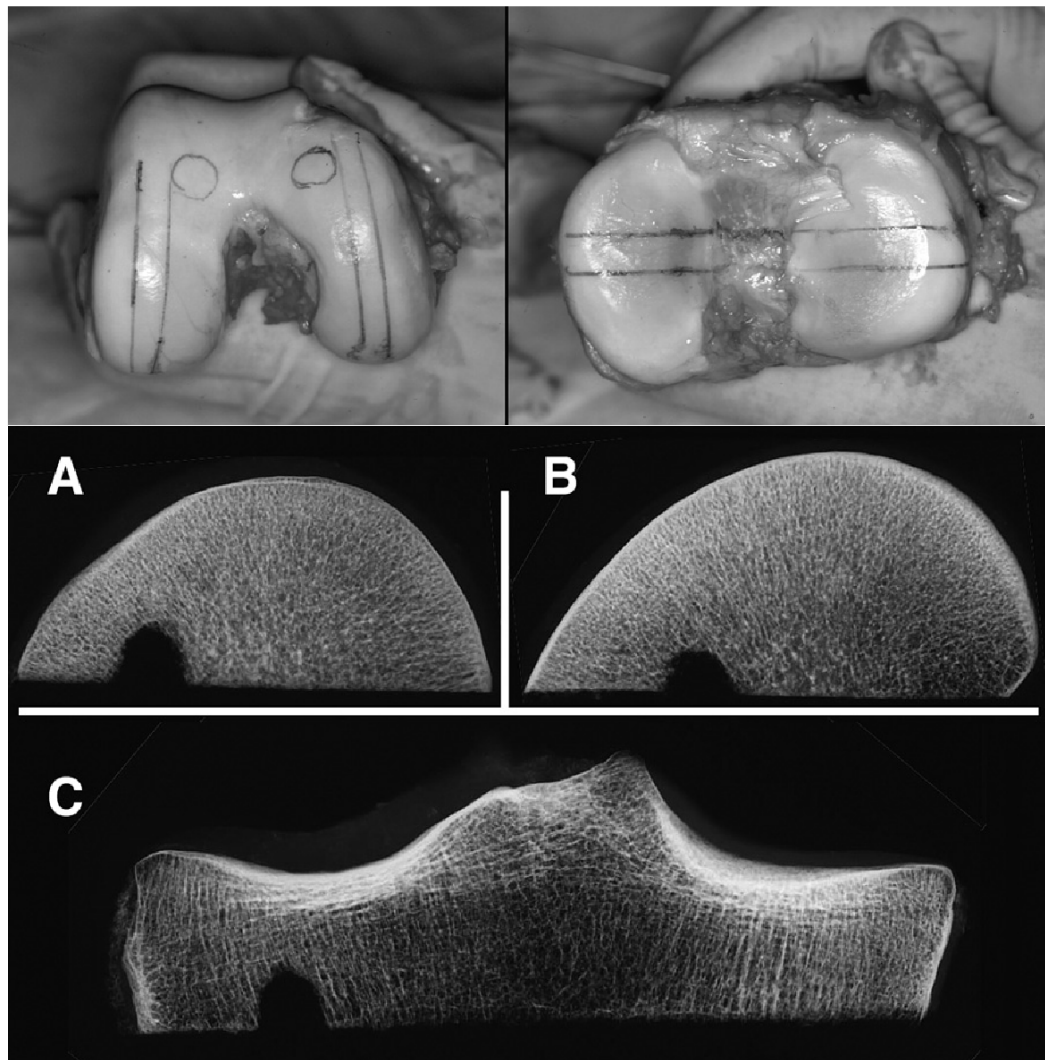


Figure 1.9 Bone structure in the knee. [from Yamada 1983]

1.3.3 Bone structure used in our cutting and milling experiments

In order to realise the first two objectives of this thesis relating to the mechanics of bone cutting, cortical bone specimens from the diaphysis of bovine femurs are used in the orthogonal and oblique cutting (chapter 2) and milling (chapter 3) experiments. Although the structure of this bone is very

different from that found in the human knee, we feel that this does not invalidate the model or the experiment results. As described above, all bone material is made up of a basic building block: the mineralized collagen fibril. Adult cancellous bone (i.e. each trabecula) is typically made up of primary lamellar bone or fragments of secondary osteonal bone [Currey 1984], which is very similar to the fibre arrangement of the bovine cortical bone specimens used in our experiments. Thus we could imagine that the cutting properties of the bone material as measured in our experiments could be extended to other bone structures by adapting for the geometrical structure. For example, the energy measured to cut fibrolamellar bone material in the three primary directions (transverse, parallel, across) could be applied to cancellous bone by considering the dimensions and orientations of the individual trabecular struts or plates that engage each cutting tooth at the various stages of the milling rotation cycle. Alternatively, a simpler approach could be envisioned using only the porosity and anisotropy parameters of the local cancellous structure as a function of its epiphyseal location. Application of the model to this extend was however beyond the scope of this thesis.

1.4 Chapter Overview

Chapter 1: Objectives, background and literature review.

Chapter 2: Orthogonal (2D) and oblique (3D) single edge cutting experiments are carried out in bovine cortical bone samples using a high-speed pendulum apparatus for three cutting blade shapes and directions relative to the bone structure (or the predominate bone fibre direction), and for several depths of cut from 2-200 μm . A new logarithmic model is used to quantify the cutting forces as a function these parameters, and is compared to previous ones proposed in the literature. Microscopic and macroscopic analysis of the chips produced during the cutting experiments were performed in order to gain a better understand of the physical mechanisms of failure governing the cutting process.

Chapter 3: The orthogonal and oblique cutting data derived in chapter one is used to formulate a model for predicting the instantaneous components of force during milling operations. Milling experiments were then carried out in bovine cortical bone for several different cutting tool speeds, shapes, directions, and milling modes (full and partial immersion up- and down-milling). Cutting force simulations were conducted using the bone-milling model and the results were compared to forces measured in the milling experiments. These data are then used to provide recommendations for an optimal milling tool cutter design, as well as an optimal manual cutting technique for bone milling in TKA.

Chapter 4: A miniature bone-mounted robot is designed for positioning cutting guides in conventional (open) computer-assisted TKA. A hybrid manual/motorised architecture is employed such that only two degrees of freedom (DoF) are aligned manually and three DoF are automated using only two motors. In addition, the cutting tool plane can be positioned automatically for any implant size or shape, making the device universal and eliminating the need for cutting blocks. An analysis of the robot design parameters and workspace is conducted in order to optimize the robot positioning and geometry.

Chapter 5: The robot initially developed in Chapter 4 is refined for use in MIS-TKA. The robot is designed to mount only on one side of the femur and cutting is carried out using a new side milling technique such that the patella does not have to be everted and the quadriceps muscles can be spared. The stiffness of two different types of fixation techniques are tested on decalcified porcine femurs. The accuracy of the device is quantified on synthetic bones and cadavers.

Chapter 5: Conclusions, future work and perspectives.

Chapter 2: High-Speed Orthogonal and Oblique Bone-Cutting

2.0 Chapter Summary

Orthogonal cutting data is extremely useful since the measured force relationships can be used to model virtually any machining process. However, previous orthogonal cutting investigations in bone have not tested conditions representative of clinical operations – i.e. very high tool speeds and small depths of cut, as in high-speed milling. In this chapter, we aim to build a mathematical model that quantifies the forces acting on a single cutting edge as a function of the depth of cut, or the uncut chip thickness. Experimental results are presented for the cutting force components and the specific cutting energy of bovine cortical bone as a function of cutting tool geometry, depth of cut, and relative orientation between the cutting edge and bone structure. The cutting force magnitudes and trends prove to be different from those previously reported in low-speed experiments, which confirms the strong dependence of machining forces on cutting speed. Two numerical force models – an exponential one and a new logarithmic model – are formulated and compared with the experimentally obtained non-linear force curves. The logarithmic force model was shown to have a better fit to the data for both small ($<50\mu\text{m}$) and large ($<200\mu\text{m}$) chip thicknesses. Microscopic observations of the cutting chips indicate a shift in the mode of failure from a more-or-less continuous to a discrete fracture mechanism with increasing depth of cut.

2.1 Introduction

Bone-cutting operations are of considerable importance in orthopaedic surgery. In total knee and hip replacement procedures, for instance, the geometrical accuracy of the prepared bone surface is particularly relevant to achieving accurate placement and good fixation of implants. Recently, robotic guidance has been introduced into these procedures to improve bone-cutting precision, typically by rigidly attaching a high-speed milling tool to a large robotic arm [Borner 2004]. Although these techniques may improve accuracy, many practitioners feel that such instrumentation is not optimally suited to the operating room due to size and safety issues; most existing systems use costly, industrial-sized robots that autonomously mill bone, giving the surgeon little control during cutting. Moreover, emerging less invasive techniques which require slender tools present even greater challenges and risks due to the reduced exposure of the bones and changes in the tool geometry and flexibility.

A model of the bone-cutting process would therefore be an invaluable tool not only for analysing stability and improving cutting performance in surgery, but also for designing compact and cost effective robotic guides and safer cutting techniques that directly involve the surgeon. In developing robotic systems, quantitative cutting force predictions would enable us to determine the strength and power requirements, the ‘chatter’ vibration characteristics, and the geometrical machining accuracy as a function of the mechanical stiffness and dynamic properties of the robot. A quantitative model would also allow us to simulate and optimize different surgical techniques and cutting tools, to analyse intra-operative force measurements, and to provide quantitative intra-operative guidance on key physical and safety parameters.

In this chapter, orthogonal (2D) and oblique (3D) cutting (see figure 2.5) is used to study and to develop a mathematical model of the fundamental process of bone-cutting. The force components tangential and normal to the cutting tooth velocity are presented for bovine cortical bone as a function of the cutting tool geometry, depth of cut, and relative orientation between the cutting edge and bone structure (cutting mode). In addition, the ‘specific cutting energy’ required to remove a unit volume of bone by cutting is presented for the above parameters.

Orthogonal cutting data has been previously acquired for very low cutting speeds ($<10\text{mm/s}$ [Jacobs 1974][Wiggins 1978]), but since a ‘softening effect’ has been identified in bone when machining at higher speeds (see [Jacobs 1976] for example), we need to re-evaluate the cutting properties of bone at

clinically relevant cutting velocities since they are almost three orders of magnitude greater (~2-5m/s). For example, a cutting speed of ~3.5m/s corresponds to ~20,000 and ~7000 RPM for a 3 and 10 mm diameter tool, respectively. To our knowledge there are no published studies on the oblique cutting of bone. We also examine the role of parasitic or edge forces which are present as the depth of cut approaches zero (typical of high-speed milling where chips are very thin).

2.1.1 Previous Work

We found four studies on the orthogonal cutting of bone [Jacobs 1973, 1974] [Wiggins 1978][Krause 1987][Mitsubishi 2005]. The ranges of the experimental parameters investigated in each study are summarized in Table 2.1, and the parameters are illustrated in figure 2.4a.

Jacobs et al [1973, 1974] were the first to report on the chip-force relationship in bovine tibial shafts for various tool geometries. Cutting tests were performed at constant speed ($v = 7.7$ mm/s) and the resultant cutting forces (F) were plotted against the uncut chip thickness ($t = 76\text{--}304$ μm) for a series of tool rake angles ($\alpha = -5, 0, 15, 35, 45^\circ$) and cutting directions (transverse, parallel, and across) relative to the predominant osteon direction. Note that there is a discrepancy between the tested depths of cuts reported in [Jacobs 1973] and [Jacobs 1974] (in the latter the measured depths of cuts were reported to be 12-48 μm); the values taken in the former are regarded as true here as the forces seem more reasonable in magnitude. The resultant cutting force curves increased linearly with uncut chip thickness (t) and intercepted the vertical axis at positive values when extrapolated. For any particular tool geometry and cutting depth, the cutting forces were highest when cutting transversely to the osteons, intermediate when cutting parallel, and lowest when cutting across to the osteon direction. The rake angle also had an influence; higher (positive) rake angles decreased the cutting forces in all cutting modes.

Other researchers have also measured higher machining forces when cutting the osteons transversely and when cutting with decreased rake angles [Wiggins 1978]. In the orthogonal bone cutting study performed by Wiggins [1978], bovine and human tibiae were cut at a constant speed ($v = 8.5\text{mm/s}$) with tools having rake angles of -30° to 40° and at six different orientations relative to the bone structure (in two normal directions within each of the three orthogonal planes). The depth of cut was varied from $\sim 10\text{--}500\mu\text{m}$ and it was found that the relationship between cutting forces (F_x, F_r) and depth of cut (t) became increasingly non-linear with increasing cutting depth. For all cutting conditions, the cutting force increased at a rate less than in direct proportion to the uncut chip thickness. This trend has also been observed in cutting certain metal and composite materials, and has been termed the ‘size effect’ [Backer 1952][Oxley 1989]. The ‘size effect’ describes the sensitivity of the material to micro defects, where materials with high sensitivity require a decreasingly amount of energy per unit volume to remove larger amounts of the material [Puw 1996].

In an orthogonal cutting study aimed at optimizing the sawing process, Krause [1987] examined the effects of cutting speed in the range of $\sim 1.3\text{--}409\text{mm/s}$. Negatively raked tools from $-30^\circ\text{--}0^\circ$ were used to cut bone samples in the across cutting mode at a fixed cutting depth of $t = 76\mu\text{m}$. He used samples from the mid-diaphysis of bovine bull femurs, cut to a width of 1.2mm to approximate the thickness of a saw-blade. He found that tangential cutting forces increased slightly with cutting speeds in the 1-25 mm/s range, and then decreased at a higher rate in the 100-400mm/s range. Radial cutting forces were also lower in magnitude in the higher speed ranges, though they tended to increase slightly in each of the two speed ranges.

The main goal of our study was therefore to examine how cutting force components vary in proportion and in magnitude as a function of cutting depth, cutting tool geometry, and cutting direction at high speeds as encountered in motorized milling operations.

Table 2.1. Experimental parameters tested in previous orthogonal cutting studies

	Jacobs [1973]	Wiggins [1978]	Krause [1987]	Mitsuishi [2005]
Rake angle, α	-5 – 45°	-30 – 40°	-30 – 0°	5 – 30°
Clearance angle, ξ	10°	10°	10°	5°
Tool velocity, v [mm/s]	7.83	8.47	~1–25 & ~100–400	0.2
Cutting direction [Transverse, Parallel, Across]	T, P, A	T, P, A	A	T,P,A
Depth of cut, t^* [μm]	76–304	~8 – 500	76	~1 – 100
Tool material	AISI M2 HSS	–	17-4 PH SS	Diamond
Work-piece material (Bone)	Bovine, Tibial	Bovine & Human*	Bovine Femoral	Porcine Femoral

* Some data acquired in tibial bone from a 15 year old accident victim for comparison

2.2 Materials and Methods

2.2.1 Workpiece Material – Bovine Bone

Six cortical bone specimens were harvested from the mid-diaphysis of fresh bovine femurs (figure 2.1) using an Exact diamond-blade band-saw under a continuous supply of irrigation. The cut specimens were screwed and potted into metal frames with dental cement and milled to a constant width of ~5mm and length of ~40mm on an industrial milling machine (figure 2.2). The specimens were potted so that when they were clamped in the apparatus, the cutting direction was either across, parallel, or transverse to the predominant bone fibre direction. Bovine bone was chosen as the workpiece material because of its similar orthogonal cutting properties to human bone [Wiggins 1978]. In addition, it is readily available and more practical to handle in comparison to human bone.

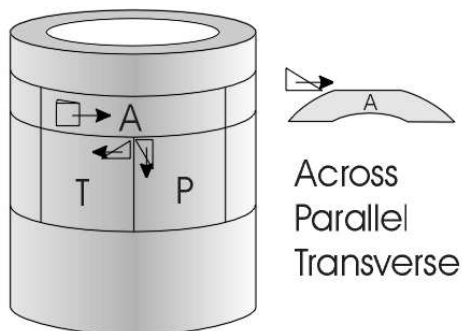


Figure 2.1.Schematic diagram illustrating how specimens for different cutting directions were removed from bone diaphysis for the different cutting modes.

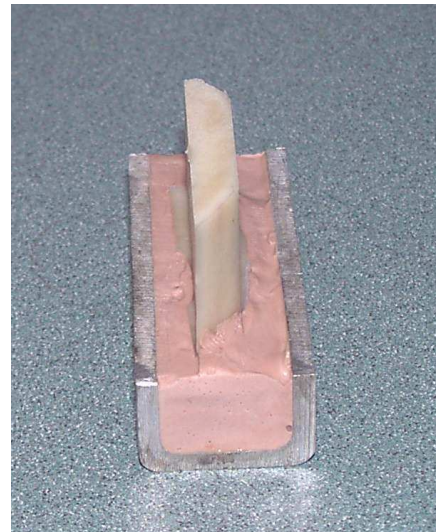


Figure 2.2. Example of potted specimen milled to constant width (cutting direction transverse to osteons).

The microstructure of the specimens as seen in the plane transverse to the bone axis is shown in figure 2.3. The anisotropic structure of the bone is clearly evident, with a mixture of mostly primary laminar and intermittent secondary osteonal bone. The structure of bovine cortical bone is relatively uniform and the direction of bone growth is readily discernible, as it is in human bone [Wiggins 1976].

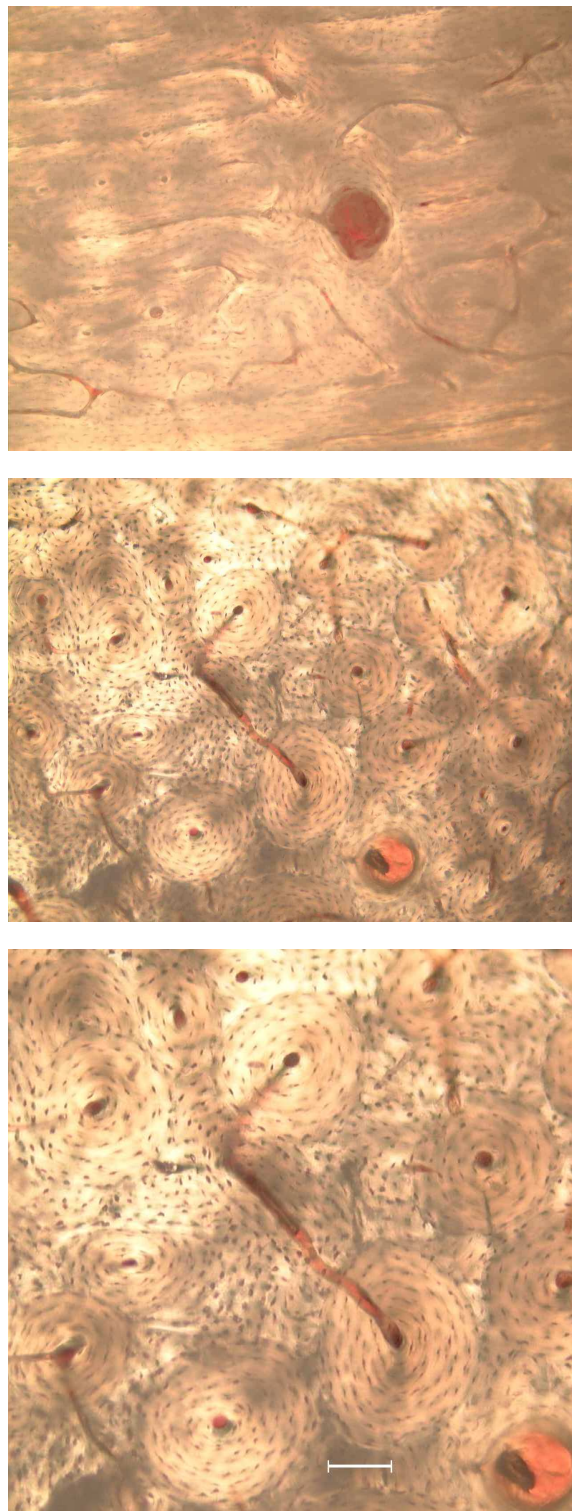


Figure 2.3. Microscopic images showing the structure of the bovine cortical bone specimens in the transverse plane. Both fibro-laminar (or plexiform, top micrograph) and osteonal (or Haversian, middle micrograph) structured bone is present. Bottom micrograph: Enlarged image illustrating osteon size (~200 μ m in diameter). Scale bar represents 100 μ m.

2.2.2 Orthogonal and Oblique Cutting Experiments

Description of variables. In the orthogonal (two dimensional) and oblique (three dimensional) cutting process, a single edge tool moves in a straight line with a velocity v parallel to the surface of the workpiece, and the relationship between the force acting on the tool and the area of workpiece material being cut by the edge (uncut chip size) is examined (figure 2.4). The measured cutting forces (F_t , F_r , F_l) and the uncut chip area (normal to v) are normalized by the specimen width (w), and the cutting force components per unit width (F_t , F_r , F_l) are correlated to the depth of cut (t).

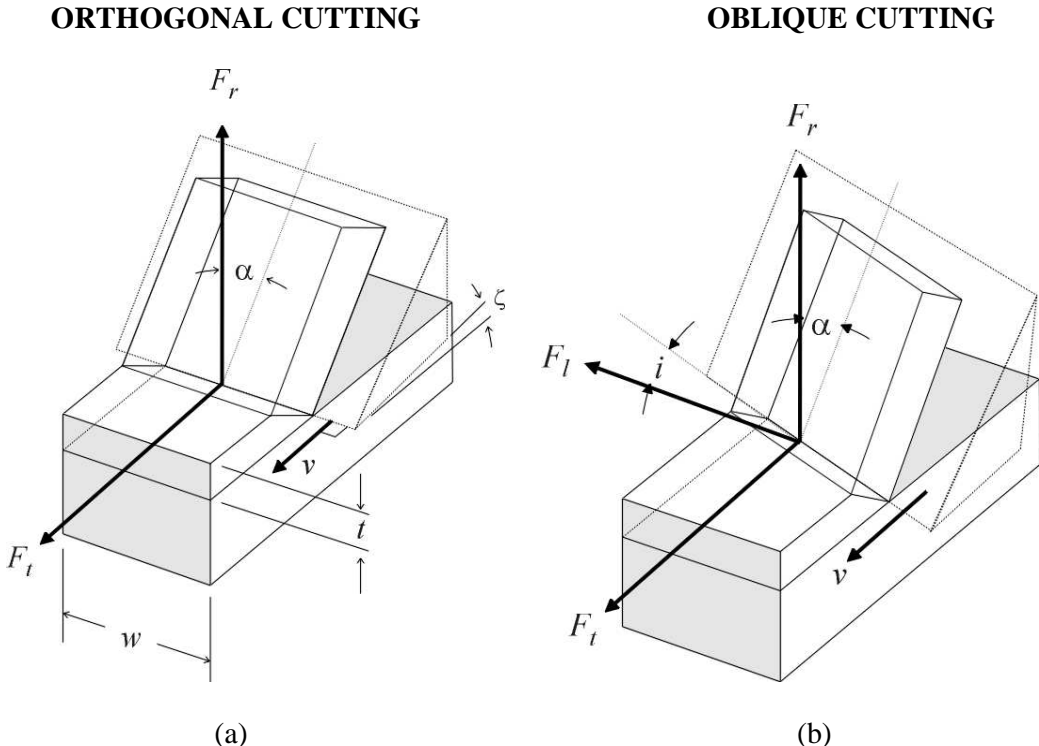


Figure 2.4. (a) Orthogonal (2D) and (b) oblique (3D) cutting parameters:

F_t – tangential cutting force; F_r – radial (or normal) cutting force; F_l – lateral cutting force
 t – depth of cut or uncut chip thickness; α – rake angle; ξ – clearance angle;
 i – angle of inclination or obliquity; v – cutting tool velocity; w – workpiece width;

The so-called ‘specific cutting energy’ (or ‘specific cutting pressure’) is a parameter commonly used in machining science to express the amount of work expended per unit volume of material removed in the cutting process. It is defined by the input cutting power ($F_t \cdot v$, where F_t is expressed in N/mm) divided by the material volume removal rate ($v \cdot w \cdot t$, where w and t are in mm). In orthogonal machining, this is simply equal to cutting force per unit cross-sectional area normal to the cutting direction:

$$E_c = F_t / t. \quad [N/mm^2] \quad \text{or} \quad [J/mm^3] \quad (2.1)$$

Experimental: In order to achieve high cutting-tool velocities (v) and small depths of cut (t) as encountered in high-speed milling operations, we used a pendulum apparatus specially designed for carrying out cutting experiments (figure 2.4). All experiments were conducted with a constant tool velocity of 3.5 m/s, which was achieved by limiting the release height of the pendulum arm with a mechanical stop. A cutting tool speed of 3.5m/s is equivalent to a 5mm diameter milling tool operating at 13,369RPM. The tool advancement in the depth of cut direction was measured with a dial gauge: a $\pm 2.54\mu\text{m}$ resolution dial gauge (Teclock Corporation) was use for most cuts, while a $\pm 1\mu\text{m}$ resolution dial gauge (Mitutoyo, Japan) was used for chip thicknesses of $1-2\mu\text{m}$. The potted specimens were clamped on a piezoelectric dynamometer that measured cutting forces for tools with a range of positive rake angles ($\alpha = 0, 20, \text{ and } 40^\circ$), depths of cut ($t = 2-200\mu\text{m}$), and directions relative to the bone axis (transverse, parallel, and across the predominant bone fibre direction, Table 2.2). All cutting tools were precision ground on an industrial grinding center from high-speed steel and had a clearance angle (ξ) of 10° (figure 2.4). The bone specimens were kept wet with physiologic saline throughout the cutting tests. For any particular set of cutting conditions ($\alpha, t, \text{ cutting mode}$), at least one pre-cut was made using the same cutting conditions before each series of measurements were recorded in order to ensure the cutting process had reached steady state conditions. After each cut, the formed chips were collected from a tray that lay beneath the apparatus and stored in labelled containers for microscopic analysis.

Tests were also performed to investigate the relationship between tangential, radial, and lateral cutting forces and the cutting tool inclination angle (obliquity) for inclination angles of $i = 25^\circ$ and $i = 45^\circ$. All three rake angles ($\alpha = 0, 20, 40^\circ$) were tested at depths of cuts of $t = 2, 12, 25, 50, \text{ and } 75\mu\text{m}$ in the across cutting mode.

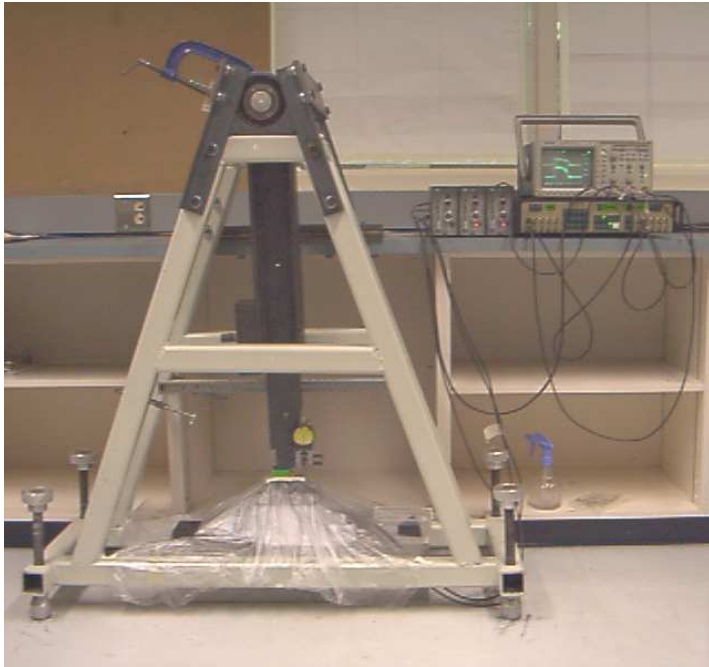


Figure 2.5. High-speed pendulum apparatus.

Additional experiments were carried out on a single bone specimen (parallel cutting mode) and tool (40°) to study the effects of cutting speed on the force components for three depths of cuts (2.54, 12.7, and $25.2\mu\text{m}$). Cutting tool velocities of 1.3, 2.4, and 3.5m/s were achieved by releasing the pendulum from three different heights.

Table 2.2. Range of experimental cutting parameters tested

Rake angle, α	0, 20, 40°
Clearance angle, ξ	10°
Tool velocity, v [mm/s]	3500
Cutting direction	Transverse, Parallel, Across
Depth of cut, t^* [μm]	2.54, 7.62, 12.7, 25.4, 50.8, 101.6, 25.4, 50.8, 101.6, 203.21
Angle of inclination, i	0, 25, 45°
Tool material	High Speed Steel

*In addition, some data was acquired at 1 and $2\mu\text{m}$ depths of cut

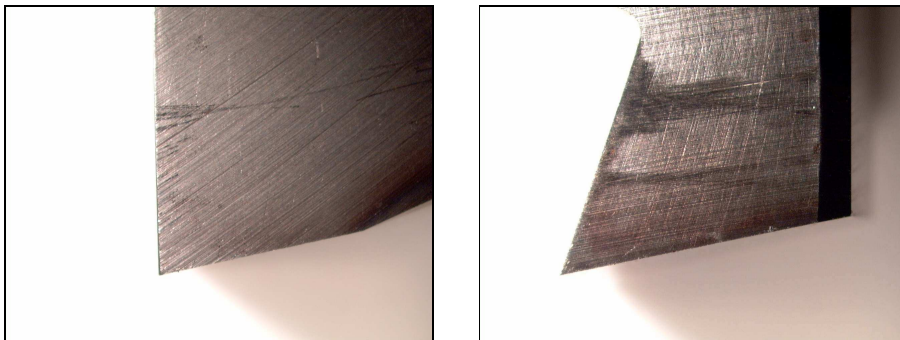


Figure 2.6. Profile images of the $\alpha=0^\circ$ (left) and $\alpha=20^\circ$ (right) rake angle cutting tools.

2.2.3 Data collection:

The piezoelectric force signals were amplified with Kistler charge amplifiers, low pass filtered at 150Hz with a six order Butterworth analog filter, and displayed on a four channel digital oscilloscope (Techtronics, figure 2.7). The oscilloscope was configured so that the filtered signals were superimposed directly onto the amplified force components. The unfiltered force signals exhibited some degree of fluctuation during the cutting process, where the proportional fluctuation in cutting force was generally more pronounced at larger depths of cut. To provide a repeatable measure of the average forces during cutting, the arithmetic mean across the force plateau region of the filtered curve was recorded (this value was calculated by the oscilloscope using the vertical crosshairs to define the start and end points). The averaging window was taken in the mid-region of the specimen (where the specimen width was constant) to reduce the influence of cut entry and cut exit effects. The duration of the cutting force was on the order of 10ms.

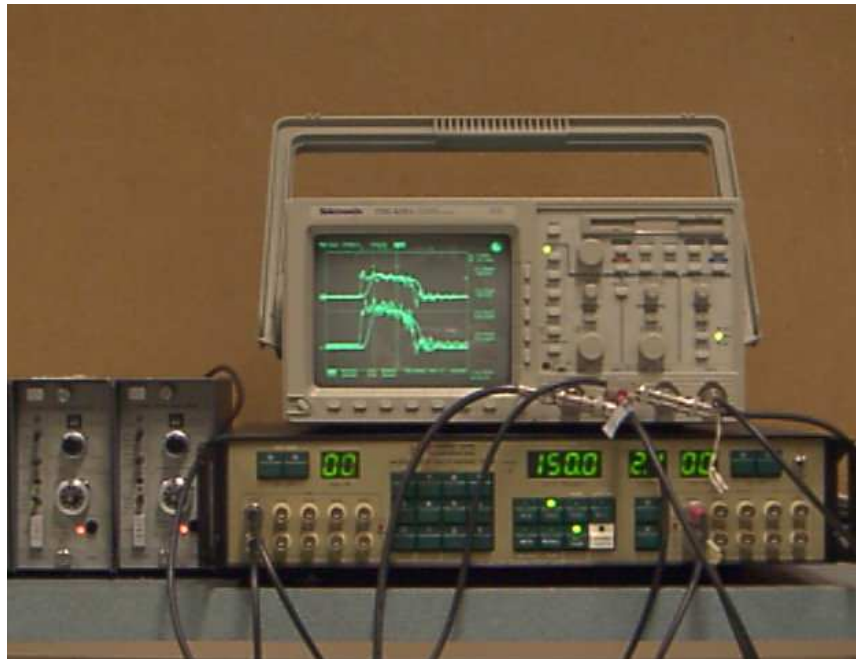


Figure 2.7. Data acquisition system: Piezoelectric force signal charge amplifiers (left), analogue filter (bottom right), digital oscilloscope (top right)

2.2.4 Data analysis:

The cutting force components per unit width tangential (F_t) and normal (F_r) to the cutting velocity are expressed as a function of depth of cut (t) for each tool geometry and cutting orientation. Two non-linear cutting force models were investigated. The first was a power law commonly used in machining mechanics [Wiggins 1976][Oxley 1989]:

$$F = K_c t^n + F_e \quad (2.2)$$

where n ($0 < n < 1$) are the constant parameters characterizing the ‘size effect’ of the particular workpiece material, and K_c are the constant ‘cutting’ parameters which characterize the local cutting mechanics and are dependent on the tool geometry and cutting direction relative to the bone anisotropy, and F_e are the residual force components per unit width at zero depth of cut (also referred to as ‘edge’ or friction forces [Yellowley 1985]). It can be seen from Equation 2.2 that when the cutting force/depth of cut relationship is linear and there are no edge forces (i.e. $n = 1$ and $F_e = 0$), the specific cutting energy is constant and equal to K_c . However, when $n < 1$ or $F_e \neq 0$ the energy required to remove a unit volume decreases as the depth of cut increases.

A new logarithmic cutting force equation was also investigated:

$$\log_{10}(F_i) = K_3 \log_{10}^2(t) + K_2 \log_{10}(t) + K_1 \quad (2.3)$$

This empirical fit is obtained by plotting F vs t on log-log coordinates, and fitting in a least-squares sense a 2nd order polynomial to the data points (where each data point is the average of ~4 measurements), to obtain the three characterization constants K_1 , K_2 , and K_3 . An example of the behaviour of this function is presented in figure 2.8 for a sample dataset in the logarithmic and arithmetic domains. For the power law, the constants K_{ic} , n_i and F_{ie} were determined for each cutting

curve using a non-linear least-squares optimization that minimized the total error between the power law curve and each averaged data point. All calculations were preformed in Matlab R12.1 (The Mathworks, Inc.) using the *lsqnonlin* and *polyfit* routines to determine the power and logarithmic curve constants, respectively.

The unpaired Student's t-Test (two sample equal variance) was used to determine if there were any significant differences between the mean forces measured at the different cutting speeds.

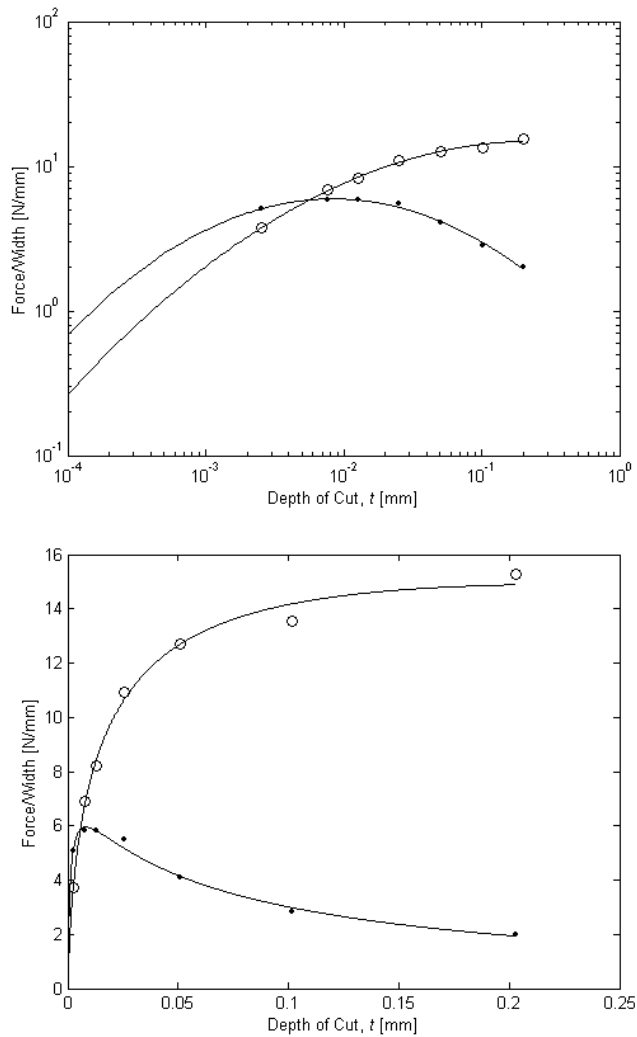


Figure 2.8. Example of the non-linear cutting force curve fit in the logarithmic and arithmetic domains.

Upper: Cutting constants K_1 , K_2 , and K_3 were determined by transforming the force vs depth of cut (F vs t) data in the logarithmic domain and fitting a 2nd order polynomial to the averaged data points. Lower: F vs t and resulting fitted curve plotted on a linear scale.

2.3 Results

2.3.1 Orthogonal Cutting Force Curves

The radial and tangential cutting force component data for cutting parallel, transverse, and across the fibre direction with three different tool geometries are plotted for the $t < 200\mu\text{m}$ (figure 2.9a) and $t < 50\mu\text{m}$ (figure 2.9b) depth of cut ranges. Each point on the graph represents the average of four cuts, though the standard deviations (which were generally less than 5%) are omitted for clarity. The curves fitted to the data points in figures 2.9a,b correspond to the logarithmic cutting force equation 2.3 (see Appendix A1 for the exponentially fitted curves).

As can be seen in both figures 2.9a,b, the tangential cutting force component tended to increase with cutting depth, though the rate of increase in cutting force declined as the depth of cut increased for all rake angles and cutting directions. The increase in cutting force with cutting depth is least pronounced for the across cutting mode, particularly for larger rake angles and cutting depths. The radial force component tended to increase with cutting depth up until $\sim 2\text{--}50\mu\text{m}$ (depending on the conditions), upon which the force began to decrease for all but one set of cutting conditions (rake angle $\alpha=0^\circ$, parallel cutting mode). The rate of decrease in radial force was least pronounced when cutting with the 0° rake angle for all cutting directions.

Both the tangential and radial cutting force components tended to decrease as the tool rake angle increased from 0 to 40° , though this decrease was considerably less pronounced and less consistent for the radial cutting force. Forces in the across cutting mode were least sensitive to changes in rake angle and were generally lower than the parallel and transverse cutting modes for both the thin and the thick chip ranges. The tangential to radial force ratio (F_t/F_r) was generally less than one for cutting depths less than $\sim 10\mu\text{m}$ (range $5\text{--}20\mu\text{m}$), upon which the ratio began to increase past unity with cutting depth. The average ratios $F_{t,\alpha=40^\circ}/F_{t,\alpha=0^\circ}$ and $F_{r,\alpha=40^\circ}/F_{r,\alpha=0^\circ}$, in the $50\text{--}200\mu\text{m}$ depth of cut range are 50% and 33% respectively, which indicates the improvement in cutting efficiency with positive rake angle. As the depth of cut approaches zero, however, the measured tangential and radial forces (i.e. at $t \sim 2.5\mu\text{m}$) tended to near constant values of ~ 3.5 and ~ 5.5 N/mm respectively, largely independent of the tool rake angle.

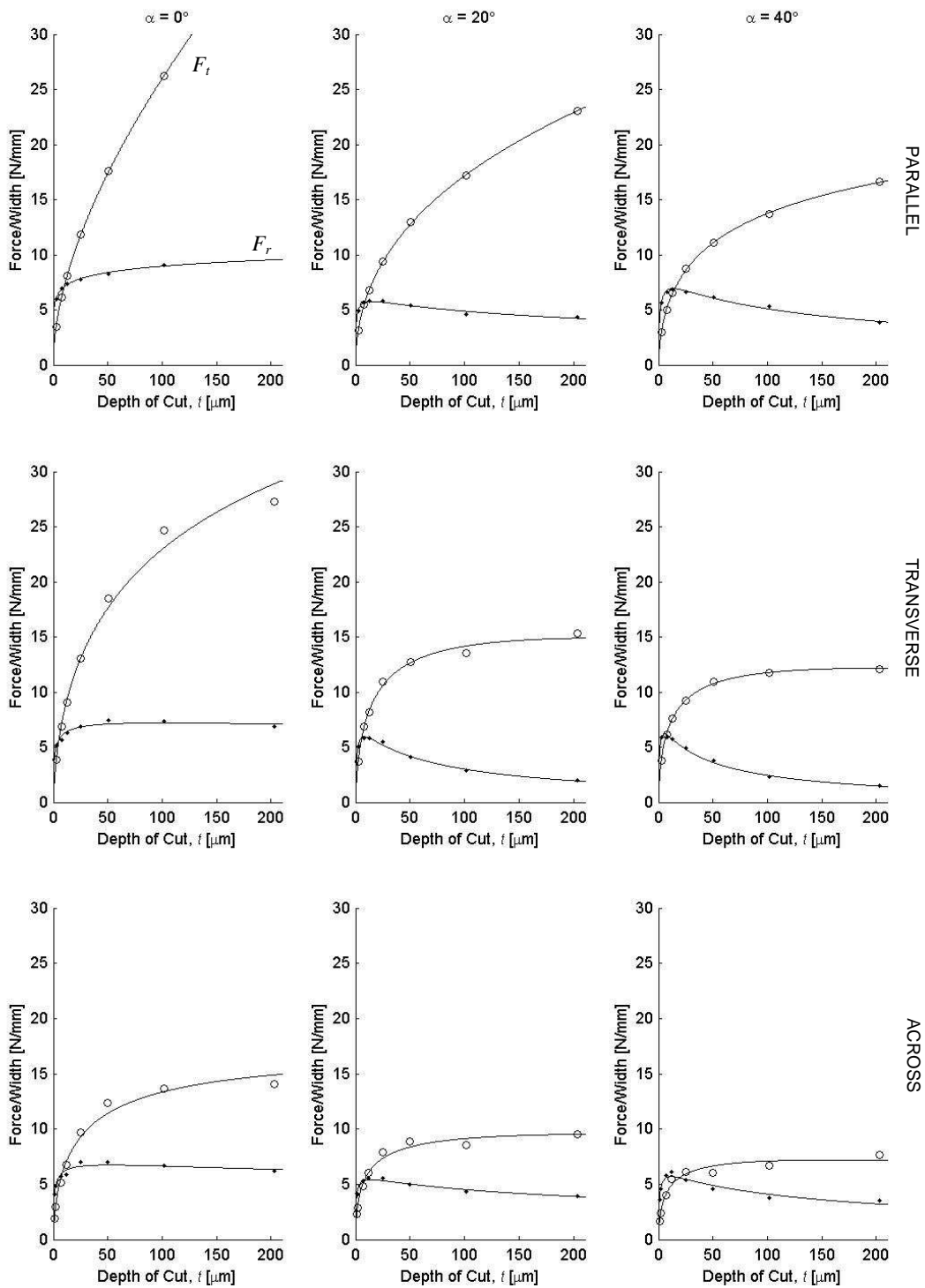


Figure 2.9a: Tangential (\circ - F_t) and radial (\bullet - F_r) force components plotted against depth of cut for three different rake angles and cutting modes for large scale chip thickness (0-200 μm).

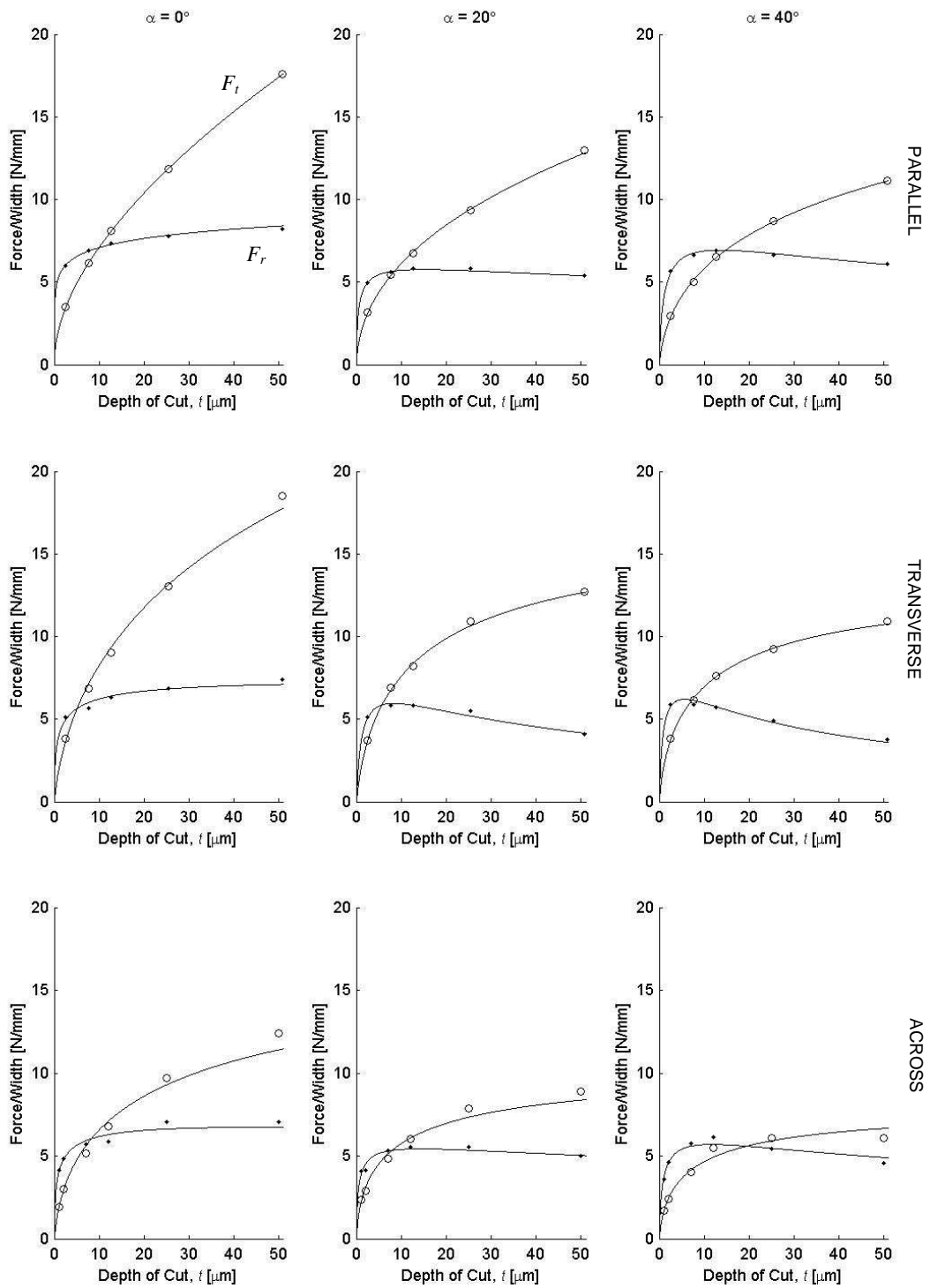


Figure 2.9b. Tangential (\circ — F_t) and radial (\blacktriangle — F_r) force components plotted against depth of cut for three different rake angles and cutting modes for small scale chip thickness (0–50 μm).

2.3.2 Oblique Cutting Force Curves

The effect of inclination angle on the tangential, radial and lateral cutting forces is presented in figure 2.10 for the three rake angles in the across cutting mode. The lateral cutting force curve is similar in shape to the tangential force curve, increasing in magnitude with the inclination angle. The angle of obliquity in general had very little effect on the tangential and radial cutting force curves, though the radial force was higher in magnitude for the $i = 45^\circ$, $\alpha = 0^\circ$ cutting condition.

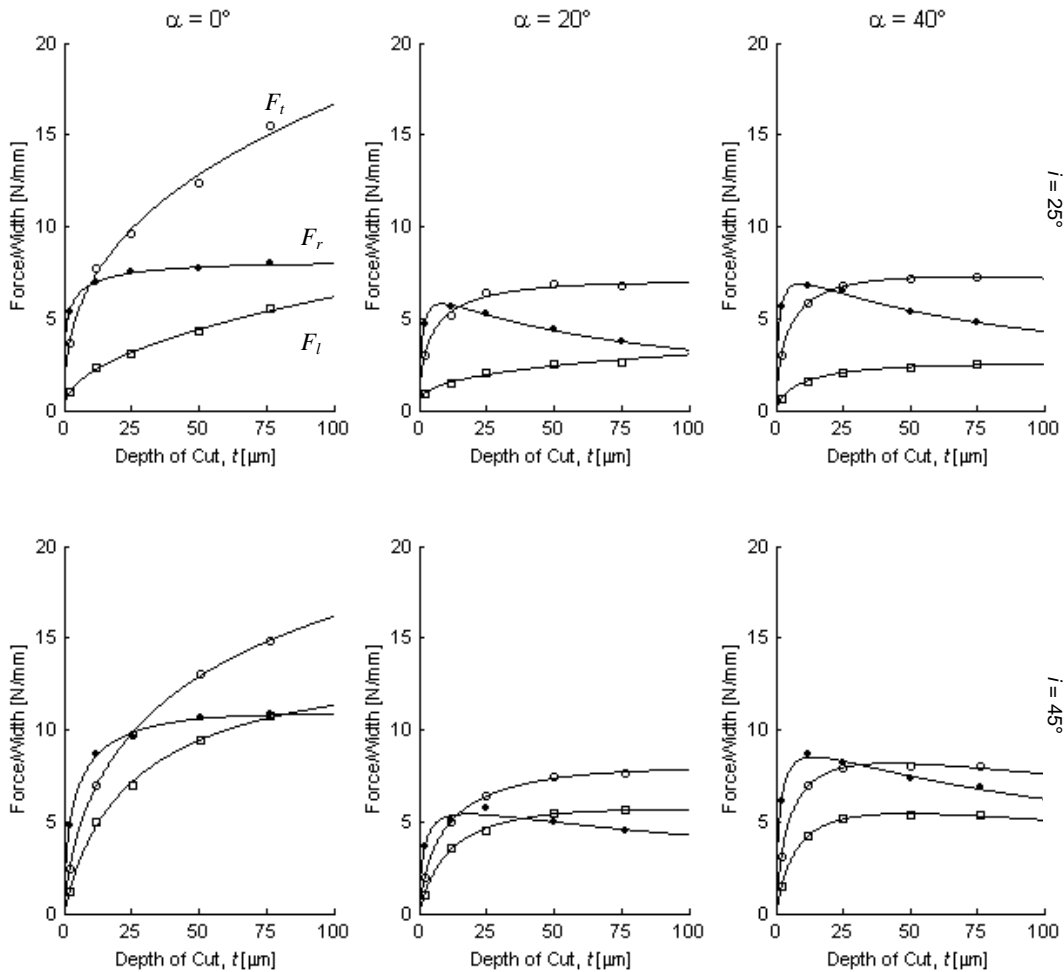


Figure 2.10. Tangential (\circ — F_t), radial (\bullet — F_r) and lateral (\square — F_l) force components plotted against depth of cut for obliquity angles $i = 25^\circ$ (upper row) and $i = 45^\circ$ (lower row) for three different rake angles in the across cutting mode.

2.3.3 Effect of Cutting Velocity

The effect of cutting tool velocity on the tangential and radial force components at three depths of cut are presented in figure 2.11 for a single bone sample and cutting tool (tool rake angle $\alpha=40^\circ$, parallel cutting mode). No data is available at the $t = 24.5\mu\text{m}$ cutting depth for the 2.4m/s cutting velocity due to the lack of specimen size.

The radial force component increased with increasing cutting speed for all cutting depths tested. The percentage increase in radial force in going from 1.3 to 3.5m/s was ~25% at the smallest cutting depth of $t = 2.54\mu\text{m}$, and ~6.5% for both $t = 12.7\mu\text{m}$ and $t = 25.4\mu\text{m}$ ($p<0.0001$ for all three cutting depths).

The relationship between the tangential cutting force and cutting speed depended on the cutting depth. At the lowest cutting depth of $t = 2.54\mu\text{m}$, the tangential force increased significantly ($p<0.0001$) by ~18% from 1.3 to 3.5m/s, while at $t = 12.7\mu\text{m}$ there was no significant change. At $t = 25.4\mu\text{m}$ the mean tangential force decreased slightly by ~3.3% ($p<0.0001$).

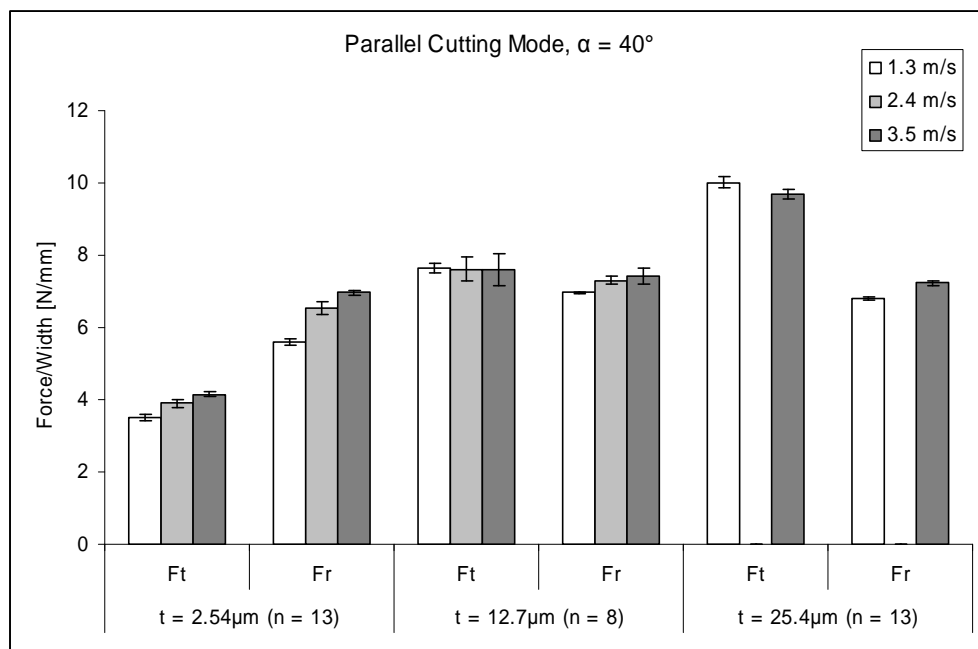


Figure 2.11. Effect of cutting velocity on tangential (F_t) and radial (F_r) force components at three depths of cut (t) in one bone sample. Parallel cutting mode, tool rake angle $\alpha=40^\circ$.
 n indicates number of cuts made for each different set of cutting conditions.

2.3.4 Specific Cutting Energy

The relationships between the specific cutting energy and depth of cut for three different rake angles and three different cutting modes are shown on log-log coordinates in figure 2.12. It can be easily seen that as the depth of cut increases, the amount of work required to machine a unit volume of bone decreases for all tool geometries and cutting modes. This decrease in specific cutting energy with depth of cut is a direct result of the nonlinear increase in the tangential cutting force component as seen in figures 2.9a,b. The decrease in specific cutting energy with increasing rake angle is also evident.

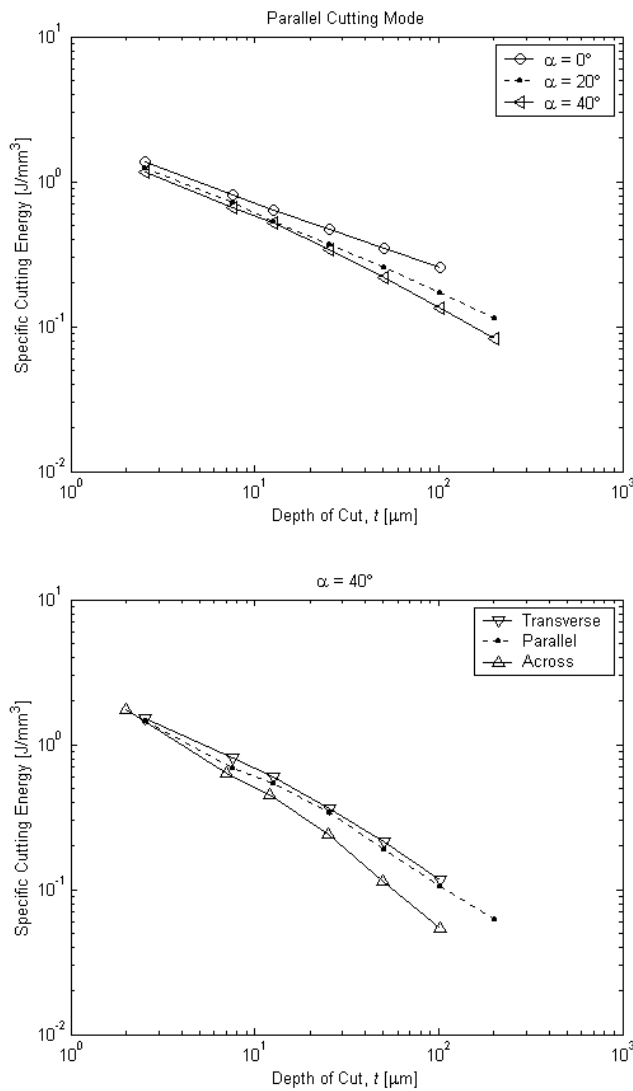


Figure 2.12. Specific cutting energy vs. depth of cut plotted on log-log coordinates.

Top: three rake angles and one cutting mode (parallel).

Bottom: three cutting modes and one tool angle ($\alpha=40^\circ$).

The specific cutting energy was lowest for the across cutting mode. Cutting in the parallel direction resulted in either slightly lower or higher energies than cutting in the transverse direction, depending on the specimen tested (the parallel specimen presented in figure 2.12 was different from that presented in figures 2.9a,b).

2.3.5 *Observations on Chip Formation and Sub-Surface Damage*

Typical micrographs of the various bone chips produced for the range of cutting conditions tested are presented in figures 2.13 through 2.17 (none of the microscope images have been cropped in order to preserve their relative scale). The chip formation mechanism at small depths of cut (i.e. $<15\mu\text{m}$) tended to resemble a continuous process where chips were more-or-less unbroken structures which slid up the tool rake face, curling as the tool progressed through the bone (figures 2.13ab–2.15ab). The orthogonal cutting chips at these low depths of cut were generally coiled in a single plane while oblique cutting conditions produced chips that were spiral shaped with the spiral angle increasing with the tool inclination angle (figure 2.17a). The chips were observed to disperse in the direction perpendicular to the cutting edge for both orthogonal and oblique cutting [Stabler 1951]. Macro and microscopic evaluation of the dry chip specimens revealed small cracks or micro-fractures running primarily in the direction parallel to the cutting tool edge throughout the length of the curled chip (figure 2.13c). Crack width, size and number seemed slightly larger for the transverse cutting mode (figure 2.13a) than the parallel (figure 2.14a) or across (figures 2.15a and 2.16) modes. Scrape lines or grooves in the direction parallel to the cutting tool velocity were also evident (figure 2.13c), likely due to profile of the cutting tool edge and the micro-texture of the rake/clearance face surfaces, which were ground but not polished (figure 2.20).

As the depth of cut increased past $25\mu\text{m}$, the chip formation mechanism began to change to one of discrete fractures for both orthogonal and oblique cutting, where the chips tended to appear more undeformed and segmented in nature (figures 2.15d, 2.15e, and 2.17b). Bone material began to build-up and stick onto the tool rake face near the cutting edge, particularly for the lower rake angled tools. At the maximum depth of cut of $203\mu\text{m}$, large bone fragments were observed to ‘fracture off’ the specimen during cutting, projecting from the cutting site with a high velocity (figures 2.15f, 2.16, 2.18). The fracture surface is not uniform or flat throughout the length of the chip, but appears to have propagated along the weak lines or planes between the laminar layers (cement interface) in the specimen (figure 2.18). These trends in chip formation were generally observed for all three cutting modes and tool geometries (figure 2.13–2.16), though the extent of fracture failure and the size of the undeformed chip fragments observed at the large depths of cut (ie. $>100\mu\text{m}$) seemed to be slightly less for the parallel cutting mode (figures 2.14c and 2.14d) than the transverse or across directions (figures 2.15–2.17).

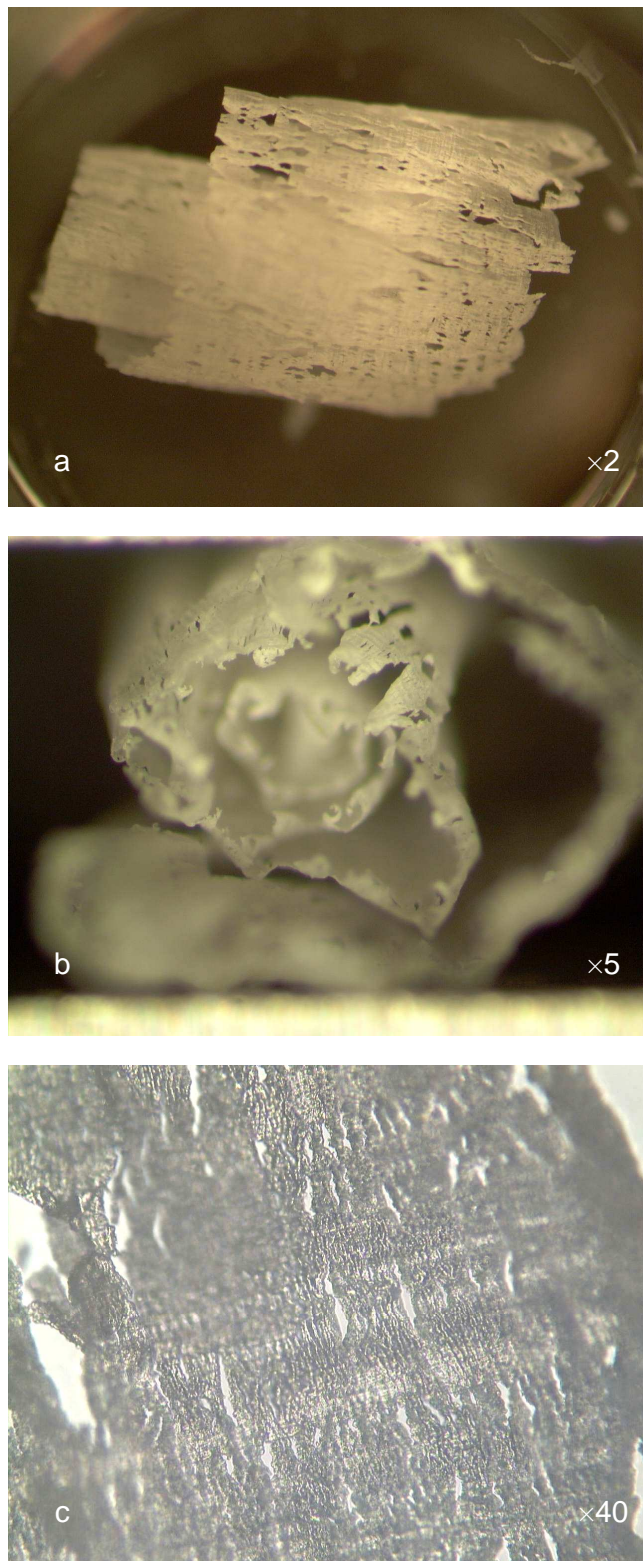


Figure 2.13. Macro- and microscopic images of a dry bone chip at various magnifications.

Depth of cut $t = 2.5\mu\text{m}$, rake angle $\alpha=40^\circ$, transverse cutting mode.
(a) view from above (b) profile view of chip (c) view from above

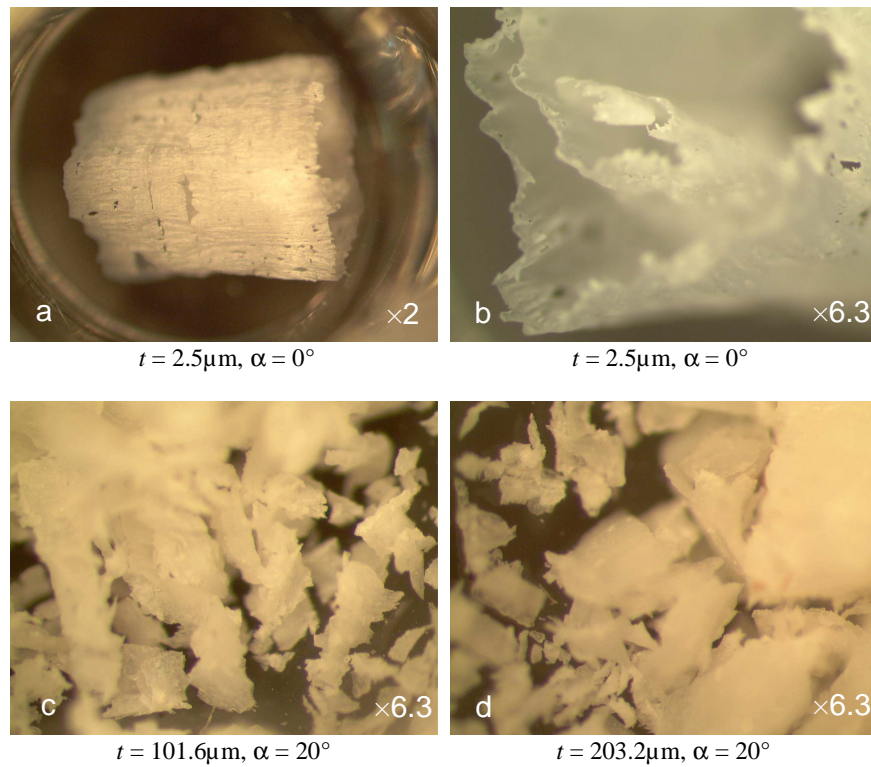


Figure 2.14. Various macroscopic images of bone chips for the parallel cutting mode.

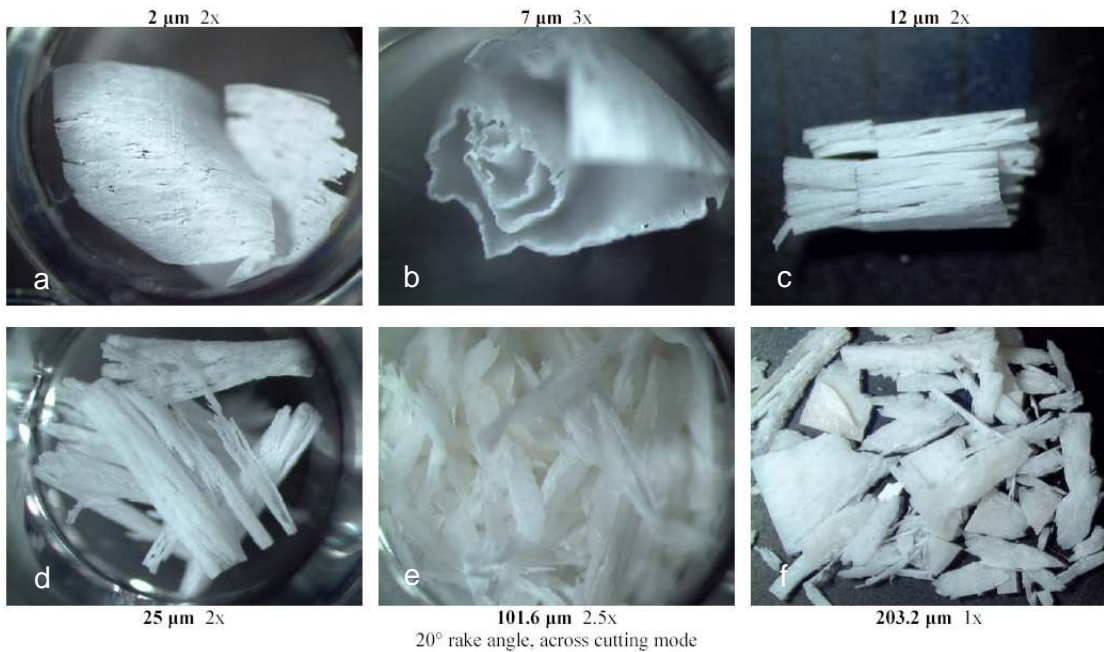


Figure 2.15. Macroscopic images of cut bone chips illustrating change in chip formation mechanism with cutting depth, for 2.5–203 μm depths of cut.

Rake angle $\alpha=20^\circ$, across cutting mode.

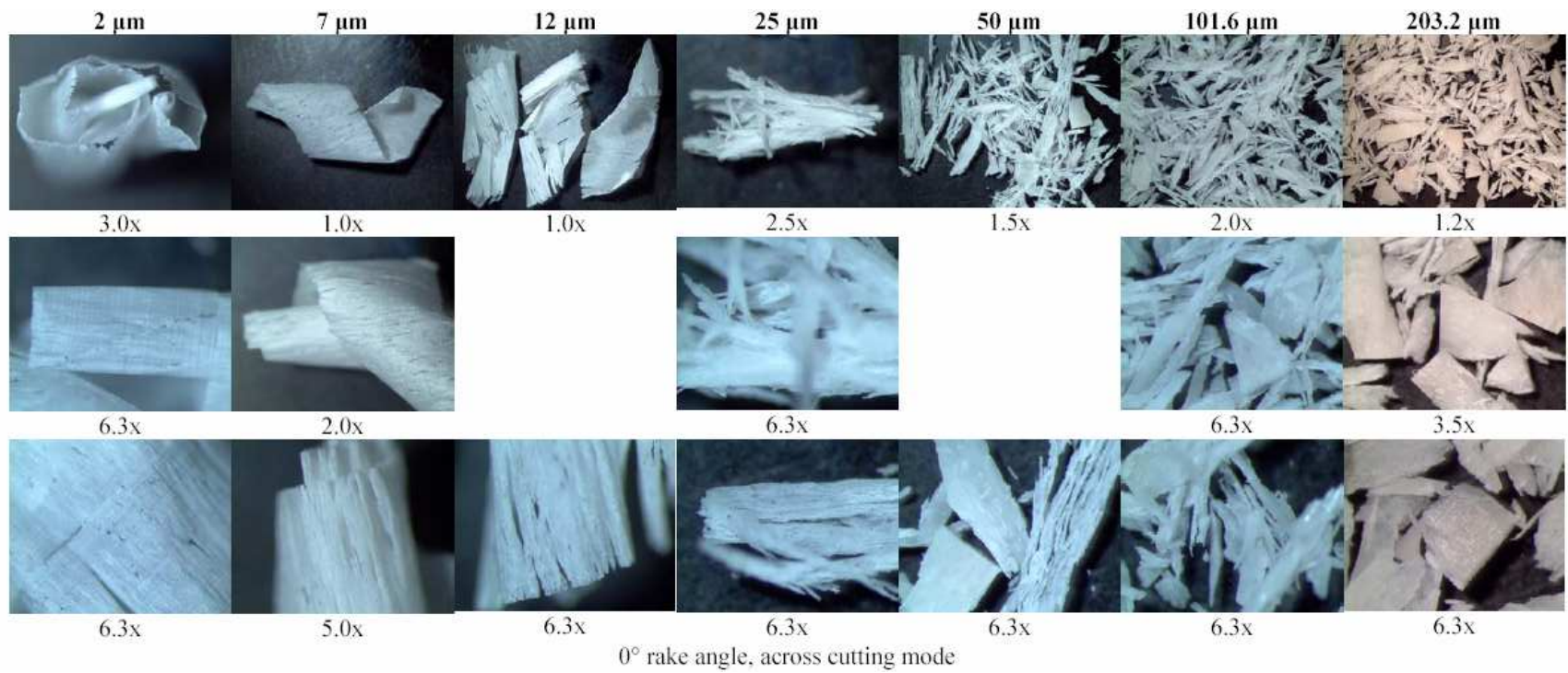


Figure 2.16. Macroscopic images of cut bone chips illustrating progressive change in chip formation mechanism with cutting depth, for 2–203 μm depths of cut – rake angle $\alpha=0^\circ$, across cutting mode.

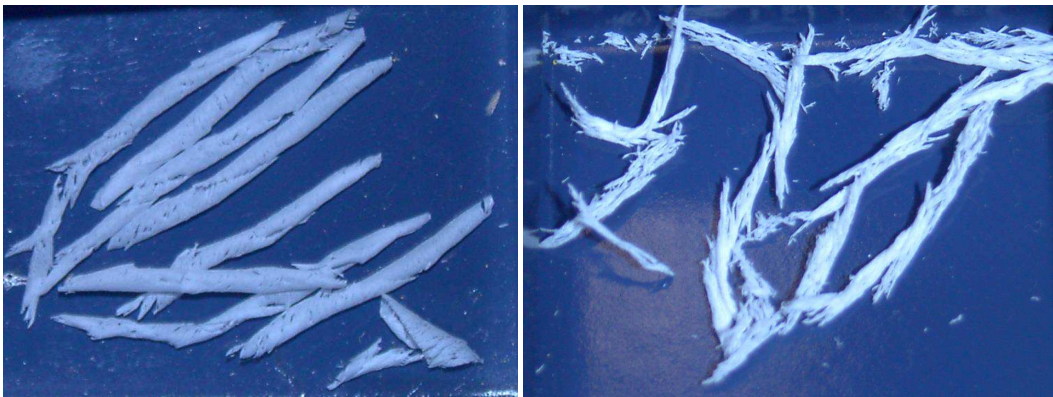


Figure 2.17. Digital photographs of oblique bone cutting chips for small ($t=2\mu\text{m}$, left) and medium ($12< t < 25\mu\text{m}$, right) depths of cut – across cutting mode.

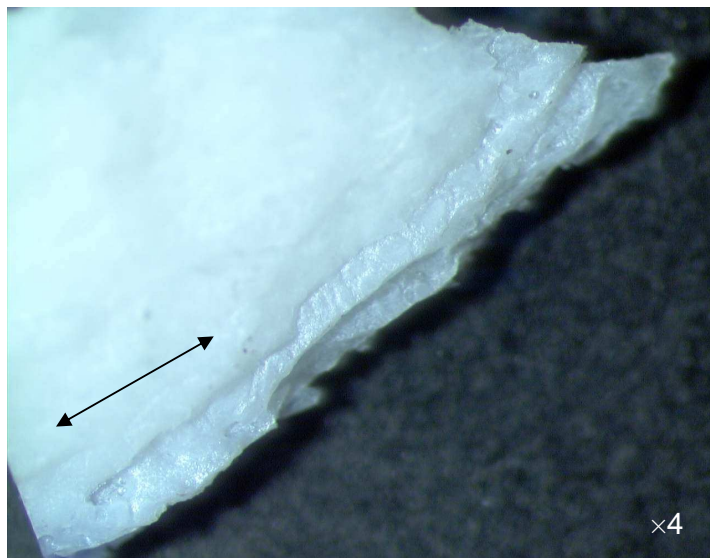


Figure 2.18. Macroscopic photograph illustrating fracture path on a large bone chip fragment – depth of cut $t = 200\mu\text{m}$, tool rake angle $\alpha=20^\circ$, across cutting mode.

Arrow indicates direction of long bone axis.

The degree of subsurface damage below the cutting plane was observed to increase significantly with cutting depth. At very small depths of cut, the bone surface finish appeared visually very smooth and polished in nature. As t approached the maximum cutting depth of $203\mu\text{m}$, the uncut bone surface began to appear increasingly pitted and cracked. Large craters and cracks were observed on the cut surface particularly when cutting with lower rake angles and in the transverse cutting mode (likely due to the fracture propagating down into the specimen along the fibres). These cutting conditions were typically characterized by large, erratic fluctuations in the unfiltered force signal. The worst case of subsurface damage occurred when making a transverse cut with a 0° raked tool at a depth of $203\mu\text{m}$ (figures 2.19a and 2.19b) directly after a $102\mu\text{m}$ thick cut (which caused relatively less subsurface damage). After repeated cuts at depths of $200\mu\text{m}$, however, the degree of damage reached a less severe, steady-state condition (figures 2.19c).

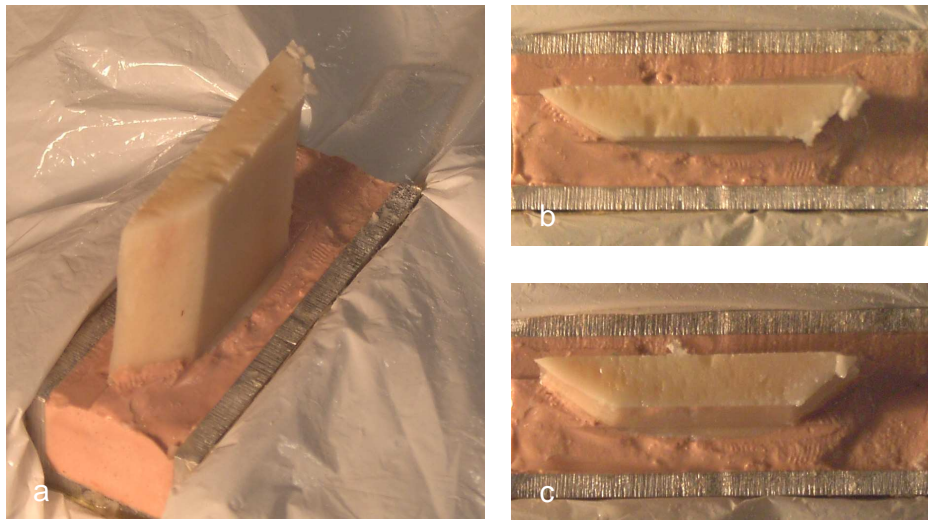


Figure 2.19. Subsurface damage was evident at very large depths of cut and low rake angles – depth of cut $t = 203\mu\text{m}$, rake angle $\alpha=0^\circ$, transverse cutting mode.

- (a, b) Subsurface damage was most severe when going from a $100\mu\text{m}$ to $200\mu\text{m}$ depth of cut
(c) Damage seemed to reach a less severe, steady-state condition after repeated cuts of $200\mu\text{m}$ depth

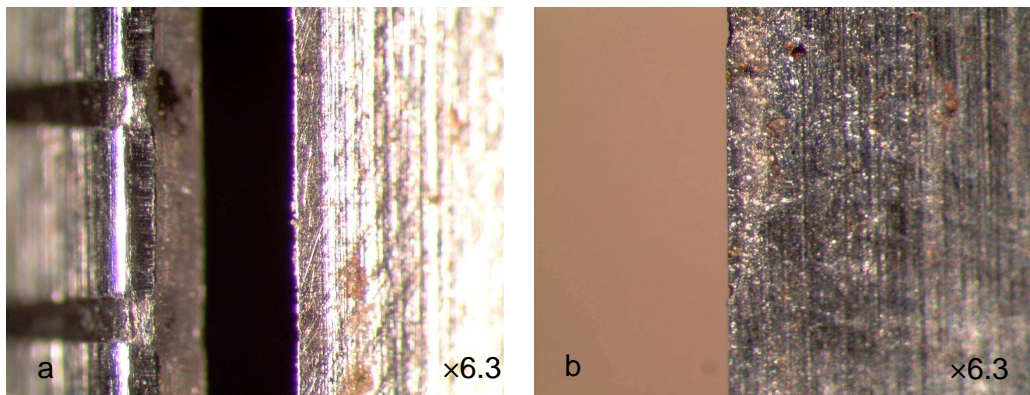


Figure 2.20. Macroscopic photographs of the tool rake (a) and clearance (b) faces taken after the cutting tests (tool rake angle $\alpha=20^\circ$).

Scale bar on the left side of image (a) indicates 1mm.

2.4 Discussion

High-speed cutting operations such as milling, drilling, sawing, are commonly performed in modern orthopaedic surgery, though relatively little is known about the mechanics of such processes. Previous works have studied the interrelationships of orthogonal cutting variables in bone at relatively low speeds and large depths of cut. The goal of this study was therefore to quantify the interrelationships of cutting force, depth, tool geometry, and direction at higher speeds as encountered in surgical milling operations.

2.4.1 Effect of Cutting Velocity – Comparison with Previous Low-Speed Data

On the bases of the experiments reported here, we can see that the relationship between orthogonal bone-cutting forces and depth of cut is highly non-linear at speeds on the order of a few meters per second (figures 2.9a,b). Although non-linear relationships have also been measured at very low speeds of less than 10mm/s [Wiggins 1978], these reported relationships are different from those we measured. Cutting at high speed with large rake angles (20–40°) causes the radial cutting force (F_r) to increase with cutting depth (t) for $0 < t < \sim 15\mu\text{m}$, after which F_r begins to taper off for all cutting directions (where the highest rate of decrease was observed for the transverse cutting mode). For low speeds and for tool rake angles of 10° and 40°, Wiggins [1978] report an increase in the radial force component with cutting depth from 0 up to 100–200 μm and beyond, depending on the cutting conditions. Jacobs [1973] reported near constant, decreasing and even negative radial forces for cutting with 35° and 45° raked tools in the 76–305 μm depth of cut range. The magnitudes of the radial forces at low speeds reached levels ~2–10 times larger than those measured here, depending on the cutting depth and direction [Jacobs 1973][Wiggins 1978].

On the other hand, the general shapes of the tangential cutting force (F_t) versus depth of cut curves (t) for high-speed cutting were similar to those reported at low cutting speeds [Wiggins et al. 1978]. The force magnitudes in the direction tangential to the tool velocity were, however, ~30–50% of the low-speed values for all rake angles and cutting directions tested. This observation can also be clearly seen by comparing our high-speed data with the low-speed data of Jacobs [1973] for the rake angles of 0°, 15° and 35° (figure 2.21).

Krause's [1987] results detailing the influence of cutting velocity in the range of 1.3–409mm/s for a single depth of cut and cutting mode ($t = 76\mu\text{m}$, across cutting mode) are presented in figure 2.22 for the 0° rake angle tool. The results at 3.5m/s represent my data averaged between the 50 and 102 μm cut depths for the same conditions (across cutting mode and 0° rake angle tool). It is evident that at this depth of cut the tangential force continues to decrease with cutting speed above $v = 100\text{m/s}$. A decrease in cutting force with cutting speed has also been observed in the cutting of metals, though this phenomenon is thought to be a result of an increase in temperature in the so-called shear plane or primary shear zone, and an associated decrease in the yield shear stress of the material. We observed primarily a fracture rather than a shear mechanism in cutting bone at the larger depths of cuts, however, which is agreement with previous low-speed studies [Jacobs 1976][Wiggins 1978][Krause 1987]. The decrease in bone-cutting forces at the higher depths of cut may be due to the change in bone properties at extremely high strain rates. Saha and Hayes [1976] observed a weakening effect of the Haversian systems when fracturing bone in tensile impact tests at very high strain rates. Krause reasoned that the decrease in cutting force with velocity could possibly be due to the existence of a critical crack velocity, as the crack initiation energy in bone has been suggested to decrease with an increase in strain rate [Pope 1976]. From his results, Krause postulated that this critical crack velocity is ~50mm/s.

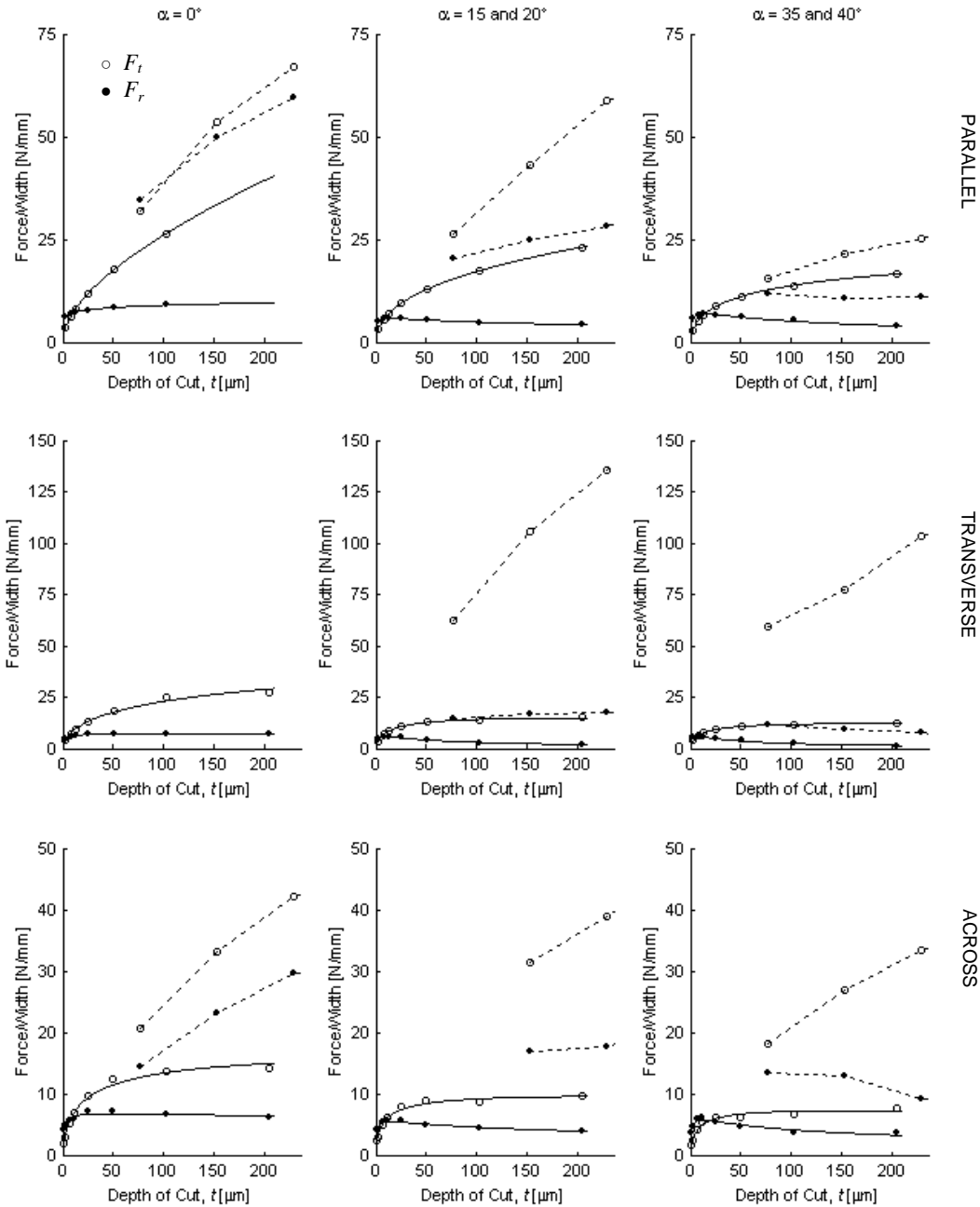


Figure 2.21: Comparison between high-speed (solid line, $v = 3.5\text{m/s}$) and low-speed (dashed line, $v = 7.7\text{mm/s}$) data.

Low speed orthogonal data taken from Jacobs [1973] for the rake angles of 0° , 15° and 35° .

Our results also indicate a decrease in the tangential cutting force with cutting speed for depths of cut greater than $t > 20\mu\text{m}$ (figure 2.11). However, F_t was found to increase with cutting speed at very small depths ($t = 2.54\mu\text{m}$), and F_r was found to increase for both depths. These results suggest that the force/speed relationship is also a non-linear one as it depends on the cutting depth and possibly the cutting tool geometry. To my knowledge, however, we currently know very little about the yield and fracture proprieties of primary bone structure (i.e. collagen fibril arrays) and their dependence on strain rate, particularly at the ultra-high strain rates found in high-speed cutting operations.

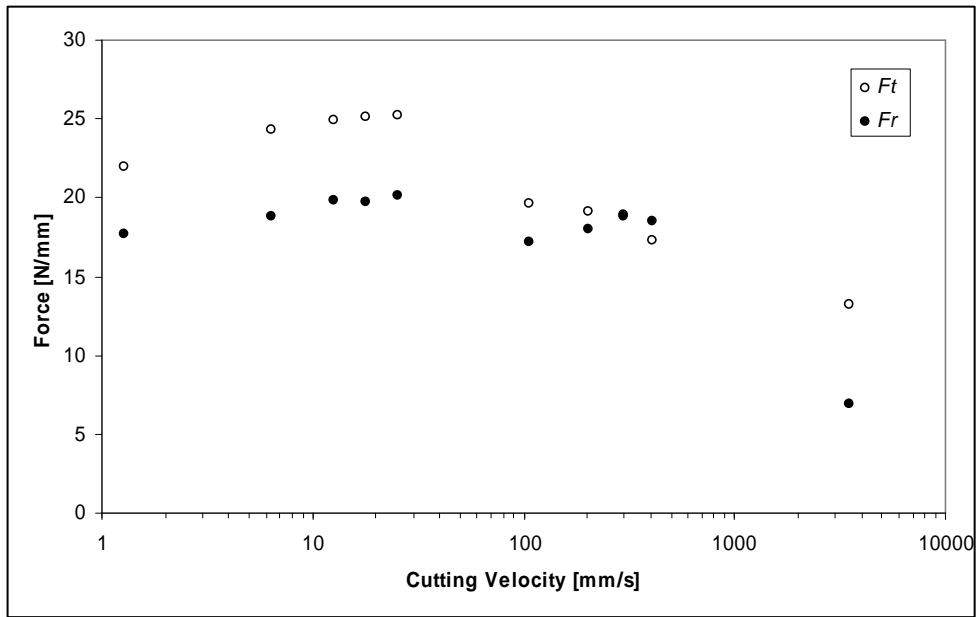


Figure 2.22: Effects of cutting velocity on orthogonal forces – depth of cut $t = 76\mu\text{m}$, rake angle $\alpha=20^\circ$, across cutting mode.

Cutting data in the 1.3–409 mm/s velocity range taken from Krause [1987]. Cutting data for 3500 m/s were averaged from our $t = 50$ and $t = 102\mu\text{m}$ data for identical conditions.

2.4.2 Specific Cutting Energy

As the depth of cut decreases, the amount of energy required to remove a unit volume of bone increases at both low and high speed (figure 2.12). Although most available cutting theories (for example, shear plane or Merchant analysis for metals [Merchant 1944]) do not predict an increase in specific cutting energy with a decrease in cutting depth, several researchers have observed and attempted to explain this phenomenon [Backer 1952][Armarego 1962][Oxley 1989]. Backer [1952] reasoned that as the depth of cut is reduced the probability of finding dislocation sources in the material is also reduced and as a result the flow (or shear) stress would increase. Although primarily a fracture rather than shear mechanism has been observed in the cutting of bone, Backer's hypothesis may still be viable. Micrographics of the cutting chips produced at larger depths of cut (i.e. $t > \sim 50$, figures 2.14–2.17) indicate that cutting occurs by a series of discrete fractures at high and low speeds [Wiggins et al. 1978, Krause 1987]. For a wide range of different machining conditions, the fracture lines are observed to propagate along weak planes within the bone matrix, such as between adjacent osteons or along the cement lines between lamellae (figure 2.17). These interfaces are known to be weaker structural elements within the bone matrix [Weiner 1998]. If one considers that the approximate distance between successive secondary laminar layers or the diameter of an osteon is on the order of 100–200 μm (figure 2.3), it would be very likely for a crack to find a weak path (for example, a cement line) to propagate along at large depths of cut. Therefore, it is reasonable to assume that the probability of the fracture surface encountering a weaker plane to propagate across would reduce with the cross-sectional area of the cut, resulting in an increase in specific cutting energy at smaller cutting depths.

At the very small chip thicknesses encountered in high speed milling (i.e. in the micrometer or nanometre scale), fractures would have to propagate through the primary bone structure – the arrays of mineralized collagen fibrils (a single fibril is $\sim 200\text{nm}$ in diameter), instead of in between the array bundles or osteons ($\sim 200\mu\text{m}$ in diameter). As secondary bone structures such as osteons have weaker ultimate failure properties in comparison to primary bone [Lui 2000], this may also contribute to the non-linear increase in specific cutting energy with decreasing chip size.

2.4.3 Application to the modelling of high-speed milling

2.4.3.1 Parasitic or edge forces

Although the chip thicknesses encountered in high-speed milling operations are dependent on the feed rate applied to the cutting tool, they tend to be extremely small since the rotational velocity (RPM) is much higher than the linear velocity (feed rate) of the cutting tool. Our results indicate that as the depth of cut or chip thickness approaches zero, the measured tangential and radial forces tended to near constant values of ~ 3.5 and ~ 5.5 N/mm respectively (i.e. at $t \sim 2.5\mu\text{m}$), regardless of the tool rake angle. This could be due to the tool nose radius, which was likely similar for all tools considering that they were all prepared in the same manner. It could also be likely that at these small depths of cut, a relatively large portion of the forces are primarily the result of ‘parasitic’ or frictional forces acting between the bone and the tool clearance face, which was 10° for all tools. A constant F_t/F_r ratio across all cutting modes at zero depth of cut suggests that a simple Coulomb friction law ($\mu = F_t/F_r \sim 0.7$) would be adequate to describe the physical process acting on the clearance face (or bottom face, figure 2.4) of the tool. Here, the radial force component (F_r) could be primarily a result of the bone being compressed under the tool clearance face (i.e. material ‘spring-back’), and the tangential force ($F_t = \mu F_r$) could be largely due to the frictional force that acts on this face as the tool slides over the bone. These force values were only slightly affected by fibre orientation, exhibiting a variation of $\sim 10\text{--}20\%$ across all directions, which suggests that the coefficient of friction between wet bone and ground unpolished steel is not very sensitive to fibre orientation.

2.4.3.2 Chip formation

The chip formation mechanism at these small depths of cut tended to resemble the classical ‘shear plane’ process commonly seen in metal cutting much more so than at the higher cutting depths. Chips were observed to be more-or-less continuous structures which slid up the tool rake face, curling as the tool progressed through the bone (figures 2.13–2.16). This is in agreement with the observations of Jacobs [1973] for low-speed cutting with a highly raked tool ($\alpha=45^\circ$) at a depth of $t=0.76\mu\text{m}$. A curled chip would be indicative of some plastic deformation occurring during the cutting process, however, which differs considerably from the chip fracture mechanism observed for larger depths of cuts [Jacobs 1974][Wiggins 1978]. Plastic deformation could arise from shear, bending and/or compression forces (for example near the free surface of the uncut chip) in the primary deformation zone, in combination with microfractures propagating in front of the cutting tool and up to the free surface during chip formation. Microscopic examination of the chips revealed microcracks throughout the length of the chip (figures 2.13–2.16). Wiggins and Malkin [1976] observed with optical and scanning microscopy that the curled chips produced during bone-drilling were formed primarily by a fracture process, in combination with localized plastic deformations resulting from the chisel tip of the tool. As our chips are somewhat similar to those formed in bone-drilling operations, this suggests that the high-speed orthogonal cutting mechanism we observed at small cutting depths is representative of actual surgical operations.

2.4.4 Fit of models

We compared the fit of an exponential (Equation 2.2, Appendix A1) and a logarithmic (Equation 2.3, figures 2.9a,b and 2.10) force model to the cutting data, each curve being characterized by three constants (K_c , n , F_e) and (K_1 , K_2 , K_3). The general shapes of the F_t vs t curves for high- and low-speed cutting were similar [Wiggins 1978], indicating that the tangential cutting force is reasonably modeled by Equation 2.2 for a large range of cutting speeds and depths (Appendix A1). The magnitudes of F_t were, however, $\sim 30\text{--}50\%$ of the low-speed values for all rake angles and cutting directions tested, indicating that the cutting coefficients K_c and n exhibit a strong dependence on tool velocity. Forces normal to the tool velocity (F_r) displayed a different relationship at high speeds, where F_r tended to decrease with increasing t (i.e. $n_r < 0$), particularly when using highly raked tools. As can be seen in figure A1.1 and A1.2, the power law is not capable of capturing the non-linear trends exhibited by F_r .

Although the logarithmic model may have limited applicability for aiding the understanding of the underlying physical processes happening, this mathematical model did provide a better fit to the high-speed data for both the tangential and radial cutting forces.

2.5 Conclusions

Orthogonal and oblique bone-cutting forces were investigated in fresh-frozen bovine femurs at high speeds not previously tested. Bone cutting forces under these conditions were different from those obtained at low speeds, and although low speed cutting studies may be useful for examining general bone-cutting mechanics, such data is not directly applicable to modelling high-speed milling. The new logarithmic model used to quantify the forces acting on a single edge provided a better fit to the data than the conventional power law. Microscopic analysis of the cut chips indicated a shift in the chip formation mechanism from a continuous to a fracture process with increasing depth of cut.

3.0 Chapter Summary

In the previous chapter we quantified the relationship between the force acting on a *single* cutting edge as it moves through the bone for various cutting depths, directions, and rake angles. In this chapter we extend our analysis to include multiple edges rotating about a common axis with varying kinematic and geometrical conditions to approximate realistic bone *milling* operations. The objectives of this study were therefore (a) to measure the instantaneous force components during bone *milling* operations as a function of cutter rotation for various milling tool geometries, speeds, feed rates and feeds per tooth, radial and axial cutting depths, and cutting directions and modes, and (b) to formulate and evaluate a milling model that uses orthogonal and oblique cutting data quantified in the previous chapter to predict the instantaneous milling force components as a function of the above parameters. Experimental results in bovine cortical bone demonstrate that milling force components are periodic signals with their curve shape, mean, and amplitude changing dramatically with the milling tool geometry and kinematics. Simulated and measured instantaneous milling forces are presented for the illustrative cases of full and half immersion down- and up-milling with two and four fluted cutting tools. Average slot milling forces at various feeds per tooth are also presented for two different cutting velocities. The model predictions are in good agreement with the measurements, though they generally tend to overestimate cutting forces at very small feeds per tooth.

3.1 Introduction

A generalised model of the bone milling process is invaluable for gaining a better understanding of how both mean and instantaneous milling force components vary in magnitude and in proportion as a function of the cutting conditions. Comprehension of these force relationships and their dependence on the machining parameters, such as milling speed, feed rate, radial and axial cutting depth, and cutter geometry, is essential for analysing stability and improving safety, as well as optimising cutting accuracy and time.

Although bone milling is commonly performed in many orthopaedic and neurosurgical procedures, the process is often regarded as being somewhat unstable and difficult to control [Giraud 1991]. The magnitude and direction of the overall milling force can change suddenly and unexpectedly during milling, causing the tool to slip from the planned trajectory and compromising surgical safety and accuracy.

Despite these difficulties, we were able to find only a few detailed studies in the literature that quantify milling force components and trends as a function of several relevant parameters. Krause et al. [1982] reported on feed forces for milling bovine bone with high-speed burrs operating at various feed rates and cutting depths. Although the rotational velocity during cutting was not measured, they did find that average peak feed forces generally increased with cutting depth and feed rate, and decreased with cutting speed. For equivalent depths of cut, however, the effect of tool geometry on cutting force was dependent upon the rotational speed. Denis et al. [Denis et al 2001] measured milling forces in the feed and normal directions for human proximal tibial bone as a function of milling speed and feed per tooth. Average peak forces in either direction increased with feed per tooth, though the rate of increase was different for each force component and cutting speed. Moreover, they found that the influence of speed was not constant across specimens or component directions.

Clearly, a mathematical model of the milling process would be an invaluable tool to aid in the analysis of different milling operations. The objectives of this study were therefore to (a) measure instantaneous milling force components in bovine cortical bone as a function of the cutter rotation for various tool geometries, cutting speeds, feed rates and feeds per tooth, radial and axial cutting depths, and cutting directions and modes, and (b) to formulate and evaluate a model of the milling process that uses the single edge orthogonal and oblique cutting data quantified in the previous chapter to predict the instantaneous milling force components as a function of the above parameters.

3.2 Milling Model Formulation

The basis of our modeling approach is to relate the specific cutting energy or pressure of cortical bone as determined from orthogonal cutting tests to the instantaneous kinematics and geometry of the cutting tool edges in the milling operation. Each cutting edge or flute of the milling tool is partitioned axially into a series of small ‘edge elements’ (figure 3.1), and for any cutter orientation within a tool revolution cycle (i.e. $\theta = 0, 1, 2, \dots, 360^\circ$) the tooth elements that are actively engaged in cutting are identified [Altintas 2000]. For a particular set of cutting conditions (f, ω, a, r, n) the instantaneous thickness of the cutting chip removed by each edge element is determined. The corresponding tangential and radial force components acting on the tooth element can then be approximated by the relationships measured in the orthogonal and oblique cutting tests. These elemental force components are then transformed into the fixed milling coordinate system (x, y) and summed along each cutting tooth to obtain the instantaneous milling force components in x and y .

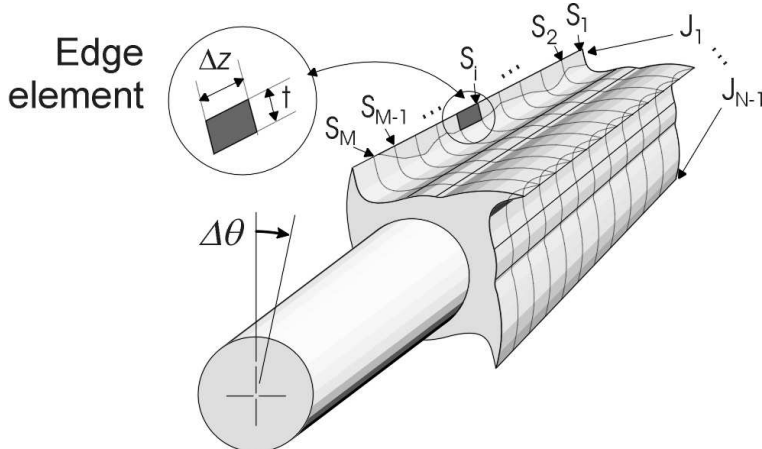


Figure 3.1. A milling tool with J_N cutting flutes and S_M axial segments

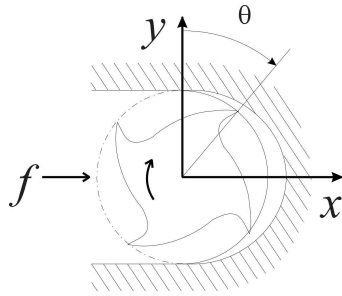


Figure 3.2. Coordinate system for full immersion down-milling.

3.2.1 Variation of Specific Cutting Energy with Specimen Orientation.

Our experimental measurements, as well as previous ones made in fibre reinforced composites [Puw 1996, Mahdi 2001], wood [McKenzie 1961], and bone [Jacobs 1974][Wiggins 1978][Mitsuishi 2005], indicate that the cutting mechanism and specific cutting energy are dependent on the cutting direction with respect to the material anisotropy. In the milling process, the cutting edges are continuously revolving about the axis of the tool and the orientation of each cutting edge is continuously changing with respect to the direction of anisotropy. Therefore the materials' specific cutting pressure as experienced by any particular cutting edge also varies with the direction of the edge velocity [Puw and Hocheng 1993, 1996]. If we consider the bone in the cutting zone to be a transversely orthotropic material with the predominate osteon direction aligned with the long bone axis [Reilly 1975], the specific cutting properties would depend on the edge position. Considering for example the case of full immersion milling when the feed direction (x) is perpendicular to the bone axis and y is parallel (figure 3.2): at $\theta = 0$, the edge velocity is normal to the predominate fibre direction and the cutting mode is transverse; at $\theta = \pi/2$, the edge velocity is parallel to the fibre direction and the cutting mode is parallel; at $\theta = \pi$, the edge velocity is again normal to the fibre direction and the cutting mode is transverse. The instantaneous forces per unit width acting tangential ($F = F_t$) and perpendicular ($F = F_r$) to the velocity of each tooth segment at these principal orientations are:

$$\theta = 0, \pi: \delta F(T, t) = 10^{K_{3T} \log_{10}^2(t) + K_{2T} \log_{10}(t) + K_{1T}} \quad [\text{N/mm}] \quad (3.0a)$$

$$\theta = \pi/2: \delta F(P, t) = 10^{K_{3P} \log_{10}^2(t) + K_{2P} \log_{10}(t) + K_{1P}} \quad [\text{N/mm}] \quad (3.0b)$$

where T and P denote the (transverse and parallel) cutting mode, K_1 , K_2 , and K_3 are the constant parameters obtained from the orthogonal bone cutting data in the previous chapter, and t is the uncut chip thickness. For milling perpendicular to the axis of continuous fibre reinforced composites, Puw [1993, 1996] approximated the cutting forces in feed (x) and normal (y) directions with the following empirical formula:

$$F_x(\theta) = F_{t,T} \cos \theta + F_{r,P} \sin \theta \quad [\text{N/mm}] \quad (3.1a)$$

$$F_y(\theta) = F_{r,T} \cos \theta - F_{t,P} \sin \theta \quad [\text{N/mm}] \quad (3.1b)$$

Many mathematical models have been developed to estimate the variation of mechanical properties in bone as a function of specimen orientation relative to the principle directions [Reilly 1975, Wagner 1992]. The complex hierarchical structure of bone makes this a very challenging task. Although experimental values of Young's modulus have been collected at various off-axis orientations to the predominate fibre direction, we could find no such relevant cutting data for bone. Hankinson [1921]

introduced a simple empirical criterion to describe the ultimate compressive strength of wood (which is an extremely anisotropic material) at various orientations to the fibre axis. Reilly and Burstein [1975] used this empirical criterion to describe the ultimate strength of bone at orientations between the principal directions. Since no other cutting theory exists, we use their criterion here to approximate the cutting force at intermediate orientations to the principal directions:

$$F_*(\theta) = \frac{F_T F_p}{[F_T \sin^n(\theta) + F_p \cos^n(\theta)]} \quad [\text{N/m}^2] \quad (3.2)$$

where $F(\theta)$ is the off-axis specific cutting pressure at some angle of rotation θ , F_T and F_p are the transverse and parallel cutting forces, respectively, and $n = 2$.

3.2.2 Chip Geometry in Milling.

The uncut chip thickness t (*equation 3.3*) is a key parameter in predicting the milling force. Martellotti [1941, 1945] studied the kinematics of the milling process and derived the equations of motion of the cutter path as well as the uncut chip thickness as functions of the process parameters. Although Martellotti showed that the true path of a milling tooth is trochoidal, a circular tooth path is a good approximation if the feed rate of the tool is much smaller than the rotational velocity of the mill, which is the case for most powered milling operations. The instantaneous uncut chip thickness can therefore be expressed as a function of the angular position of the cutting edge θ , and the feed per tooth c :

$$t(\theta) = c \sin(\theta) \quad [\text{mm}] \quad (3.3)$$

$$c = 60f / (\omega N) \quad [\text{mm}] \quad (3.4)$$

where ω is the rotation velocity (RPM) and f is the feed velocity [mm/s] of the cutter, and N is the number of cutting teeth.

For full immersion down-milling (figure 3.2), where the entry (θ_{st}) and exit (θ_{ex}) angles for each tooth are $\theta_{st} = 0$ and $\theta_{ex} = \pi$, respectively, the uncut chip thickness varies periodically with the rotation of the mill; from zero (at $\theta = 0$) to a maximum value of c (at $\theta = \pi/2$) and then back to zero (at $\theta = \pi$). An edge is considered to be in the ‘cutting zone’ when $0 \leq \theta \leq \pi$. For $\pi < \theta < 2\pi$, no cutting occurs and therefore the force on the tooth element is zero. For the case of half immersion down-milling, where the entry and exit angles into the workpiece are $\theta_{st} = \pi/2$ and $\theta_{ex} = \pi$, respectively, the chip thickness instantaneously jumps from 0 to c upon tooth entry and then decreases to zero as the tooth exits the workpiece. The reverse occurs in half immersion up-milling.

3.2.3 Milling Force Prediction Algorithm.

We discretize the milling process into small angular rotations of $\Delta\theta$ and the forces acting on the mill are calculated at each incremental rotation. The milling tool is segmented into a series of axial slices (S_m) each of elemental thickness Δz (figure 3.1). For each axial slice (S_i), the algorithm determines which cutting flute segments ($J_{1\dots N}$) are currently engaged into the bone and calculates the normalized tangential and radial forces acting on each immersed flute segment. A flute segment is considered to be engaged and cutting into the bone if $\theta_{st} \leq \theta_j \leq \theta_{ex}$, otherwise the force is zero. The tangential and radial cutting force contributions for each edge element (calculated from Equations 3 and 5) are then resolved into force components in the feed (x) and normal (y) directions:

$$\delta F_{x_j}(\theta) = -\delta F_{t_j}(\theta) \cos \theta_j - \delta F_{r_j}(\theta) \sin \theta \quad [\text{N/mm}] \quad (3.5a)$$

$$\delta F_{y_j}(\theta) = \delta F_{t_j}(\theta) \sin \theta_j - \delta F_{r_j}(\theta) \cos \theta \quad [\text{N/mm}] \quad (3.5b)$$

The total forces acting on each axial slice in the feed and normal directions are:

$$\Delta F_{x_s} = \sum_{j=1}^N [\delta F_{x_j}(\theta_j) \times \Delta z] \quad [N] \quad (3.6)$$

$$\Delta F_{y_s} = \sum_{j=1}^N [\delta F_{y_j}(\theta_j) \times \Delta z]$$

where N is the total number of cutting flutes. The elemental cutting forces can be positioned at the upper or lower boundaries of each axial slice.

Feed and normal force predictions for cutting speeds $\leq 100\text{RPM}$ are performed using the low speed orthogonal cutting data of Wiggins and Malkin [1978], using the exponential power law and force data from $\alpha=10^\circ$, parallel/perpendicular cutting modes for all tools. All force predictions for speeds higher than 100RPM are performed with the orthogonal and oblique data presented in the previous chapter. Predictions for the feed and normal forces were calculated using the transverse and parallel orthogonal cutting data. Force were interpolated linearly between 0° and 20° rake angles to simulate the 10° rake angle tools. To model axial forces for helical flutes, the oblique cutting data from the across cutting mode was used regardless of the milling direction, with the forces linearly interpolated to obtain an angle of obliquity of 30° .

3.3 Materials and Methods

3.3.1 Experimental Procedure

We conducted a series of bone milling experiments on a computer numerically controlled (CNC) horizontal machining center (Mori Seiki SH-403, Japan) and measured force components in the feed and normal directions with a three component dynamometer designed specifically for measuring dynamic machine forces (Kistler Instruments, type 9255B, Switzerland). The piezoelectric force signals were passed through Kistler charge amplifiers and into a PC based data acquisition system that was configured for each test to sample at a rate equivalent to 1° of the tool rotation.



Figure 3.3. Industrial Milling machine (left) and force sensor (right) used for the milling experiments
[Photos taken from Mori Seiki and Kistler websites, respectively].

Cortical bone specimens were dissected from the mid-diaphysis of fresh bovine femurs with a diamond blade band saw under a constant supply of irrigation, and then milled into slices of constant

thickness (~5–10mm) on a milling machine. For the milling tests, the bone specimens were clamped so that the milling tool end projected from the far end of the slice, thereby avoiding tool tip end effects (i.e. face milling) and allowing the generated bone chips to escape freely from the cutting zone and not influence the measured cutting forces (figure 3.4). The bone specimens were kept wet with physiologic saline solution throughout the experiments, though no irrigation was directly applied to the cutting zone during the cutting-force measurements.

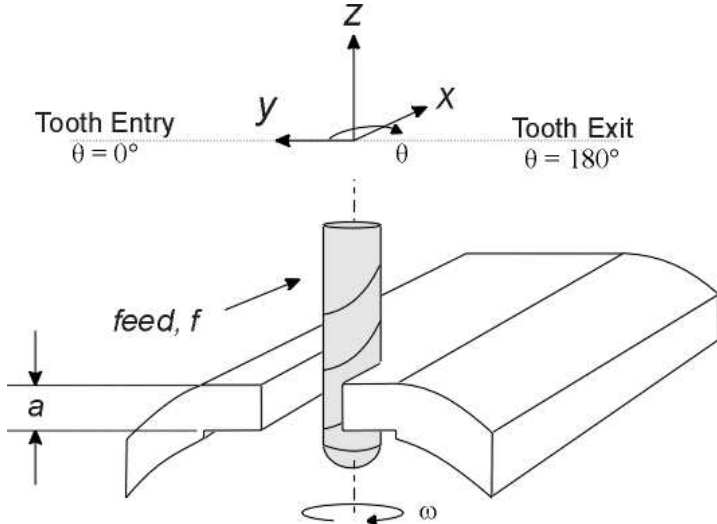


Figure 3.4. Schematic diagram of experimental setup and milling tool coordinate system.

Table 3.1. Range of experimental conditions tested

Feed rate, f [mm/min]	0.4–500
Feed per tooth, c [mm]	0.0005–0.350
Cutting velocity, ω [RPM]	100–5,000
Radial depth of cut, r [mm]	$2*R, R$ (full and half immersion)
Axial depth of cut, a [mm]	~5–10mm
Milling mode	Up and down milling
Milling direction	Parallel, Transverse
Work-piece material	Bovine femur cortical bone

The ranges of experimental conditions tested are summarized in Table 3.1. The feed per tooth c is the linear distance the cutter travels between each successive tooth pass (i.e. $c = f / (\omega \times n)$ [mm], where f is the feed rate [mm/min], ω is the angular velocity [RPM] and n is the number of cutting teeth). A schematic diagram of the milling trajectories relative to the specimen orientation is presented in figure 3.5. Milling was performed with the cutting tool fully and partially (half) immersed into the specimen to test the influence of radial cutting depth. To evaluate the influence of bone anisotropy on cutting forces, milling was carried out with the feed direction both parallel to and transverse to the long axis of the bone. Four different cutting tool geometries were used in total (Table 3.2).

Table 3.2. Tool geometries used, as specified by the manufacturer

Tool	A	B	C	D
Rake, α [°]	0	10	10	5
Helix, λ [°]	30	30	30	0
Clearance, γ [°]	10	10	10	10
Radius, R [mm]	3.175	3.175	3.175	9.525
No. of flutes, n	2	2	4	4
Material	Carbide	HSS*	HSS*	HSS*

* High Speed Steel

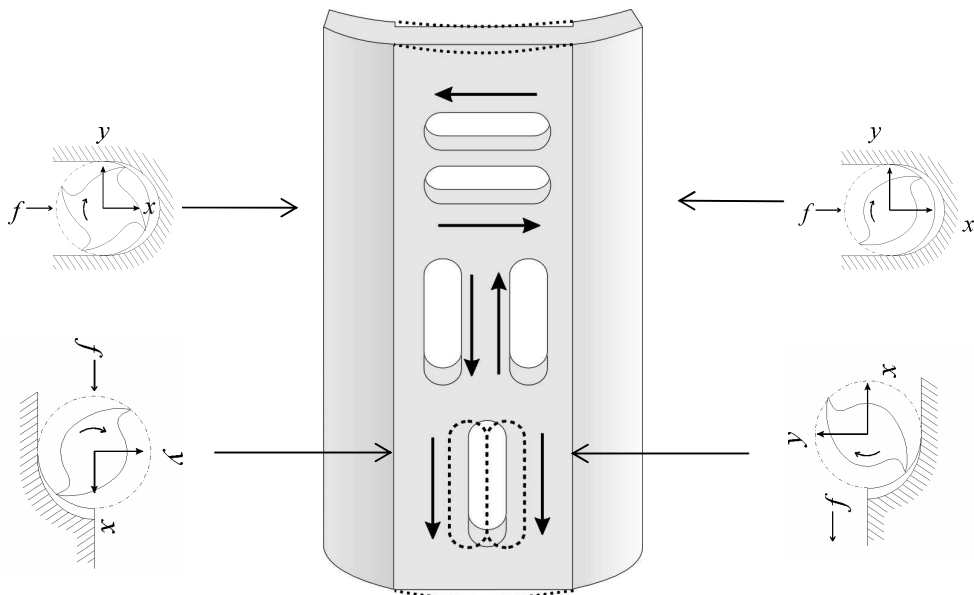


Figure 3.5. Various milling trajectories were tested for full immersion (slot), half immersion down-, and half immersion up-milling. Milling feed directions where either parallel or transverse to the bone long axis.

3.3.2 Data Analysis

Milling force data from the dynamometer was acquired at a sampling rate equivalent to 1° of tool rotation. Figure 3.6 provides examples of typical measurements for the three milling force components F_x , F_y , F_z for feeds per tooth of $c=100\mu\text{m}$ and $2\mu\text{m}$. The forces are presented in the coordinate frame of the machine spindle, i.e. they act on the cutting tool and not on the bone specimen. Measurement noise was reduced by averaging the data at every individual 1° point over several revolutions of the tool. Cutter ‘runout’, which is the eccentricity between the cutting tool axis and the machine spindle axis, was treated averaging the first half with the second half of the rotation cycle to obtain a full symmetric revolution.

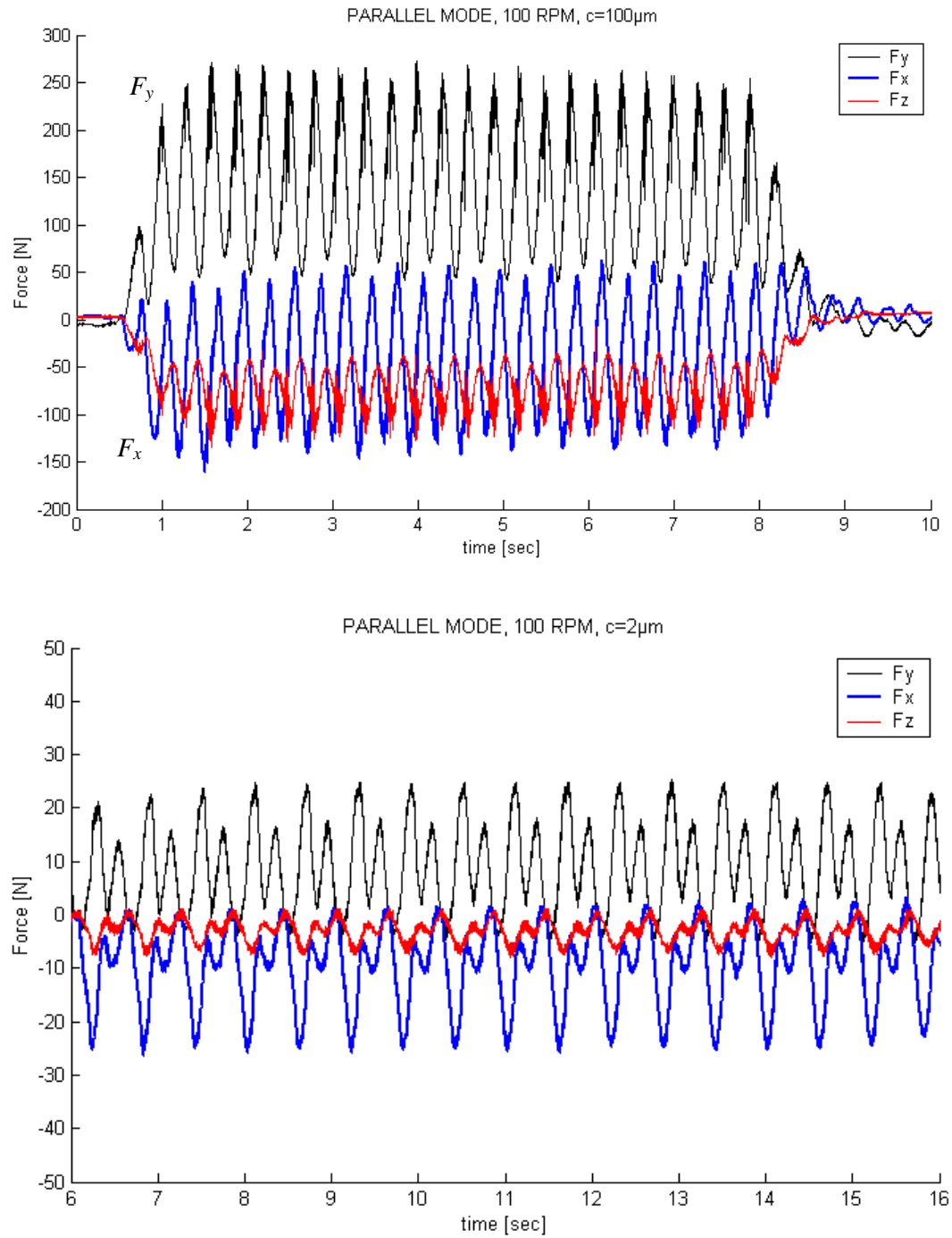


Figure 3.6. Sample milling measurements (i.e. raw data before averaging for tool run-out) of the instantaneous force components in x and z directions for slot (full-immersion) milling with a cutter having two helical teeth (Tool 'B'). Cutting conditions: feeds per tooth $c = 100\mu\text{m}$ (upper plot) and $c = 2\mu\text{m}$ (lower plot); rotational velocity $\omega = 100 \text{ RPM}$; axial depth of cut $a = 9.1 \text{ mm}$. Feed direction is parallel to the bone axis.

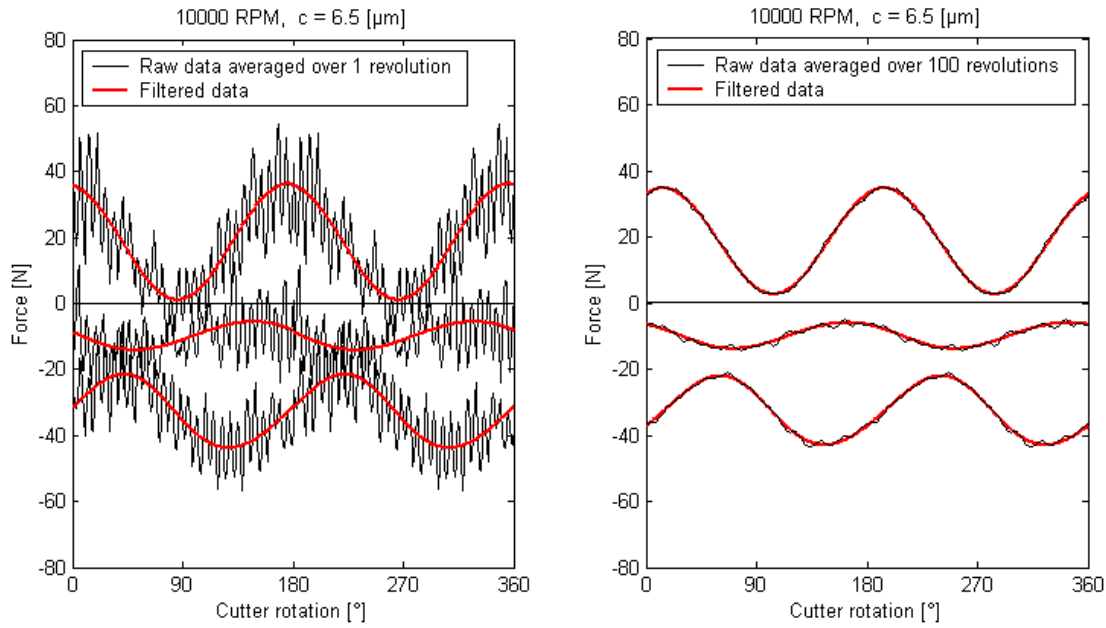


Figure 3.7. Effects of averaging for tool runout over one (left plot) and one hundred (right plot) revolutions for 10000 RPM data. Bold red curves represent the averaged data after low-pass filtering with a ninth order Butterworth zero-phase forward and reverse digital filter. Cut off frequency is equal to two times the tooth passing frequency. Cutting conditions: Full-immersion milling, tool ‘B’, feed per tooth $c = 6.5\mu\text{m}$; rotational velocity $\omega = 10000 \text{ RPM}$; axial depth of cut $a = 9.6\text{mm}$.

Certain high-speed data at low feeds per tooth were low-pass filtered before averaging, using a ninth order Butterworth zero-phase forward and reverse digital filter with a cut-off frequency equal to ten times the tooth passing frequency. These data are labelled as so in the results. All other mean and instantaneous force data were simply averaged over several revolutions. The effects of averaging and filtering are presented in figure 3.7.

3.4 Results

The measured milling force components were periodic signals with the curve shape, mean, and variation changing dramatically with the milling tool geometry and kinematics.

3.4.1 Influence of feed-rate and cutting tool geometry on slot milling forces at low-speed

The instantaneous milling force components in the feed (x) and normal (y) directions are presented in Figure 3.8 as a function of the tool rotation angle (cutter rotation, θ) while slot milling with a cutting tool with four straight flutes (tool D) at two different feeds per tooth of $c = 25\mu\text{m}$ and $50\mu\text{m}$. The tool rotational velocity is $\omega = 100$ RPM, which corresponds to a cutting tool surface velocity of $v=99.75\text{mm/s}$, and the feed direction is parallel to the long axis of the bone.

The magnitudes of the mean milling forces in the feed and normal directions are plotted in Figure 3.9 over a range of feed rates (or feeds per tooth, $c=3.5\text{--}200\mu\text{m}$) for the same cutting conditions as in figure 3.8. The relationship between mean forces and feed-rate is non-linear, resembling that of the cutting force curves in orthogonal cutting. The mean normal force increased with feed across the entire range of feeds tested, while the feed force tended to plateau to a constant value of $\sim 50\text{N}$ after $c > \sim 25\text{--}50\mu\text{m}$. Although the force predictions are able to predict these trends, they tended to overestimate the mean measured forces in both directions for feed rates $\geq 75\mu\text{m}$.

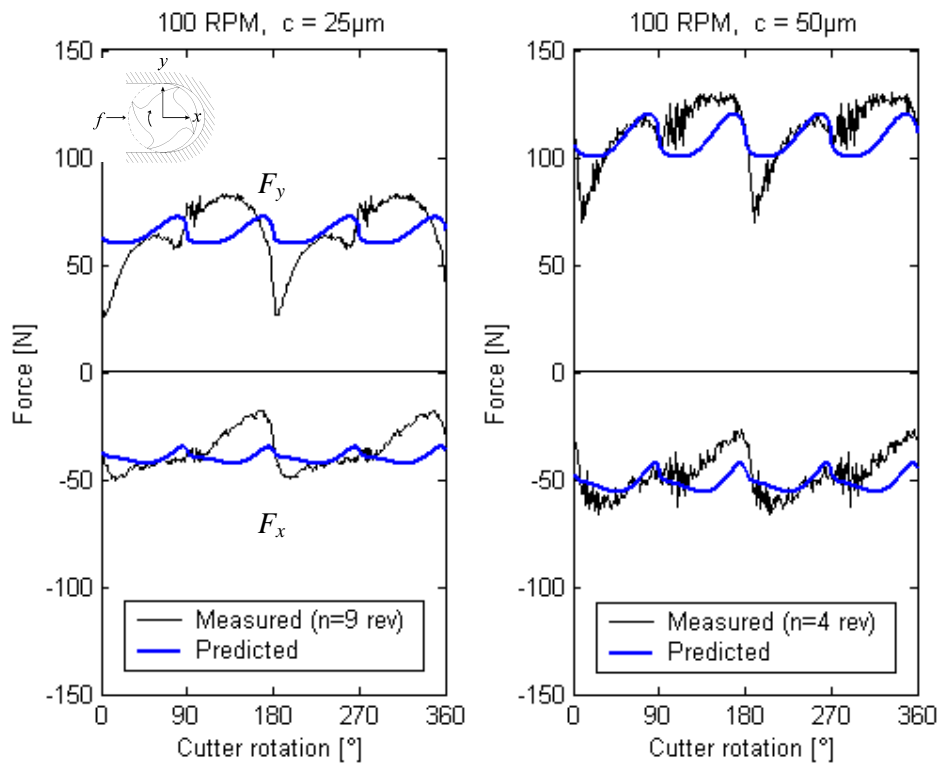


Figure 3.8. Measured and predicted instantaneous milling force components in x and y for slot (full-immersion) milling with a cutter having four straight teeth (Tool 'D'). Cutting conditions: feeds per tooth $c = 2\mu\text{m}$; rotational velocity $\omega = 100$ RPM; axial depth of cut $a = 9.1\text{mm}$; Feed direction is parallel to the bone axis. ($n =$ Number of revolutions data has been averaged over)

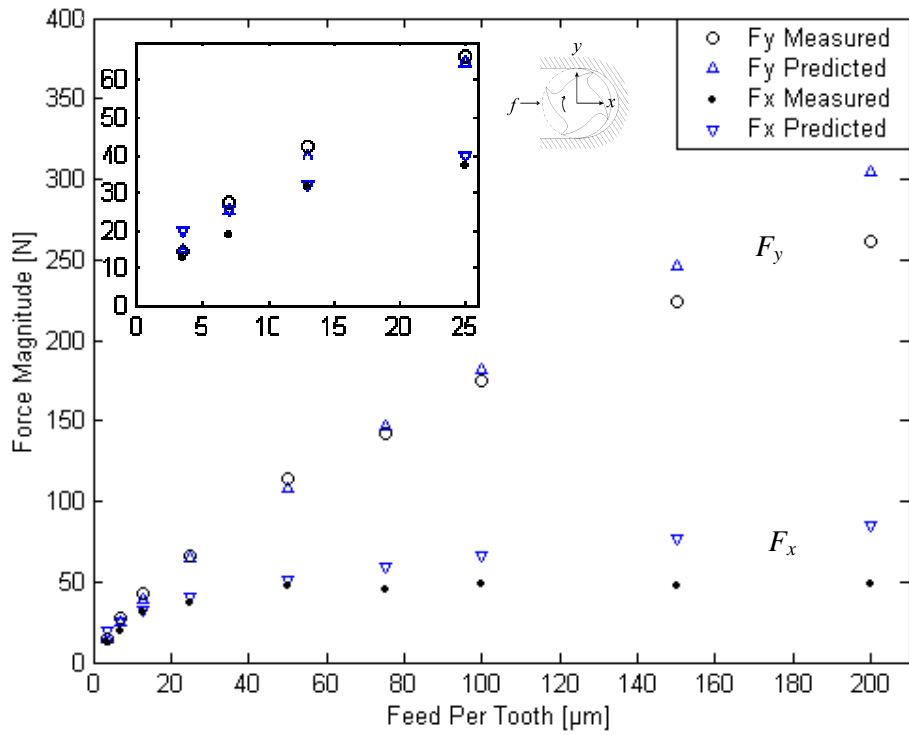


Figure 3.9. Measured and predicted mean milling force magnitudes in x and y for slot (full-immersion) milling with a cutter having four straight teeth (Tool 'D'). Cutting conditions: feeds per tooth $c = 3.5\text{--}200\mu\text{m}$; rotational velocity $\omega = 100$ RPM; axial depth of cut $a = 5.05\text{mm}$; Feed direction is parallel to the bone axis. Inset in top left corner corresponds to $c = 0\text{--}25\mu\text{m}$ data plotted on a larger scale.

3.4.2 Influence of cutting speed on slot milling force components

The magnitude of the measured and predicted mean milling forces in the feed (F_x), normal (F_y) and axial (F_z) directions as a function of the feed per tooth for cutting speeds of 100 RPM ($v=33.3\text{mm/s}$) and 5000RPM ($v=1662.4\text{mm/s}$) are presented in figure 3.10. There are no axial force predictions plotted for the 100RPM velocity since no oblique cutting data exists for low-speed cutting. The percentage increase in the measured mean forces with the decrease in cutting speed from 1662.5mm/s to 33.3 mm/s ranged from ~20-60% for the feed and normal directions across the range of feeds (Table 3.3). The corresponding instantaneous milling forces for the measured and predicted feed and normal forces are presented in figures 3.11 and 3.12.

Table 3.3. Percentage increase in the measured mean force magnitudes with decreased cutting speed from 1662.5mm/s (5000RPM) to 33.3 mm/s (100RPM) at equivalent feeds per tooth c .

c [μm]	2	7	13	25	50
F_x [%]	54.4	39.7	24.1	37.9	63.7
F_y [%]	35.2	61.2	20.0	19.5	24.0
F_z [%]	-81.5	-32.6	-10.7	2.1	12.4

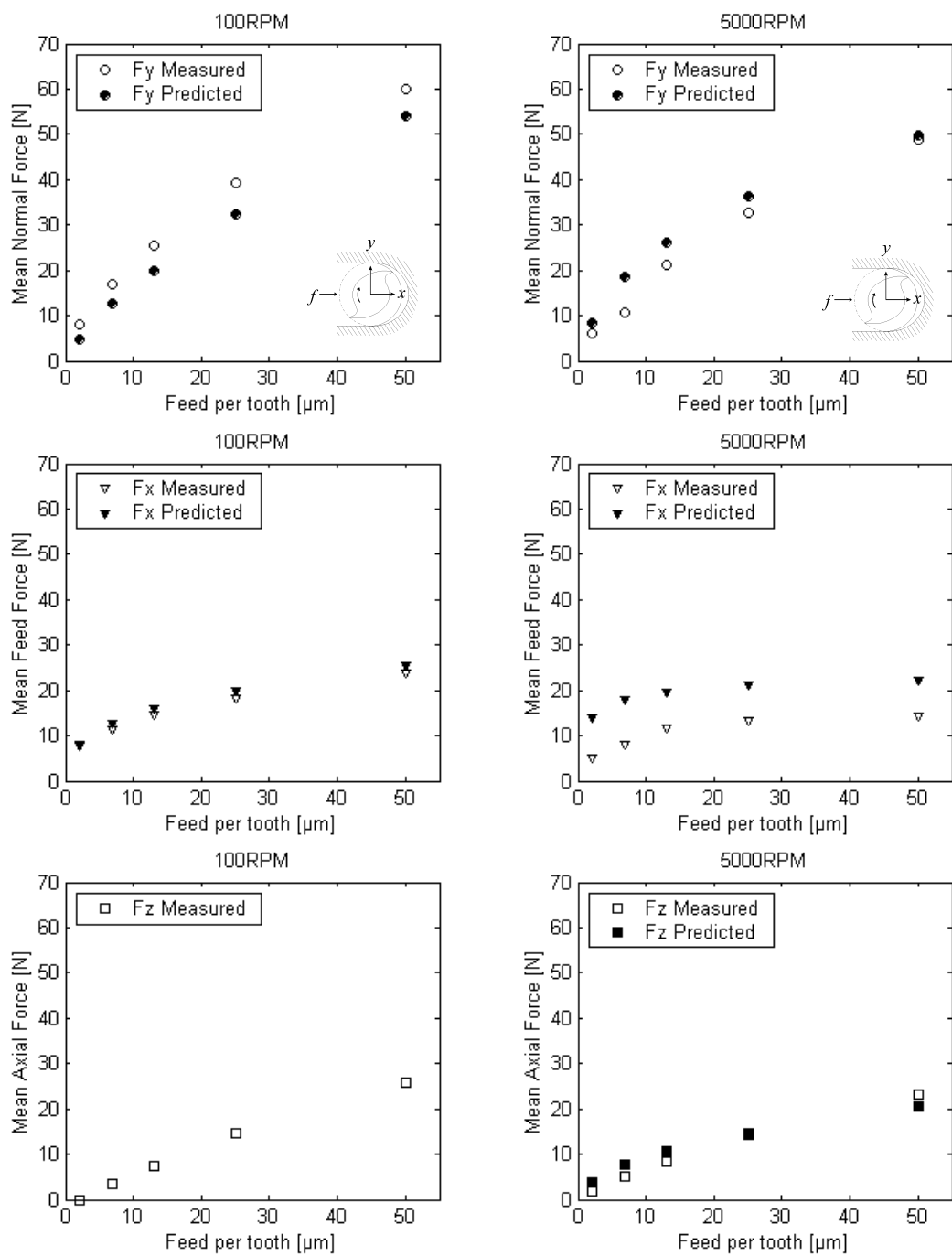


Figure 3.10. Measured and predicted mean milling force magnitude in x , y and z for slot milling with a cutter having two helical teeth (Tool 'A'). Cutting conditions: cutting speed is $v=33.3\text{mm/s}$ (100 RPM, upper plot) and $v=1662.4\text{mm/s}$ (5000RPM, lower plot); axial depth of cut is 5.05mm; feed direction is parallel to the bone axis.

Experimental trials: #12-16(A012_A016_100RPM.m) and #2,4,5,6,8 (A001_A010_5000RPM.m)

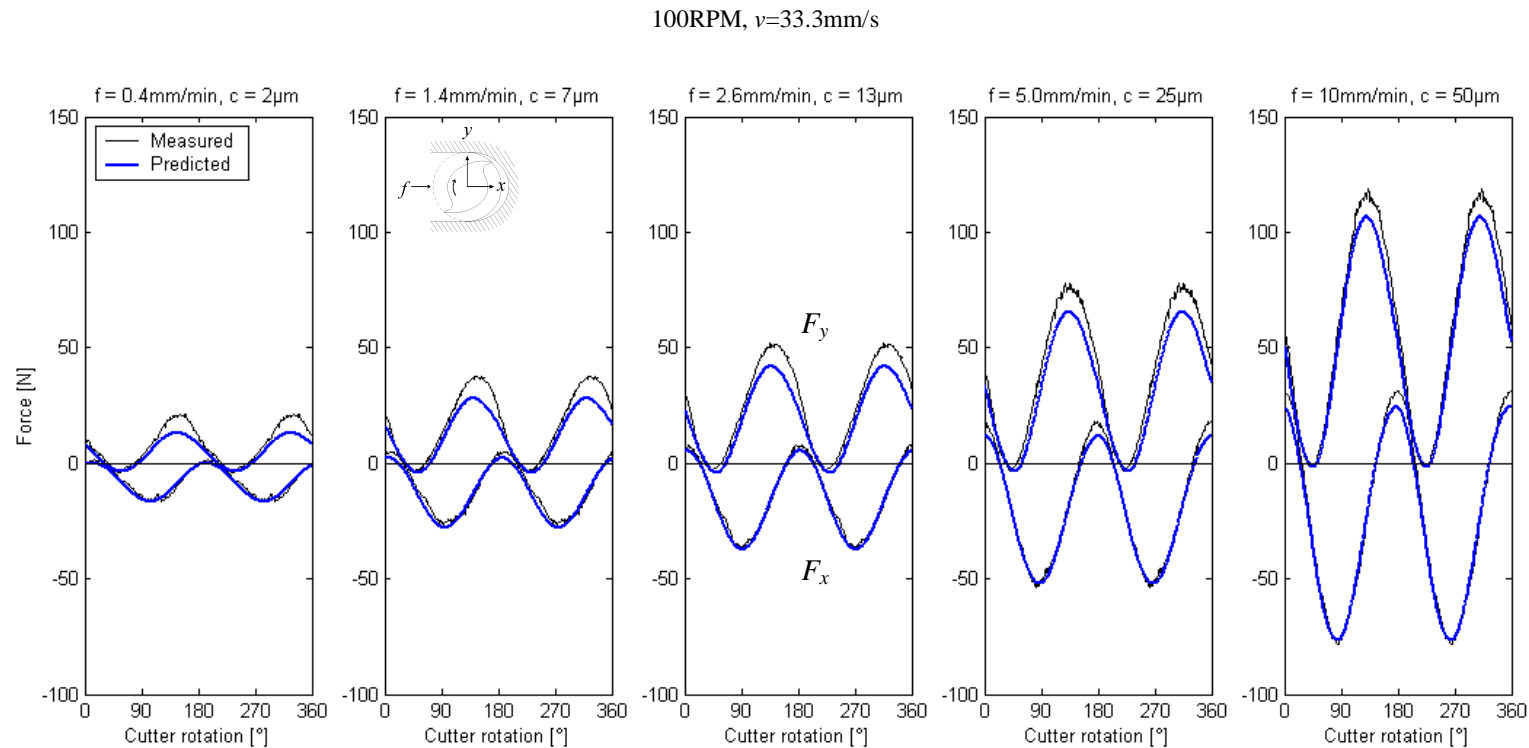


Figure 3.11. Measured and predicted instantaneous milling forces in x and y for full-immersion down-milling with a two fluted helical tool (Tool ‘A’). Cutting conditions: feed rates $f = 20, 70, 130, 250, 500 \text{ mm/min}$; rotational velocity $\omega = 100 \text{ RPM}$; feed direction is parallel to bone axis; axial depth of cut $a = 5.05\text{mm}$.

Experimental trials: #12-16. (A012_A016_100RPM.m)

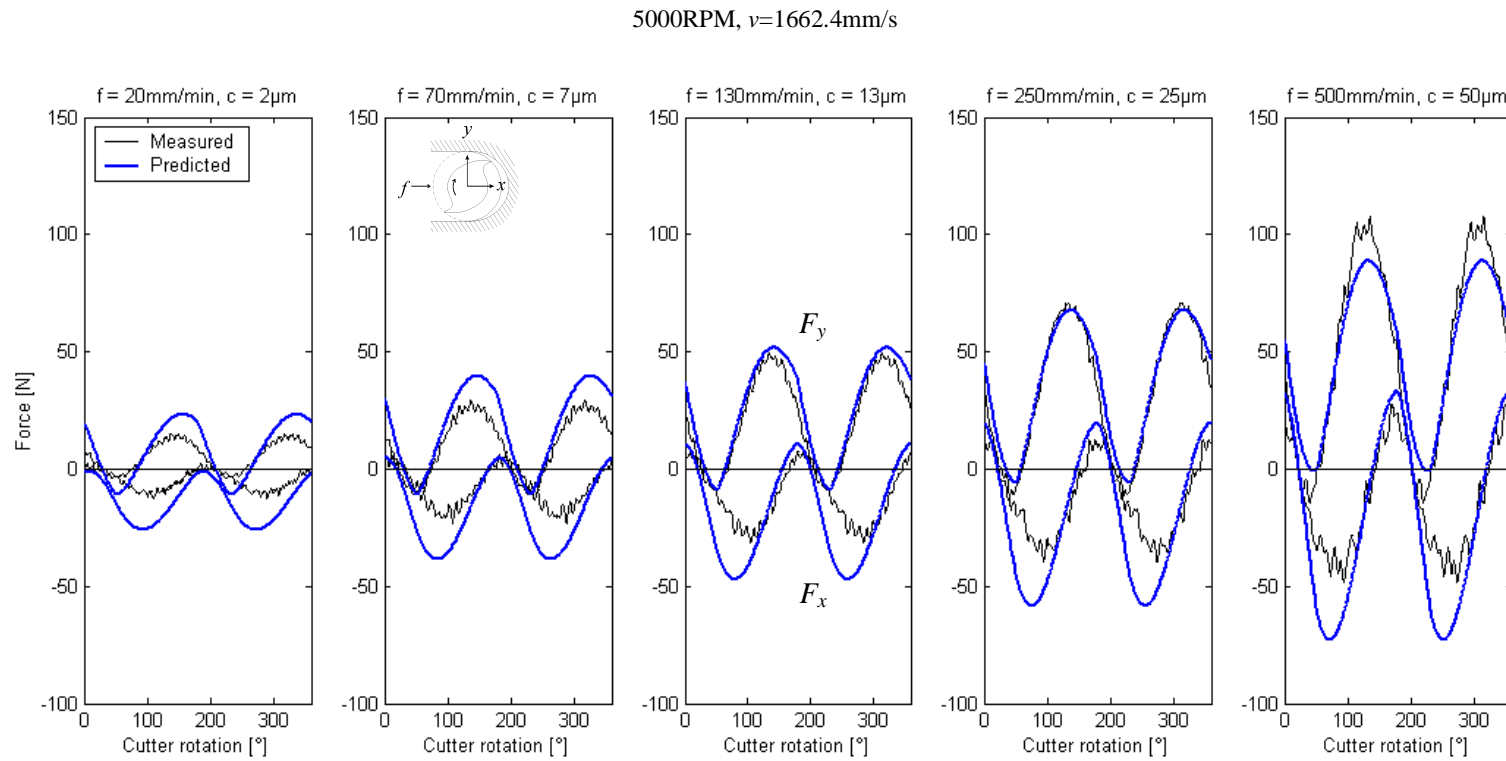


Figure 3.12. Measured and predicted instantaneous milling forces in x and y for full-immersion down-milling with a two fluted helical tool (Tool 'A'). Cutting conditions: feed rates $f = 20, 70, 130, 250, 500 \text{ mm/min}$; rotational velocity $\omega = 5000 \text{ RPM}$; feed direction is parallel to bone axis; axial depth of cut $a = 5.05\text{mm}$. Experimental trials: #2,4,5,6,8. (A001_A010_5000RPM.m)

Equivalent feed rates

Equivalent feeds per tooth

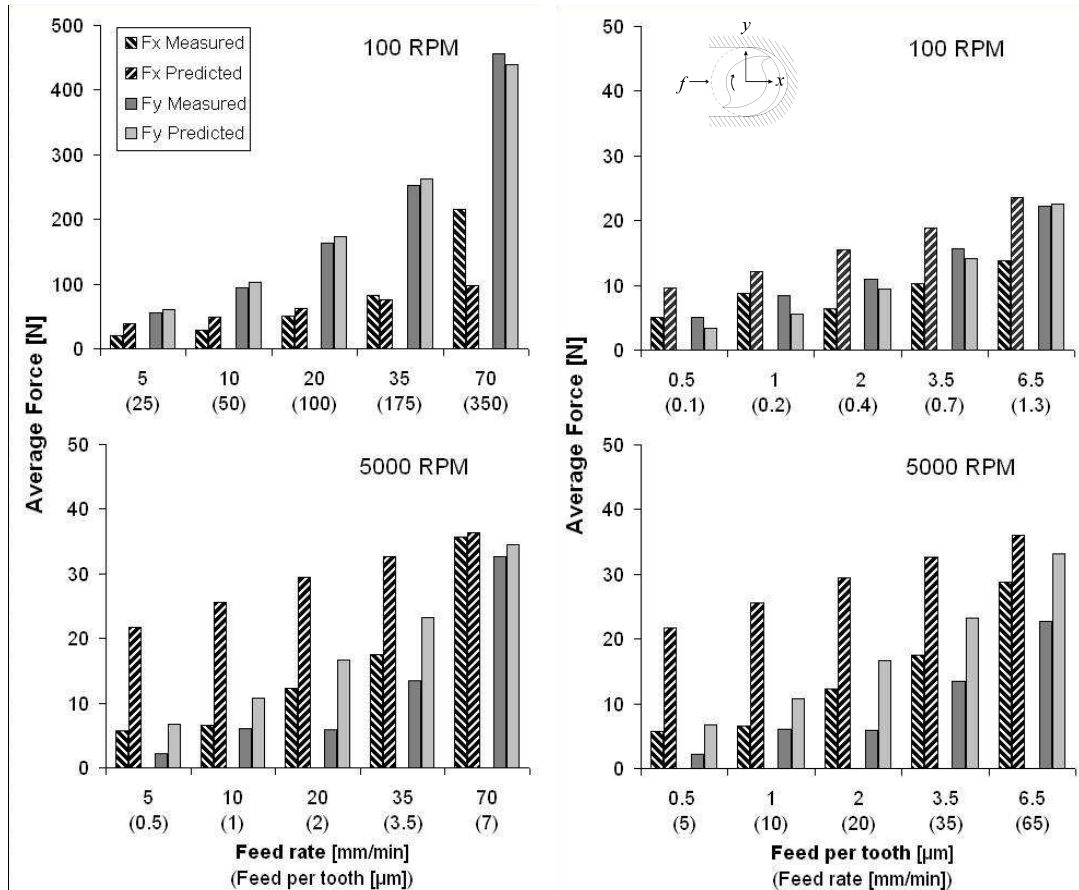


Figure 3.13. Measured and predicted mean cutting force magnitudes in x and y for slot milling with tool ‘A’ at 100 RPM and 5000 RPM, for equivalent *feed rates* (left column), and equivalent *feeds per tooth* (right column). The axial depth of cut was $a = 9.6\text{mm}$.

Experiment #103-109 (5000RPM), 115-119 and 122-126 (100RPM).

Mean measured and predicted forces in x and y are presented in figure 3.13 for slot milling at equivalent *feed rates* (left graphs) and *feeds per tooth* (right graphs) at 100 RPM and 5000 RPM. For equivalent *feed rates* (left column) the 100 RPM force data are generally ~5 times greater than the 5000 RPM data in the x direction, and ~20 times greater in the y direction. At equivalent *feeds per tooth* (right column), the measured force magnitudes at each cutting speed are comparable, though the rate of increase in force with c is ~3 times higher in the x direction for the 5000 RPM data. Normal forces are generally lower for the high-speed data while feed forces are higher. The high-speed model predictions consistently overestimate both forces at these low feeds per tooth (i.e. $<7\mu\text{m}$), though the errors are greater in the feed direction.

3.4.3 Influence of radial cutting depth on milling force components

The instantaneous milling force components in the feed (x) and normal (y) directions during half-immersion down-milling are presented for cutting tools having *two* and *four* helical teeth in figures 3.14 and 3.15 respectively. Similar to full immersion slot milling, there are large variations in each cutting force component with time when cutting with the two fluted cutting tool, while this variation is

relatively small for the four toothed tool. For both half immersion cases, however, it is observed that the feed force (F_x) shifts from negative to positive with increasing feed per tooth (table 3.5). This is a result of the proportional difference between the tangential and the radial force components acting on each tooth element at different chip thicknesses. Comparing full (figure 3.12) and half (figure 3.14) immersion milling with the two fluted tool, it is apparent that the feed force direction also depends on the radial cutting depth. In surgery these forces would tend to pull or push the cutting tool in opposite directions along the feed path, depending on the radial cutting depth and feed rate applied.

3.4.4 Influence of up- and down-milling on milling force components

Instantaneous milling feed and normal force components during half-immersion up-milling are presented in figure 3.16 for a two helical fluted cutter. The feed direction is now opposite to positive x and positive y is pointing away from the cut surface. The mean feed force at the higher feeds per tooth is no longer in the feed direction as during half-immersion down milling (figure 3.14). The normal force F_y is now directed into the cut surface, tending to push the tool down into the cut.

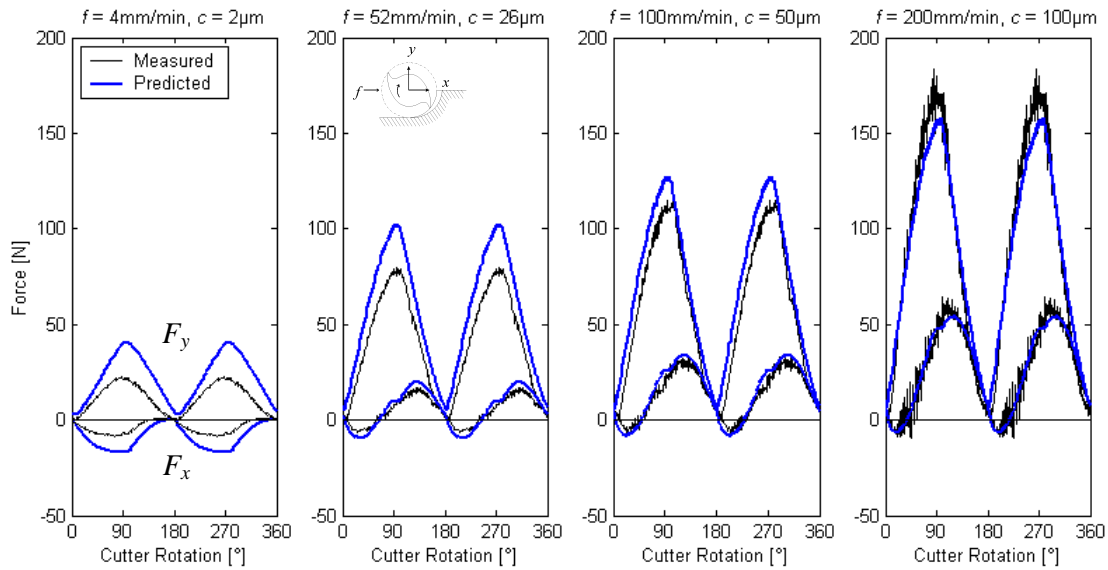
1000RPM, $v=332.5\text{mm/s}$ 

Figure 3.14. Experimental and simulated milling forces in x and y for half-immersion down-milling with a two fluted helical tool (Tool 'A'). Cutting conditions: feed rates $f = 4, 52, 100, 200 \text{ mm/min}$; rotational velocity $\omega = 1000 \text{ RPM}$; axial depth of cut $a = 9.6\text{mm}$.

Experiment #159-162

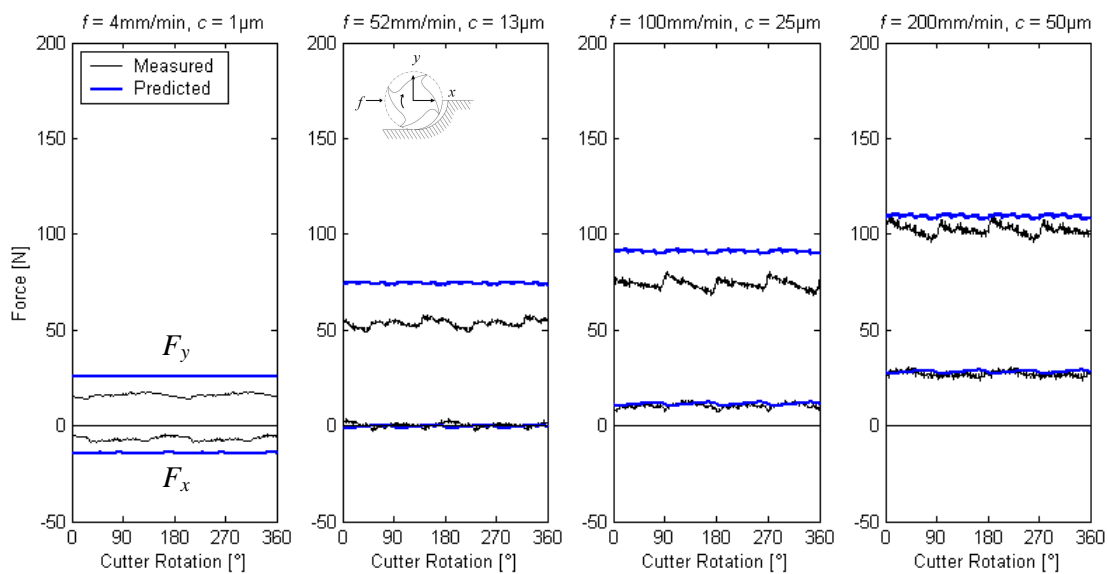
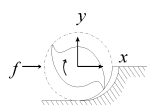
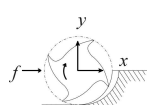
1000RPM, $v=332.5\text{mm/s}$ 

Figure 3.15. Experimental and simulated milling forces in x and y for half-immersion down-milling with a four fluted helical tool (Tool 'C'). Cutting conditions: feed rates $f = 4, 52, 100, 200 \text{ mm/min}$; rotational velocity $\omega = 1000 \text{ RPM}$; axial depth of cut $a = 8.8\text{mm}$ for Tool 'C'.

Experiment #151-154

Table 3.4. Measured and predicted mean forces for half-immersion down milling with 2 and 4 fluted tools for equivalent feed rates (1000RPM, $v=332.5\text{mm/s}$)

Flutes	Force	$f [\text{mm/min}]$			
		4	52	100	200
 # 2	F_x	-3.8	5.1	13.3	26.7
		-9.0	5.7	14.6	26.7
	F_y	11.6	41.0	58.3	87.1
		22.5	56.1	69.7	86.2
	F_z	-1.6	-15.2	-24.6	-41.4
		-3.4	-12.8	-16.8	-21.8
 # 4	F_x	-6.8	0.4	10.4	27.1
		-14.2	-0.2	11.7	28.4
	F_y	16.1	53.6	74.1	102.3
		25.9	74.6	91.2	109.6
	F_z	-2.8	-16.6	-29.0	-45.7
		-4.1	-17.1	-23.1	-30.9

100RPM, $v=33.3\text{mm/s}$

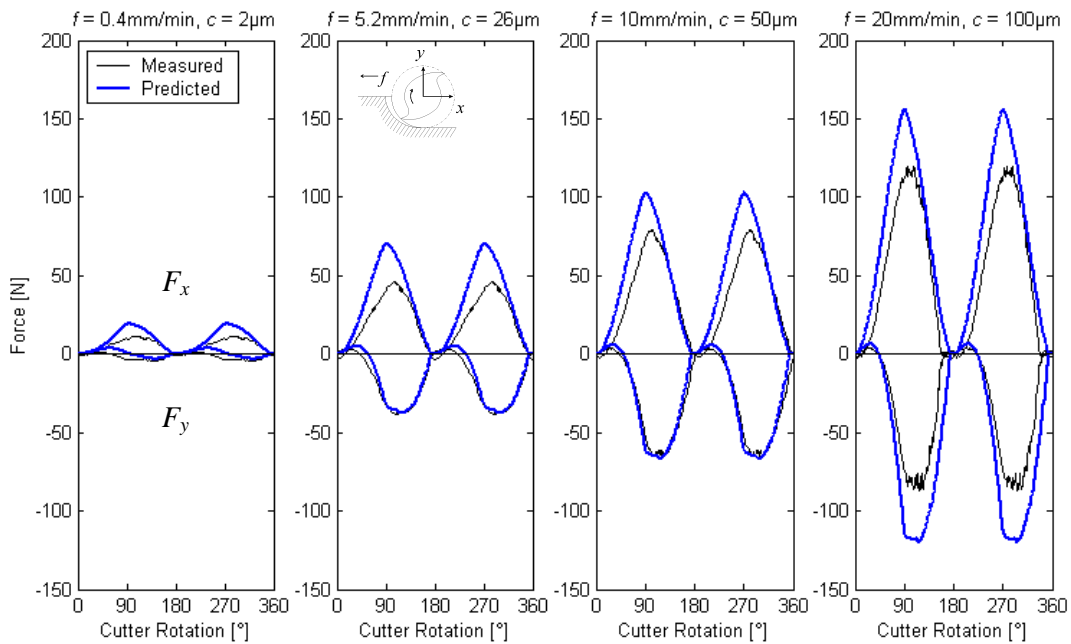


Figure 3.16. Experimental and simulated milling forces in x and y for half-immersion up-milling with a two fluted helical tool (Tool 'A'). Cutting conditions: feed rates $f = 0.4, 5.2, 10.0, 20.0 \text{ mm/min}$; rotational velocity $\omega = 100 \text{ RPM}$; axial depth of cut $a = 8\text{mm}$.

Experiment #164-167

3.4.5 Influence of the number of cutting teeth

The mean force components for slot milling with two and four fluted helical cutters having both having the same rake, helix and clearance angles are presented in table 3.5 for equivalent feed rates. Although the four fluted tool exhibited less variation in force with time (figures 3.17 and 3.18), the mean forces (especially the feed force) were larger in magnitude for the four fluted tool. Although the force predictions were able to predict these trends, the magnitude of the mean force estimates at these small feeds were significantly greater than the measured means, particularly in the feed direction.

Table 3.5. Measured and predicted mean forces for full-immersion down milling with 2 and 4 fluted tools for equivalent feed rates (5000RPM, $v=332.5\text{mm/s}$)

Flutes #	Force [N]	f [mm/min] (c [μm])			
		10 (0.5)	20 (1)	70 (3.5)	130 (6.5)
	F_x	-4.0 -19.9	-7.2 -23.8	-18.6 -29.3	-24.8 -30.9
	F_y	4.1 8.8	7.4 13.7	15.1 27.9	27.6 38.0
	F_z	-1.3 -3.6	-1.3 -5.7	-8.8 -11.3	-8.5 -15.5
		(1)	(2)	(7)	(13)
	F_x	-11.4 -32.1	-13.6 -39.9	-29.5 -53.1	-29.8 -58.2
	F_y	7.2 11.0	10.6 17.7	25.3 38.28	30.5 53.7
	F_z	-1.0 -4.6	-0.5 -7.3	-3.2 -15.6	-7.6 -21.9

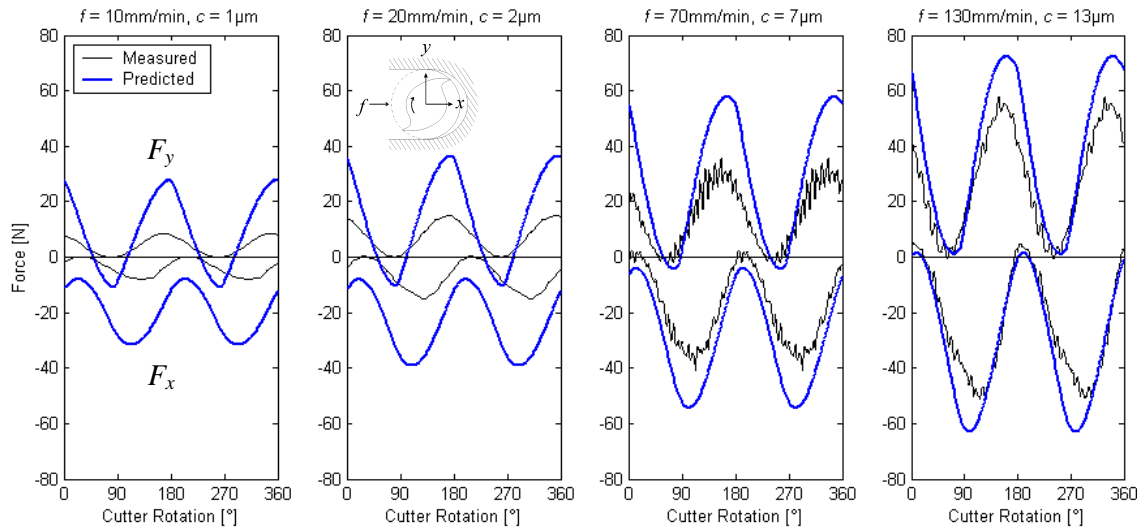
5000RPM, $v=1662.4\text{mm/s}$ 

Figure 3.17. Measured and predicted milling forces in x and y for full-immersion down-milling with a two fluted helical tool (Tool 'B'). Cutting conditions: feed rates $f = 10, 20, 70, 130 \text{ mm/min}$; rotational velocity $\omega = 5000 \text{ RPM}$; axial depth of cut $a = 8\text{mm}$.

$f = 10$ and 20 mm/min data low pass filtered with cut-off equal to 10 times the tooth passing frequency
Experimental trials: #97,98,101,102 (plot_simA096toA99.m)

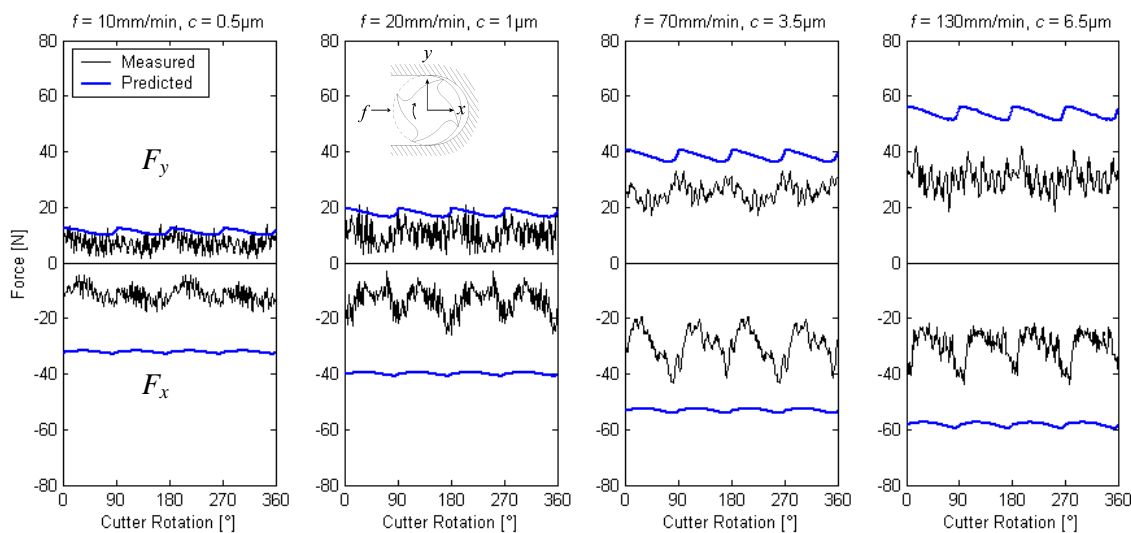
5000RPM, $v=1662.4\text{mm/s}$ 

Figure 3.18. Measured and predicted milling forces in x and y for full-immersion down-milling with a four fluted helical tool (Tool 'C'). Cutting conditions: feed rates $f = 10, 20, 70, 130 \text{ mm/min}$; rotational velocity $\omega = 5000 \text{ RPM}$; axial depth of cut $a = 8\text{mm}$.

Experimental trials: #91-95 (plot_simA091toA95.m)

3.4.6 Influence of cutting direction with respect to fibre orientation

Instantaneous feed and normal force components are presented as a function of the tool rotation angle for slot milling with a double fluted helical cutting tool for feeds per tooth of $c = 2, 50$ and $100\mu\text{m}$ (figure 3.19). The feed direction is parallel (left plot) and transverse (right plot) to the long axis of the bone. The tool rotational velocity is $\omega = 100$ RPM ($v=33.25\text{mm/s}$). The peak forces in the normal direction are slightly higher when milling parallel to the bone axis for both small and large feeds. This is a likely result of the increase in specific cutting energy when the edge elements are cutting transverse to the predominant fibre direction at low speed (i.e. at $\theta = 90^\circ$ with the milling feed direction parallel to the bone axis). Similarly, the peak forces measured in the feed direction are higher when the feed direction is transverse to the bone axis.

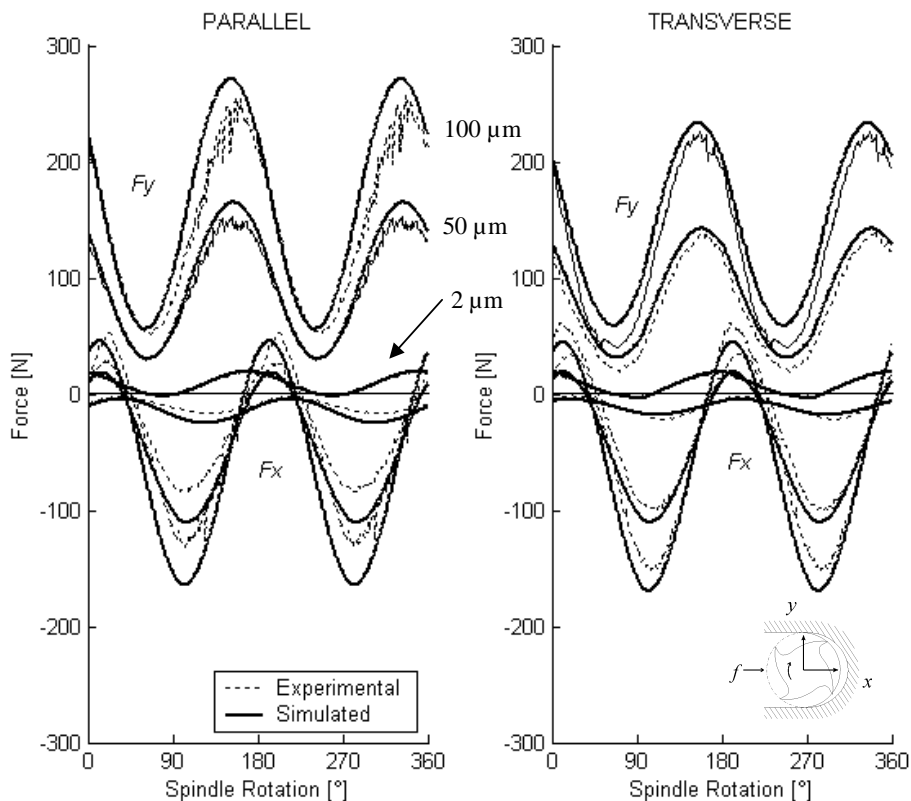


Figure 3.19. Experimental and simulated instantaneous milling force components in x and y for slot (full-immersion) milling with a cutter having two helical teeth (Tool 'B'). Feed direction is parallel (left plot) and transverse (right plot) to the bone axis. Cutting conditions: feeds per tooth $c = 2, 50, 100\mu\text{m}$; rotational velocity $\omega = 100$ RPM; axial depth of cut $a = 9.1\text{mm}$.

3.5 Discussion

Bone milling forces are dependent on several parameters, including tool geometry, cutting speed, feed rate, radial and axial cutting depth, and cutting direction and mode. To our knowledge, this is the first study to present cutting force patterns for bone milling as a function of the tool rotation. These data are useful for gaining a better understanding and for validating models of the physical mechanisms governing in the bone milling process. In this section, we first discuss the effects of various kinematic and geometrical parameters on the milling force components and their clinical implications. The model is then extended to provide some insight on milling temperatures, surface accuracy and surgical techniques. Finally, some recommendations on tool design are given.

3.5.1 Feed rate and radial immersion

When milling with a fully immersed four straight-fluted tool at low-speeds, it was observed that the mean feed force did not increase with increasing feed per tooth after a critical feed ($c \sim 25\text{-}50\mu\text{m}$), even though the mean normal force continued to elevate (figure 3.8). This trend was also observed when cutting with a double helical fluted tool at 5000RPM though the critical feed per tooth was lower ($c \sim 12\text{-}25\mu\text{m}$, figure 3.10). This phenomenon can be related to the behaviour of the radial force component in orthogonal and oblique cutting with increasing chip thickness. The maximum chip thickness in milling occurs when the tooth is directly in front of the tool, i.e. when the radial force component is directly in line with the feed ($\theta = \pi/2$). Since the radial force F_r in orthogonal and oblique cutting either decreases or remains essentially constant as the chip thickness increases, the projection of F_r in the feed direction over one integral revolution is also essentially constant with increasing feed per tooth (the tangential force component does not influence the mean feed force because of the chip symmetry about x).

The surgeon therefore could potentially optimize cutting time without applying excessive feed forces by increasing the rate at which he or she moves the tool through the bone. As this would significantly increase the force on the tool tip in the direction normal to the cut surface, however, it is important to appropriately select an axial depth of cut to keep overall forces manageable. Surface accuracy and patient safety could otherwise be compromised. High normal forces could cause the tool to deflect away from the surface, and could be transferred to the guide fixation pins causing motion or even failure at the fixation site. Advancing the tool at a higher rate without consequences in the feed force might also give the false impression that overall cutting forces are low and in a relatively stable manageable state, especially if the tool is constrained vertically by the guide. The net resultant force applied to the cutter could however suddenly escalate or change direction (for example if the radial cutting depth decreases) which could cause the tool to slip out of control in an oblique direction.

Increasing the feed rate with the cutting tool half-immersed into the bone resulted in the mean and maximum feed forces changing directions from negative to positive for both the two and four fluted helical cutters (figures 3.14 and 3.15). During partial immersion milling the chip is no longer symmetric. The change in feed force direction is therefore a result of the proportional difference in the force components acting tangential and radial to the cutting teeth as a function of the feed per tooth c . In orthogonal and oblique cutting the radial cutting force F_r was measured to be proportionally greater than the tangential cutting force F_t at small feeds per tooth (i.e. $t < \sim 10\mu\text{m}$, figures 2.10a,b). When these components are transformed into the milling tool coordinate system, the cutting conditions correspond to a resultant force acting on the tool that is oriented upward and negatively with respect to the feed direction (F_R , figure 3.20a). As the feed per tooth increases, the tangential force component increases while the radial force component typically decreases or remains constant, resulting in a positively oriented feed force component (F_x , figure 3.20b).

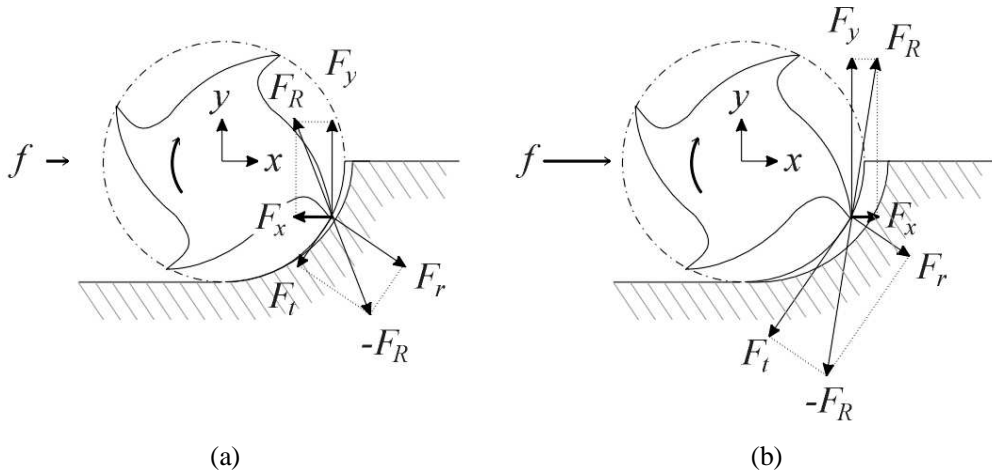


Figure 3.20. Influence of feed rate (f) on the feed force direction (F_x) during half-immersion down milling.

When milling at lower feed rates with the cutter only half immersed into the bone, the surgeon would have to push the tool through with a relatively small feed force. If the feed rate is increased to the critical feed, the mean feed force would diminish to zero and the cutter would move almost effortlessly along the cut, assuming that the tool was constrained in the normal direction by the milling tool guide. Beyond this critical feed the mean feed force acting on the tool would continue to increase in the cutting direction, ‘pulling’ itself further into the cut, possibly further increasing the feed per tooth and causing the tool to suddenly ‘get sucked’ into the cut. In addition, due to the corresponding increase in the normal cutting force with feed rate, the resultant milling force acting on the tool (F_R , figure 3.20b) would tend to push the slender cutter up and over the cut, causing the cutting tool to ‘jump’ or ‘skid’ over the bone surface.

This was a problem that we observed during one of our cadaver trials while milling away the patellar groove in the anterior femoral cut. As the milling tool moved from medial to lateral into the hard cortical bone, the tool suddenly jumped into the cut, climbing laterally up the groove surface until it jammed in the hard subcondylar bone. This could be prevented by increasing the stiffness of the milling attachment and by reducing the diameter of the tool from 9mm to \sim 5mm so that the cutter is almost fully immersed in the bone during most of the cuts.

3.5.2 Number of cutting teeth

Both the average milling force and the force variation with time are significantly affected by the number of teeth milling. When full or partial immersion milling with a helical double-fluted cutter the amplitude of the force variation was observed to be approximately equal to the mean force (figures 3.11, 3.14 and 3.17). When full or partial immersion milling with a cutter having four helical or straight flutes, however, the feed and normal forces exhibited relatively little variation with respect to their corresponding mean values (figures 3.8, 3.15, 3.18). This is simply a result of the geometry of the cutting conditions, and how many cutting teeth are actively engaged in the cut at any given instant in time. When slot milling with a double straight-fluted cutter at a given feed rate only one tooth is engaged in cutting at any given instant in time. The chip thickness is simply equal to $t(\theta) = c \cdot \sin(\theta)$ for the cutter rotation $0 < \theta < \pi$ (the period of t is π and $c = f/2$, where f is the feed per revolution). The standard deviation in the chip thickness across one cutter revolution is therefore $\sim 50\%$ of the mean chip thickness, assuming that there is no cutter runout. When slot milling with a straight four-fluted cutter two teeth are engaged in the cut at any given instant in time. With a tooth pitch of $\pi/2$ the total

chip thickness acting on both engaged flutes for the same feed rate is $t(\theta) = c*\sin(\theta) + c*\sin(\theta+\pi/2)$ for $0 < \theta < \pi/2$ (the period of t is $\pi/2$; $c = f/4$). Thus the chip variation is only ~10% SD for the same mean value. Similarly, the chip variation would be ~2.5% (SD) of the mean for eight flutes (figure 3.18).

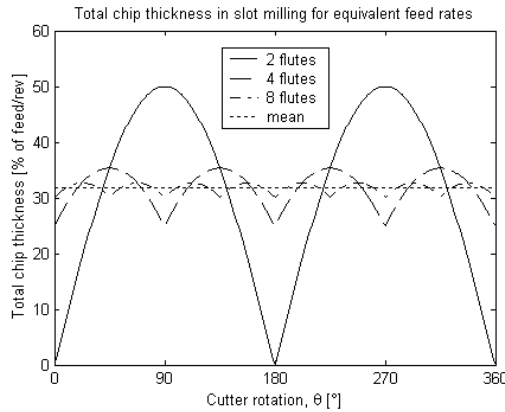


Figure 3.18. Total instantaneous chip thickness during slot milling with 2, 4 and 8 straight-fluted tools for an equivalent feed rate, assuming no runout.

Although there is no change in the theoretical mean total chip thickness when slot milling with cutters having different numbers of teeth, the mean normal and especially the mean feed force were observed to be higher when milling with a four versus two fluted cutter (table 3.5). This is a result of two factors (a) the non-linearity of the F vs. t curves measured in orthogonal and oblique cutting, and (b) the parasitic forces acting on the edge and clearance face of the tool. Each time the feed per tooth is reduced by cutting with more teeth, the specific cutting energy required to machine the smaller chip thickness increases at each tooth (figure 2.12). Therefore the total force summed over all engaged cutting teeth increases in comparison to fewer teeth cutting the same total amount. In addition, the edge forces acting on the each cutting tooth becomes proportionally more important at very small feeds. Increasing the number of cutting edges increases the friction contact length zone and the total edge force. Because frictional forces affect the radial cutting force component more than the tangential one at low chip thicknesses, the mean feed forces increased more than the normal ones when slot milling at the very small feeds per tooth ($c=0.5$ and $1\text{ }\mu\text{m}$, table 3.5).

3.5.3 Cutting rotational and surface speed

The most common means for increasing the cutting surface speed in surgery is to increase the tool rotational velocity. This has a less obvious but important consequence on the geometry of the cutting conditions, as it essentially reduces the thickness of the chips produced. When milling at 100RPM the mean forces were measured to be ~5 and ~20 times greater in the feed and normal directions respectively, compared to milling the same feed rates at 5000 RPM (figure 3.13, left column). The difference in force *magnitudes* between the two speeds is largely due to the difference in the chip thickness since the feed per tooth increased by a factor of 50 for the same material removal rate. The difference in the force component *proportions* between x and y at each speed is however due to the different rates of change between the tangential and radial force components at the different chip thicknesses.

The effect of cutting surface speed on forces at equivalent feeds per tooth was less obvious. When cutting with tool A at $c=2\text{-}50\mu\text{m}$, forces increased by ~20-60% percent when the cutting speed was decreased from 5000RPM to 100RPM, depending on the feed and direction (table 3.3). In a similar experiment with a different bone specimen where feeds per tooth ranged from $c=0.5\text{-}7\mu\text{m}$, however, the mean normal forces were lower while the mean feed forces were higher at the higher speed. This exception could possibly be due to some local variability in the specimen.

3.5.4 Temperature considerations

Thermal necrosis of bone is dependent on both the magnitude and the duration of the temperature elevation of the tissue. The temperature elevation in bone-milling is dependant on the total amount of energy expended in making the cut, which is a function of the forces exerted in cutting (i.e. material deformation and separation) and friction at each tooth edge. Therefore, decreasing the number of cutting teeth and increasing the feed velocity of the tool should significantly reduce the total frictional forces and the bone-edge contact time, and thus the risk of tissue necrosis due to heating. Increasing the rotational velocity for any given cutting tool and material removal rate increases the total number of revolutions and tooth passes required to make the cut, however, which should result in an increase in temperature.

Therefore a simplified model for the temperature elevation at the cutting surface could be:

$$T = K \cdot (l \cdot \omega \cdot N / f) + T_o$$

where T_o is the initial temperature, l is the edge contact length, ω is the rotational velocity, N is the number of cutting teeth, f is the feed rate, and K is a coefficient that takes into account the material properties of the bone and the edge properties of the cutter (geometry and surface roughness).

Krause [1982] investigated the temperature elevation in cutting bovine cortical bone with a spherical and oblong burr operating at 20,000 and 100,000 rpm for various feed rates and axial depths of cuts. Temperatures decreased as a result of increasing feed rate, but increased as the depth of cut increased. The temperature increase due to an increase in rotational speed was dependant on the particular burr geometry. They concluded that an increase in feed rate had a greater effect on the temperature response than an increase in rotational speed, so that cutting with a 100,000 RPM tool is satisfactory if a fast feed rate is used.

The specific cutting energy of bone (i.e. the amount of force expended in removing a unit quantity) increases with decreased chip thickness. Since the chip thickness is dependent on the number of cutting teeth, the feed rate, and the rotational speed (equation 3.4), this energy or ‘size effect’ phenomenon generally causes an unfavourable consequence on temperatures when milling at high rotational speeds. Thus the decrease in milling forces with increased rotational speed for a given material removal rate comes at the expense of increased temperatures. It is therefore advised that irrigation should always be applied directly at the cutting site when milling at high speeds, especially when the feed rate is relatively low.

3.5.5 Optimizing Surface Accuracy

We observed during our cadaver tests with the robot (described later in Chapter 4) that the surgeons performed the cut using both forward and backward motions of the tool, i.e. milling conditions that correspond to down- and up-milling respectively. The normal force component is typically oriented away from the cut surface during down-milling and towards the cut surface when up-milling (figures 3.12 and 3.16). This caused respective overcutting and undercutting errors on the cadaver bone surface, leaving steps of different heights with each tool pass. Although it is likely not possible to prevent the inversion of the normal force with feed direction and the corresponding reversed tool deflection, one method to minimize the surface errors could be to standardize the feed direction in the milling technique. For instance, imagine that a first ‘rough cut’ is made by making a quick pass in the down-milling mode to remove the majority of the hard bone material. The normal milling force would tend to push the tool away from the surface during this pass, leaving an initial surface that is slightly higher than the intended one (<<1mm). The surgeon could then reverse the direction of feed, backtracking over the cut in the up-milling mode to machine away the slight remainder (performing a finishing a cut at this low immersion level would cause negligible forces and tool deflections, leaving a surface which is nearly perfectly flat). This could be efficiently implemented in surgery simply by swinging the cutter back and forth once during each pass before advancing the tool forward to

complete the subsequent pass. Moreover, the robot would not have to reposition the guide at different levels for the roughing and finishing passes.

3.5.6 Model accuracy and relevance

Although the algorithm demonstrated reasonable accuracy for milling at higher feeds per tooth, proportionally less accurate results were obtained when milling at very small feeds per tooth (i.e. for c on the order of a few microns). The radial forces measured in our orthogonal cutting experiments at $2.5\mu\text{m}$ depths of cut appear to be ~50% higher than what we measured in the milling experiments, which could be due in part to some small geometrical differences between the milling cutter teeth and those used in the orthogonal tests (which may have changed the coefficient of friction). At very small chip thicknesses, the complex frictional and ploughing forces acting between the bone and the tool rake and clearance faces have a proportionally greater influence on the force components in comparison to the cutting action (material failure) itself. The dependence of these parasitic forces on machining parameters such as cutting velocity and chip thickness is still not clear and remains a topic of ongoing research. Nevertheless, it is apparent that the simple chip load model presented here can be useful for helping understand and predict the complex interrelationships between milling conditions and forces.

3.6 Conclusions and Tool Design Recommendations

In summary, a mathematical model of the bone-milling process has been developed and evaluated using experimental data. Force predictions and measurements were compared for several different sets of milling conditions including different milling geometries, immersion levels, directions, modes (up and down), feeds and speeds. The model provided valuable insight as to why and how milling forces change as a function of those milling conditions. In addition, we used the milling force model to better understand the effects of the milling conditions on bone-cutting temperatures and surface accuracy.

Based on the experimental and theoretical results obtained in this chapter, we can make the following tool design recommendations:

- The cutter should have the minimum number of cutting teeth to minimize the mean cutting forces and temperatures. This number could be selected keeping in mind the operating speed of the cutter and the vibration response characteristics of the robot structure mounted on the bone (with the surgeon's hand on the milling motor). Four teeth could make a good compromise between vibration amplitude and mean force for high speed cutting.
- The cutter should be of the smallest diameter as possible to minimize the variability in radial immersion and the torque applied to the milling motor.
- The cutter should be of relatively short axial length to permit higher feed rates to keep cutting forces manageable and to minimize temperatures.
- The cutting speed should be relatively high to minimize forces for any given feed rate, and irrigation should be incorporated directly at the cutting site when high-speed milling.
- The benefits of helical teeth include reducing the sharp increase in forces upon cut entry, and improving the chip removal mechanism. Helical teeth do not significantly change the mechanics however and they add a third force component in the axial direction. Therefore they are likely not necessary if there is an appreciable increase in the cost of manufacturing.

- The tool rake angle should be sharp, and a new tool should be used for every procedure to minimize the effects of tool wear on the cutting forces, temperatures, and time.
- The ‘bite’ of each tooth (i.e. the volume above the rake face) should be relatively large to minimize clogging of the flutes with bone debris.

4.0 Chapter Summary

The overall goal of this work is to develop a compact, accurate, safe, and easy-to-use surgical robot for conventional and minimally invasive total knee arthroplasty (TKA). The function of our bone-mounted robot, named after the Greek sculptor *Praxiteles*, is to precisely position a surgical bone-cutting guide in the appropriate planes surrounding the knee so that the surgeon can perform the planar cuts manually using the guide. The robot architecture is comprised of 2 motorized degrees of freedom (DoF) whose axes of rotation are arranged in parallel and are precisely aligned to the implant cutting planes with a 2 DoF adjustment mechanism. Two robot prototypes have been developed, an initial version for open TKA and a new version for minimally invasive TKA. In this chapter we describe the concept and construction of the initial version for open TKA; the MIS version is presented in the following chapter. After a review of the current state-of-the-art in knee robotics, the specifications for the robot design are provided. We then describe our robot architecture and initial design and construction in detail. The accuracy of the robotic system in terms of mechanical backlash, stiffness, positioning reproducibility and calibration is measured and discussed. A mathematical study is undertaken to optimize the robot geometry, kinematics, and workspace in order to improve on the design. Based on the promising results obtained with first prototype, recommendations are made for the refinement of the design in a second version for further testing.

4.1 Introduction

Robotized surgical instrumentation can potentially increase the precision and capabilities of the surgeon, improve outcomes and recovery times for the patient, and reduce the large number of mechanical instruments required in the operating room. Previous and currently available robotic TKA systems have been mainly categorized by two factors: size and function. Over the past decade, several groups have proposed relatively large floor or table mounted robotic systems [Kienzle 1995][Ho 1995][Delp 1998][Jakopec 2001][Matsen 1993][Davies 1997][Van Ham 1998][Borner 2004]. Recently, an increasing amount of development has been aimed at smaller, bone-mounted robots [Ritschl 2004][Berardoni 2003][Wolf 2005][Shoham 2003]. Both types of systems can either position cutting-guides for the surgeon, or they can carry out bone-milling autonomously. They have been classified as being either semi-active or active, respectively [Delp 1998][Stindel 2002]. Most large research systems use industrial type robotic arms that have been modified for use in surgery, by for example, incorporating a force sensor in the end-effector and redundant encoders in the joints.

The passive system described in [Kienzle 1995], for instance, uses a large industrial six-axis PUMA 560 robot. The surgeon communicates with the arm during the operation via pushbuttons on a handheld control box which directs the robot through a series of predefined steps. Other motion control modes include performing large “passive” movements of the robot by the surgeon (i.e. force following) to bring the robot into the vicinity of the desired position, and small precise adjusting movements made autonomously by the robot. Matsen et al [1993] report on a smaller, six-axis PUMA 260 robot (16kg) for positioning saw or drill guides around the knee. The surgeon uses a computer touch-screen to slowly advance the robot from one position to the next. The authors selected a smaller, lower payload arm to minimize the space occupied in the OR and to maximize safety in the event of a controller malfunction. Although the low payload arm was initially thought to be adequately stiff because the robot was immobile while the surgeon carried out the cutting/drilling, stiffness tests revealed that a force of 18N on the saw-guide produced an unacceptable displacement of 2.5mm, which required the addition of stiffening links.

The ACROBOT system (The Acrobot Company Ltd, UK) was one of the first specially built large robots for TKA that uses a ‘hands-on’ approach where the surgeon controls the position of the milling tool using a handle instrumented with a force sensor (figure 4.1) [Ho 1995][Jakopec 2001]. The robot architecture is comprised of a unique backdrivable roll-pitch-yaw mechanism mounted on a gross positioning arm which brings the ACROBOT head into the vicinity of the knee [Davies 1997]. This active constraint control scheme allows the surgeon to move the milling tool under servoassistance within preprogrammed regions as determined from pre-operative CT scan reconstructions, providing enhanced control during the milling process while preventing the milling tool from entering forbidden regions of the patient.

One current drawback to these large types of robot assistants is that the tibia and femur bones usually have to be immobilized to the operating table as rigidly as possible, typically by connecting a number of bone clamps to the OR table. Kienzle and colleagues [1995] describe a 6 DoF fixturing arm equipped with heavy duty locking joints. The fully active ‘ROBODOC’ system (Integrated Surgical Systems, Davis, California) uses a milling tool rigidly attached to a 3 DoF wrist on a large RRP (SCARA) arm, and has a mechanical sensor to monitor if any bone motion has occurred with respect to the robot base during cutting [Borner 2004]. If a certain amplitude of motion is detected during the autonomous milling stage, cutting is automatically stopped and the surgeon must re-register the patient and robot coordinate systems. This system also employs an emergency stop button and an instrumented end-effector which monitors the forces during milling and stops the process automatically if forces exceed a certain threshold value.

Miniature robotic guide positioning devices have more recently become available for TKA [Ritschl 2004][Berardoni 2003]. The PI-Galileo Positioning Device (PLUS Orthopedics AG, Switzerland) system uses a hybrid navigated-robotic device which is fixed to the anterior-distal portion of the femoral shaft [Ritschl 2004]. This system allows the surgeon to navigate the guide orientation in the frontal and transverse planes with a 2 DoF mechanical adjustment mechanism. A motorised linear DoF in the proximal/distal direction then positions a distal cutting-guide to the correct cutting depth so that the surgeon can make the distal cut. A second linear DoF then slides a conventional 4-in-1 saw guide in the anterior-posterior direction so that one cutting block with four angled slots can be used for the entire size range of one specific implant geometry. This system can precisely control the cutting-guide position in the proximal-distal and anterior-posterior directions, though some drawbacks include no control of sagittal plane alignment, reduced visibility during cutting due to the conventional cutting block, and the need for different cutting blocks for different implant shapes. A relatively high degree of bone exposure is also necessary to mount the robot base/motors on the distal shaft clear of the distal cut. Another commercially available system (Medacta, Switzerland) uses a 5 DoF motorized architecture which automates positioning of each cutting plane in all DoF. The robot mounts on the medial, lateral, and anterior portions of the exposed femur and occupies a cubic volume of $\sim 20^3 \text{ cm}^3$ around the knee [Berardoni 2003].

Similar to the ‘MARS’ [Shoham 2003] miniature orthopaedic robot (Mazor Surgical Technologies, Israel, www.mazorst.com), the ‘MBARS’ [Wolf 2005] robot employs a parallel platform architecture. This active bone-mounted system has been demonstrated for patellofemoral joint arthroplasty, where a small pocket surface is machined in the trochlear groove area of the femur. The parallel 6 DoF architecture allows for automated ‘computer numerically controlled’ like machining of complex implant bed surfaces within a relatively small workspace. Rigid fixation of the miniature platform is achieved with three pins in the medial, lateral, and anterior femoral regions.

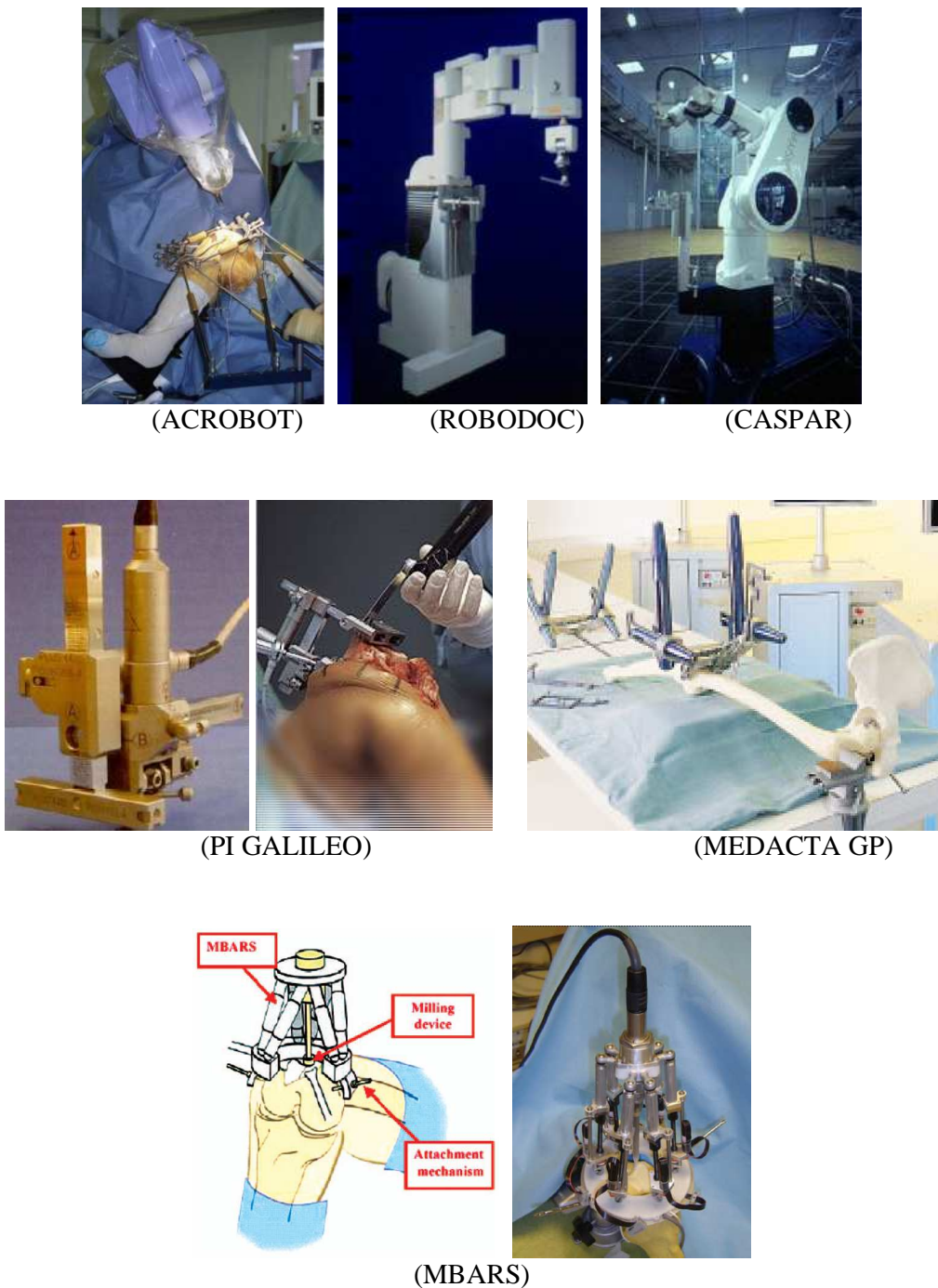


Figure 4.1 State of the art in large and mini TKA robots

A primary difference between floor/table mounted robots and bone mounted systems is that in the former, the bones have to be immobilized as rigidly as possible, typically by clamping them to the operating table. More technically complex alternatives involve tracking and compensating for small bone motions during cutting [Ranftl 2005]. The size and weight of the robot also has an impact in the operating room environment. Large robots occupy valuable space surrounding the operating table,

making it difficult for the surgeons and assistants to access the patient. The integration challenging into the operating room has been a strong focus for the GMCAO research team at UJF, leading to the concept of ‘synergistic’ robotic tools such as the PADyC system that work in co-operation with the surgeon [Troccaz 1996], as well as a number of light and compact robots that are placed directly on the patient and have a specially designed architecture to suit the clinical task [Berkelman 2004][Taillant 2004]. A key advantage of bone mounted robots is that there is no need to immobilize the limb or compensate for motion, and hence they impose a less dramatic departure from the conventional surgical technique. A current drawback to most bone-mounted robotic TKA systems, however, is that they require substantial incision of the quadriceps muscle and reflection of the patella in order to rigidly fix the robot to the three sides (medial, lateral, anterior) adjacent to the bone cutting area.

4.1.1 *Objectives*

The goal of this chapter is to report on the development of a miniature robotic bone-milling and sawing guide positioner for conventional CA-TKA. After specifying some key design parameters in §2.2, we describe the bone-mounted robot prototype that we initially developed for conventional TKA (§2.3). We then present in §2.4 a study that we conducted to optimize the geometry, kinematics, and workspace of this initial design.

4.2 Robot Design Specifications

4.2.1 *Accuracy Requirements*

To attain an overall frontal plane leg alignment within the critical 3° window $>95\%$ of the time [Ritter 1994], we would need to achieve a final cut reproducibility better than $\sim 1^\circ$ standard deviation (SD) both on the distal femur and on the proximal tibia. Additionally, to consistently attain a precise fit of the femoral component, we would need similar accuracy in the sagittal plane for all five femoral cuts. The accuracy in determining the mechanical axis of the femur (i.e. the line joining the hip and knee centers) using computer assisted techniques is relatively high, introducing only $\sim 0.3^\circ$ of variability in the frontal and sagittal planes [Stindel 2002]. The variability of the manual sawing process for an experienced surgeon using a slotted guide has been estimated to be on the order of 0.3° in the frontal plane and 0.7° SD in the sagittal plane [Plaskos 2002]. Summing the variances leaves us with a narrow frontal plane error margin of $\sim 0.4^\circ$ SD, and virtually no room for error in sagittal plane positioning.

4.2.2 *Load Bearing Requirements*

The first step in specifying an adequate motor size and transmission ratio was to estimate the loads applied to the cutting guide during surgery. To estimate the maximum forces that occur in bone-milling, we use the results obtained in the previous chapter. In order to have a conservative estimate, we assume that the bone at the cutting site is comprised completely of solid cortical bone (instead of cancellous or porous bone, which is known to be easier to cut). For the 5000RPM data, the maximum peak forces measured in the direction normal to the cut surface (i.e. the forces acting on the guide, F_y) were 100N for full immersion down milling with a two fluted tool for the highest feed rate tested (500mm/min or 8.3mm/s) and for an axial cutting depth of 5mm (figure 5.12). Note that most forces for 5000RPM were considerably less than 100N even for larger axial cutting depths of up to 9.6mm (see for example, figures 3.13, 3.17 and 3.18). Assuming an average cut area of $\sim 60 \times 30$ mm for each of the five femoral cuts, it would take less than one minute to make each cut with a feed rate of ~ 8 mm/s and an axial cutting depth of 5mm (not included the time lost to practical tasks such as changing the milling directions, repositioning retractors, etc...). In this force estimate we do not however consider the force that the surgeon applies to the guide, as this variable is currently unknown.

Unfortunately, we could not find any published studies that have measured the forces applied to a surgical cutting guide during manual sawing. Moctezuma et al [1997] measured the forces and the moment in the plane of an unguided saw-blade while cutting bovine cortical bone blocks with a conventional oscillating saw. The saw was rigidly connected to and constantly advanced by an industrial milling machine. Maximum forces were on the order of 10N. Due to the inhomogeneous nature of the epiphyseal bone at the knee, as well as the interaction between the vibrating saw-blade and the interior walls of the guiding slot, however, we suspect that maximum forces encountered in manual surgery would be significantly higher. Indeed, conventional saw-blades have been known to jam in the slot and ‘kick-back’ in the surgeons hands during cutting [Laskin 1991]. We therefore estimated our target for load bearing capability as 100N applied perpendicular to the guide plane, which corresponds to an applied torque of 2Nm (for a 50mm moment arm) about the mediolateral axis.

4.2.3 Sterilization Conditions

Sterilization is defined as the process of killing all microorganisms including bacteria, fungi, viruses, and spores with the use of either chemical or physical agents. The typical procedure employed by many hospitals to prepare instruments for invasive surgery is to first clean them by washing, scrubbing, and/or soaking them in a toxic bath of diluted glutaraldehyde solution for ~10-30 minutes. It is mandatory that the instruments then undergo steam sterilization in an autoclave under the following conditions: temperature 135°C, water vapour pressure 2.1 bar, relative humidity 100%, duration of cycle >20 minutes. We therefore require a completely waterproof design in which components could be easily disassembled for cleaning/washing. We also needed to encapsulate the electrical system and connectors, to employ only chemically stable materials such as stainless steel, titanium, polyetheretherketone (PEEK), etc., and to use biocompatible lubricants for the mechanical actuation system.

4.2.4 Safety Considerations

Several contrasting articles have been published on the safety issues related to medical robotics in orthopaedic surgery [Davies 1992][Troccaz 1996]. In general, we feel that systems which allow the surgeon to carry out the actual bone cutting are more easily accepted by clinicians than automated cutting systems in which the robot is in control of the cutting path. Although incorporating a system of position or velocity constraint could potentially enhance the cutting process, we felt that this would make our bone-mounted robot too large and cumbersome. We therefore decided at this stage to implement a fully passive cutting system in which the surgeon is in full control of the cutting process, as in conventional surgery. We then considered several possible scenarios in which the robot could potentially cause harm to the patient or surgeon, including power/motor failure, control malfunctions, etc. For each of the following potentially hazardous scenarios, a corresponding preferred result is specified (Table 4.1).

Table 4.1 Risk table of guide positioning

<i>Potential Problem</i>	<i>Desired Result</i>
disruption of the robot power supply during cutting	the guide should maintain its current position
irreversible actuator failure during surgery	actuators should be easily replaceable at any stage of the procedure
controller malfunctions	actuators should be physically incapable of moving the guide, unless authorised by surgeon
	the system should be back-drivable to allow manual positioning to safe zones

4.3 Initial Robot Concept and Prototype Development for Conventional TKA

An initial bone-mounted prototype of a ‘universal’ mini-robotic guide positioner for bone sawing and milling in conventional TKA was first developed. The device is universal in the sense that it can be used to position a single saw or mill guide at any cutting plane orientation and depth in the sagittal plane so that the distal femoral bone surface can be prepared for any implant geometry that is comprised of planar cuts (figure 4.2).

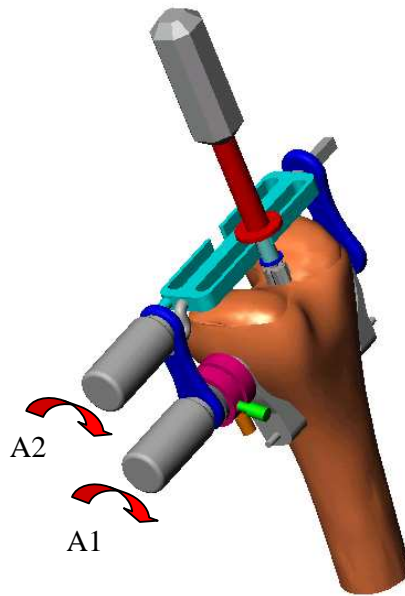


Figure 4.2. Initial concept for the Praxiteles surgical robot for conventional TKA

4.3.1 Description of robot architecture and components

The modular device consists of three primary components:

- a fixation and adjustment system that secures the robot to the bone and incorporates a 2 DoF adjustment mechanism which permits the surgeon to manually align the robot motor axis to the implant profile in the frontal and transverse (or axial) planes;
- a cutting tool interface that guides a saw-blade or milling tool.
- a 2 DoF actuation unit which has two motorised rotational axes (A1 and A2) arranged in parallel and moves the cutting guide interface relative to the bone fixation/adjustment system.

The modular design permits attachment of the guide interfaces for the various supported cutting techniques. We chose a robot architecture that has two motorised rotational DoF that can be aligned perpendicularly to the profile of the implant cuts (i.e. in line with all 5 cutting planes, figure 1.1) so that we could precisely control the following variables:

- global implant alignment in the sagittal plane,
- global anteroposterior (AP) implant positioning,
- global proximal-distal (PD) implant positioning,
- implant geometry (shape), and
- implant scaling (size).

This leaves the surgeon with two variables to adjust manually during surgery: (1) global frontal plane and (2) global transverse plane implant alignment, both of which are controlled using the 2 DoF manual adjustment mechanism under computer navigation.

4.3.2 Initial prototype construction

Before conducting any rigorous workspace or kinematic analysis, we manufactured an initial prototype of nominal dimensions to investigate the general feasibility of using this architecture in conventional TKA (Figure 4.3). In this initial system we rigidly connected the medial and lateral fixation bases with an arch shaped frame that traverses the anterior aspect of the femur. This helped to better distribute the loads on either side of the bone and keep the axis straight. We incorporated the orthogonal adjustment mechanism on the inner side of the frame in-between one of the fixation bases and the arch so that the surgeon can fine-tune the arch orientation after it is clamped onto the femur. On the opposite side, we put a clamping mechanism that advanced the opposing fixation base into the bone so that we could clamp the frame onto different size femurs. A slot was machined in the arch to allow for placement of a rigid body. Screw holes were added on either side of the frame so that the arch could be rigidly fixed after initial clamping and adjustment of the axis. The 2 DoF motor and a sawing or milling guide is then mounted on the fixed frame. The milling guide tested had two rotational DoF that constrained the milling tool in a plane, and a long milling cutter was used to access the entire cut area. We also tried this milling configuration in uni-compartmental knee arthroplasty (UKA), by fixating the arch percutaneously through the lateral side of the knee.

4.3.3 Computer Assisted Surgical Protocol (CASP)

The phases of the CASP for TKA are generally the same as with conventional image free navigation [Stindel 2002]. The knee joint first is exposed as in conventional surgery and an optical marker ('F' rigid body) is fixed onto the femur and the tibia. The relevant information to register the mechanical axis of the leg relative to the rigid bodies is gathered with the point probe and by manipulating and analysing kinematic motions of the leg. Bone-morphing and planning of the optimal implant position in all DoFs is then carried out intra-operatively, and the surgeon has the option of utilising the soft tissue balancing capabilities of the CASP during the planning phase. There is no need to immobilise the leg to the operating table.

Once the optimal implant position is planned intra-operatively using the hip centre and *BoneMorphing* algorithms [Stindel 2002] (figure 4.3a), the surgeon can navigate the fixation of the arch using the 'G' rigid body inserted into the arch slot. The nominal position and alignment of the arch in varus/valgus and internal/external rotation is first navigated 'free-hand' on the computer screen (figure 4.3b). Frontal and rotational alignment is then more precisely 'fine-tuned' under navigation by two adjustment screws on the arch, permitting the surgeon to correct for any orientation errors that may have occurred during the 'free-hand' mounting phase. Once the arch is fixed, the 2 DoF motor unit and saw-guide is attached, assuming the robot had not been preassembled before. The position of the first robot axis with respect to the femur is determined by the G position (the position of the first axis with respect to G is pre-calibrated *a priori* using kinematic measurements and a circle fitting routine). The angular positions of each motor axis (i.e. the encoder constants) are then calibrated with respect to the bone reference frame by using placed in the G cutting-guide slot. The surgeon can then cycle through each femoral cut position by pressing the foot switch. Before making each cut, the surgeon can visually and numerically verify the position of the guide-plane with respect to the planned cutting plane on the computer screen by using the G rigid body (figure 4.3d). After making each cut, the cut surface on the bone can also be verified with the probe.

The following subsections discuss the accuracy we achieved with this initial design configuration and surgical protocol.

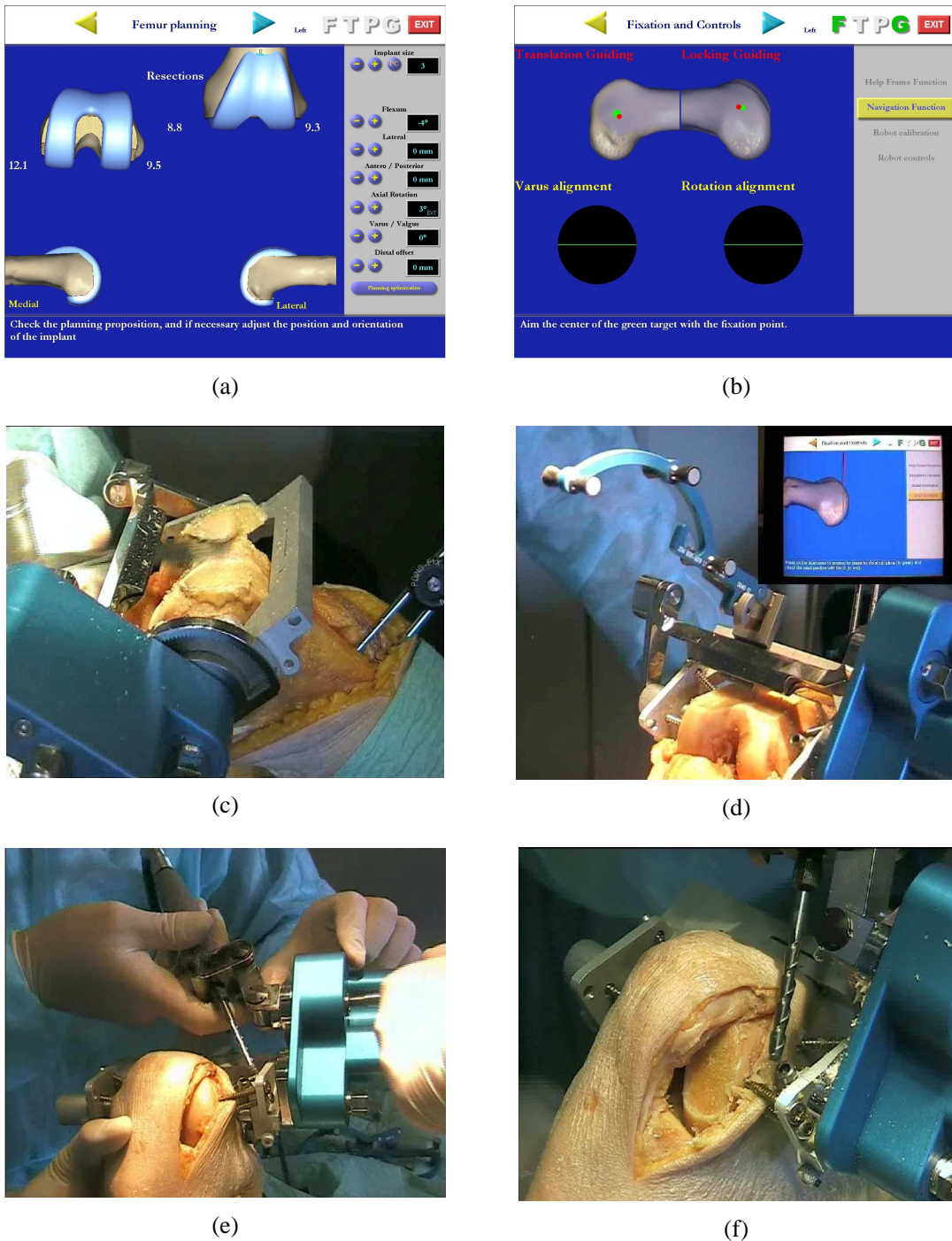


Figure 4.3 Cadaver experiments with our first prototype robot:
 a) intra-operative planning of the femoral component position and size;
 b) navigation of the fixation arch on the bone;
 c) making the anterior chamfer cut with the saw-guide in position;
 d) verifying guide position before making the distal cut;
 e) percutaneous fixation of the arch and attachment of the milling guide
 e) milling the distal cutting plane in uni-compartmental knee arthroplasty (UKA).

4.3.4 Manual adjustment and navigation system accuracy

Frontal and axial plane alignment is set manually under computer navigation by adjusting the pose of the robot axis with the manual adjustment screws. The adjustment screws selected had a thread pitch of 0.5mm per rotation. Assuming the smallest femur that we are likely to encounter would have a trans-epicondylar width of ~50mm [Poilvache 1996], this would give us an angular adjustment resolution of $\sim 0.5^\circ$ per screw rotation in the worst case. We found that in general a user equipped with a tool could rotate each screw such that the final positioning resolution was better than 0.1° . In addition, the clamping force applied through the frame helped to eliminate any backlash in the adjustment mechanism. The final axis orientation was often offset, however, when additional fixation screws were inserted to secure the arch to the bone. The extent of this offset generally depended on how much care and time the user spent during screwing, though this was typically on the order of 1° – 3° .

The precision with which a Polaris optical camera (Northern Digital, Waterloo, Canada) can localize a rigid body with three retro-reflective spherical markers spaced ~50mm apart has been reported to be 0.46mm and 0.713° SD (95% confidence interval) at the time of camera characterization [Wiles 1994]. The measurement frequency is on the order of 60Hz. This level of noise made it nearly impossible for a user to manually adjust the axis orientation in real time to sub-degree precision using only the raw data. To reduce noise and keep latency unnoticeable, we implemented a simple moving average filter that selectively discards any measurement within the current window that is greater than 2 times the current SD. We found empirically that updating the display at the capture frequency with the average of the last 10 acceptable measurements provided a stable readout within $\sim 0.1^\circ$ with virtually no detectable delay.

4.3.5 Motor positioning accuracy and load capabilities

Guide positioning in the sagittal plane (cut orientation and depth) is actuated with the two parallel motors. Positioning reproducibility is thus a function of the angular measurement system resolution, the gear reduction factor and the system backlash, among other factors. We could not find any sterilizable encoders on the market, so we selected a brushless DC-servomotor motor (FAULHABER, Germany) that had an integrated linear Hall sensor for position feedback, and lifespan rating of 100 autoclave cycles minimum. We measured the motor sensor repeatability in reporting a static position to be $0.24 \pm 2.0^\circ$ and $-1.2 \pm 4.1^\circ$ (mean \pm SD, $n = 25$), for the first and second motor, respectively. Based on the sensor precision, we would need a transmission ratio on the order of 100:1 to keep positioning precision well below 0.1° at each shaft output.

In constructing the initial prototype a 37 watt motor was used with an 86:1 planetary gearhead for both axes. The overall dimensions and weight of each component set were $\sim \varnothing 20 \times 80$ mm and 100g, respectively. The gearhead is specified to have a backlash of $\leq 1^\circ$ at no load, and a torque capacity of 0.5Nm for continuous operation and 0.7Nm for intermittent operation. To reduce the backlash and increase the torque capacity, we added an additional 8:1 reduction stage between the gearhead outputs and each final output shaft of the 2 DoF unit using precision machined straight spur gears. This resulted in a total reduction ratio of 688:1 and a theoretical maximum torque capacity of ~5Nm for each axis, assuming the spur teeth could sustain the load. We turned the final output shafts from stainless steel (304L), leaving a wide flange at the output side for the spurs. To increase the number of engaging teeth and to reduce the maximum tooth stress on each spur, we machined the output shaft teeth so that they meshed with the teeth on the far side of the gearhead output spur (i.e. akin to a planetary system). We slightly over-drilled the motor mounting holes so that the gearhead outputs could be abutted against the final output spur teeth during assembly. The centre distance between each gearhead and the flanged output shaft was ~26mm, so we limited the sweep angle of the first and second output shaft to 100° and 80° respectively, and put the flanges on the outside of the motor

housing to keep the unit relatively compact (the exposed flange of the first output shaft can be seen in figure 4.3e). This provided a kinematic workspace just large enough to allow us to perform all five femoral cuts using a side milling or sawing approach.



Figure 4.4. A 0.01mm resolution dial gauge was used to measure the mechanical backlash, stiffness, and positioning reproducibility of the robot prototype.

We measured the backlash, stiffness and positioning reproducibility at the saw-guide of our initial prototype by rigidly clamping a 0.01mm resolution dial-gauge to the fixation frame. The individual backlash measured for the first and second axis was 0.24° and 0.14° , respectively. This resulted in a final angular and linear backlash of $\sim 0.4^\circ$ and 0.25mm at the tip of the saw-guide (Table 4.2). The stiffness of the guide was measured by hanging a weight at various points along the guide and measuring the deflection at the point of the applied load. A static load of 10.6N applied at the saw-guide at distances of 50 and 100mm from the 2 DoF unit resulted in corresponding deflections of 0.04 and 0.13 mm.

Table 4.2
Mechanical Backlash, Stiffness, and Positioning
Reproducibility Measurements for the Initial
Prototype for Open TKA

<i>Backlash</i>	
1 st Axis only	0.24°
2 nd Axis only	0.14°
Guide Output	0.4°
Guide Output	0.25mm
<i>Stiffness</i>	
10.6 N load, 50mm ^a	0.04mm
K_{50}	265N/mm
10.6 N load, 100mm ^a	0.13mm
K_{100}	81 N/mm
<i>Positioning Reproducibility (n = 7)</i>	
Guide Output (SD)	0.04mm
Guide Output (Range)	0.12mm

^aLoad application and deflection measurement point along saw-guide, referenced from the output shaft of the motor unit.

The robot positioning repeatability was determined by rotating both motors by a random value, returning them to their initial positions, and then noting the dial-gauge value. The variability in positioning was 0.04 mm SD, with an error range of 0.12mm. Backlash did not significantly influence the static positioning repeatability results since gravity proved a biasing force which consistently kept the guide at one side of the backlash window.

4.3.6 Robot calibration and positioning accuracy

The calibration and positioning procedure for the two motorized robot axes ($A1$ and $A2$, figure 4.2) is as follows:

1. The 3D position of the first robot axis $A1$ in the femoral reference frame F is determined after the robot frame (or arch) is fixed to the bone, by taking the average of 30 measurements of the position of the G rigid body which is attached to the arch. The geometrical relationship between G and $A1$ was determined *a priori* by rigidly attaching another rigid body V to the 2 DoF motor unit and repeatedly recording the position of V relative to G while rotating the motors about $A1$ by $\sim 300^\circ$. A least squares fitting routine was used to fit a circle to the acquired data, and the transform between G and $A1$ was stored in a calibration file.
2. With the robot motors locked in the on position, a point on axis $A2$ is digitized with the pointer P , by placing the pointer tip in a cone machined into the shaft of axis $A2$ and taken the average of 30 measurements. The orientation of $A2$ is assumed to be parallel to $A1$.
3. The G rigid body is removed from the arch and a planar probe is attached, calibrated by palpating three calibration cones with P , and then inserted in the cutting guide slot (as in figure 4.3d). With the robot motors still locked, the orientation of the cutting guide slot is determined by averaging 30 measurements of G with respect to F .
4. The angular reference positions of the hall sensors (encoders) C_1^0 and C_2^0 for axis $A1$ and $A2$, respectively, can now be calibrated using the following equation:

$$\begin{aligned}\theta_1 &= K_1(C_1 - C_1^0) \\ \theta_2 &= K_2(C_2 - C_2^0)\end{aligned}\quad (4.1)$$

where K_1 and K_2 are the gear ratios for each motor axis, C_1 and C_2 are the current Hall sensor values as returned from the robot controller, θ_1 and θ_2 are the robot joint angles. θ_1 is the angle between the line joining $A1$ and $A2$ and the anteroposterior axis, and θ_2 is angle between the line jointing $A1$ and $A2$ and the guide plane.

Once the C_1^0 and C_2^0 values are determined the guide is positioned to each cutting plane. The implant position determined in the intra-operative planning stage is transformed to the robot coordinate frame, and aligned to the robot axis $A1$. Each of the five cuts is then expressed in the robot coordinate frame in the form $Ax + By + Cz + D = 0$, and the robot joint angles θ_1 and θ_2 are calculated for all five cuts based on the position of $A1$ and each cutting plane. The desired encoder values C_1 and C_2 corresponding to each cut are then determined using equation 4.1. The robot is then aligned to each cut by sending the corresponding encoder values to the controller, which is configured to operate in position control. The integration of the calibration and positioning algorithms into the CASP was implemented by a computer science summer student who completed an industrial placement at *Praxim*, and the full details of the implementation can be found in another report [Perrenlot 2003]. The guide positioning accuracy achieved using this calibration and positioning procedure was on the order of $1^\circ/\text{mm}$ for each cut.

4.4 Analysis of Optimal Robot Positioning, Geometry, and Workspace

In this section we analyse how the geometrical design parameters and the placement of the robot on the femur affect the kinematics of the guide positioning and the workspace. From our preliminary feasibility experiments with sawing on cadavers, we found that for some femoral cuts placement of the saw-guide was such that the saw-guide tip was some distance (~10-20mm) away from the bone and/or edge of the cutting plane (see figure 4.3c). Because of the flexibility of the saw-blade and its tendency to deflect or skive on the hard bone surface as it enters the cut, this gap presents a potential source for cutting errors to occur, and it also limits the reach of the saw blade. We would thus like to minimise this distance either by optimizing the dimensions and placement of the robot, or by adding an additional passive DoF in the cutting guide plane to bring the guide tip closer to the bone surface. Moreover, minimizing the gap distance would make it easier to design a stiff extra DoF by minimizing the required guide travel. The particular research questions that we therefore address in this study are therefore:

- can we optimize the robot placement on the femur relative to the planned implant position (i.e. intra-operative variable) such that the maximum distance between the cutting-guide tip and bone is always <10mm for any available implant shape and size, and
- can we optimize the distance between the two motorized robot axes and the depth of the cutting- guide (i.e. design parameters) such that the kinematic workspace of the robot can accommodate the full range of TKA implant sizes and geometries whilst remaining as compact as possible?

4.4.1 Model formulation

4.4.1.1 Analysis dimensions and implant co-ordinate system

Since the present objective is to optimize the kinematic workspace and intra-operative positioning of a two DoF parallel axes robot, we can simplify the analysis to two dimensions (i.e. to the plane that is perpendicular to the robot axes and to all of the femoral cutting planes). We digitised the inner surfaces of ten commercially available implant geometries, each offering a range of five to seven sizes. We defined a global co-ordinate frame for all implants as having an origin that is coincident with the distal cutting plane midpoint, with positive y pointing anteriorly along the plane and positive x pointing distally perpendicular to the cutting plane (figure 4.5). Figure 4.6 illustrates the proposed robot positioning sequence for the five femoral cuts using the two different cutting techniques: sawing and side milling.

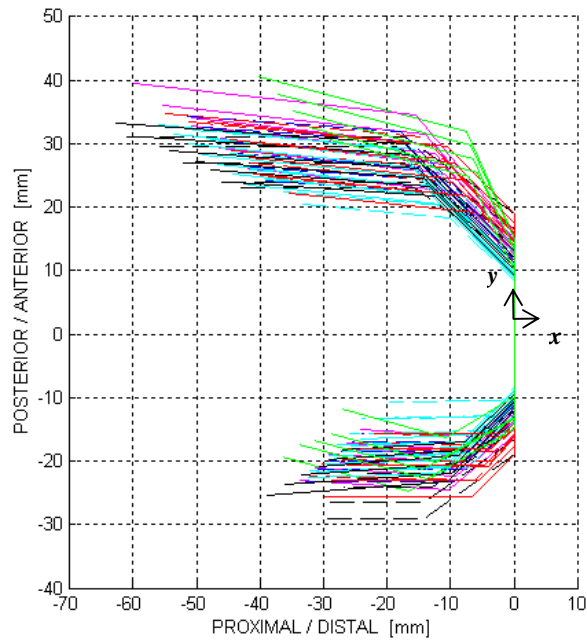


Figure 4.5. All implants are aligned so that the distal cuts are collinear with the y axis, with the midpoints coincident with the origin.

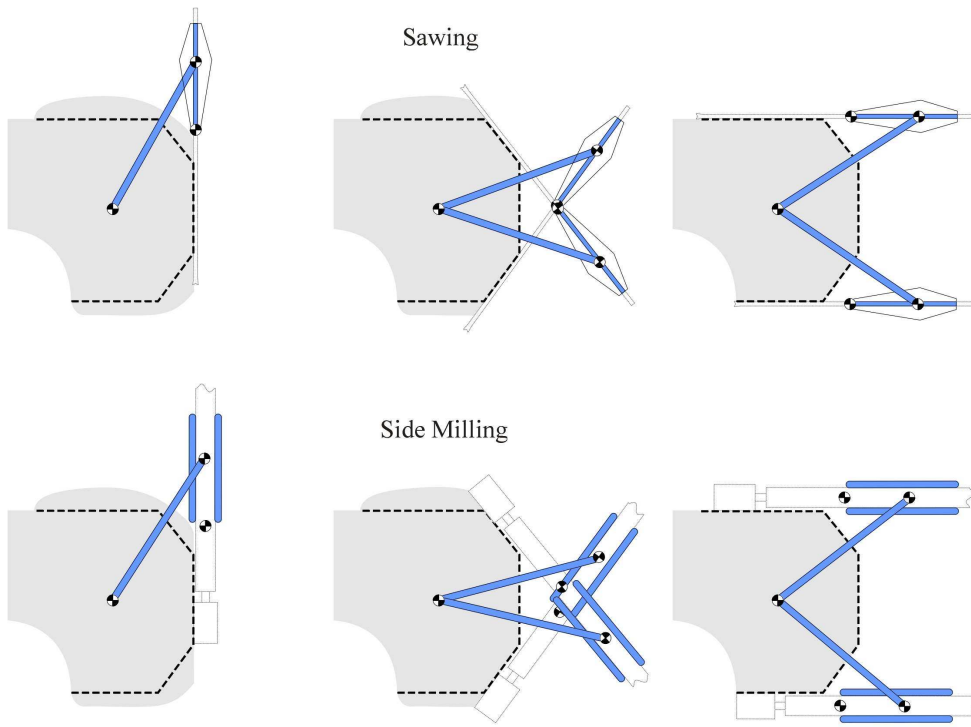


Figure 4.6. Robot positioning sequence for sawing, side milling, lateral milling.

4.4.1.2 Description of variables

$X_0 = (x_0, y_0)$, $X_1 = (x_1, y_1)$, and $X_2 = (x_2, y_2)$ are the location of the first axis, second axis, and far edge of the cutting guide, respectively (figure 4.7a); L_1 is the scalar distance between the first and second axes, and L_2 is the scalar distance between the second axis and the far edge of the cutting guide; \mathbf{c}_i is the cutting plane vector, starting from the entry point and ending at the far end of the cut (i.e. \mathbf{c} contains the vectors describing the inner implant surface, with each vector pointing in the direction of cutting); \mathbf{b}_i is a vector in the cutting plane starting from the exposed bone surface and ending at \mathbf{c}_i ; \mathbf{d}_i is the gap distance vector from \mathbf{b}_i to X_2 .

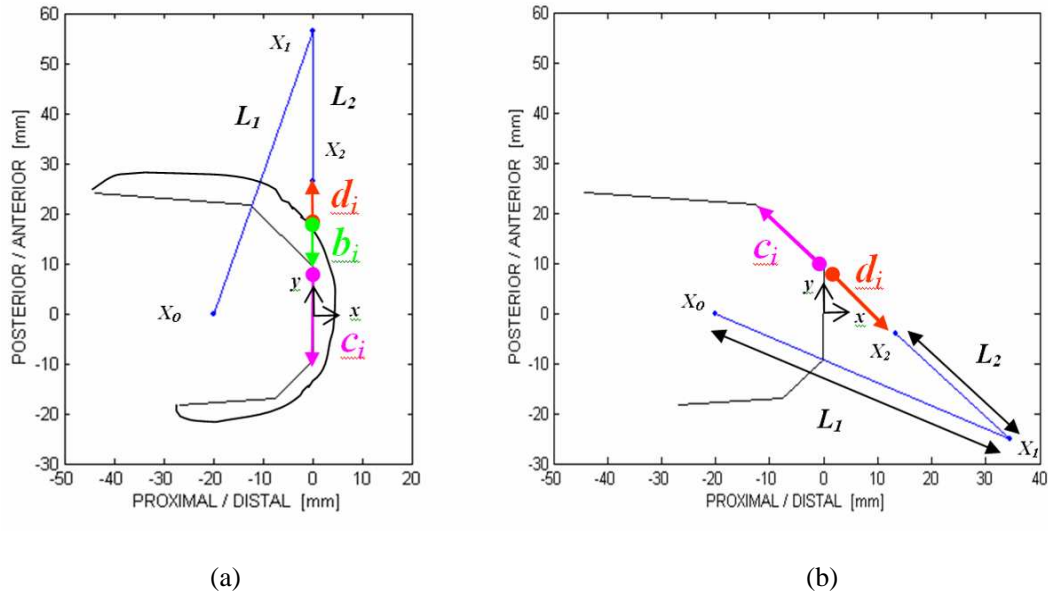


Figure 4.7. Description of variables: positioning for the (a) distal cut and (b) anterior chamfer cut.
Note that b_i is zero for all cuts except the distal.

4.4.1.3 Kinematic model

In order to determine the desired guide position for each cutting plane, it is necessary to compute the robot inverse kinematics. We assume that we want X_1 and X_2 to be co-linear with c_i , which can be expressed as an equation of a line in the form $y = c_{1i}x + c_{0i}$. The thickness of the saw-blade or milling tool is taken into account during positioning by offsetting each desired cutting plane by the half of the cutting tool thickness in the direction normal to the plane (the thickness offset is typically less than a millimetre for a saw blade and 3-5mm for a side milling tool). Given X_0 , L_1 , L_2 , and c_i , we can find X_1 by calculating the intersection point between the cutting plane line and the circle with centre X_0 and radius L_1 , i.e., we can solve for x_1 and y_1 in the following system of equations:

$$(x_1 - x_0)^2 + (y_1 - y_0)^2 = L_1^2 \quad (2.2)$$

$$y_1 = c_{1i}x_1 + c_{0i} \quad (2.3)$$

There are two real solution sets for X_1 if the cutting plane is within the robot workspace, and if c_i is outside of the circle, the solution is complex. Depending on the cut, we can choose the desired real solution by selecting the most distal or anterior position (for example, we chose the solution with maximum y_1 for the distal cut). Alternatively, we can select the solution that has the lowest d_i value, assuming the solution does not violate the optimization constraints (see below). Similarly, X_2 is found by replacing X_0 with X_1 and L_1 with L_2 in the above set of equations.

4.4.1.4 Optimization cost function and constraints for calculating optimal robot placement

To calculate the optimal robot placement X_0 with respect to the planned implant position, we minimise the maximum value in the vector $\mathbf{d}_{i=1\dots 5}$ for all cutting planes given a particular implant ($c_{i=1\dots 5}$) and robot (L_1 , L_2) geometry. To ensure that the robot is not placed such that any cut is positioned outside the workspace, we implement constraint equation (2.4). To ensure that the guide is not positioned within the bone for any cut, we implement constraint equation (2.5) for all five cuts.

$$X_0 \in \mathbf{R} \quad (2.4)$$

$$(b_i + c_i) \bullet d_i < 0 \quad (2.5)$$

For the distal cut, b_{distal} is a 2D vector that is collinear with the distal cut plane (y axis), starting from the anterior edge of c_{distal} to the most anterior point on the bone surface. Intra-operatively, this value would be obtained from a geometric or morphometric model of the femoral surface and the planned implant position. For the purposes of this study, we estimated $|b_{distal}|$ to be in the range of ~5–10mm from the geometry of various implant shapes and sizes. To be on the safe side, we use a distance value of $|b_{distal}| = 10\text{mm}$ for all implants. For all other cuts, we set $|b_i|$ equal to zero. In other words, we assume that the distal is made first, and that the posterior and anterior cuts (or secondary cuts) are made after their respective chamfer cut. We decided to make the distal cut first in our protocol since this is typical practice in TKA; it is more intuitive to start with the distal cut, and it permits the surgeon to gauge overall alignment before making the other cuts. Additionally, making a chamfer cut before the corresponding secondary cut allows the guide to be positioned slightly closer to the secondary cut plane edge than with a conventional cutting block.

4.4.1.5 Calculating optimal robot geometry

To determine how the geometric parameters L_1 and L_2 influence the gap distance d for a particular implant shape, we first calculate the optimal robot placement X_0 for each implant such that the maximum distance d_{max} is minimised for each implant. This is calculated for each combination of L_1 and L_2 (to the nearest millimetre) within a range of L values, and the cost function is then plotted in 3D. To limit the overall size of the two DoF motor unit, we chose a nominal value of 75mm for the upper bound (ub) of L_1 . To determine globally the optimal combination of L_1 and L_2 which results in the lowest d_{max} value, we minimise the largest d_{max} value for all implant shapes and sizes (Figure 4.8). In addition, we also calculate the combination of L_1 and L_2 that minimises the mean of all the d_{max} values for each implant shape.

4.4.1.6 Optimization tools

All routines were written in the MATLAB R12.1 programming language (The Mathworks Inc. MA, US), and all optimizations were carried out using the ‘*fmincon*’ function in the optimization toolbox. *fmincon* uses a ‘Sequential Quadratic Programming’ method (see help files for more information) to find the minimum of a constrained non-linear multivariable objective function. Convergence was checked using the *exitflag* option, and local minimums were avoided by plotting the objective function in the entire region of interest for several cases.

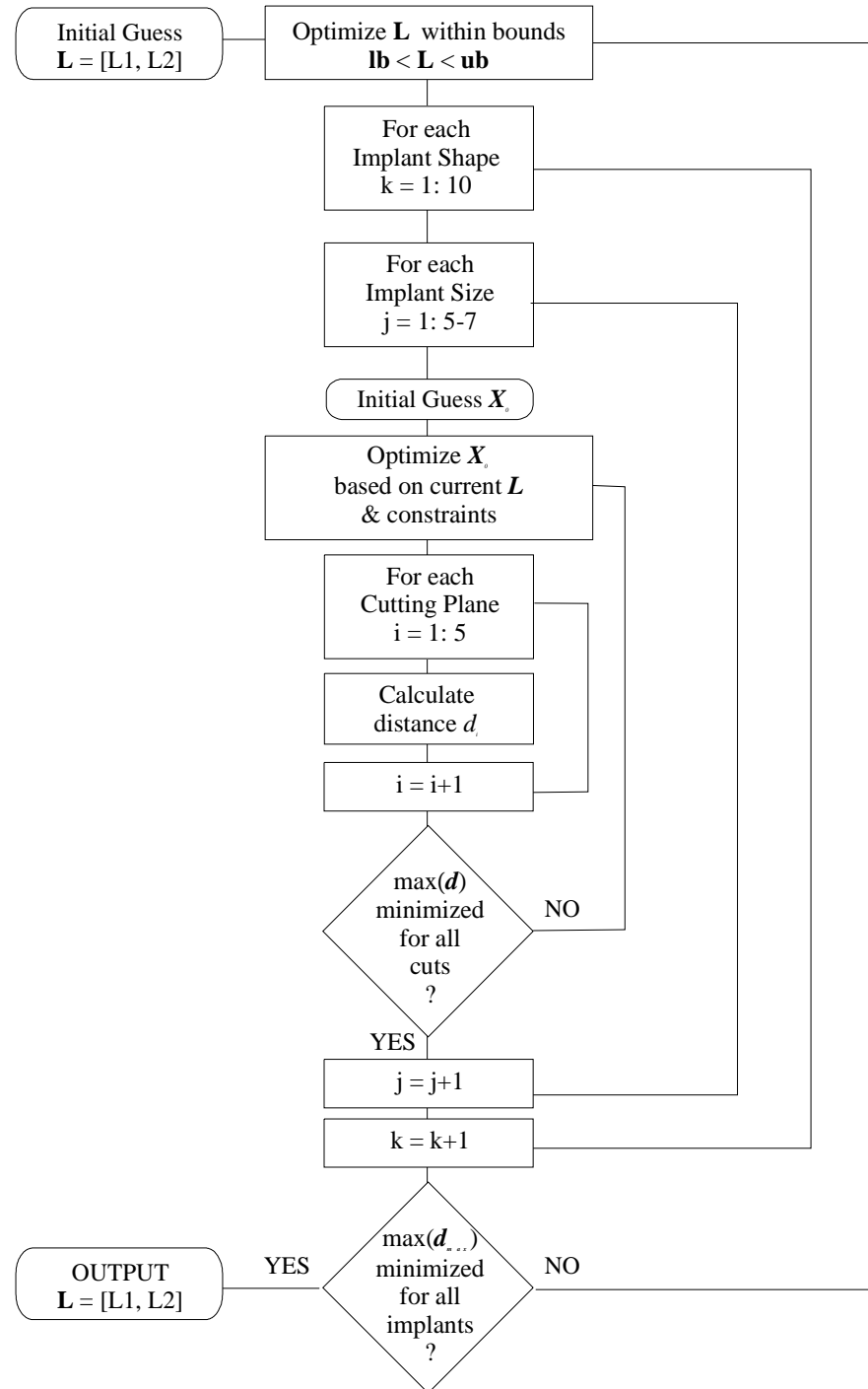


Figure 4.8. Optimization routine to determine the single combination of L_1 and L_2 that results in the lowest d_{max} value for all implant shapes and sizes.

4.4.2 Results

4.4.2.1 Optimal robot positioning

For our nominal prototype dimensions of $L_1 = 60\text{mm}$ and $L_2 = 30\text{mm}$, the optimal placement algorithm converged for all implant shapes and sizes, indicating that the robot workspace is sufficiently large to accommodate all implants tested. Table 4.3 summarises the maximum distance values (d_{max}) over all five cuts for each implant shape and size when the robot is placed at optimal position $X_{0,optimal}$. For most implant shapes, d_{max} generally increases by ~20-50% from the smallest to largest size, with the largest d_{max} values ranging from 7.6 to 15.4 mm among implant shapes.

Figure 4.9 illustrates how the optimal placement location $X_{0,optimal}$ of the prototype geometry changes with implant size for each implant shape. The optimal position generally migrates slightly anteriorly by ~2.8–5mm as each shape increases in size from smallest to largest (except for implant shape #4, which migrates posteriorly). Migration in the proximal/distal (x_0) direction is in the range of 0.5–3.3mm. The mean ($\pm SD$) of X_0 of all implant sizes is summarised in Table 4.4 for each of the ten shapes.

Table 4.3. d_{max} values [mm] for all implant shapes and sizes : $X_0 = X_{0,optimal}$, $L_1 = 60\text{mm}$, $L_2 = 30\text{mm}$, and $|b_{distal}| = 10\text{mm}$.

Size	Implant Shape									
	#	1	2	3	4	5	6	7	8	9
1	4.3	4.1	9.8	9.8	7.8	7.5	5.6	15.4	4.3	6.8
2	4.9	4.7	10.8	13.0	7.7	6.4	6.5	13.2	4.9	6.5
3	5.5	5.2	12.0	12.0	8.1	8.6	7.3	13.8	5.5	7.3
4	6.1	5.9	13.4	14.5	8.6	10.2	8.1	14.6	6.1	6.9
5	6.6	6.8	15.0	13.6	9.3	11.0	9.0	15.4	6.6	7.9
6	7.4	7.6	-	-	9.2	-	9.3	13.5	7.4	8.5
7	8.1	-	-	-	9.5	-	-	-	8.1	8.8
Max.	8.1	7.6	15.0	14.5	9.5	11.0	9.3	15.4	8.1	8.8
Ave.	6.1	5.7	12.2	12.6	8.6	8.7	7.6	14.3	6.1	7.5
SD.	1.4	1.3	2.1	1.8	0.8	1.9	1.5	1.0	1.4	0.9

Table 4.4 Mean ($\pm SD$) $X_{0,optimal}$ position values [mm] for all implant shapes : $L_1 = 60\text{mm}$, $L_2 = 30\text{mm}$, and $|b_{distal}| = 10\text{mm}$

X_0	Implant Shape #									
	1	2	3	4	5	6	7	8	9	10
x_0	-35.8 (± 0.3)	-35.4 (± 0.3)	-29.2 (± 1.0)	-33.3 (± 0.9)	-32.1 (± 0.6)	-34.0 (± 1.4)	-33.3 (± 0.2)	-29.2 (± 0.4)	-35.8 (± 0.3)	-32.0 (± 0.4)
y_0	1.6 (± 1.0)	2.5 (± 1.1)	3.6 (± 1.8)	6.0 (± 1.8)	3.1 (± 1.3)	5.9 (± 1.9)	2.0 (± 1.3)	2.6 (± 1.1)	1.6 (± 1.0)	0.8 (± 1.6)

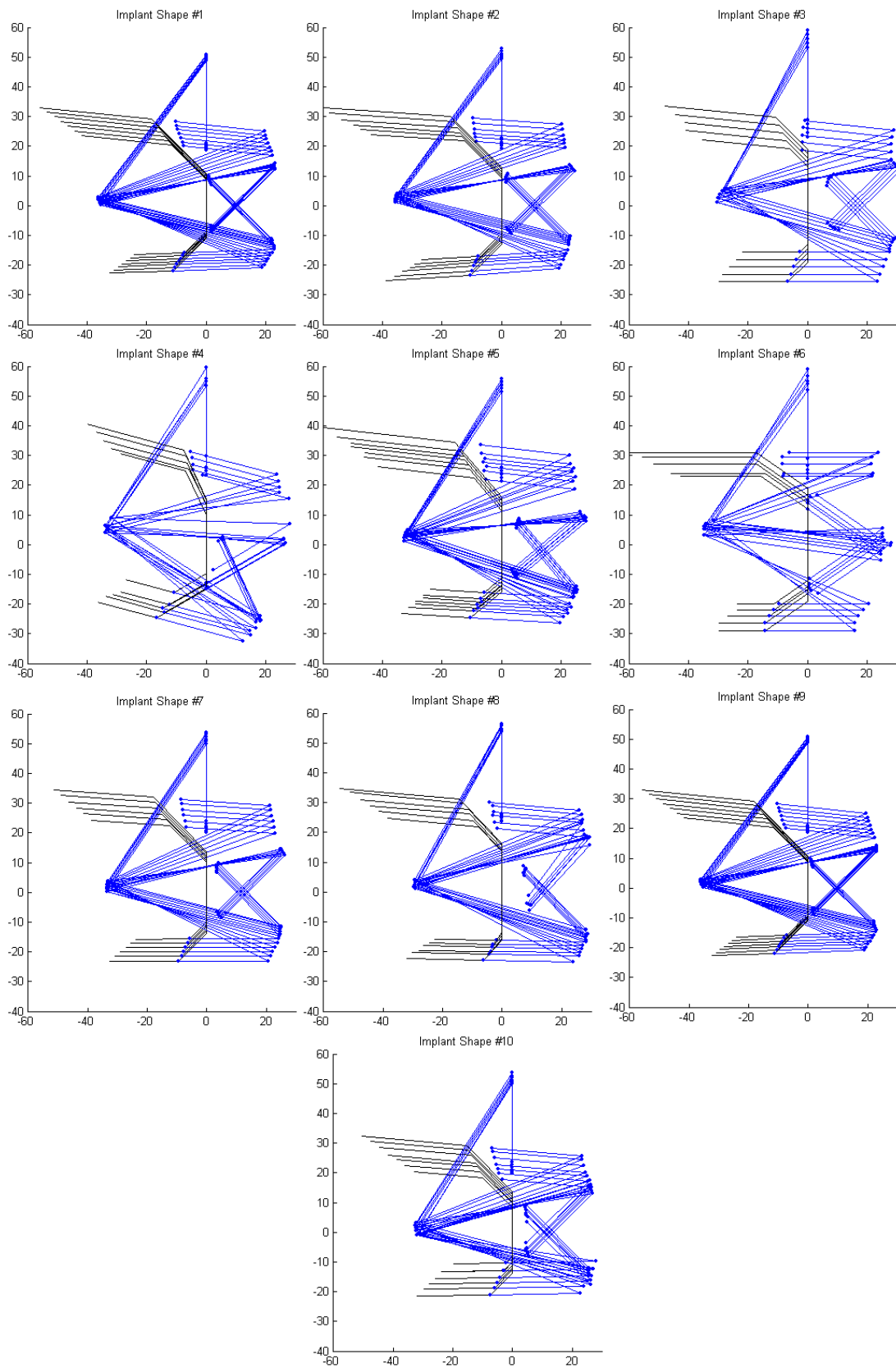


Figure 4.9. Optimal robot positioning and pose for all implant sizes, grouped by each shape : $L_1 = 60\text{mm}$, $L_2 = 30\text{mm}$, and $|b_{distal}| = 10\text{mm}$.

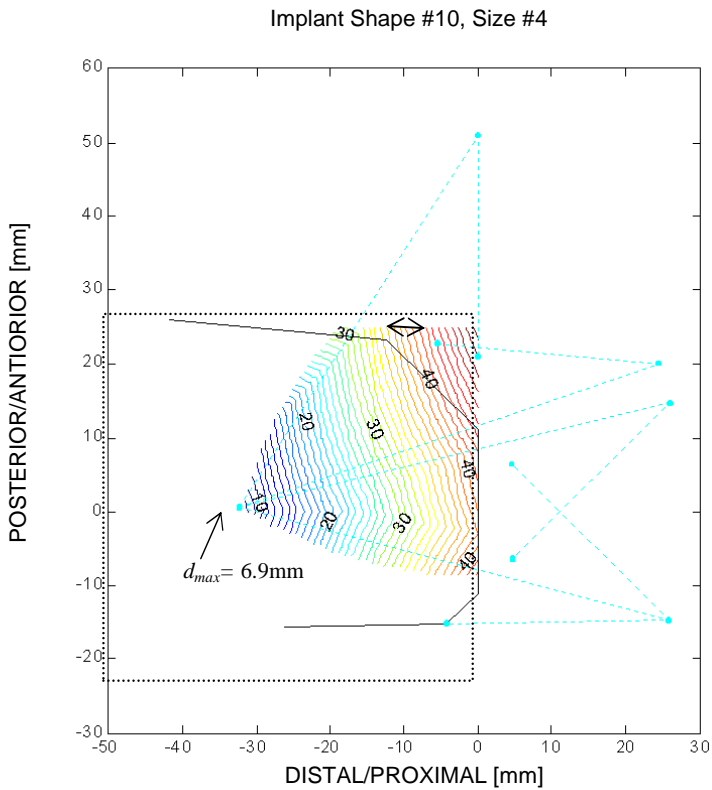


Figure 4.10. Contour plot of d_{max} values as a function of robot position X_0 for a typical implant. Contour lines are calculated within the bounds $(-50, -25) < X_0 < (0, 25)$ and are drawn at 1mm intervals ($L_1 = 60\text{mm}$, $L_2 = 30\text{mm}$, and $|b_{distal}| = 10\text{mm}$). The robot is shown in five configurations corresponding to the five cuts for the optimal position. The largest gap distance of $d_{max} = 6.9\text{mm}$ is for the anterior cut

4.4.2.2 Sensitivity of maximum distance value as a function of robot placement

Figure 4.10 illustrates on a typical implant size and shape how the maximum distance d_{max} changes as a function of robot placement within the bounds $(-50, -25) < X_0 < (0, 25)$. The non-plotted area within this box (i.e. outside the colour contour plot region) indicates X_0 placements that would result in either one or more of the five cuts lying outside the robot workspace, or the guide colliding with the bone for at least one of the five cuts. For all implants, the global minimum of d_{max} is located at the proximal limit of all possible X_0 positions.

Table 4.5 summarises the mean ($\pm SD$) $\partial d_{max}/\partial X_0$ gradient values at the optimal position $X_{0,optimal}$ of all sizes, for each implant shape. The average gradient for each implant shape is on the order of 1.1 and 0.4 mm/mm in the proximal/distal and anterior/posterior directions, respectively, with standard deviations generally <0.05 mm between implant sizes.

Table 4.5. Mean (\pm SD) $\partial d_{max}/\partial X_0|_{x_0_{optimal}}$ values over all sizes for each implant shape : $L_1 = 60\text{mm}$, $L_2 = 30\text{mm}$, and $|b_{distal}| = 10\text{mm}$

$\partial d_{max}/\partial X_0$ [mm]	Implant Shape #									
	1	2	3	4	5	6	7	8	9	10
$\partial d_{max}/\partial x_0$	1.04 ($\pm .005$)	1.03 ($\pm .003$)	1.21 ($\pm .049$)	1.02 ($\pm .054$)	1.11 ($\pm .004$)	1.00 ($\pm .00$)	1.03 ($\pm .004$)	1.16 ($\pm .038$)	1.04 ($\pm .005$)	1.04 ($\pm .019$)
$\partial d_{max}/\partial y_0$	0.36 ($\pm .043$)	0.38 ($\pm .039$)	0.21 ($\pm .049$)	-0.63 ($\pm .024$)	-0.37 ($\pm .004$)	0.37 ($\pm .035$)	0.42 ($\pm .050$)	0.33 ($\pm .063$)	0.36 ($\pm .043$)	0.28 ($\pm .027$)

4.4.2.3 Optimal robot geometry

Figure 5.3 illustrates how d_{max} changes as a function of robot geometry within the range of $40 < L_1 < 75$ and $5 < L_2 < 40$ mm for implant shapes 1 and 8 – implants that exhibit low (~8mm) and high (~15mm) d_{max} values, respectively, for the prototype geometry. Here, d_{max} is the maximum distance value of all five cuts and all five to seven implant sizes for each shape (i.e. row ‘Max.’ in Table 4.3).

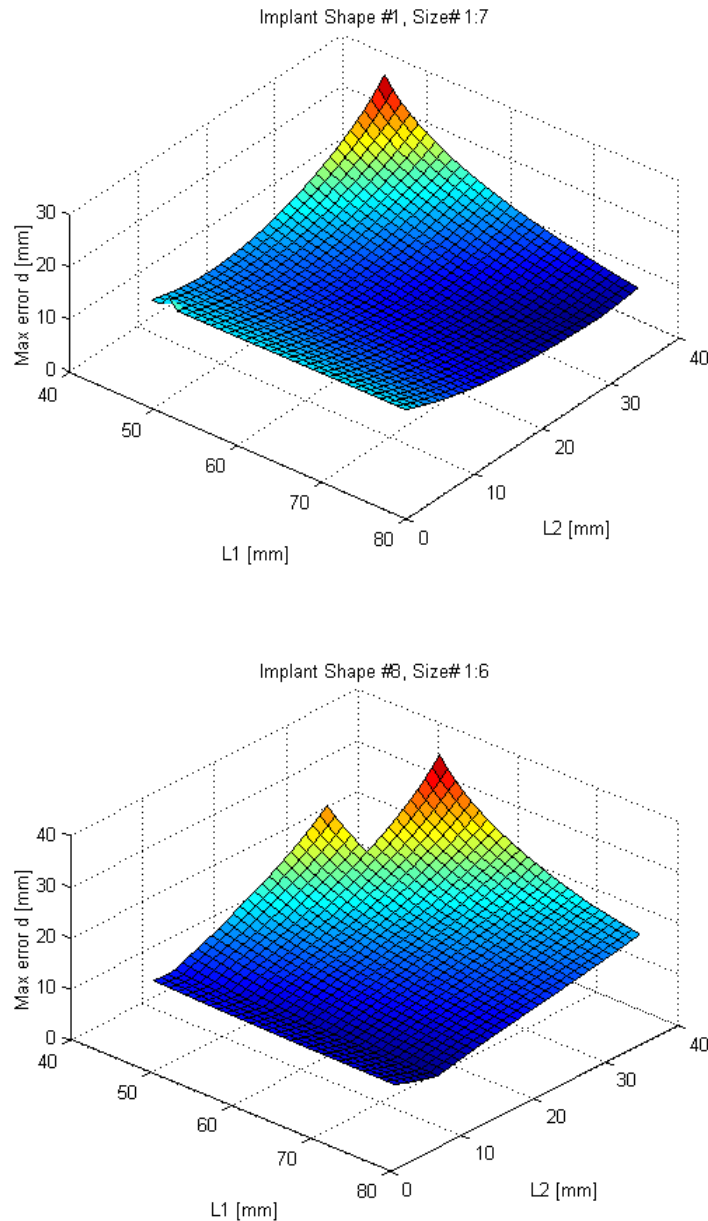


Figure 4.11 Cost function output (d_{max} values) as a function of robot geometry for implant shapes #1 and #8: $40 < L_1 < 75$ mm, $5 < L_2 < 40$ mm, and $|b_{distal}| = 10$ mm.

Table 4.6 Optimal individual robot geometries^{*} L_1 and L_2 [mm] with minimized d_{max} values [mm], and partial derivatives [mm/mm] at the optimal lengths for each implant shape.

[mm]	Implant Shape #									
	1	2	3	4	5	6	7	8	9	10
L_1	75.0	75.0	75.0	75.0	75.0	75.0	75.0	75.0	75.0	75.0
L_2	34.4	28.6	16.2	5.0	16.9	34.8	26.3	12.0	33.8	19.2
$Min(d_{max})$	5.1	4.07	4.11	10.7	3.7	6.3	5.3	6.8	5.1	5.2
$\partial d_{max}/\partial L_1$	-0.05	-0.16	-0.20	0.00	-0.02	-0.14	-0.15	-0.10	-0.05	-0.10
$\partial d_{max}/\partial L_2$	-0.05	0.00	0.33	0.00	-0.14	0.00	-0.00	-0.37	-0.05	-0.15

* $40 < L_1 < 75$ mm, $5 < L_2 < 40$ mm, and $|b_{distal}| = 10$ mm

For all shapes, d_{max} generally tends to increase as L_1 decreases and L_2 increases, with maximum d_{max} values in the range of ~30-50mm as L_1 and L_2 tend to 40mm. The minimum d_{max} for all implants is at the upper bound of $L_1 = 75$ mm, though the optimal length L_2 is different for each implant shape (Table 4). The particular robot geometry that resulted in the lowest global d_{max} for all implant shapes and sizes was found to be $L_1 = 75$ mm, $L_2 = 8$ mm, with a global maximum $d_{max} \sim 12$ mm for implant #6 (Table 4.7). The mean of all ten d_{max} values (i.e. the mean of the maximum gap distances for each implant shape) reaches a global minimum of 6.8mm at $L_1 = 75$ mm, $L_2 = 20$ mm (Table 4.7).

Table 4.7 d_{max} values [mm] for two ‘optimal’ robot geometries

Implant Shape #	$[L_1, L_2] = [75, 8]$ mm	$[L_1, L_2] = [75, 20]$ mm
1	11.1	6.1
2	10.1	4.9
3	6.4	5.1
4	11.0	14.2
5	6.6	4.3
6	11.9	8.9
7	10.5	5.7
8	8.4	7.5
9	11.1	6.1
10	9.1	5.0
max.	11.9*	14.2
mean	9.6	6.8*
$\pm SD$	1.9	2.9

*minimised value

4.4.3 Discussion

The optimal placement algorithm proved effective in reducing the maximum gap between the guide tip and bone to <10mm for 74% (45/61) of all implants considered, for our initial prototype robot geometry of $L_1 = 60\text{mm}$ and $L_2 = 30\text{mm}$. Our initial placement protocol for the cadaver experiments involved choosing a placement location that would result in collision free motion of the guide and the uncut bone surface when the cutting guide is fully retracted (i.e. when X_2 lies in the line X_0-X_1). Although this guarantees impingement free motion of the guide during positioning for all cuts, this fixation site typically results in placements in the area of $X_0 \sim [-20,0]$, which is generally in the 20mm maximum gap range for our prototype geometry (figures 4.10 and 4.3c). Gaps of this size could allow for considerable saw-blade deflection and skiving upon contact with the hard sclerotic bone at the start of the cut, especially with the sharply-curved surfaces of the femoral condyles [Laskin 1991, Krackow 1991, Minns 1992].

The results of this study suggest that overall d_{max} values for all implants could be even further reduced by increasing the distance between the two robot axes to our nominal upper limit of $L_1 = 75\text{mm}$. If we were developing a dedicated robotic tool to be used with only one implant shape, we could in theory reduce d_{max} to <7mm for almost any implant design by selecting the appropriate combination of L_1 and L_2 for a particular shape (9/10 implant shapes had d_{max} values within 3.7-6.8mm for their entire size range, Table 4.6). Since we are developing a universal robotic guide for TKA, however, we would prefer that our system be optimized for all shapes and sizes of implants. The particular robot geometry that resulted in the lowest global d_{max} for all implant shapes and sizes had a maximum d_{max} value of 11.9mm across all implants, though this design combination still produced 6/10 implant shapes with gaps >10mm (Table 4.7). Minimising the mean d_{max} value over all ten implant shapes resulted in a maximum gap value of ~14mm for one implant (#4), though the nine other implants all had d_{max} values <10mm (average $d_{max} = 6.8\text{mm}$, Table 4.7).

Taking into account, however, that the sensitivity of d_{max} is approximately directly proportional to robot placement in the proximal/distal direction (see figure 4.10), and that placement errors on the order of a few millimetres will likely be unavoidable in surgery, actual gap distances in practice could be considerably larger than those calculated in this study. Moreover, optimal placements were always located at the proximal tip of a ‘triangle-shaped’ zone of allowable placements (figure 4.10). This point would be a dangerous target to aim for since there is a high risk of mounting the robot outside of the boundary, in which case the surgeon would have to reinstall the device. Although creating a ‘safe zone’ somewhere within this triangle shaped region would reduce the risk of mounting out-of-bounds, this would further increase the maximum gap distance for all implants by ~1mm for each 1mm of malplacement. Even if the robot could be placed precisely as planned, however, the maximum gap distance can still be considerable for a significant number of implant shapes and sizes (16/61 or 26% >10mm for our prototype robot).

Although adding a manual sliding DoF in the cutting plane may increase the complexity of the device design and of the surgical procedure if the surgeon has to manually extend and retract the guide before and after each cut, this alternative does have several advantages as listed below:

Advantages of adding a manual sliding joint in the cutting plane :

- eliminate the gap distance completely for all femoral cuts for all implant sizes and shapes
- give the surgeon greater freedom in choosing the robot fixation site and saving time
- reduce the risk of installing the robot such that the guide is positioned within the bone or the planned implant position is outside of the robot workspace
- can make L_1 very compact (~40mm), thus reducing the overall size and weight of the 2-DoF motor unit

Another potential advantage is that we could avoid having to navigate the initial placement of the robot on the femur (figure 4.3b), and thus avoid having to install a separate rigid body on

the femur. If the range of the manual adjustment mechanisms are made large enough such that the pin-bases could be manually installed within this range (perhaps with the aid of an extra-medullary jig), and if we could ensure that the pin-bases are designed so that they are adequately stable during the sawing process, we could incorporate a rigid body directly into the design of the pin-bases and navigate the guide-pose after the femoral registration and planning phases are complete. Considering that fixation of the rigid bodies is invasive and time-consuming [Marchant 2004], this option certainly adds considerable benefit to the overall procedure.

4.5 Conclusions and Recommendations

We have designed and developed a novel robot for positioning sawing and milling guides in conventional TKA. The robot is compact enough such that it can be mounted directly on the bone, thus eliminating the need to immobilize the leg to the operating table, and measurements of the robot compliance show that the device is stiff in comparison to the values reported in the literature for other table mounted robots [Matsen 1993]. However, the accuracy of robot positioning needs to be addressed by (1) eliminating the need to fix the robot base to the bone after it is adjusted in the frontal and transverse planes (2) reducing the mechanical backlash of the motorized 2 DoF positioning device, and (3) improving the calibration procedure. In addition, to reduce the surgical exposure required to mount the robot on the bone, the fixation should be from only one side. This would allow minimal incision into the extensor mechanism and eversion of the patella.

Although optimising the robot geometry and placement reduced the need for having an additional sliding DoF in the cutting plane, the advantages of the latter alternative seem to outweigh the drawbacks, adding considerable robustness, precision, and overall benefit to the procedure. We therefore recommend that an extendable or ‘telescopic’ sliding cutting guide be incorporated into the design of the saw-guide, and that the design of the motor unit be made as small as possible. The results of the optimization study are therefore useful for determining the corresponding dimensions and range of motion for the telescopic saw-guide, and the optimization model is can be used for minimizing the size of the telescopic guide.

Chapter 5: Robot Redesign for Minimal Access TKA

5.0 Chapter Summary

In the previous chapter we presented our initial prototype robot for open TKA. In this chapter we present our second prototype version for minimally invasive TKA. The design refinements that were necessary based on our experience with the previous prototype are presented and evaluated. These included (1) redesigning the fixation and adjustment systems such that the robot mounts on only one side of the femur (2) redesigning the side milling technique for better milling control and accuracy, and (3) improving the accuracy and safety of positioning with the motorized guide and reducing its overall size and weight. To address (1) two new fixation techniques, one using two threaded pins inserted bicortical and the other using two threaded pins inserted through a short intra-medullary rod, are tested on demineralised pig bones to evaluate their compliance in a range of bone qualities. For (2) a novel side-milling technique is developed that uses passive 2 DoF guide having one linear and one rotational DoF. This technique is also applied to the tibial cut using a 3 DoF tibial cutting guide. To improve the accuracy and safety of the 2 DoF motor unit, backlash-free Harmonic Drive gears and a spring loaded brake mechanism are integrated into the design and tested. Finally, a proposed surgical technique and some first experiences using the new device on saw-bones and cadavers are presented.

5.1 Introduction

In “open” total knee arthroplasty (TKA) the standard anterior/midline approach uses a 25-30cm skin incision that extends proximally from just distal to the tibial tubercle level, followed by a medial 20-30 cm parapatellar arthrotomy which extends superiorly through the quadriceps tendon (figure 1.4). Although the incision allows for lateral eversion and dislocation of the patella, dividing the quadriceps muscle can cause [Tria 2003]

- increased pain,
- increased blood loss,
- increased time to ambulation,
- prolonged hospital stays
- prolonged rehabilitation,
- decreased range of motion
- decreased knee strength.

More and more surgeons now are beginning to use MIS techniques for TKA, some of which preserve the quadriceps mechanism entirely, while others make a small incision along the fibres of the vastus medialis to facilitate patellar subluxation [Tria 2003][Bonutti 2004]. Femoral cuts are made from the anterior or medial side through a 6-14cm ‘mobile’ incision that is moved to expose different aspects of the joint by flexing and rotating the knee. A typical exposure is illustrated in figure 5.1.

Although bone-mounted robotic systems have great potential to improve bone-cutting precision in TKA, current systems require substantial incision of the quadriceps muscle and reflection of the patella in order to rigidly fix the robot to the three sides (medial, lateral, anterior) adjacent to the bone cutting area.



Figure 5.1 Actual incision and exposure obtained in less invasive TKA procedures.

5.1.1 *Objectives*

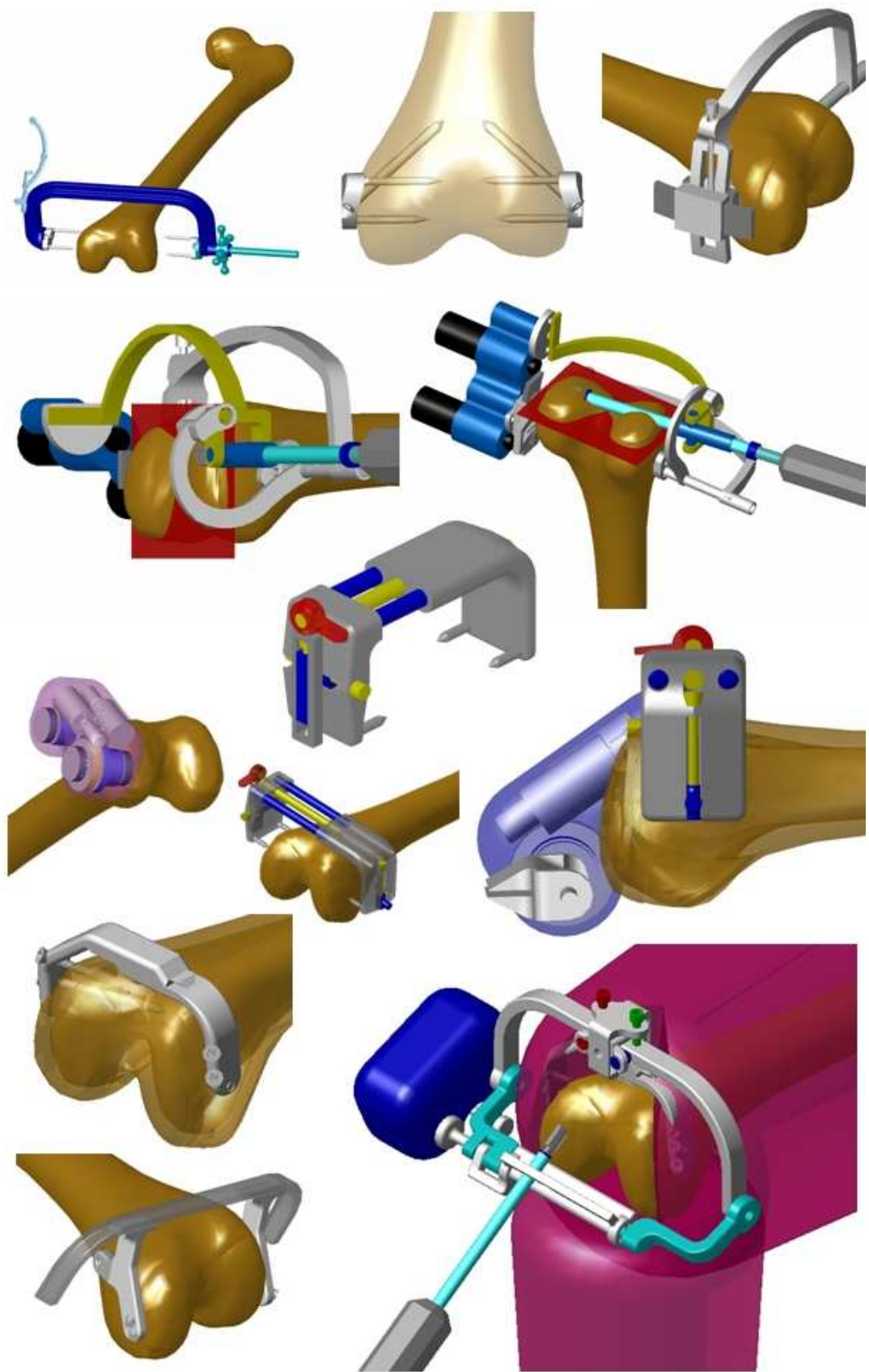
Our goals are to refine the design of our initial miniature robotic guide positioner such that it is sufficiently light and compact enough that it can be mounted on the medial side of the knee, and can precisely position a milling tool guide such that the approach follows the “mobile window” for each of the five femoral cuts.

5.2 Second Robot Concept and Prototype Development for MIS TKA

From our preliminary feasibility experiments on cadavers with our first prototype, we found that the usability, visibility and stability of the guide during cutting were in general very satisfactory. However, it was evident that a number of modifications had to be made to use the devise in minimally invasive TKA. These included:

1. redesigning the fixation and mechanical adjustment systems such that the robot could be mounted only on one side of the bone, completely within the MIS incision with minimal disruption of the surrounding soft tissues
2. redesigning the passive milling tool guide to improve milling ergonomics and kinematics
3. improving the accuracy and safety of positioning with the motorized guide and reducing its overall size and weight
4. improving the precision of the calibration procedure

After numerous conceptual design iterations (some of which are shown in figure 5.2), we settled on the design presented in figure 5.3 for our new robot version for MIS surgery. The following sections describe in more detail the abovementioned design refinements for our final chosen design illustrated in figure 5.3.



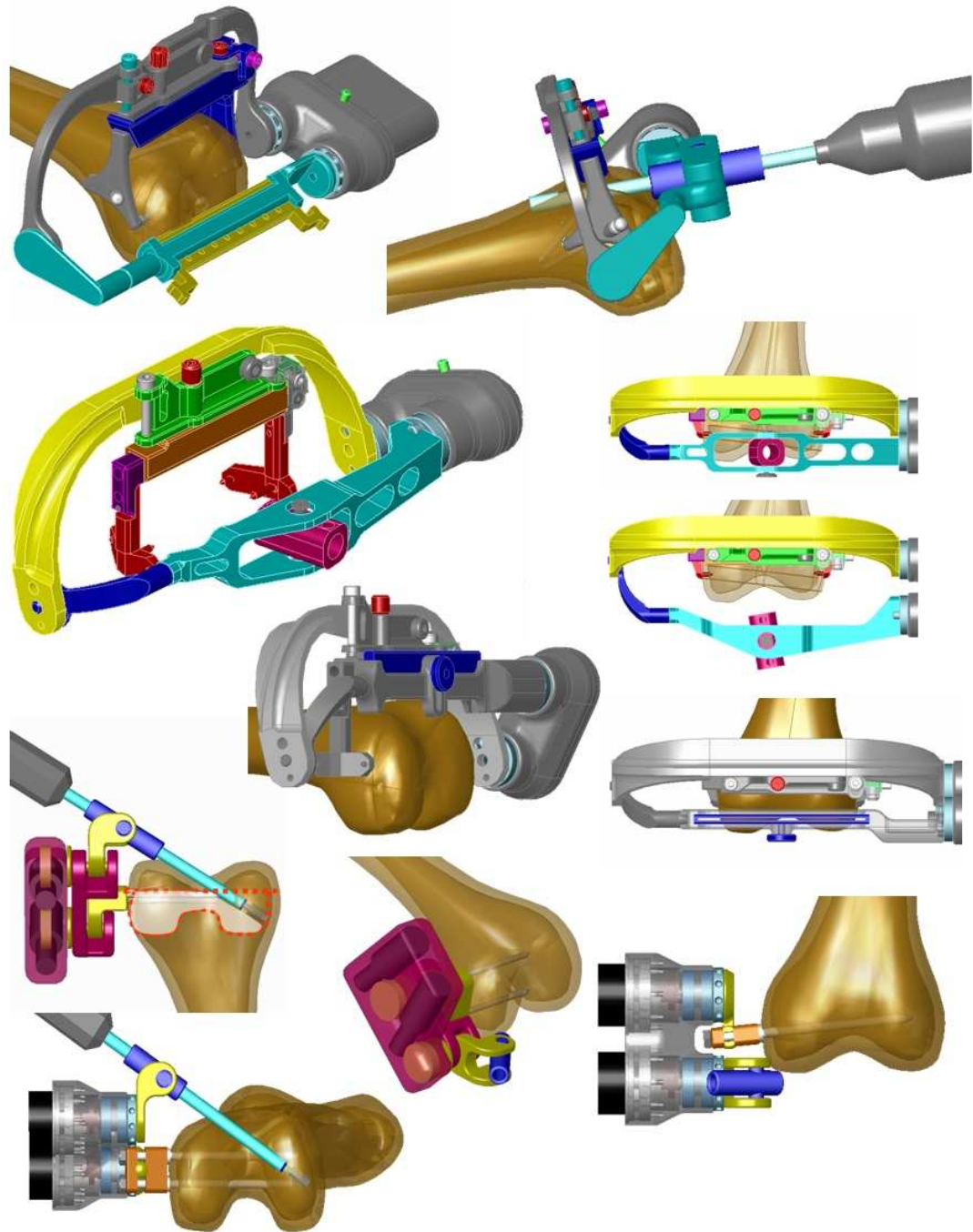


Figure 5.2 Various designs considered during the evolution of the robot.

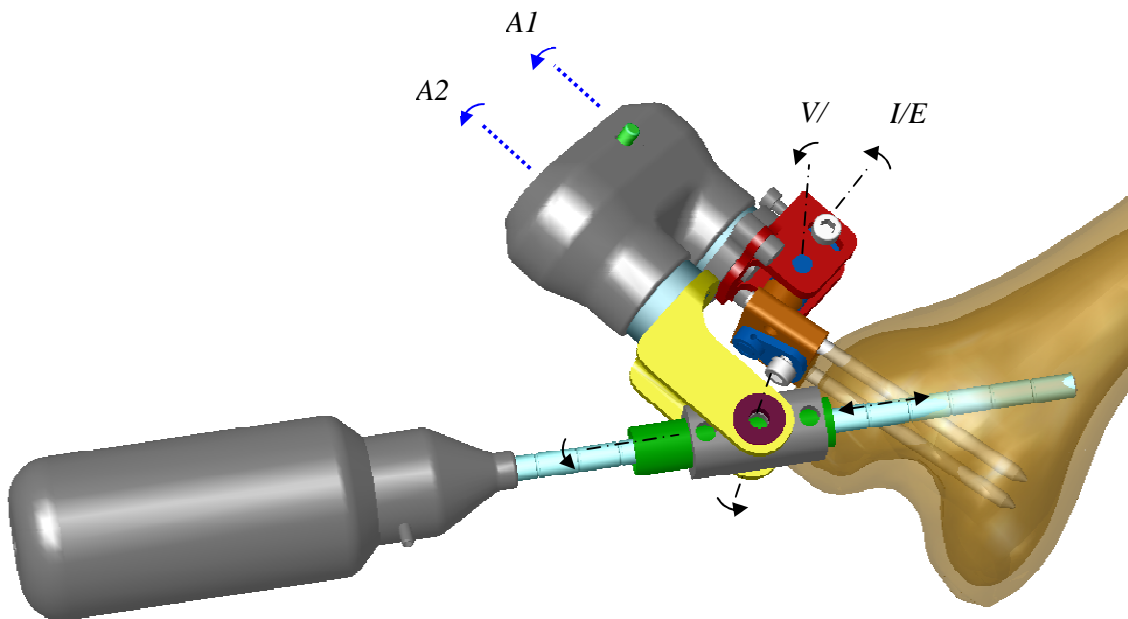


Figure 5.3 CAD model illustrating the various manual (—•—) and motorized (.....) DoF of the second version of the Praxiteles robot for minimal access TKA.

5.3 Redesigning the Fixation and Mechanical Adjustment Systems

To make our prototype system compatible with the constraints of MIS TKA, we reduced the size of the 2 DoF manual adjustment and fixation system so that we could attach it only to the medial side of the bone using two pins (percutaneous fixation on the opposite side could cause vascular issues or nerve injury). The adjustment system is similar to a universal joint, with two lockable rotational axes arranged perpendicular to each other (figure 5.3).

There are two possible methods to realise the fixation: (1) **Bicortical 2 pin**: the two threaded pins are inserted bicortically, i.e. all the way through the femur such that they pierce the far cortex; (2) **Augmented 2 pin**: a short ‘intramedullary’ rod is inserted into the bone first, and then the two threaded pins are driven through the two holes in the rod (figure 5.4). The latter method was intended to augment and stabilize the fixation in patients with severe osteoporoses where bone quality is very soft and weak. The device was designed to guide the insertion of the pins through rod in the central area of the femur, and to help ensure that the pins do not intersect any of the five femoral cutting planes. Additionally, this system avoids the requirement of having to insert the pins bicortically, which can be difficult if the lateral side is not exposed. The intramedullary rod is modular with available lengths of 4 and 7cm.

5.3.1 Experiments on fixation rigidity

We conducted an experimental study in animal bones in order to assess the rigidity of the two different fixation techniques in different bone qualities.

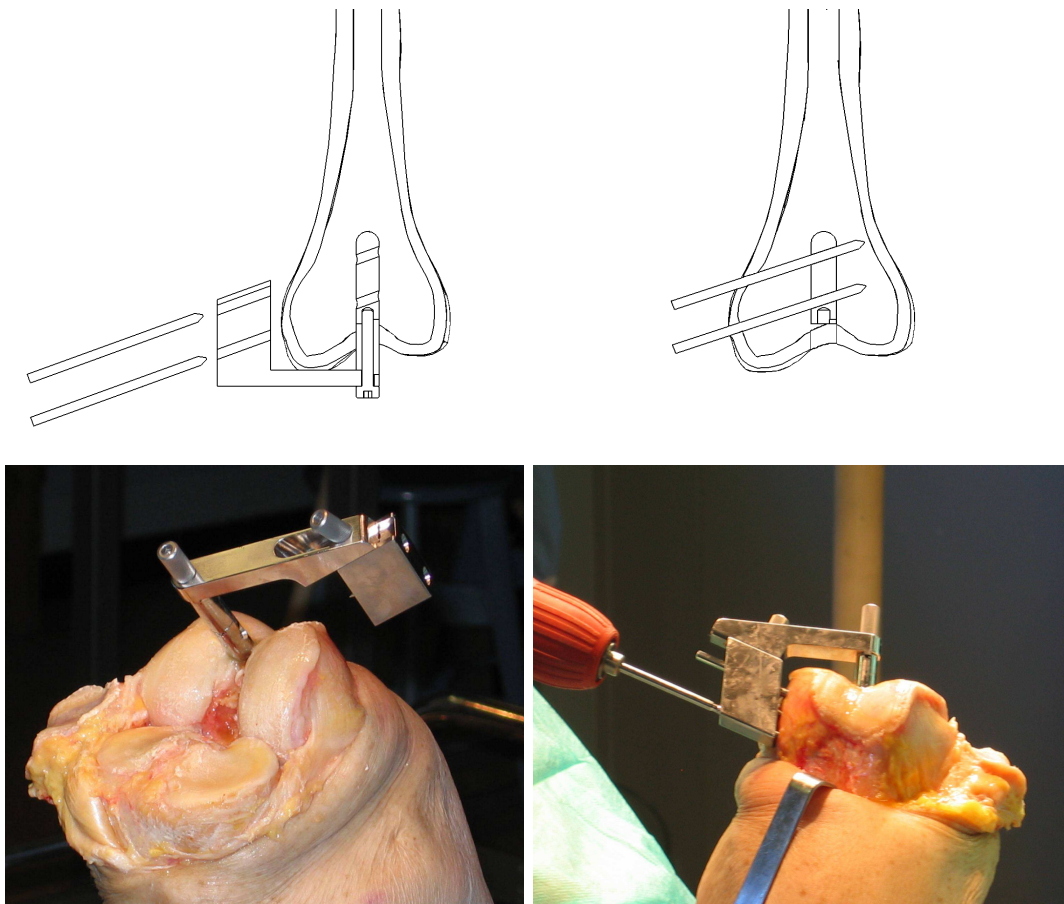


Figure 5.4. Conceptual drawings (top) and cadaver photos (bottom) of the *Augmented 2 Pin* fixation: a short 'intramedullary' device used to augment the two pin fixation and guide the insertion to prevent intersection with femoral cutting planes.

5.3.1.1 Materials and methods - specimen preparation

To approximate the conditions of soft or weak bone, six fresh porcine knees (tibias and femurs) were obtained and demineralised to various degrees by soaking them in decalcification solution (formic acid). The first pair of specimen were soaked for one day, the second pair for two days, and the third pair for three days. Dual energy X-ray absorptiometry (DEXA) was then used to quantify bone mineral density (BMD) after demineralisation in one specimen from each of the three pairs (i.e. specimen numbers 1, 3 and 5 were scanned and numbers 2, 4, and 6 were not scanned but were assumed to have similar BMD values since they were soaked for the same amount of days). In addition, DEXA scanning was also performed in one non-demineralised specimen for comparison (specimen number 0, table 5.1, figure 5.5).

Bone mineral density measurements have been correlated to the ultimate compressive strength in human vertebral trabecular bone [LANG 1998], so we assumed that significant demineralization would produce a similar effect in our porcine specimens. It should be kept in mind however that results obtained on porcine bone are not applicable to humans and that these data are only useful for comparison purposes and for getting a rough estimate of guide compliance.

Two 4mm diameter self-taping surgical bone pins were inserted into the medial/lateral side of each femur using a low-speed drill without drilling a pre-hole. The threaded pins were inserted in parallel

with an inter-axis distance of 20mm, ~20mm proximal to the distal condyle and rotated anteriorly by ~15° in the transverse plane. The drill guide was designed so that the pins are 20° to the axis of the intramedullary rod. Only the 7cm long version was tested. Each specimen within each pair was instrumented with either 2 bicortical pins ('**Bicortical 2 pin**') or with 2 pins augmented with the intramedullary rod ('**Augmented 2 pin**') but did not pierce the far cortex. A bolt was inserted mediolaterally through a hole drilled in the diaphysis, and the bolt was clamped in a vice with the posterior aspect of the distal femur resting on the vice jaws. The orientation of the femurs in the vice approximated those commonly found in a TKA procedure. A rigid body "F" was attached to the opposite side of the distal femur with two 3mm diameter bone pins (figure 5.6). Care was taken not to interfere with the guide fixation pins. A second rigid body "G" was rigidly attached to the guide block base used to insert the pins, and a clamp was secured to the guide block from which a 1.3kg liquid container could be supported. The point of load application was not directly beneath the fixation base which resulted in an applied force and moment, though the relative direction of the offset may have varied somewhat for each specimen due to variations in the specimen orientation with respect to the gravity vector.

Table 5.1
BMD values as a function of duration in decalcification solution

Specimen n°	Duration [Days]	BMD [g/cm ²]	Fixation Technique
0	0	0.918	-
1	1	0.721	Augmented
2	1	-	-
3	2	0.674	Bicortical
4	2	-	Augmented
5	3	0.520	Bicortical
6	3	-	Augmented

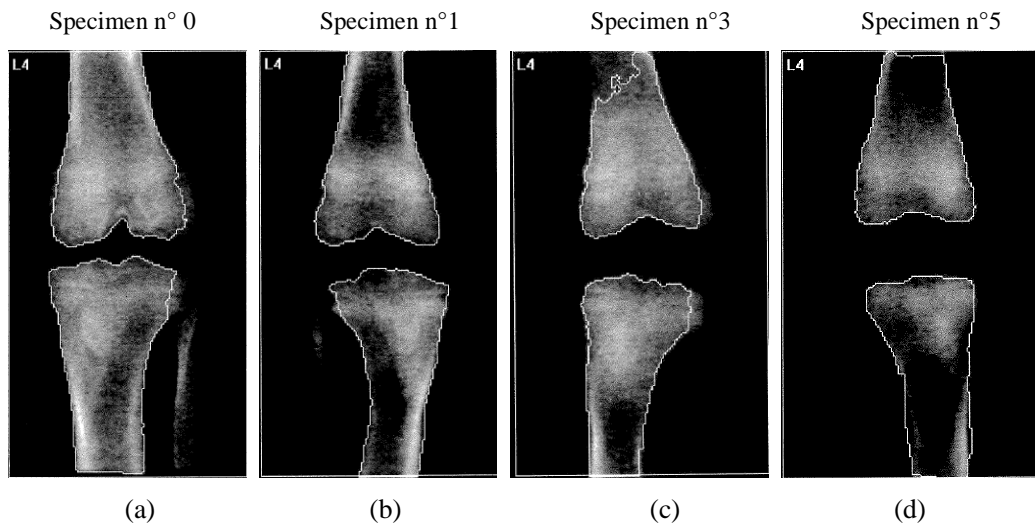


Figure 5.5 DEXA scan images of porcine knee specimens: non-decalcified (a); and decalcified for 1 (b); 2 (c); and 3 (d) days.

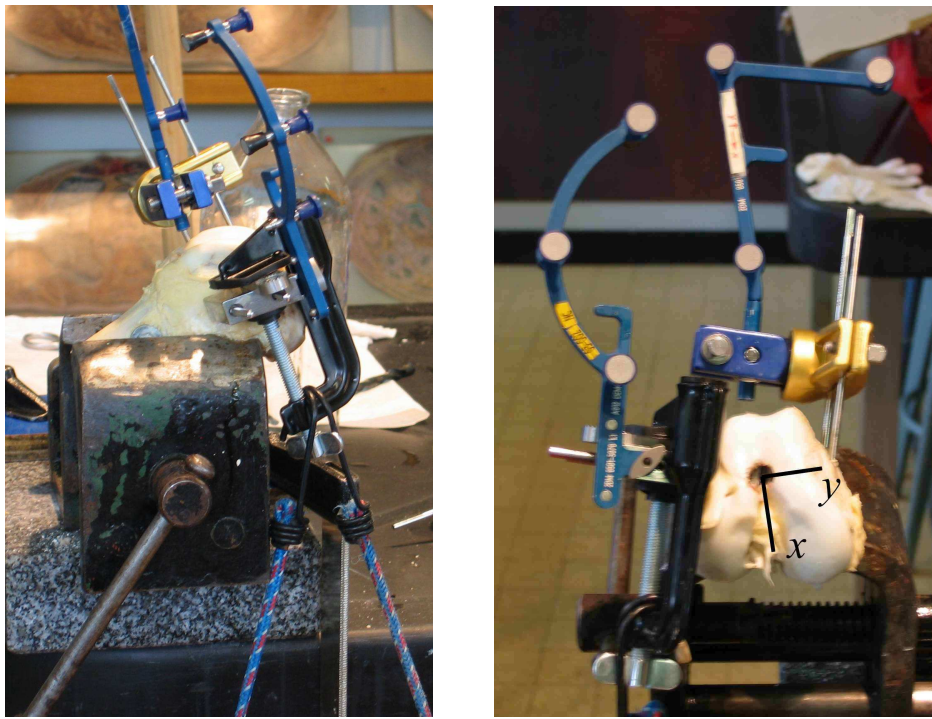


Figure 5.6. Experimental setup for load vs displacement measurements (left) and coordinate system (right) used to report the results.

5.3.1.2 | Measurement coordinate system and data collection

All results are reported in a bone coordinate system nominally aligned to the bone anatomy with x pointing posteriorly, z pointing distally and y pointing away from the fixation base. Water was poured into the container at intervals of 0.5 litres until $\sim 200\text{N}$ and the position of the G rigid body was recorded with respect to the reference frame of the F rigid body. The collected position and rotation data was averaged over several measurements (typically 10-30) after each load application, and is presented as the difference from the initial position with no load applied (i.e. before the 1.3kg container was mounted on the base). The position/rotation vs applied load data were fit with straight lines having an unconstrained y intercept, where: dP , dx , dy , dz [mm] are the magnitude ($dP = [x^2 + y^2 + z^2]^{1/2}$) and the three components in x , y , and z , respectively, of the displacement vector of a point near the outside edge of the base block, and dRx , dRy , dRz [$^\circ$] are the Euler angles in x , y , and z , respectively.

5.3.1.3 | Results

The load vs. displacement and load vs. rotation curves for each test are presented in figure 5.7a,b. The linear regression equations and square of the correlation coefficient (R^2) are presented in Table 5.2. One specimen failed by fracture in the diaphysis at the bolt hole made for clamping the specimen in the vice (specimen n° 4 – augmented 2 pin fixation, 2 day decalcification), while another specimen was not tested (specimen n° 2 – 2 pin fixation, 1 day decalcification) due to the time constraints of the facilities in the Grenoble anatomy department where the experiments took place. None of the other specimens failed during the tests.

Displacements magnitudes at 100N and 200N ranged from ~ 0.6 - 1.5mm and ~ 1.2 - 3.0mm , respectively, depending on the number of decalcification days. There was a significant increase in the slope of the

displacement magnitude dP vs. load curve from $K = 0.0026$ to $K = 0.0154$ [N/mm] between the two and three day decalcified specimens for the augmented 2 pin fixation due to the increased deflection in the x direction for this specimen (figure 5.4b). Rotational stiffness was proportionally different in the z and x directions for the two and three days specimens for both fixation techniques, with dRx being higher in the three day bones. This could be due in part to slight variations in the orientation of the specimen (i.e. the flexion angle) with respect to gravity.

Table 5.2 Linear regression coefficients ($y = m x + b$) and square of the correlation coefficients (R^2) for the fixation compliance tests

Days	Dir.	Displacements						Rotations					
		Augmented			Bicortical			Augmented			Bicortical		
		m	b	R^2	m	b	R^2	m	b	R^2	m	b	R^2
1	x	.0035	.0445	.930				.0018	.0022	.568			
	y	.0007	.0181	.512				.0024	.0171	.4735			
	z	.0012	.0049	.365				.0043	.0371	.8175			
	dP	.0030	.0615	.900									
2	x	.0031	.2394	.777	.0079	.1902	.959	.003	.0638	.7299	.0052	.2171	.8498
	y	.0013	.000	.570	.0007	.0262	.346	.0031	.047	.5295	.0017	.0027	.4598
	z	.0032	.1118	.541	.0035	.0631	.802	.0036	.4065	.6626	.0099	.1574	.9770
	dP	.0026	.1815	.679	.0084	.1928	.9657						
3	x	.016	-.113	.997	.0074	.1857	.964	.0169	.1425	.9978	.009	.2844	.9837
	y	.0023	-.053	.919	0	.0491	0	.0016	.0165	.541	.0004	.0473	.1435
	z	-.0002	.0924	.055	.0026	.0828	.633	.0116	.1210	.9974	.0051	.1167	.8982
	dP	.0154	.1168	.996	.008	.1687	.958						

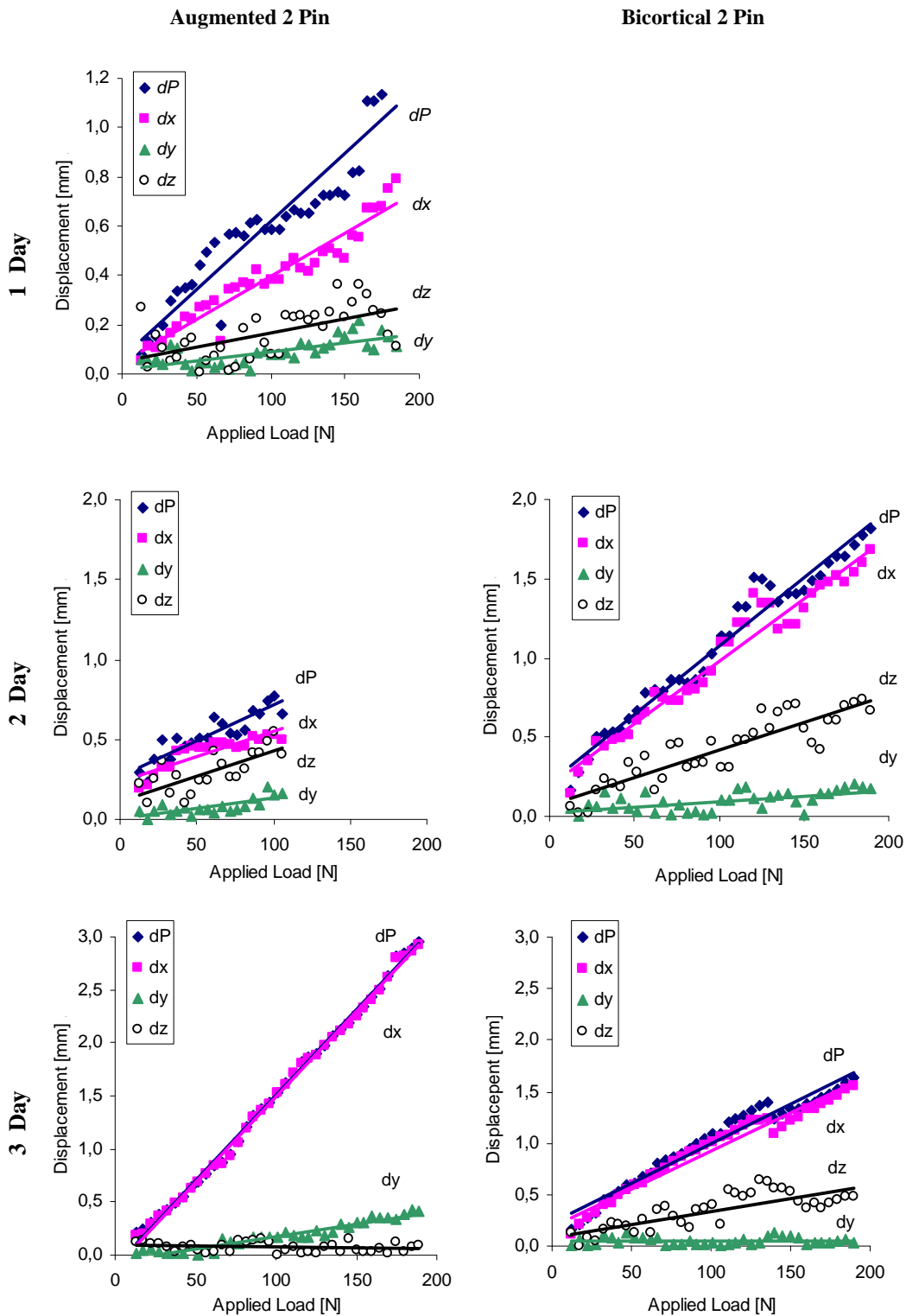


Figure 5.7a Displacement [mm] v.s. applied load [N] curve for the augmented 2 pin and the bicortical 2 pin fixation tests in the 1, 2 and 3 day decalcified bone specimen.

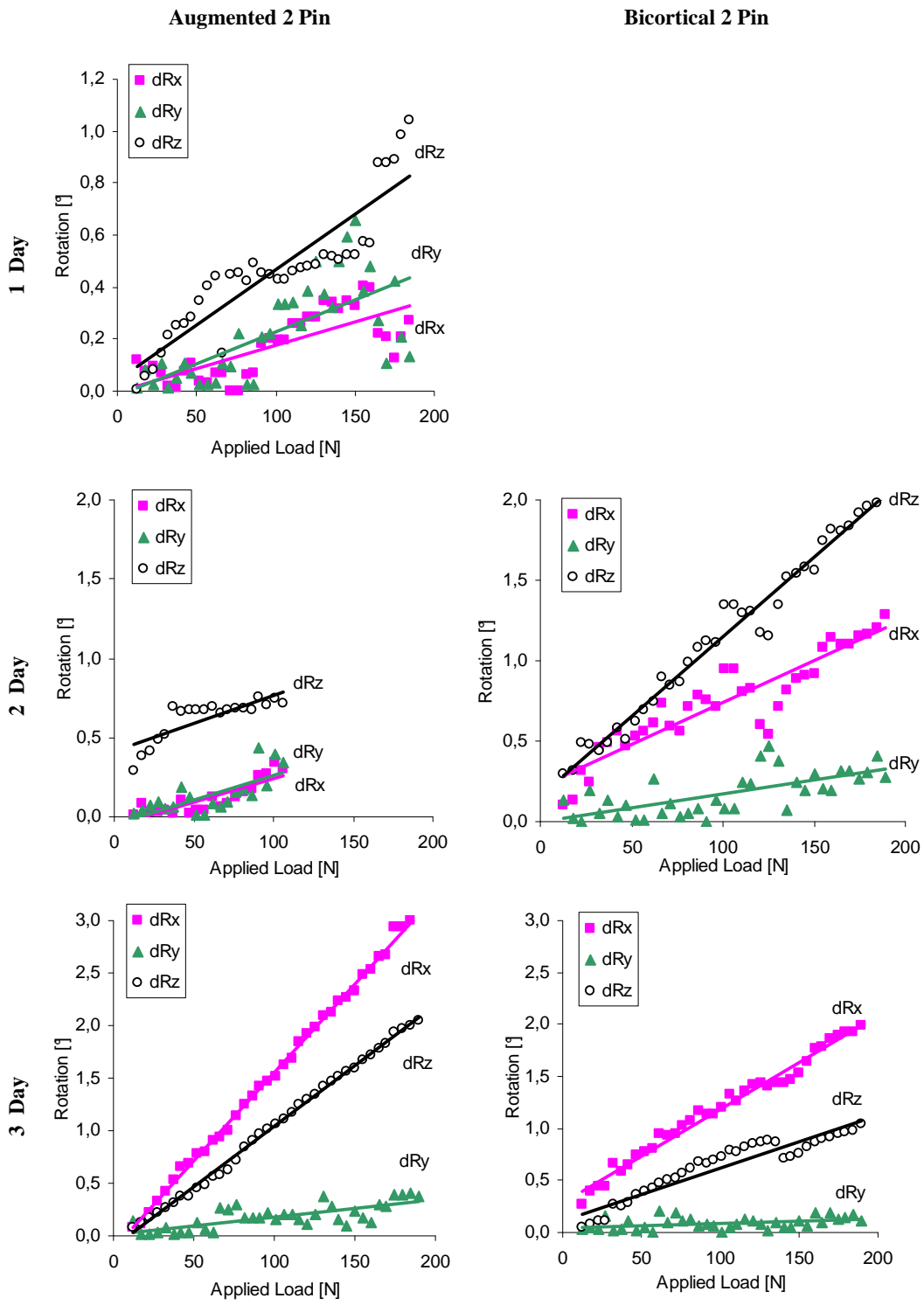


Figure 5.7b Rotation [$^{\circ}$] vs. applied load [N] curves for the augmented 2 pin and the bicortical 2 pin fixation tests in the 1, 2 and 3 day decalcified bone specimen.

5.3.1.4 Discussion

The two different fixation techniques performed comparably in the two day decalcified bones, while the bicortical 2 pin fixation performed slightly better in the three day decalcified specimens. We had expected that the augmented 2 pin fixation would have preformed better in the very soft bone specimens. Two possible reasons for this include:

- 1) The mechanical play between the pins and the intramedullary rod was large enough to cause movements on the order of a few millimetres at the far extremity of the pins
- 2) The pins were not inserted far enough into the bone specimens (i.e. bicortically), which is a critical parameter for obtaining good fixation stability in soft bone.

With regard to 1), the holes the intramedullary rod must be slightly larger than the diameter of the pins to permit a smooth engagement of the self tapping pins with the rod without producing wear particles during the drilling. Because the hole depth-to-diameter ratio is rather small (~2) however, the resulting angular play of the pins is on the order of ~2°. One possible method to reduce this play without reducing the hole size is to rotate the rod axially within the bone once the pins have been inserted. Turning the rod in direction of external rotation for example would take up the pin play in the posterior direction (i.e. in the primary direction of the load) for pins placed in the medial side.

If we assume that average forces applied to the fixation base in surgery are on the order of ~50N, the results of this study indicate that average displacements would be on the order of ~0.5 mm/° for normal or even ‘soft’ bone quality with either fixation technique.

It should be noted that although the bone stiffness was significantly reduced with the reduced BMD of the specimen, the effect on the failure properties of the specimen is not known. It was observed that the demineralized bones did not seem brittle in nature, and the 3 day decalcified specimens resembled somewhat elastic or rubbery structures which exhibited considerable elastic deformation when twisted or bent. It is recommended therefore that the risk of fracture of both fixation techniques be investigated in further experiments on human osteoporotic bone (fresh cadaveric). Although this would be optimal, such specimens were not available to us during the course of this study.

5.4 Improving the Accuracy and Safety of Positioning with the Motorized Guide and Reducing its Overall Size and Weight

Although the system backlash in the robot 2 DoF motor unit did not significantly influence the position reproducibility tests on our first prototype, this play becomes more problematic during actual cutting with a vibrating sawing or milling tool. Vibrations from the sawing or milling tool could cause the entire guide to vibrate within the 0.4° backlash range while making the cut (Table 4.2). To stay within our specified precision goal of <0.1° for positioning in the sagittal plane (from §2.2.1), it was necessary to investigate more precise gear solutions for our second prototype.

Harmonic drives are a compact alternative commonly used for high precision/ratio/torque applications. The gears are comprised primarily of three components (figure 5.8): a fixed rigid circular spline, an elliptical wave generator (gear input), and a deformable flexspline (gear output). The flexspline has a slightly smaller outer diameter with two fewer teeth than the inner diameter of the circular spline. The elliptical wave generator causes the flexspline to deform and engage the circular spline in the two areas at the ellipse’s major axis. Thus one revolution of the wave generator input causes the flexspline to rotate in the opposite direction, by a value equal to two tooth pitches. Backlash is extremely low and torque capacity is high because of the large tooth engagement area as compared to planetary spur gears of comparable size.

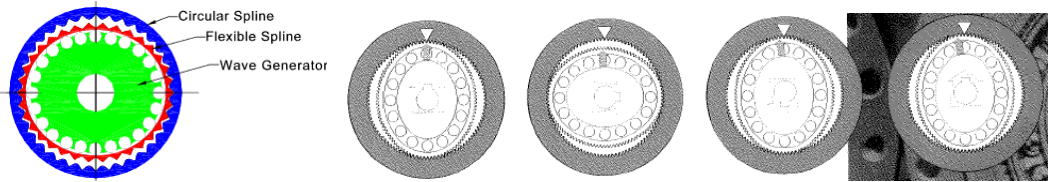


Figure 5.8 Harmonic Drives - Principle of operation (from the Harmonic Drives® catalogue)

We selected a small ($\varnothing 30 \times 22\text{mm}$) component set that had a high reduction ratio (100:1) and torque capacity (4.8 and 9 Nm maximum for repeated and momentary peak torque, respectively). Based on a torsional stiffness calculation using empirical data from the manufacturer's catalogue, this gear should yield a deflection of $\sim 0.1^\circ$ for an applied torque of 2 Nm (figure 5.9a), equivalent to our nominal load bearing limit specified in §2.2.2. For a load applied at 40mm from the first robot axis (ie. at the milling guide), the corresponding deflection in the normal direction (i.e tangential to the radius) is presented in figure 5.9b.

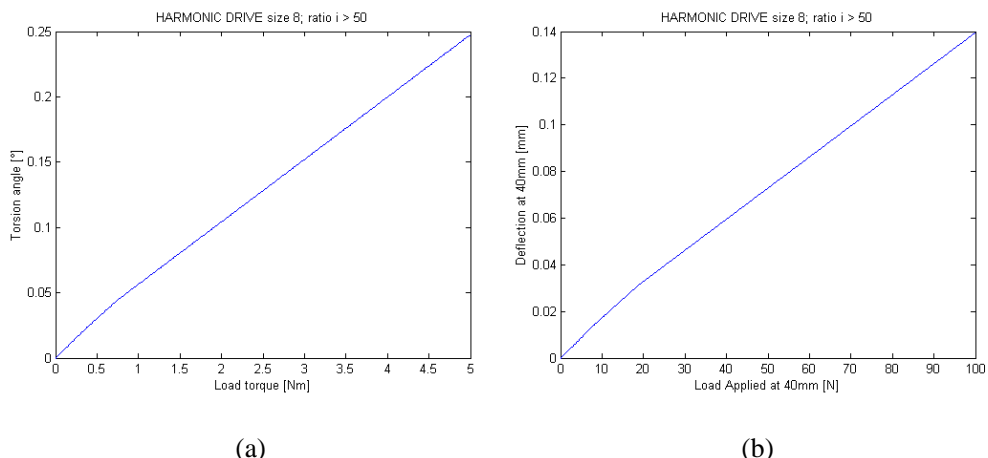


Figure 5.9 Torsional stiffness characteristics of a Harmonic Drive Gear, HFUC size 8. (a) Angular deflection vs. applied torque; (b) Deflection vs. applied load at a distance of 40 mm from gear axis.

We incorporated a spring loaded braking system between the motor outputs and the harmonic drive inputs (figure 5.10a). The mechanism functions as a manual “safety” or ‘dead-man’ button that the surgeon must hold down in order to allow motion of both actuators (figure 5.10b). This ensures that (1) the cutting guide maintains its position during cutting regardless of the state of the actuators, and (2) the motors cannot move the guide unexpectedly at any time if the button is not pressed down. In addition, since the brake mechanism bears the loads applied to the guide during the cutting phase, the motors need only provide enough power to position the cutting guide. Thus the small low-torque motors we use provide sufficient power to lift the cutting guide but not enough force to pose significant threat.

For the case of an actuator or electrical cable failure in surgery, we designed a modular system in which both actuators are encapsulated in a separate housing so that they could be easily detached from the gear unit and replaced. As the chemical sterilization protocol (washing in a toxic bath of diluted glutaraldehyde solution) and autoclave (temperature 135°C, water vapour pressure 2.1 bar, relative

humidity 100%, duration of cycle >20 minutes) inflict harsh conditions on the actuators, electrical cable, and connections, we assumed that after a certain number of sterilization cycles the actuator unit with integrated electronic positioning sensors may need to be replaced. The configuration allows the hospital to use the actuators until the end of their lifespan, and then to dispose of and replace them in surgery without having to dismount the robot from the bone. Additionally, the motor unit and power cable do not need to be connected to the robot during the cutting or milling phases (when the surgeon is typically standing directly beside the knee) making the guide very compact and lightweight. This feature may be more important in patients having very poor quality bone, where the fixation rigidity could be compromised.

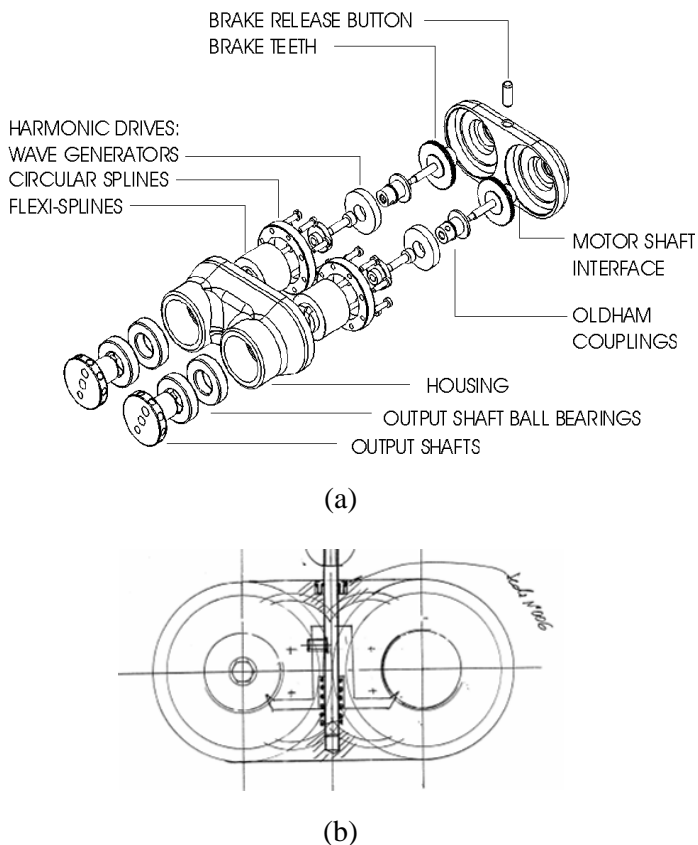


Figure 5.10 Details of the robot 2 DoF gear unit. A spring-loaded brake mechanism in between the Harmonic drive inputs and the motor outputs insures that the guide maintains its position and doesn't move unexpectedly. (a) exploded view of the robot gear unit (b) brake detail.

5.5 Milling and Guide Systems

Our current approach uses a fully passive cutting system in which the surgeon is in full control of the cutting rate and trajectory, as in manual surgery. Although automated cutting systems in which the robot is in control of the cutting process would have great potential to optimize and standardize cutting rates and depths, these types of systems currently do not seem to be very easily accepted by clinicians. Active constraint systems which allow the surgeon to make the cut but prevent the cutting tool from leaving the bone boundary at the cutting plane present an improvement over automated ones. The

surgeons that we have talked to however expressed concern that the soft tissues often cross the bone boundary and thus could still be injured by the cutting tool. Moreover, motorizing another 2 DoF either to automate cutting or to implement an active constraint control scheme would make our bone-mounted system significantly more bulky and heavy. We therefore intend to minimize the risk to soft tissues by using a soft tissue guard at the tip of the milling tool, and possibly by controlling the function of the milling motor in relation to the relative position to the bone.

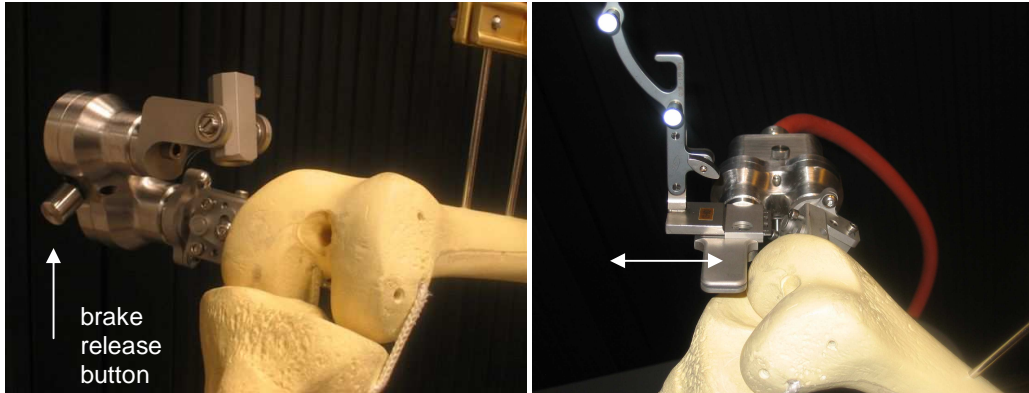


Figure 5.11 *Praxiteles* second prototype for milling and sawing in MIS TKA.
 (left) the 2 DoF milling tool guide allows rotation and translation of the milling tool within the cutting plane. A single brake release button frees both axes of rotation when pressed.
 (right) a sliding joint in the plane of the saw-guide allows the guide tip to be abutted directly against the bone surface before making each cut. Robot shown with detachable motors.

5.5.1 Femoral milling guide

Bone-cutting in our new robot version is performed with an anteromedial approach using a side-milling technique and a novel method of tool guidance (a sawing technique could also be used with a sliding cutting guide, figure 5.11). The passive 2 DoF milling guide allows the tool to both rotate and slide in the cutting plane while having a fixed entry point into the cut. The milling tool guide is positioned for each of the five femoral cuts such that the entry is through the minimal incision window. A third DoF allows the milling attachment to rotate about its long axis within the guide. This prevents moments about this axis from being transferred to the robot, and provides better ergonomics as user ‘swings’ the tool back and forth.

An indexing system was also devised that permitted discrete advancement of the milling tool into the cut after making each cutting swing. Grooves were turned in the attachment piece at intervals equivalent to the cutter length. The grooves engage with a spring in the guide, clicking at each groove as the tool is advanced forward. This decoupling of the rotational and translational DoF is intended to facilitate efficient and rapid cutting and to make milling easier to control as each DoF can be controlled independently.

5.5.2 Adjustable tibial milling guide

The same kinematic principle for the 2 DoF passive milling guide is applied to the design of a modular guide for milling a single plane on the tibia. We designed a four DoF manipulator that mounts directly

on the fixation base of the tibial rigid body '*T*'. This base is fixed percutaneously to the tibial diaphysis at the beginning of the procedure with two bicortical 4 mm diameter self-tapping pins. The tibial rigid body is attached to the guide base with two rotational DoF to orient it with respect to the camera for visibility. The tibial cutting guide with manipulator attached is slid onto the rigid body base only once it is time to navigate and perform the tibial cut, and is removed after the tibial cut is performed. This avoids having to use extra pins to attach the tibial cutting guide to the bone, and allows for a very limited exposure as there is no need to place any pins within the incision. The guide was designed to have a particularly large dimension along the bone axis (i.e. between the cutting plane and the most proximal bone pin) to ensure that the pins would not interfere with the tibial implant stem or keel. An appreciable inter-pin distance of 30mm was included so that reasonably high loads could be applied to the guide without risking motion of the rigid body base or fracture of the bone. The position of the pins with respect to the tibial anatomy is very similar to that used in arthroscopic computer-assisted anterior cruciate ligament surgery.

Manipulator architecture: Starting from the base, a linear DoF allows adjustment in the proximal/distal (P/D) direction, followed by a biaxial joint which allows adjustment in flexion/extension (F/E) and varus/valgus (V/V) directions. The range of motion of the linear and rotational DoF are ~20mm and 35° respectively to allow for less restrictive placement of rigid body base. After morphing of the tibia, the position of the calibrated planar probe attached to the rigid body *G* is projected in the anatomic coordinate frame and displayed on the navigation screen while the surgeon manually aligns and locks each adjustment. Finally, the mill or saw-guide can slide and be locked in the anterior/posterior direction to allow the cutting guide to be positioned as close as possible to the start of the cut (the guides can be detached at this joint).

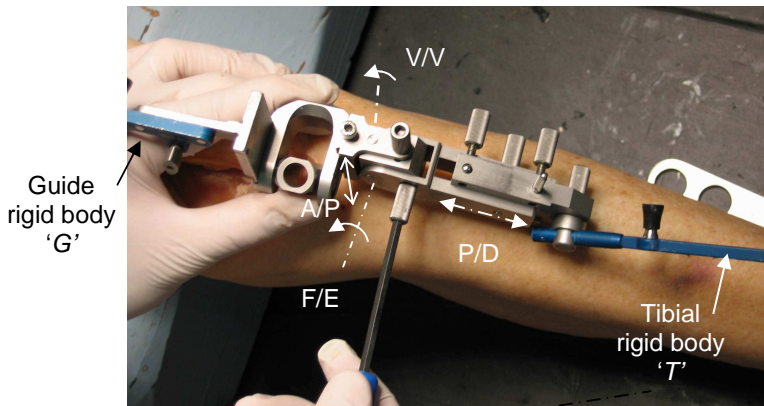


Figure 5.12 Tibial milling guide: 4 DoF (white dash-dot lines) are used to position the 2 DoF (not labelled) planar milling guide.

5.5.3 Integrated milling tool with irrigation supply.

A custom built milling hand-piece was designed and manufactured to carry out the bone milling tests. The motor we selected was a sterilizable DC-servomotor with brushless communication (Faulhaber, model 3564024B), measuring 35mm in diameter and 64mm in length, weighting 310g, and having a maximum recommended speed of 27000 RPM. The motor was rated with an output power of 101 Watts at 22000RPM and torque of 47 mNm, with a no-load operating speed of 11300 RPM at 24 volts. Although this motor was larger in size and weight by ~50% from what we had initially specified, we decided to select a motor that was slightly larger in order to be sure that we would be able to perform the cut. The motor is controlled using the same controllers that we use for the robot. Therefore we are

able to control the milling tool operating function and speed digitally using the system foot pedal and touch screen.

An integrated irrigation system was devised in which the water enters at the base of the attachment piece, flows along the attachment tube and exits through the bearing at the tube tip just behind the cutting tool. This assures that water is distributed directly at the cutting site without needing an assistant to hold the supply. This also allows the cutting tool to be easily removed and inserted from the cutting guide as there are no cumbersome irrigation tubes attached to the tube near the cutting tip.

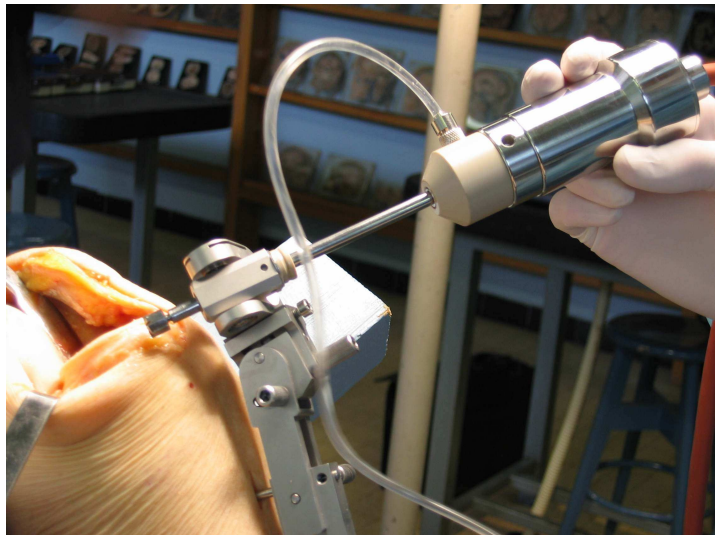


Figure 5.13 Integrated milling tool with irrigation supply.

The external and internal diameters of the attachment tube are $d_{Te} = 6$ and $d_{Ti} = 4$ mm respectively, and shaft diameter of the cutting tool is $d_{Ce} = 3.17$ mm. The structural stiffness of the tube and cutter shaft assembly at the cutter tip can be estimated from simple static beam theory:

$$K = \frac{\Delta F}{\Delta x} = \frac{3E(I_T + I_C)}{L^3} \quad (3.0)$$

where E is Young's modulus, I_T and I_C are the cross-sectional area moment of inertias of the tube and cutter shaft respectively, and L is distance that the attachment tube is extended beyond the guide support. Taking $E = 197$ GPa and $I_T = \pi(d_{Te}^4 - d_{Ti}^4)/64$, for a tube extended at an average and a maximum distance of ~50 and ~90mm respectively, the stiffness at the tool tip would be $K_{50} = 264.8$ [N/mm] and $K_{90} = 45.4$ [N/mm]. Note that the stiffness is inversely proportional to the cube of the extended length, and so the unsupported tool length is a critical parameter contributing to cutting errors (figure 5.14a). For example, a nominal cutting force of 50N would result in a deflection at the tool tip of $\Delta x_{50} = 0.2$ mm and $\Delta x_{90} = 1.1$ mm at the average and maximum extended lengths (figure 5.14b). Although we could have increased the external diameter of the attachment tube to make the system stiffer, we wanted to use the smallest diameter of milling tool as possible to minimize the amount of bone removed and the torque applied to the milling motor. Furthermore, the tube we selected was of a standard size to facilitate the manufacturing of the prototype. In order to keep tool deflections smaller than 0.5mm when the tool is fully extended to a length of 90mm, it would be necessary to keep cutting forces below 22N.

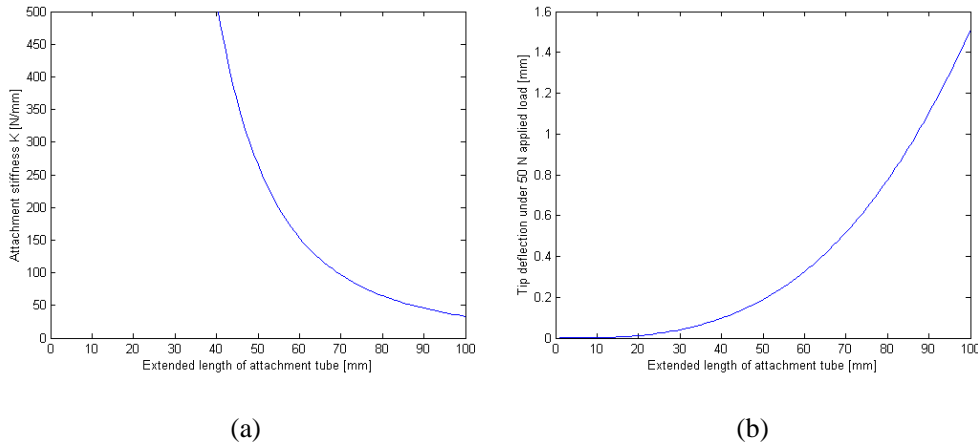


Figure 5.14 (a) Attachment + cutter stiffness, K [N/mm] and (b) cutter tip deflection [mm] under 50N applied load vs. the extended length of attachment tube for our prototype.

5.6 Robot Calibration Procedure

The calibration procedure begins directly after the robot has been manually aligned and locked in V/V and I/E rotation with the blade guide G inserted in the milling guide slot. The robot calibration is performed in two phases, a passive (i.e. manual) one followed by an active (automated) one, figure 5.15. In the following description ‘BP’ is used to denote the pressing of the Blue Pedal or footswitch, and ‘automatically’ means that the action starts automatically after the last event is completed.

Passive phase:

- (P1) The robot is passively aligned nominally with the distal cut. This position is stored as a ‘safe’ position for calibrating axis $A2$ later on. BP: 30 measurements are taken of the G and the robot Hall sensors $H1$ and $H2$.
- (P2) Without moving axis $A2$, axis $A1$ is moved passively such that the robot is in the most posterodistal position possible without impinging on the tibia or femur and without obstructing the visibility of G . This position defines the most distal ROM limit. BP: 30 measurements are taken of the G and $H1$ and $H2$.
- (P3) Without moving axis $A2$, axis $A1$ is moved passively such that the robot is in the most anteroproximal position possible without impinging on the thigh and without obstructing the visibility of G . This position defines the most proximal ROM limit. BP: 30 measurements are taken of the G and $H1$ and $H2$.

Active phase:

- (A1) With axis $A2$ locked by the second motor, axis $A1$ begins to move actively and automatically from the most anterior position (P3) to the most posterior position (P2), stopping automatically every $\sim 10^\circ$ to take 30 measurements of G until the most posterior position (P2) is reached. Robot axis $A1$ moves actively and automatically from the most posterior position (P2) to the safe position (P1).
- (A2) With axis $A1$ locked by the first motor, axis $A2$ moves actively and automatically from the safe position (P1) in the proximal direction by 70° , stops and takes 30 measurements of G .

Axis A2 moves actively and automatically towards the distal direction, stopping automatically and taking 30 measurements of G every 10° until a total of 120° are reached.

(A3) Robot axis A1 and A2 move actively and automatically to the first (distal) cut.

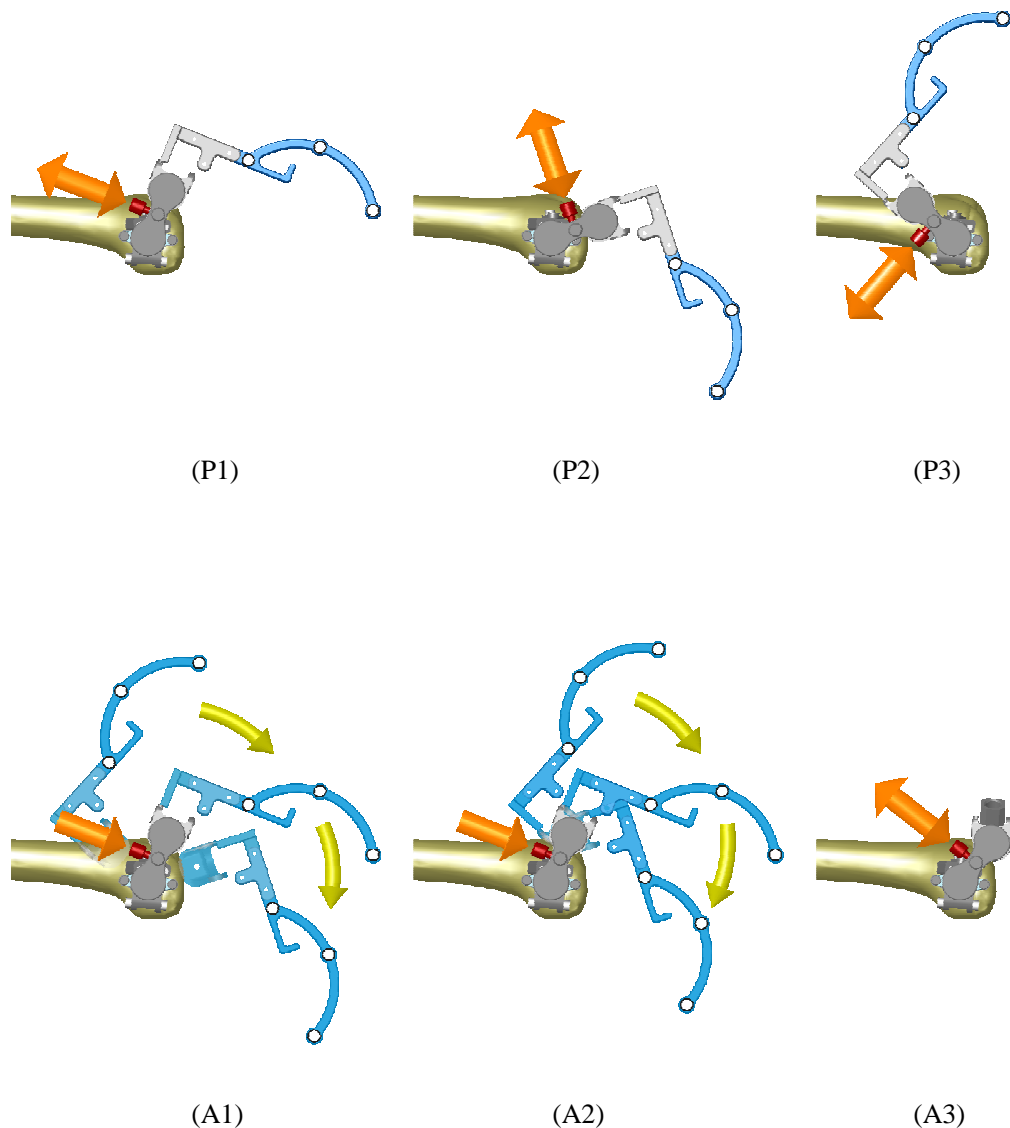


Figure 5.15 Kinematic calibration procedure consisting of passive (P1-3) and active (A1-2) steps. The guide is automatically positioned to the distal cut (A3) after calibration. These images are displayed in the graphical user interface to guide the surgeon through the calibration procedure. The double headed arrow signifies that the brake can be released during the acquisition.

During the active phase, data is collected about each joint axis separately. For each axis, first a plane and then a circle are fit to the data using least squares minimization (a weighting is given to each 10° position dataset that is inversely proportional to the variability in the 30 measurements to reduce the influence of noise). The transforms relating the positions of axes $A1$ and $A2$ with respect to F and G , respectively, are now known. The Hall sensors $H1$ and $H2$ are now calibrated with respect to the bone and guide coordinate systems using these two transforms and the three measurements made in (P1), (P2) and (P3). The constants C_1^0 and C_2^0 for axis $A1$ and $A2$, respectively, are calculated using equation 2.0 three times for each position and averaged. The robot is now calibrated and moves automatically to the distal cut.

Note that after the position of the robot axes are calibrated, the desired implant position is slightly rotated in V/V and I/E rotation about the center of the knee in the femoral coordinate system, so that the implant cutting planes are perfectly aligned to the robot axes and the congruency of the implant is conserved. The magnitude of this rotation is a function of the accuracy of the manual adjustment phase, though it is typically $<1.0^\circ$ in each direction.

Although the entire calibration procedure may seem lengthy on paper with many steps, the surgeon has only to step on the blue pedal three times and in less than 2 minutes the robot is already aligned with the first (distal) cut. The brake button must be held down by the surgeon during the entire active phase, and the robot can be instantly stopped by releasing the button. If the brake is released unexpectedly, both robot motors are blocked and the controllers automatically change the fault status bit for ‘overvoltage’ from low to high (where low = no error and high = error). The motors are then automatically disabled (i.e. the power is cut) and the surgeon can backdrive the robot to a safe position.

5.7 Results on Robot Positioning and Milling Accuracy, Repeatability, and Stiffness

There are several factors which influence the final positioning repeatability of the robotic cutting guide, including the rigidity of the fixation and mechanical systems, the accuracy and precision of the manual adjustment mechanisms, mechanical drive systems, Hall actuator sensors, manufacturing accuracy, and the optical camera. In this section we summarize the relative contributions of each system component, and the overall final positioning accuracy.

The stiffness of the two pin fixation in the three day decalcified bone (i.e. the slope of the displacement magnitude dP vs. applied load graph, figure 5.7a) was measured to be $K = 125 \text{ N/mm}$. To evaluate a user’s ability to orient and lock the mechanical adjustment mechanism relative to a planned implant position, we had two untrained users adjust and lock the guide on a synthetic ‘sawbone’. Adjustment precision measured with the G rigid body was found to be $<0.3^\circ$ standard deviation (SD, $n=5$ trials each) in both DoF for both subjects using an averaging filter to reduce the camera measurement noise and to stabilize the readings (table 5.3). We quantified the positioning reproducibility, stiffness, and backlash of the robot by rigidly clamping a 0.01mm resolution dial-gauge to the fixation base and measuring the deflection at the cutting-guide plane. The motor and gear positioning repeatability was determined by commanding both motors to rotate by a random value, returning them to their initial positions, and then noting the dial-gauge value. The variability in positioning was $<0.01 \text{ mm SD}$, with a maximum error range of 0.04mm ($n = 13$). The stiffness of the mechanical system (adjustment mechanism, gears, brake, and cutting guide) was measured by hanging a weight on the cutting guide with the brake engaged, and measuring the deflection at the point of the applied load. Masses of 540 and 1080 grams suspended from the milling guide support resulted in deflections of 0.04 and 0.09 mm, respectively (stiffness $K \sim 125 \text{ N/mm}$). No measurable backlash was recorded on the dial gauge for either axis.

Table 5.3
Mechanical Backlash, Stiffness, and Positioning Reproducibility Measurements for the Second Prototype for MIS TKA

<i>Backlash</i>	
1 st Axis only	<0.01°
2 nd Axis only	<0.01°
Guide Output	<0.01°
Guide Output	<0.01mm
<i>Stiffness</i>	
5.3 N load	0.04mm
10.6 N load	0.09mm
<i>K_{ave}</i>	125N/mm
<i>Positioning Reproducibility (n = 13)</i>	
Guide Output (SD)	<0.01mm
Guide Output (Range)	0.04mm

The final robot positioning accuracy after calibration was evaluated by measuring the guide position with the *G* rigid body for each of the five cutting planes. The errors relative to the planned implant position after adjusting for the manual orientation error in *V/V* and *I/E* rotation are presented in table 5.4.

Table 5.4
Final Guide Positioning Error

<i>Manual Adjustments (n = 5×2)</i>	[° SD]
<i>V/V</i>	<0.3
<i>I/E</i>	<0.3
<i>Automated Positioning, F/E (n = 5)</i>	
Anterior Cut	0.1
Anterior Chamfer Cut	1.1
Distal Cut	0.2
Posterior Chamfer Cut	0.2
Posterior Cut	0.2
Average	0.4

Initial milling experiments were also conducted on a sawbone to gauge the accuracy and repeatability of the milling system. Milling was carried using a standard medical side-cutting burr (Midas Rex AM14, 9.1mm diameter, 7mm length, 12 straight flutes) with our custom built milling motor operating at 12000 RPM without irrigation (figure 5.15). The final bone-cut surface was measured on each medial and lateral condyle, and across both condyles using a flat plate and the planar probe. Cut surface repeatability was found to be $1.0 \pm 0.5^\circ$ (mean absolute error \pm SD) with a range of $0\text{--}2^\circ$ for all measurements. The largest errors were on the lateral distal and posterior condyle, where the extended milling tool length was the greatest, indicating that it would be necessary to remove the grooves from the attachment tube to increase its stiffness. In addition, there was some noticeable play in between the attachment tube and the linear joint, due to the tolerance of the PEEK plane bearing. We are currently investigating other possible solutions for this linear joint, including linear ball bearings.



Figure 5.15 Preliminary milling experiments using a custom built milling tool on synthetic bones.

5.8 Proposed Surgical Technique with New Prototype Robot

We are currently integrating the robotic cutting guide into the Surgetics Station® (Praxim medivision), an open platform surgical navigation system that uses image-free BoneMorphing® (deformable statistical) models to reconstruct the three-dimensional shape of the femoral and tibial surface intra-operatively [Stindel 2002].

The overall surgical workflow is presented in figure 5.16. First the ‘T’ and ‘F’ shaped rigid bodies are fixed to the tibia and femur, respectively, and the point probe ‘P’ and planar guide probe ‘G’ are calibrated. These rigid bodies and probes each have at least three passive planar retro-reflective markers that are localized in three-dimensional space by the optical infrared camera.

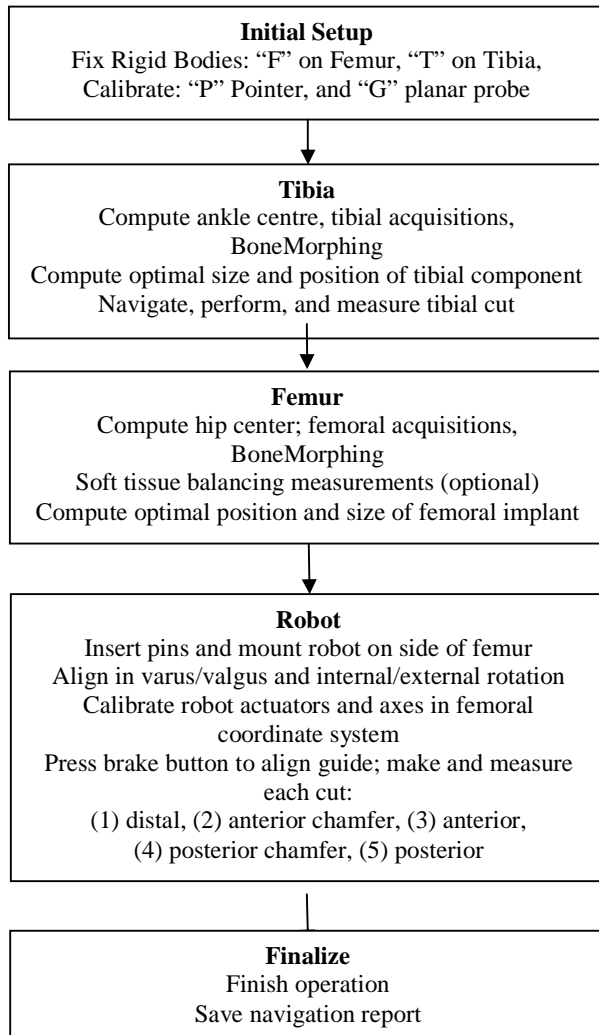


Figure 5.16 Surgical Workflow

The tibial malleoli are first digitized to compute the ankle centre, followed by the tibial plateaus which determine the initial attitude of the BoneMorphing® model. The tibial surface acquisitions are then made in three zones: medial, lateral, and anterior. The points acquired in each zone are displayed in real time and turn from orange to green once a sufficient acquisition density has been reached in each zone. The acquisition can be stopped and the surface accuracy checked by pressing the blue pedal. The adjustable cutting guide is then mounted on the rigid body base, adjusted and locked using the navigation screen. The tibial cut is made either with the mill or saw and its accuracy verified.

The femoral acquisition begins with kinematic identification of the hip centre without any rigid bodies in the pelvis. The posterior condyles and the anterior cortex are then digitized, followed by the femoral BoneMorphing® surface acquisition. Ligament gap measurements between the uncut femoral condyles and the tibial cut surface can be performed at various flexion angles to optimize femoral component positioning and sizing [Stindel 2002]. The system then automatically suggests the optimal position and size of the femoral implant based on the mechanical axis, the bony landmark features extracted from the BoneMorphing model, and the ligament balancing acquisitions (if preformed). This proposed position can then be checked and modified using the tactile screen, with the cutting planes and their intersection with the bone model superimposed on the image. Once the femoral implant size

and position has been validated, the locations of the five cutting planes are stored in the femoral coordinate system.

Two pins are then fixed bicortically in the medial femoral condyle. To ensure that the pins do not intersect any of the five cutting planes, each cutting plane location, along with the position and orientation of the probe tip are displayed in real time on 3D models. The pre-assembled robot can then be mounted onto the fixation pins. With the calibrated planar probe inserted in the slot of the guide, the robot axis is aligned in varus/valgus and internal/external rotation using the navigation display. Each DoF can be navigated and locked separately for ease-of-use.

Once the adjustments are aligned relative to the planned implant profile, the motor unit is attached if not yet already and the two kinematic axes and motor angles of the robot are calibrated. This is accomplished by pressing the brake release button on the 2 DoF gear unit, and manually rotating the first robot axis through a range of motion of $\sim 100^\circ$. Simultaneous measurement of the actuator positions and of the ‘G’ rigid body location with respect to the ‘F’ femoral reference frame are made using the motion controller and the optical camera, respectively. Using the inverse kinematic model which considers the robot geometry, the radius of the milling tool and the position of each cutting plane relative to the robot kinematic axes the system calculates which motor command values correspond to each of the five cutting planes. At this point the robot motors are enabled and the guide is advanced to the first cut. The controller monitors the Hall sensor values, notifying the surgeon to engage the brake once the guide is in position, and the planar guide probe can be inserted in the mill or saw-guide slot to verify the guide position before making a cut.

The default cutting order is (1) distal, (2) anterior chamfer, (3) anterior, (4) posterior chamfer, and (5) posterior cut. The distal cut is typically made first because it allows the surgeon to visually gauge overall varus/valgus and internal/external rotational alignment, as well as distal cutting depth, before making any of the femoral bone cuts. We make the anterior chamfer cut next followed by the anterior cut so that the saw-guide can be positioned directly against the start of the anterior cut, which is an improvement over most conventional 4-in-1 and 5-in-1 types of cutting guides. This can be important when using an oscillating saw, as cutting accuracy is known to diminish with extension of the saw-blade beyond the cutting guide. Although we prefer this sequence, the cutting order is not rigid and can be changed by using the forward or back switches on the system foot pedal to cycle through the cutting sequence.

Once the guide position is verified the system detects if the milling motor is detected and the milling speed can be adjusted using the touch screen. The milling tool is activated with the blue pedal and is deactivated using either the blue or yellow pedal. After each cut is made the accuracy can be checked with the planar probe. The remaining portion of the surgery is then completed as usual.

5.8.1.1 Preliminary cadaver tests

We conducted a total of four cadaver experiments throughout the development of this robot to test the feasibility of the proposed surgical technique with the constraints of both open and minimal access TKA. Four cadaver specimens were fresh frozen and one was preserved. None of the specimens were obese or overweight. Two different electric milling motors were used during the tests: one was our prototype motor described in §3.5.3 and the other was a smaller higher-speed prototype drill (table 5.5). The latter was designed for neurosurgery by a company that specialized in the manufacturing of medical power tools. The attachment piece of this motor was adapted to accept our milling attachment tube and integrated irrigation system. Three different cutting tools were tested in total. One was a standard medical side cutter (Midas Rex AM14, 9.1mm diameter, 7mm length, 12 straight flutes) which was used only with our prototype motor. The other two were prototypes modified from standard cutters to have a diameter and length of 7mm, with 6 and 8 straight flutes respectively. All cutters were capable of both side and plunge milling (i.e. cutting with the distal end of the tool).

Table 5.5
Specifications of High-Speed Milling Motor

Mechanical power	100W
Efficiency	>80%
Operating voltage	12V
Operating current	4-12.5A
Maximum current	15A
No load speed	25-40000 RPM
Weight	~160gram

To test the compatibility of the robot in MIS-TKA, we used a medial parapatellar approach with a 9.5cm skin incision (about two times the length of the patella, figure 5.1) to access the joint. The incision was continued down through the anterior joint capsule and patellofemoral ligament. A 2cm incision in the vastus medialis made in the direction of the fibres facilitated the exposure, along with resection of the tibial meniscus and crutiate ligaments. The tibial surface acquisitions were made by manipulating the tibia with respect to the femur in flexion, extension and rotation, to help bring the various bone areas into the incision (figure 5.17). The patella was not reflected but retracted or subluxed laterally.

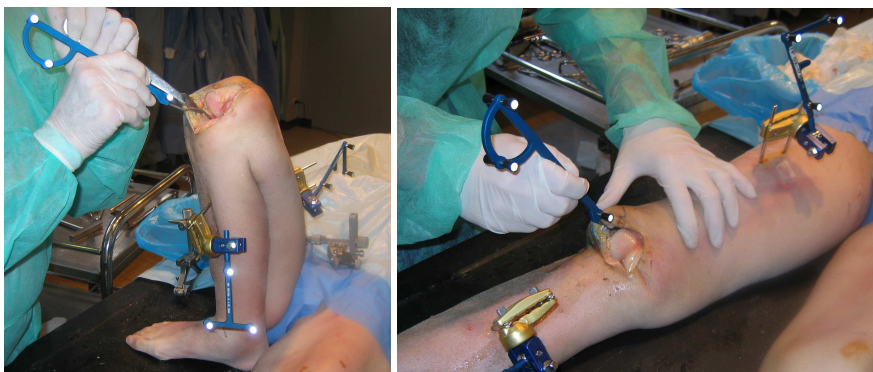


Figure 5.17 Tibial (a) and femoral (b) surface acquisitions.

(a) The tibia is flexed, extended and rotated relative to the femur to facilitate access to the anterior, medial and lateral sides of the joint. (b) There is more room in the joint to digitize the femur once the tibia cut is made. With the knee in extension and the tibia compressed against the femur, the patella is subluxed and the lateral aspects of the femur can be accessed.

The adjustable tibial cutting guide was used in every test after the first (figure 5.18). The guide was mounted onto the base of the tibial rigid body and its orientation was navigated with respect to the femoral mechanical axis and depth with respect to the unworn tibial plateau. A cutting depth of 8-10 mm was targeted, with 0° of varus and 5-7° of slope (depending on the surgeons preference). Three cuts were made using the milling-guide and one cut was made using the saw guide. The guide was locked using a T handle Allan key and did not come loose during any of the cuts. Adjustment accuracy was better than 0.5° and mm for all tests, though several adjustment iterations had to be performed due to the coupled DoF between the guide adjustment axes and the anatomical axes. For example, changing the V/V angle of the guide would have a small effect on the F/E angle displayed on the screen due to the misalignment of the guide and anatomical axes. Decoupling these axes either by digitization or using the guide geometry would appreciably reduce the time required to position the guide [Boyer 2004].

Tibial milling was conducted in two or three phases in the MIS cases. The medial side was milled first followed by the lateral side. It was necessary to remove the milling guide from the adjustment mechanism at some points to dissect the medio-proximal plateau bone surface with scissors to improve visibility and to better gauge the tool insertion depth while milling the lateral and posterior regions. It was generally difficult to mill near the ligaments, especially on the lateral side, for fear of cutting the soft tissues. Two cuts were made using the high-speed milling tool operating at 30000 RPM and one was performed with large milling tool operating at 10000 RPM. The temperature of the motor in the high-speed milling tool elevated noticeably over the cut duration, which typically took several minutes. Milling seemed to be slightly faster using the larger more cumbersome milling tool. The milling tool was fully immersed in the bone and was reasonably easy to control. Visibility in the posterior sections was very poor and there was a risk of cutting the capsule. We therefore believe it will be necessary to navigate the milling tool relative to the bone model in order to be sure not to enter into the soft tissue regions. Milling surface accuracy as measured by the blade guide was always $<0.5^\circ$ and mm.

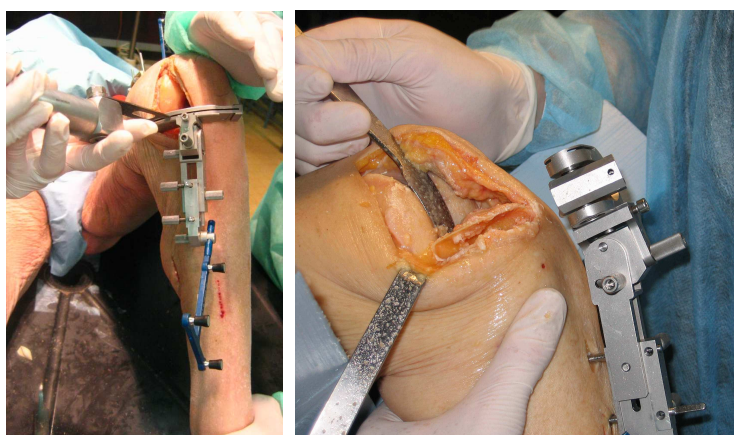


Figure 5.18 Tibial sawing and milling guide. Tibial milling in the MIS surgeries was completed in stages, first with the medial and then the lateral condyle.

The tibia is also flexed, extended, and rotated relative to the femur to expose the relevant surface areas for the femoral acquisitions. Cutting the tibial plateau first left more space in the knee, allowing the tibia to be compressed against the femur and the patella to be retracted laterally. A curved probe facilitated acquisition of the posterior femoral areas with the knee in flexion, and the lateral areas with the knee in extension (figure 5.19a).

The default planning proposed by the system was typically chosen for the desired placement of the implant. To facilitate pin insertion, the surgeon could identify the insertion points of the two robot fixation pins relative to the five cutting plans and the BoneMorphing model. No optimal pin target position was displayed on the screen. The pin insertion area on the medial femoral side is bounded by the following structures: *posteriorly* – by the anterior border of the medial collateral ligament when the knee is in full extension; *anterosuperiorly* – by the posteroinferior border of the vastus medialis muscle when the knee is in flexion; *anterodistally* – by the anterior, anterior chamfer and distal cutting planes (figure 10b). Fixing the robot in this area permitted uninhibited flexion and extension of the knee, and access to all five cuts through the mobile incision.



Figure 5.19 Insertion of the robot fixation pins.(a) the point probe can be used to guide and check pin insertion to avoid interference with the femoral cutting planes; (b) the pin insertion area on the medial femoral side is bounded by the following structures:

posteriorly – by the anterior border of the medial collateral ligament when the knee is in extension,
anterosuperiorly – by the posteroinferior border of the vastus medialis muscle when the knee is in flexion,
anterodistally – by the anterior, anterior chamfer, and distal cutting planes.

The problem of coupled DoF experienced with the tibial cutting guide was also apparent when manually aligning the robot in V/V and I/E rotation. This could be solved by digitizing the robot base and displaying the angles of the robot in the joint space coordinates (with the desired joint angles) as well as in the anatomical reference. The robot calibration phase took approximately two minutes on average.

The leg was placed in various degrees of flexion to make more room in the joint in the MIS procedures to facilitate milling (figure 5.20). For the anterior cuts the leg was typically placed in slight flexion while for the posterior the leg was put in high flexion. Making the anterior cuts before the posterior ones frees more space in the joint for making the posterior cut, which is more difficult due to the position of the tibia and the delicate soft tissues behind the knee. The planar cuts were made with ‘sweeping’ motions of the milling tool, using retractors to distract the surrounding soft tissues. All five cutting planes are accessed through the mini-incision with the milling tool guide.



Figure 5.20 The leg can be positioned in various degrees of flexion depending on the cut to make room during milling.

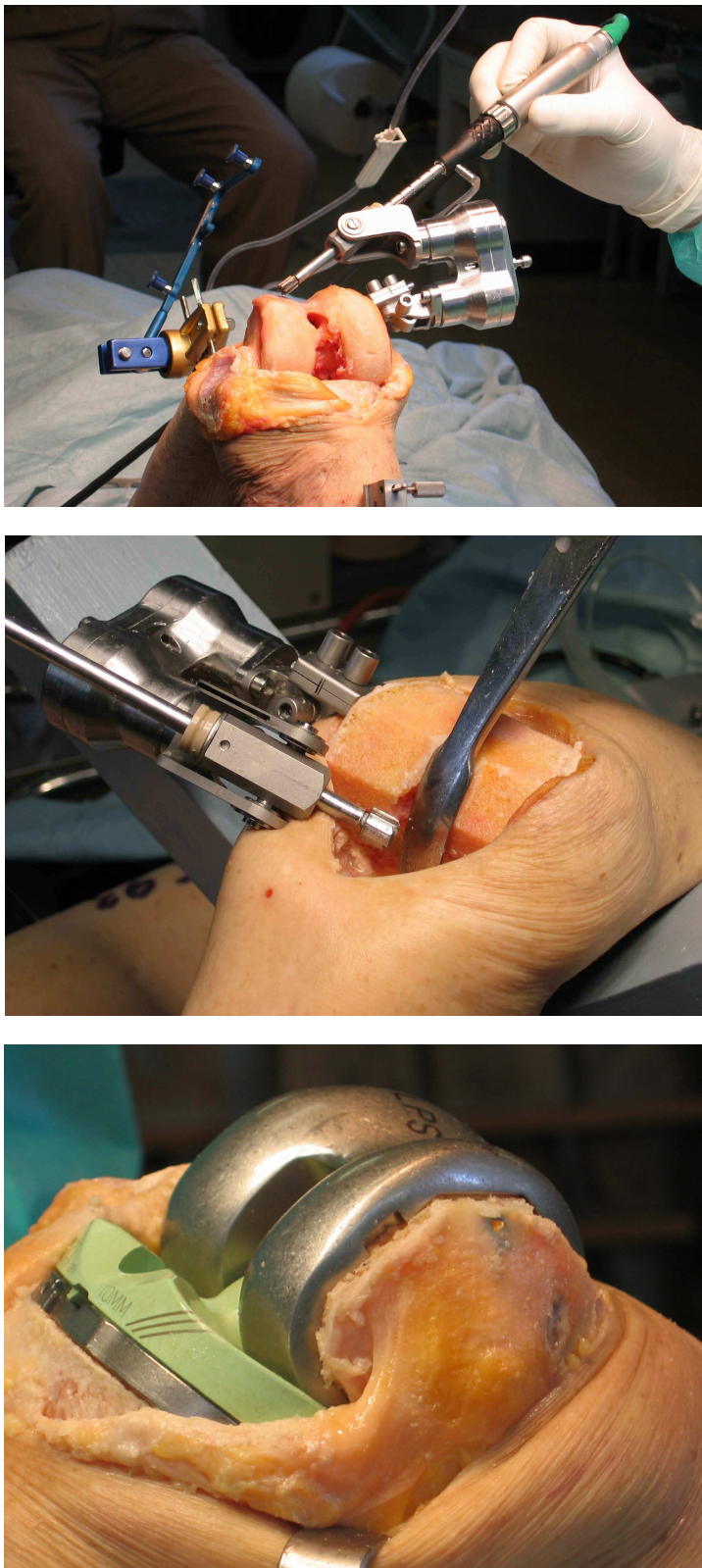


Figure 5.21 Latest *Praxiteles* milling system with refined manual adjustment mechanism and high-speed milling tool: (a) Femur before cutting in open surgery, (b) femur after all five planar cuts (c) trial components installed.

Milling the subcondral bone in the anterior groove was difficult on some femurs, as described in §3.5.1. Milling forces in the normal direction reached high values such that the combination of the attachment tube flexibility and the play in the linear bearing guide caused the milling tool to deflect upwards and climb over the bone surface until it jammed in the cortical bone. This was primarily a problem in the first experiments when we used the grooved attachment tube which had a significantly lower stiffness than the straight tube, and with the standard 9.1mm diameter cutter with 12 teeth. Unfortunately all the suitable commercially available orthopaedic burrs that had a diameter $\geq 7\text{mm}$ had 8, 12 or even 16 cutting teeth, even though the results from our milling chapter indicate that fewer teeth would be optimal for reducing mean forces and temperatures. We are therefore currently still in the process of manufacturing our own custom milling tool for this operation.

Figure 5.21 depicts the latest version of the robot, with new version of the mechanical adjustment system. The five femoral cuts were made with the milling tool and the notch cuts were made manually with a saw, allowing installation of the trial components (figure 5.21c). The surgeon described the implant fit as clinically excellent. The cutting errors in the sagittal plane with respect to the initial guide position (i.e before making each cut) and with respect to planned implant position as measured with the planar probe are presented in Table 5.6. The distal and posterior chamfer cut measurements are averaged over the medial and lateral condyles. Similarly, the average errors for the distal cut in the frontal plane (i.e varus/valgus) with respect to the initial guide position and the planned implant position were 1.10° and 1.15° respectively.

Table 5.6
Final cutting errors [°] relative to guide position
and implant planning

Resection	Guide Position	Implant Plan
Anterior cut	-0.5	0.3
Anterior chamfer cut	0.6	0.3
Distal cut	1.1	1.1
Posterior chamfer cut	0.5	-0.1
Posterior cut	-0.3	-0.9
Average absolute error	0.6	0.54

5.9 Conclusions

As surgical robots become smaller and more dedicated, their architecture can be optimized to suite the application, so as to minimise the disturbance on surgical workflow and operating time. We present a new miniature robot for positioning sawing and milling-tool guides in minimal access TKA. Initial results on sawbones and cadavers with the device are very promising, and we hope to start a series of clinical trials with the coming months.

Chapter 6: Conclusions and Future Work

6.0 Thesis Summary

Computer-assistance has brought enormous added value to surgical interventions over the past decade by providing clinicians with precise intra-operative measurement tools to quantify and to help them control their surgical actions. However, we believe that there remains a narrow yet important margin for further improvement that only robotic or ‘intelligent instruments’ can offer. In particular, the collaboration of miniature robotized instrumentation with surgical navigation systems will bring a new dimension to computer assisted medical interventions (CAMI) by not only improving the precision of surgeons’ actions but also by augmenting surgeons’ capabilities so as to allow for new surgical techniques, new implants, new possibilities. Furthermore, the synergy of compact robotics and navigation systems will help engineers and clinicians to overcome the integration challenge into the operating room. Perhaps this will be the way that surgical robotics will gain mass clinical adoption in orthopaedics to an extent that computer assistance has gained in orthopaedics and neurosurgery.

In this work the integration challenge of a miniature surgical robot for TKA was addressed. The potential clinical benefits that our system could offer include:

- (1) reducing alignment variability and outliers and improving soft tissue balance through more precise component positioning,
- (2) reducing the risk of femoral implant loosening as well as surgical time and technical difficultly for implant installation through improved femoral component fit,
- (3) reducing soft tissue exposure requirements for accessing all five cuts though optimized instrumentation design and side milling approaches,
- (4) reducing the risk of soft tissue damage through analysis and implementation of a stable milling process,
- (5) reducing the risk of thermal necrosis and delayed bone healing through optimized irrigation and bone-milling techniques and cutters,
- (6) reducing the number of instruments required in the operating room.

In the first half of this thesis we addressed the clinical problem related to bone-milling forces and stability through modelling of high-speed bone-cutting and milling processes. Experimental measurements were made in order to build and validate these models. Based on the high-speed orthogonal and oblique cutting experiments made in chapter 2, we found that the cutting forces acting on a single cutting edge increased non-linearly with cutting depth, and that the magnitude of force was lower than those previously measured in low-speed cutting. The mechanism of failure during cutting shifted from a continuous to discrete fracture process as the depth of cut increased. Finally, we found that a new logarithmic function having three coefficients better represented the experimental data mathematically in comparison to other models previously formulated, although at the expense of a loss in physical representation.

This basic knowledge was then used to build a flexible model of the milling process that was applicable to several different milling conditions. The model included as inputs the cutter geometry (number of teeth, edge rake angles, helix angle, cutter profile, etc...), the immersion level, the rotational speed and feed rate, the axial depth, the milling direction relative to the bone fibres and the milling mode (up- and down- milling). Based on a comparison with experimental measurements in which we quantified the cutting forces as a function of the rotation angle of the milling tool across one complete rotation cycle, we found that the model was capable of predicting milling force components

over a wide range of cutting conditions with reasonable accuracy (though the model tended to over predict cutting forces for very small feeds per tooth). The utility of the model was demonstrated in an analysis of milling forces, and we were able to explain why and how forces increase, decrease, and even change direction with the variation in the milling parameters. We also provided recommendations for an optimal cutter geometry and milling technique in order to facilitate the integration of milling in TKA.

Finally, we designed a novel robot for positioning bone-milling and sawing guides in TKA. We tailored the architecture and optimized the design of the robot to meet the surgical and engineering requirements, employing a hybrid manual/motorized architecture to minimize the device size and complexity. Planar resections can be carried out manually using a side-milling technique in which the milling tool is constrained to the cutting plane by one pivot and one sliding joint. The experimental results and modelling analysis of milling conducted in chapter 3 were correlated qualitatively to the clinical tendencies occurring during milling in TKA. The feasibility and the accuracy of the device were evaluated in a benchtop setting and in preliminary cadaver experiments in which we were able to demonstrate the feasibility of such a technique. The initial results on guide positioning and milling accuracy are very encouraging, indicating that milling could indeed be a very competitive solution for realising bone cuts in TKA.

The remainder of this thesis describes the work that must be completed before the device can be trialed clinically, followed by some future perspectives.

6.1 Future Work

6.1.1 Robot design finalization and validation

Refinement of the robot design is ongoing. We are currently still experimenting with different materials and bearing designs for the passive linear joint used to guide the milling tool in the cutting plane such that a smooth gliding motion is achieved with negligible play. This is essential to give the surgeon an ergonomic and safe control of the cutting trajectory without compromising cut surface accuracy. The linear joint becomes especially important when milling along the boundary of the cut, where it is useful to pivot and slide the mill at the same time.

The optimal cutter geometry as recommended in this thesis is currently under development and will need to be validated in cadaver experiments in terms of milling accuracy, force response and temperature. As the cutting technique is completely manual, the surgeon dependent variables should be validated across a few surgeons of varying skill level. Either thermography or thermocouples implanted in the bone specimens could be used to validate the effectiveness of the irrigation system and new tool design.

Since our last cadaver trial, we have manufactured a new base for the robot that incorporates an attachment for the femoral ('F') rigid body, thus minimizing the bone pins required as we have done on the tibia. This however would mean that the surgeon would not be able to check the pin insertion sites relative to the planned implant cutting planes before installation of the pins. A manual jig to ensure the pin placement does not interfere with cutting planes, such as the augmented 2 pin fixation device (short intramedullary rod) tested in Chapter 5, would likely be required. Finally, the stability and fracture risk of the 2 pin fixation technique should be evaluated on osteoporotic cadaver specimens.

6.1.2 Necessary precautions for ensuring milling safety

A soft tissue guard on the milling tool tip would be necessary for all the femoral cuts in MIS-TKA, and for at least the femoral posterior resection in open TKA. This would also be necessary for the posterior and lateral areas of the tibial cut. The use of retractors to keep soft tissues away from the cutter and to improve visibility can be helpful, though it is not a sufficient solution as it cannot guarantee that soft tissue will be protected. Moreover, this technique is not entirely effective in the posterior and lateral regions of the joint, particularly when the exposure is limited. The use of metallic retractors also introduces a risk for collisions with the milling cutter which must be avoided.

The guard should be designed such that it allows the cutter to be fully immersed in the bone without impinging on the bone surface. One could imagine a ‘flexible’ or a hinged guard which retracts and slides overtop of the bone surface while the milling occurs beneath. Such a design could also limit the spray of the irrigation fluid and bone debris in the surgical environment.

Navigation of milling tool with respect to cutting plane boundary of the bonemorphing model should also be implemented. The function of the milling tool could also be altered and controlled to warn the surgeon when they are approaching the bone boundary, and the milling could be stopped automatically if the milling tool crosses the perimeter.

Soft tissue protection on the lateral side in MIS TKA is currently a concern even with sawing, and no real solutions exist today. In femoral and tibial osteotomies fluoroscopy is commonly used to control the distance between the saw-blade tip and the bone boundary, though this method is not desirable for obvious clinical reasons. Expert TKA surgeons advice that open procedures should be learned and mastered first. The exposure should then be *gradually* limited as the surgeon feels comfortable in handling the saw with the reduced access and visibility. Training on cadavers is also typically recommended. These guidelines are entirely applicable to our instrumentation and surgeons should be trained on cadavers and they should master the milling technique in open TKA procedures before attempting MIS-TKA.

6.2 Perspectives

6.2.1 Intra-operative prediction of milling forces

Extension of the model to predict of milling force components intra-operatively could provide the surgeon with useful information and could help to train inexperienced surgeons. This could be accomplished by computing the cutting geometry based on the shape of the three dimensional bone surface above each cutting plane as obtained from the BoneMorphing model. A radial coordinate system (ϕ, z , figure 6.1) could be used to describe the position of the milling tool with respect to the bone model, with the origin of the coordinate system coincident with the rotational axis of the passive milling tool guide. For each position of the milling tool, the radial immersion level could be determined for each axial segment of the cutter, along with the axial depth of cut (a , figure 6.1). Alternatively a mean immersion level could be determined to facilitate real-time computations. By measuring the feed rate and rotational speed of the milling tool, the instantaneous or mean chip thickness could be calculated and related to the force components. Thus we could envision the display of a ‘dynamic’ force prediction map that is superimposed over the cutting plane, where the force map would be dependant on the feed rate applied.

The electrical power consumed by the milling tool could also be monitored to give an indication of the mean torque, and thus the mean tangential forces (F_t), acting on the cutter tip. Using the equations and relationships between tangential (F_t) and radial (F_r) forces quantified in Chapter 2, as well as the geometry of the cut as described above, we could estimate the radial forces acting on the cutter and then transform these forces to the milling coordinate system (i.e. in the normal and feed directions).

This could also be possible way to calibrate the system such that the force predictions are based on the bone properties of each *individual* patient and not on the bovine bone specimens used in this thesis.

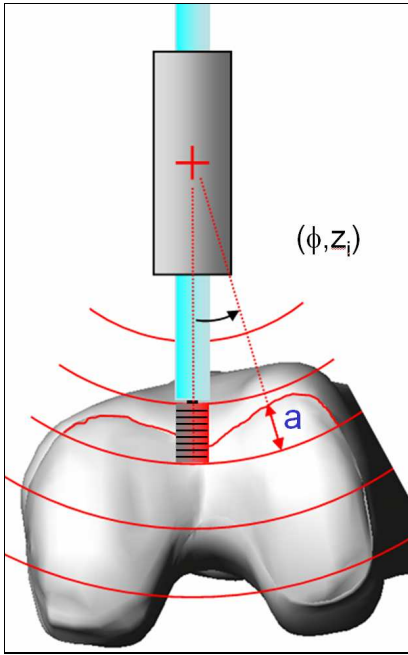


Figure 6.1 Application of milling model to intra-operative force prediction in TKA.

6.2.2 Future applications – bone conserving implants

We envision new uses for our robot in the future, for installation of more complex implants requiring non-planar resections such as spherical or curvilinear cuts, as in uni-compartmental knee arthroplasty or even for new total knee arthroplasty implants. These ‘bone conserving implants’ have the advantage of minimizing the amount of bone removed, since the resection is very similar in shape to the original bone surface. The robot could be aligned manually to the profile of the implant as we do currently, and then the robot could be used to machine contours of the implant at different depths.

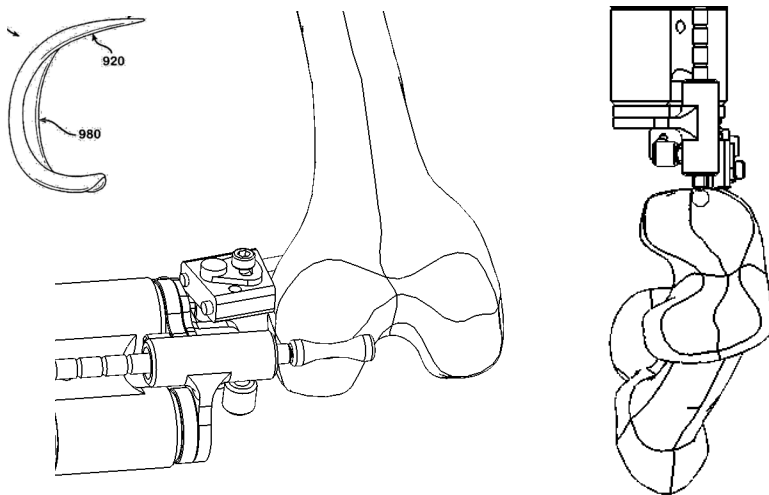


Figure 6.2 Application of the miniature robot to non-planar cuts and new implant designs.

An ‘active constraint’ or ‘virtual fixtures’ type of control algorithm could be used to keep the milling tool in the desired trajectory, allowing the surgeon to move the milling tool along the cut, feeling the forces and controlling the feed rate appropriately. Ball-shaped or other non-cylindrical shaped tools could be used to machine 3D surfaces (figure 6.2). To increase speed, cutters having profiles matching the shape of the implant could be used such that large surfaces can be made in a single pass. The force predication algorithm could be applied to such techniques by taking into account the tool profile in the geometry of the milling tool. This is easily incorporated into the model simply by appropriately varying the radius of each axial element of the tool. Finally, we could also image this technique being used for other implants and procedures such as hip arthroplasty.

References

- Altintas Y. Manufacturing Automation: metal cutting mechanics, machine tool vibrations, and CNC design. *Cambridge University Press*. Cambridge UK. 2000
- Ark TW, Thacker JG, McGregor W, Rodeheaver GT, Edlich RF. Innovations in oscillating bone saw blades. *Journal of Long-Term Effects of Medical Implants*. 7(3):279-268, 1997
- Armarego EJA, Brown RH. On the size effect in metal cutting. *Int. J. Prod. Res.* (1):75-99, 1962
- Armarego EJA, Brown RH. The Machining of Metals. *Prentice-Hall International*. New Jersey. 1969.
- Backer, W.R. Marshall, E.R. Shaw MC. The size effect in metal cutting. *Trans. ASME* 74: 61-71, 1952
- Bai B, Baez J, Testa N, Kummer FJ. Effect of posterior cut angle on tibial component loading. *J Arthroplasty*. 15:916, 2000
- Berardoni M. A computer aided cutting guide postioner to improve bone-cutting precision in total knee arthroplasty. Proceedings of the 3rd annual meeting of the International Society for *Computer-Assisted Orthopaedic Surgery*. pp 28-29, 2003
- Berkelman P, Boidard E, Cinquin P, Troccaz J. From the laboratory to the operating room: usability testing of the LER, the light endoscope robot. International Conference on Medical Robotics, Navigation, and Visualization, MRNV 2004
- Bonutti PM, Mont MA, McMahon M, Ragland PS, Kester M. Minimally invasive total knee arthroplasty. *J Bone Joint Surg Am.* 86-A Suppl 2:26-32, 2004
- Borner M, Wiesel U, Ditzten W: Clinical Experiences with ROBODOC and the Duracon Total Knee. In: Navigation and Robotics in Total Joint and Spine Surgery. Eds: Stiehl, Konermann, and Haaker. Springer.-Verlag, 2004 pp. 362-366.
- Boyer A, Vertallier L, Argenson JN, Henky P, Perrin B, Ferrier JM, P. Henri 1, and S. Lavallée Design of navigation system for 5-in-1 femoral cutting guide for TKA: on the importance of decoupling degrees of freedom. *Proc. of the 4th International Conference of Computer-Assisted Orthopaedic Surgery (CAOS)*. 2004
- Brugioni DJ, Andriacchi TP, Galante JO. A functional and radiographic analysis of the total condylar knee arthroplasty. *J Arthroplasty*. 5:173, 1990
- Brys DA, Lombardi AV Jr, Mallory TH, Vaughn BK. A comparison of intramedullary and extramedullary alignment systems for tibial component placement in total knee arthroplasty. *Clin Orthop* 263:175, 1991
- Budak E, Altintas Y. Peripheral milling conditions for improved dimensional accuracy. *Int. J. Mach. Tools Manufac.* 34(7): 907-918, 1994
- Carlsson L, Rostlund T, Albrektsson B, Albrektsson T, Branemark PI. Osseointegration of titanium implants. *Acta Orthopaedica Scandinavica*. 57(4):285-9, 1986
- Carlsson L, Rostlund T, Albrektsson B, Albrektsson T. Implant fixation improved by close fit. Cylindrical implant – bone interface studied in rabbits. *Acta Orthopeda Scandinavica*. 59: 272-275, 1988
- Coller JP, Mayor MB, Surprenant VA, Dauphinais LA, Surprenant HP, Jensen RE. Biological Ingrowth of Porous-Coated Knee Prostheses. in Goldberg VM (ed): Controversies of total knee arthroplasty. *Raven Press* N.Y. chap 10, 1991
- Cooke, T.D., Saunders, G., Siu, D., Yoshioka, Y., & Wevers, H. Universal bone cutting device for precision knee replacement arthroplasty and osteotomy. *J. Biomed Eng*, 7(1), 45-50, 1985
- Coull R, Bankes MJK, Rossouw DJ. Evaluation of tibial component angles in 79 consecutive total knee arthroplasties. *The Knee*. 6:235-237, 1999
- Currey J. The mechanical adaptations of bones. *Princeton University Press*. 1984
- Davies BL, Hibberd RD, Ng WS, Timoney AG, Wickham JEA. Mechanical constraints – the answer to safe robotic surgery? *Innovation Technol. Biol. Medicine*, 1992, 13(4), 426-436.

- Davies BL, Harris SJ Lin WJ, Hibberd, Middleton R, Cobb JC. Active compliance in robotic surgery – the use of force control as a dynamic constraint. *Proc Instn Mech Engrs.* 211H, 285292, 1997
- Delp SL, Stulberg SD, Davies B, Picard F, Leitner F. Computer assisted knee replacement. *Clin Orthop* 354:49, 1998
- Denis K, Van Ham G, et al. Influence of bone milling parameters on the temperature rise, milling forces and surface flatness in view of robot-assisted total knee arthroplasty. Proceedings of CARS – Computer assisted Radiology, 300-306 (2001).
- Devor RE, Sutherland JW, Kline WA. Control of surface error in end milling. *11th North American Manufacturing Research Conference Proceedings*. May:356, 1983
- Dippon J, Ren H, Amara FB, Altintas Y. Orthogonal cutting mechanics of medium density fiberboards. *Forest Products Journal*. 50(7):25-30, 2000
- Dorr LD, Boiardo RA. Technical considerations in total knee arthroplasty. *Clin Orthop*. 205:5, 1986
- Dueringer K, Stalcup G. Bone cut accuracy and flatness from milling and sawing – A comparative study. *Zimmer* 1996a
- Dueringer K, Stalcup G. Thermal effects in bone from milling and sawing – A comparative study. *Zimmer* 1996b
- Ewald FC, Jacobs MA, Walker PS, Thomas WH, Scott RD, Sledge CB. Accuracy of total knee replacement component position and relation to bone-cement interface reaction. P. 117. In Dorr LD (ed): The Knee. Papers of the First Scientific Meeting of The Knee Society. *University Park Press*; Baltimore, 1985
- Eriksson AR. Heat induced bone tissue injury. Thesis, University of Gothenburg, Goteborg, 1984.
- Fadda M, Marcacci M, Toksvig-Larsen S, Wang T, Meneghelli R. Improving Accuracy of Bone Resections Using Robotics Tool Holder and a High Speed Milling Cutting Tool. *J. Medical Eng. & Tech.* 22(6):280-4, 1998
- Feng HY, Menq CH. A Flexible ball-end milling system for cutting force and machining error prediction. *Journal of Manufacturing Science and Engineering*. 118:461-469, 1996
- Fisher DA, Watts M, Davis KE. Implant position in knee surgery: a comparison of minimally invasive, open unicompartmental, and total knee arthroplasty. *J Arthroplasty*. 2003, 18(7S1): 2-8.
- Goldstein SA, Wilson DL, Sonstegard DA, Matthews LS. The mechanical properties of human tibial trabecular bone as a function of metaphyseal location. *J Biomech*. 16(12):965-9, 1983
- Giraud JY, Villemain S, Darmana R, Cahuzac JP, Autefage A, Morucci JP. Bone cutting. *Clin. Phys. Physiol. Meas.* 12(1):1-19, 1991
- Haaker RG, Stockheim M, Kamp M, Proff G, Breitenfelder J, Ottersbach A. Computer-assisted navigation increases precision of component placement in total knee arthroplasty. *Clin Orthop Relat Res.* (433):152-9, 2005
- Hankinson. Investigation of crushing strength of spruce at varying angles of grain. *U.S. Air Service Information Circular No. 259*, 1921
- Hofmann AA, Bachus KN, Wyatt RW. Effect of the tibial cut on subsidence following total knee arthroplasty. *Clin Orthop* 269:63, 1991
- Ho SC, Hibberd RD, Davies BL. A force control strategy with active motion constraint for robot knee surgery. *IEEE Eng Med Biol.* May, 292-300, 1995
- Hsu HP, Garg A, Walker PS, Spector M, Ewald FC. Effect of knee component alignment on tibial load distribution with clinical correlation. *Clin Orthop* 248:135, 1989
- Hungerford DS, Kenna RV, Krackow KA. The porous-coated anatomic total knee. *Orthop Clin North Am* 13:103, 1982
- Hungerford DS, Krackow KA, Kenna RV. Alignment in total knee arthroplasty. p. 9. In Dorr LD (ed): The Knee. Papers of the First Scientific Meeting of The Knee Society. *University Park Press*, Baltimore, 1985
- Inkpen KB. Precision and accuracy in computer-assisted total knee replacement. Master's Thesis. *University of British Columbia*. 1999

- Inkpen KB, Hodgson AJ, Plaskos C, Shute C, McGraw RW: Accuracy and Repeatability of Bone Cutting and Ankle Digitization in Computer-Assisted Total Knee Replacements. In: Delp SL (ed): Medical Imaging and Computer Assisted Intervention (MICCAI'00). Lec. Notes Comp. Sc.V1935. Springer-Verlag. p.1163, 2000
- Insall JN: Technique of total knee replacement. p. 23. In Dorr LD (ed): The Knee. Papers of the First Scientific Meeting of The Knee Society. University Park Press, Baltimore, 1985
- Insall JN, Scott NW: Surgery of the knee. 3rd Ed. Churchill Livingstone Press. 2001.
- Jacobs CH. The Machining Characteristics of Bovine Bone. Master's Thesis. University of Vermont. 1973
- Jacobs CH, Pope MH, Berry JT, Hoaglund F. A study of the bone machining process – Orthogonal cutting. *J. Biomechanics.* (7):131-136, 1974
- Jacobs CH, Pope MH, Berry JT, Hoaglund F. A study of the bone machining process – Drilling. *J. Biomechanics.* (9):343-349, 1976
- Jakopec M, Harris SL, Rodriguez y Baena F, Gomes P, Cobb J, Davies BL. The first clinical application of a “hands-on” robotic knee surgery system. *Comp Aid Surg.* 6(6):329-39, 2001
- Jeffery RS. Morris RW: Coronal alignment after total knee replacement. *J Bone Joint Surg Br* 73:709, 1991
- Jenny JY. Boeri C. [Navigated implantation of total knee endoprostheses--a comparative study with conventional instrumentation]. [German] *Zeitschrift fur Orthopadie und Ihre Grenzgebiete.* 139(2):117-9, 2001
- Jenny JY, Boeri C. Computer-assisted implantation of total knee prostheses: a case-control comparative study with classical instrumentation. *Comput Aided Surg.* 6(4):217-20, 2001.
- Kagan A II: Mechanical causes of loosening in knee joint replacement. *J Biomech* 10:387, 1977
- Kelly J. The mechanical and thermal effects of a high speed rotary burr on bovine bone. M.S. Report. Clemson University 1976.
- Kienzle TC, et al. Total knee replacement – Computer-assisted surgical system uses a calibrated robot. *IEEE Eng Med Biol*, May, 301-6, 1995
- King RI. Handbook of high speed machining technology. Chapman and Hall. New York N.Y. 1985
- Kline WA. DeVor RE. Shareef JR. The prediction of surface accuracy in end milling. *ASME Journal of Engineering for Industry.* 104:272, 1982
- Koszyca B. Fazzalari N.L. Vernon-Roberts B. Quantitative analysis of the bone-cartilage interface within the knee. *The Knee* 3(1-2) 23-31 1996
- Krakow KA, Hungerford DS: Sequence of reconstruction and alignment in total knee arthroplasty. in Goldberg VM (ed): Controversies of total knee arthroplasty. Raven Press N.Y. chap 20, 1991
- Krackow, KA. Bayers-Thering M. Phillips MJ. Mihalko WM. A new technique for determining proper mechanical axis alignment during total knee arthroplasty: progress toward computer-assisted TKA. *Orthopedics.* 22(7), 698-702. 1999
- Krause WR, Bradbury DW, Kelly JE, Lunceford EM. Temperature elevations in orthopaedic cutting operations. *J. Biomechanics.* 15(4):267-275, 1982
- Krause WR. Orthogonal Bone Cutting: Saw design and Operating Characteristics. *J. Biomech. Eng.* 109:263-271, 1987
- Krause WR. Bioengineering Consultants Ltd. Personal telephone communication. Feb 06, 2002
- Lang SM, Moyle DD, Berg EW, Detorie N, Gilpin AT, Pappas NJ, Reynolds JC, Tkacik M, Waldron RL: Correlation of mechanical properties of vertebral trabecular bone with equivalent mineral density as measured by computed tomography. *The Journal of Bone and Joint Surgery,* 70(10) 1531-1538, 1988
- Laskin RS: Bone Resection Techniques in Total Knee Replacement. p. 55-74. In Laskin RS (ed.): Total Knee Replacement. Springer-Verlag London Limited, 1991
- Leitner, F., Picard, F., Minfelde, R., Schulz, H.J., Cinquin, P., & Saragaglia, D. Computer Assisted Knee Surgical Total Replacement. In J. Troccaz, E. Grimson, & R. Mosges (Eds.), CVRMed - MRCAS Proceedings '97: Grenoble, France: Springer-Verlag. 1997

- Lennox DW, Cohn BT, Eschenroeder HC Jr: The effects of inaccurate bone cuts on femoral component position in total knee arthroplasty. *Orthopedics* 11:257, 1988
- Lotke, P.A., Ecker, M.L. Influence of positioning of prosthesis in total knee replacement. *J.Bone Joint Surg.* 59A(1), 77-79, 1977
- Lui D, Weiner S, Wagner HD. Anisotropic mechanical properties of lamellar bone using miniature cantilever bending specimens. *J Biomech.* 32:647-654, 1999
- Liu D, Wagner HD, Weiner S. Bending and fracture of compact circumferential and osteonal lamellar bone of the baboon tibia. *J Mater Sci Mater Med.* 2000 Jan;11(1):49-60.
- Marcacci M, Dario P, Fadda M, Marcenaro G, Martelli S. Computer-Assisted Knee Arthroplasty. In Taylor RH et al (ed): Computer-integrated surgery: technology and clinical applications. Cambridge, Mass.: MIT Press. p41. 1996
- Marchant DC, Rimmington DP, Nusem I, Crawford RW. Safe femoral pin placement in knee navigation surgery: A cadaver study. *Comput Aided Surg* 9(6)257-260, 2004
- Mahdi M, Zhang L. A finite element model for the orthogonal cutting of fiber-reinforced composite materials. *Journal of Materials Processing Technology.* 113:373-377, 2001
- Malvisi A, Vendruscolo P, Morici F, Martelli S, Marcacci M. Milling versus Sawing: Comparison of Temperature Elevation and Clinical Performance During Bone Cutting. In: Delp SL (ed): Medical Imaging and Computer Assisted Intervention. Springer-Verlag. p1238, 2000
- Matthews LS and Hirsch C. Temperatures Measured in Human Cortical Bone when Drilling. *Journal of Bone and Joint Surgery.* 54A(2):297-308, 1972
- Martellotti ME. An Analysis of the milling Process. *Trans. ASME* 63:677-700, 1941
- Martellotti ME. An Analysis of the milling Process, Part 2-Down milling. *Trans. ASME* 67:233-251, 1945.
- Matsen FA, Garbini JL, Sidles JA, Pratt B, Baumgarten D, Kaiura R. Robot assistance in orthopaedic surgery: a proof of principle using distal femoral arthroplasty. *Clinical Orthopaedics and Related Research.* 296:178-186, 1993.
- McKenzie WM. Fundamental analysis of the wood-cutting process. *University of Michigan.* Ann Arbor, 1961
- Merchant ME. Basic mechanics of the metal cutting process. *ASME Journal of Applied Mechanics* 11: 168-175, 1944
- Mielke RK, Clemens U, Jens JH, Kershally S. [Navigation in knee endoprosthesis implantation--preliminary experiences and prospective comparative study with conventional implantation technique]. [German] *Zeitschrift fur Orthopadie und Ihre Grenzgebiete.* 139(2):109-16, 2001
- Minns RJ. Surgical instrument design for the accurate cutting of bone for implant fixation. *Clinical Materials* 10:207, 1992
- Mitsuishi M, Warisawa S, Sugita N, Suzuki M, Moriya H, Hashizume H, Fujiwara K, Abe N, Inoue H, Kuramoto K, Inoue T, Nakashima Y, Tanimoto K. Minimally invasive bone cutting system for TKA/UKA. 2nd European Summer School on Surgical Robotics, Montpellier, France, 2005
- Mocetezuma JL, Schuster D, Gosse F, Schulz HJ. A new oscillating saw for robotic aided surgery. *Proc Instn Mech Engrs.* 211:301, 1997
- Mont MA, Urquhart MA, Hungerford DS, Krackow KA. Intramedullary goniometer can improve alignment in knee arthroplasty surgery. *J Arthroplasty* 12:332, 1997
- Moreland JR: Mechanisms of failure in total knee arthroplasty. *Clin Orthop* 226:49, 1988
- Nogler N, Wimmer C, Lass-Florl C, Mayr E, Bach C, Krismer M. Is there a contamination risk for the surgical team through ROBODOC's high-speed bone cutter? Abstracts from CAOS. *Computer Aided Surgery* 4:223, 1999
- Nuno-Siebrecht N, Tanzer M, Bobyn JD. Potential errors in axial alignment using intramedullary instrumentation for total knee arthroplasty. *J Arthroplasty* 15:228, 2000
- Otani T, Whiteside LA, White SE: Cutting errors in preparation of femoral components in total knee arthroplasty. *J Arthroplasty*. 8:503, 1993

- Oxley PLB. Mechanics of Machining: an analytical approach to assessing machinability. Ellis Horwood Ltd. Chichester England. 1989
- Pal S. Bhadra N. Dutta S. Orthogonal cutting of bone. *Biomater. Med. Devices Artif. Organs* 14:124, 1986
- Perlick L, Bathis H, Tingart M, Perlick C, Grifka J. Navigation in total-knee arthroplasty: CT-based implantation compared with the conventional technique. *Acta Orthop Scand.* 75(4):464-70, 2004
- Perrenot B, Projet de fin d'études ENSIMAG: Rapport de Stage. 2003.
- Piazza SJ, Delp SL, Stulberg SD: Posterior tilting of the tibial component decreases femoral rollback in posterior-substituting knee replacement: a computer simulation study. *J Orthop Res* 16:264, 1998
- Plaskos C, Hodgson AJ, Inkpen KB, McGraw RW. Bone cutting errors in total knee arthroplasty. *J Arthroplasty*. 17(6): 698-705, 2002
- Plaskos C, Hodgson AJ, Masri BA. Improved instrumentation and technique for bone cutting in computer-assisted total knee surgery. *Proceedings of the IEEE Biovision International Conference on Biomedical Engineering*. pp. 39-44. 2001.
- Plaskos C, Hodgson AJ, Masri BA. A generalized model for predicting force and accuracy in bone milling with applications to computer-assisted total knee arthroplasty. *Proc. of the 2nd International Conference of Computer-Assisted Orthopaedic Surgery (CAOS)*. pp. 262-264, 2002
- Plaskos C, Hodgson AJ, Cinquin P. Modelling and optimization of bone-cutting forces in orthopaedic surgery. *Medical Image Computing & Computer Assisted Intervention (MICCAI)* 2003. pp. 254-261
- Poilvache PL, Insall JN, Scuderi GR, Font-Rodriguez DE. Rotational landmarks and sizing of the distal femur in total knee arthroplasty. *Clin Orthop.* 1996 Oct;(331):35-46.
- Pope MH, Outwater JO, The fracture characteristics of bone substance. *J Biomech.* 5:457-466, 1972
- Puw HY, Hocheng H. Milling force prediction for fiber-reinforced thermoplastics. *Proc. 114th ASME Winter Annual meeting, Machining of Advanced Composites.* 73-88, 1993
- Puw HY, Hocheng H. Anisotropic model of milling force prediction for fiber-reinforced plastics. *Eng. Sys. Des. Analysis. ASME* 75(3):11-20, 1996
- Rand JA, Bryan RS. Alignment in porous coated anatomic total knee arthroplasty. p. 111. In Dorr LD (ed): The Knee. Papers of the First Scientific Meeting of The Knee Society. University Park Press, Baltimore, 1985
- Ranftl A, Bruyninckx H, Gadeyne K, Vander Sloten J, De Schutter J, Bellemans J. Dynamic registration-Motion compensation during robot-assisted orthopaedic surgery. In *Proc. of Surgetica 2005, Computer assisted medical & surgical interventions*, 2005, pp 201-209
- Reilly D.T. Burstein A.H. The elastic and ultimate properties of compact bone tissue. *J Biomech.* (8):393-405, 1975
- Richards F. State-of-the-Art Electric Handpiece for Dental Surgeons. *Medical Equipment Designer*. March 1999.
- Ritschl P, et al: The Galileo System for implantation of Total Knee Arthroplasty – An Integrated Solution Comprising Navigation, Robotics and Robot-Assisted Ligament Balancing. In: *Navigation and Robotics in Total Joint and Spine Surgery*. Eds: Stiehl, Konermann, Haaker. Springer.-Verlag, 2004. pp. 281-361.
- Ritter MA, Faris PM, Keating EM, Meding JB. Postoperative alignment of total knee replacement. Its effect on survival. *Clin Orthop* 299:153, 1994
- Saha S, Pal S, Albright JA. Surgical Drilling: Design and Performance of an Improved Drill. *Journal of Biomechanical Engineering*. (104):245-252, 1982
- Saha S, Hayes WC. Tensile impact properties of human compact bone. *J Biomech.* 1976;9(4):243-51
- Saragaglia D, Picard F, Chaussard C, Montbarbon E, Leitner F, Cinquin P. [Computer-assisted knee arthroplasty: comparison with a conventional procedure. Results of 50 cases in a prospective randomized study]. [French] *Rev. Chir. Orthop. Reparatrice Appar. Mot.* 87:18, 2001

- Shoham M Burman M, Zehavi E, Joskowicz L, Batkilin E, Kunicher Y. Bone-mounted miniature robot for surgical procedures: Concept and clinical applications. *IEEE Transactions on Robotics and Automation* 19(5):893-901, 2003.
- Seki T, Omori G, Koga Y, Suzuki Y, Ishii Y, Takahashi HE. Is bone density in the distal femur affected by use of cement and by femoral component design in total knee arthroplasty?. *Journal of Orthopaedic Science*. 4(3):180-6, 1999
- Stabler GV. The fundamental geometry of cutting tools. *Proceedings of the Institution of Mechanical Engineers* 165:14–26, 1951
- Stindel E, Briard JL, Merloz P, Plaweski S, Dubrana F, Lefevre C, Troccaz J. Bone morphing: 3D morphological data for total knee arthroplasty. *Comput Aided Surg*. 2002;7(3):156-68.
- Sutherland JW, DeVor RE. An improved method for cutting force and surface error prediction in flexible milling systems. *J Eng Ind*. 108:269-79, 1986
- Taillant E, et al. CT and MRI compatible light puncture robot: architectural design and first experiments *Medical Image Computing & Computer Assisted Intervention (MICCAI)* 2004. 145-152.
- Teter KE, Bregman D, Colwell CW Jr. The efficacy of intramedullary femoral alignment in total knee replacement. *Clin Orthop*. 321:117, 1995
- TLusty J, MacNeil P. Dynamics of Cutting Forces in End Milling. *Annals of the CIRP*, 24(1):21-5, 1975
- Toksvig-Larsen S, Ryd L. Temperature Elevation During Knee Arthroplasty. *Acta Orthop Scan*. 60:4 1989
- Toksvig-Larsen S, Ryd L, Lindstrand A. Temperature influence in different orthopaedic saw blades. *J Arthroplasty*. 7(1):21-4, 1992
- Toksvig-Larsen S, Ryd L. Surface characteristics following tibial preparation during total knee arthroplasty. *J Arthroplasty* 9:63, 1994a
- Toksvig-Larsen S, Kroon PO, Ryd L. Improved bone cutting using a semirotating saw – A cadaver study of the cut surface on tibial condyles. *Acta Orthop Scand*. 65(4):412-414, 1994b
- Tria AJ Jr, Coon TM. Minimal incision total knee arthroplasty: early experience. *Clin Orthop*. 2003, (416): 185-90.
- Troccaz J, Delnondeldiou, Y. Semi-active guiding systems in surgery – A 2 DOF prototype of the passive arm with dynamic constraints (PADyC). *Int. J. Mechatronics*. 1996, 6(4), 399-42.
- Thomson EG, Lapsley JT, Grassi RC. Deformation Work Absorbed by the workpiece during metal cutting. *Trans. Amer. Soc. Mech. Engrs*. 75:591, 1953
- Van Ham G, Denis K, Vander Sloten J, Van Audekercke R, Van der Perre G, De Schutter J, Aertbelien E, Demey S, Bellemans J. Machining and accuracy studies for a tibial knee implant using a force-controlled robot. *Computer Aided Surgery*. 3(3):123-33, 1998
- Wagner HD, Weiner S. On the relationship between the microstructure of bone and its mechanical stiffness. *J Biomech*. 25(11):1311-1320, 1992
- Walker PS, Garg A. Range of motion in total knee arthroplasty. A computer analysis. *Clin Orthop* 262:227, 1991
- Weiner S, Wagner H.D. The material Bone: Structure-Mechanical Function Relations. *Annu. Rev. Mater. Sci.* 28:271–98, 1998
- Wevers HW, Espin E, Cooke TD. Orthopedic sawblades. A case study. *J Arthroplasty*. 2:43, 1987
- Whiteside LA, Amador DD. The effect of posterior tibial slope on knee stability after Ortholoc total knee arthroplasty. *J Arthroplasty* 3 Suppl:S51-57, 1988
- Wiggins KL. Machining of Bone. PhD Thesis. *University of Texas*. Aug. 1974
- Wiggins KL, Malkin S. Drilling of Bone. *J. Biomechanics*. 1976 (9)553-559.
- Wiggins KL, Malkin S. Orthogonal machining of bone. *J. Biomech. Eng* 1978 (100)122-130.
- Wiles AD, Thompson DG, Frantza DD. Accuracy assessment and interpretation for optical tracking systems. *Proceedings of SPIE*, Vol. 5367. Ed: Galloway RL. May 2004, pp. 421-432

- Windsor RE, Scuderi GR, Moran MC, Insall JN: Mechanisms of failure of the femoral and tibial components in total knee arthroplasty. *Clin Orthop* 248:15, 1989
- Wolf A, Jaramaz B, Lisien B, DiGioia AM. MBARS: mini bone-attached robotic system for joint arthroplasty. *International Journal of Medical Robotics and Computer Aided Surgery* 2005;1(1), 101-21
- Yamada K, Healey R, Amiel D, Lotz M, Coutts R. Subchondral bone of the human knee joint in aging and osteoarthritis. *Osteoarthritis Cartilage*. May;10(5):360-9, 2002
- Yellowley I, Observation on the mean values of forces, torques and specific power in the peripheral milling process. *International Journal of Machine Tool Design and Research* 25(4):337-346, 1985
- Ziv V, Wagner HD, Weiner S. Microstructure-microhardness relations in parallel-fibered and lamellar bone. *Bone*. 18(5):417-28, 1996

Appendix A1: Orthogonal Cutting Forces with Exponential Model:

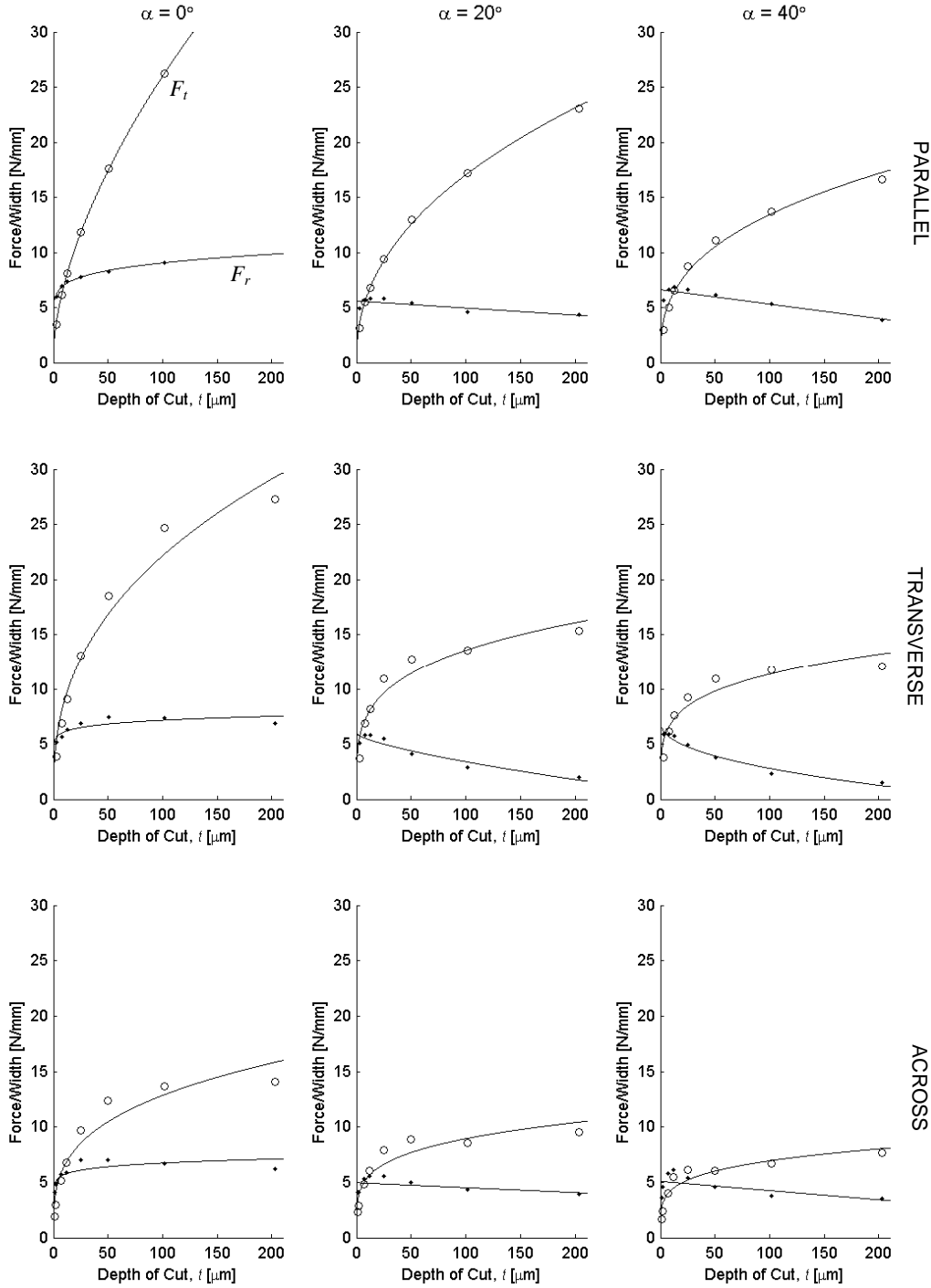
$$\mathbf{F} = \mathbf{K}t^n + \mathbf{K}_e$$


Figure A.12: Tangential (F_t) and radial (F_r) force components plotted against depth of cut for three different rake angles and cutting modes for large scale chip thickness (0-200 μm):

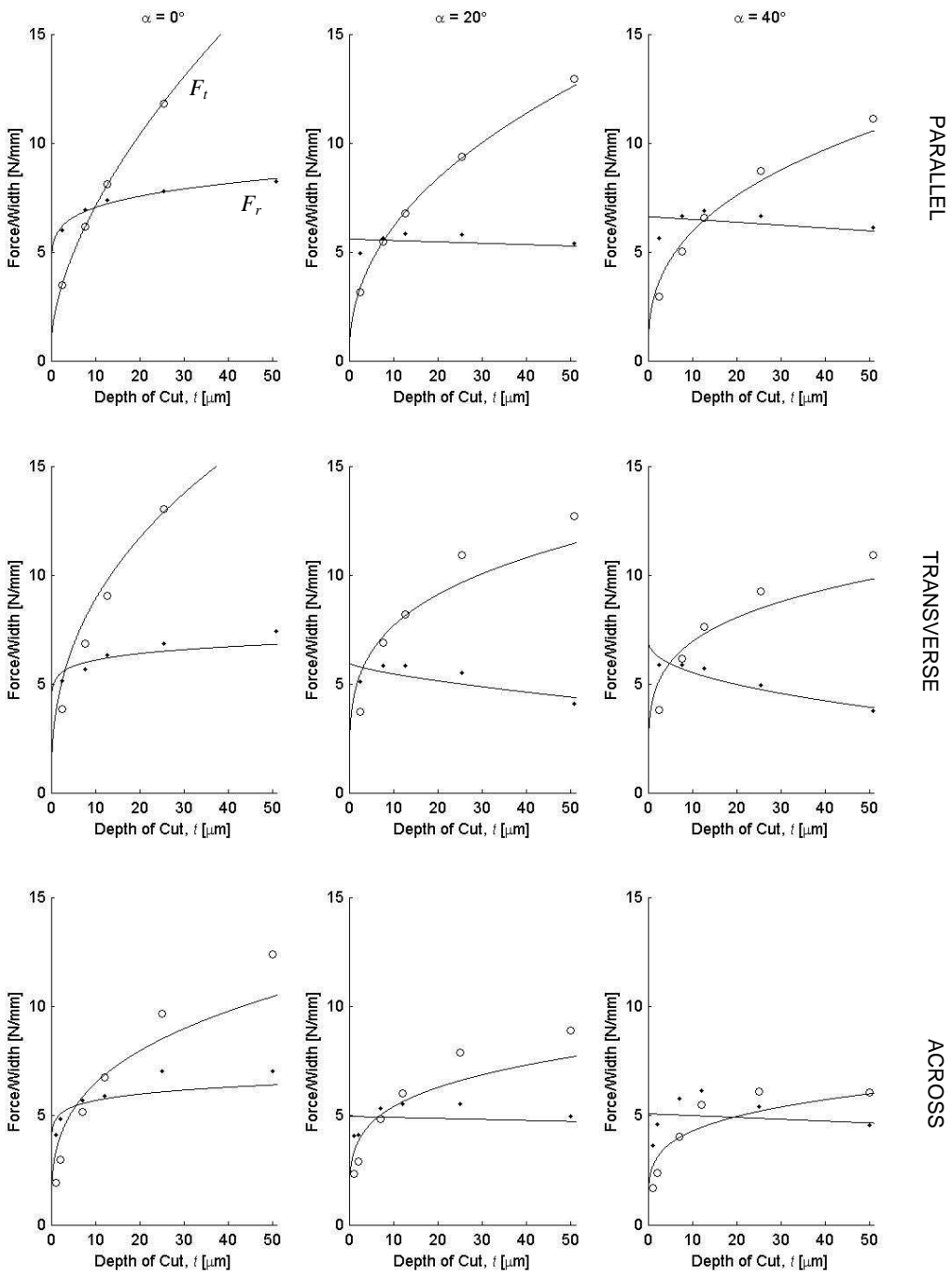


Figure A1.2. Tangential (\circ) and radial (\bullet) force components plotted against depth of cut for three different rake angles and cutting modes for small scale chip thickness (0-50 μm):